Università degli Studi di Trieste

XXXII

Dottorato di ricerca in Ingegneria industriale e dell'informazione

Numerical investigation of one-degree-of-freedom vortex-induced vibration of a rigid circular cylinder

ING-IND/01 ARCHITETTURA NAVALE

Ph.D. Student
Simone Martini

Ph.D. programme Coordinator
Prof. Fulvio Babich

Thesis Supervisor
Prof. Giorgio Contento

Thesis Co-Supervisor
Prof. Mitja Morgut

A. A. 2018/19

In memory of Prof. Giorgio Contento
"Per aspera ad astra"

Abstract

Vortex-Induced Vibrations of an elastically mounted rigid circular cylinder with one-degree-of-freedom (1-DOF) are numerically investigated. The mechanical system considered is characterised by low mass ratio and low damping ratio. A wide range of flow regimes, corresponding to a sub-critical Reynolds number, are taken into consideration. The vortex shedding around the cylinder is investigated numerically by the Unsteady Reynolds-Averaged Navier-Stokes (URANS) and by the Scale Adaptive Simulation (SAS) approaches. The results of the different numerical simulations have been compared to each other and to the experimental data from literature. The difference between bi-dimensional (2D) and three-dimensional (3D) URANS mesh models are in the upper branch region where the maximum amplitude of transverse oscillation occurs. From the analysis of the wake flow in span-wise direction, conducted with three-dimensional URANS and SAS simulation, it has been found that the three-dimensionality of the flow is stronger in the transition zone between the different branches. These zones are characterised by a hysteretic transition. Intermittency is also observed in the transition between upper and lower branches. It has been observed that three-dimensional flow behaviour is absent in the lower branch. In this region, the bi-dimensional simplification may be justified.
The quantification of the total uncertainty in the VIV quantity of interest due to the uncertainty in the value of closure coefficients of the SST turbulence model is performed. For the quantification analysis, three different flow velocities in the lower branch regime have been simulated with 2D URANS approach. The results identify a set of closure coefficients which most contribute to the uncertainty in the results.
A novel single-degree-of-freedom multi-frequency model (*sdof-mf*) for prediction of VIV is presented. The proposed *sdof-mf* model relies on the decomposition of the total hydrodynamic force in an inertia/drag force, conventionally associated with the cylinder motion in still fluid, and an additional lift force associated to pure vortex shedding. The parameters of this model are identified using a Parametric Identification (PI) procedure applied to time domain data of vortex induced forces, obtained via CFD simulations. From the overall results, the model exhibits promising capabilities in the reproduction of vortex shedding forces and cylinder motion, in terms of both amplitudes and frequencies.

Sommario

Le vibrazioni indotte dal fenomeno di distacco di vortici (VIV, Vortex-Induced Vibration) su un cilindro rigido a sezione, circolare montato elasticamente con un grado di libertà sono state simulate numericamente. Il sistema meccanico considerato è caratterizzato da un basso rapporto di massa e un basso rapporto di smorzamento. Nello studio è stata presa in considerazione un'ampia gamma di regimi di velocità del flusso incidente, corrispondenti a un numero di Reynolds subcritico.
Il distacco di vortici generato a valle da un cilindro è stato simulato numericamente tramite gli approcci Unsteady Reynolds-Averaged Navier-Stokes (URANS) e Scale Adaptive Simulation (SAS). I risultati delle diverse simulazioni numeriche sono stati confrontati tra loro e con i dati sperimentali di letteratura. La maggiore differenza nei risultati ottenuti, tramite l'applicazione del modello URANS a due differenti griglie di calcolo - bidimensionale (2D) e tridimensionale (3D) - si trova nella regione del ramo superiore (upper branch) dove si verifica la massima ampiezza di oscillazione trasversale.
Dall'analisi della scia in direzione assiale al cilindro, condotta tramite simulazioni tridimensionali URANS e SAS, è stato scoperto che la maggiore tridimensionalità del flusso si trova nella zona di transizione tra i diversi tipi di risposta. Queste zone di transizione sono caratterizzate da una risposta di tipo isteretico. Una risposta di tipo intermittente è stata osservata nella transizione tra i rami superiore (upper branch) e inferiore (lower branch). Si è osservato come non vi sia formazione di flusso tridimensionale nel ramo inferiore (lower branch). Si può considerare che, in questa regione, la semplificazione numerica bidimensionale sia giustificata.
Si è eseguita la quantificazione dell'incertezza totale e l'analisi di sensibilità del modello di turbolenza SST, dovuta ai suoi coefficienti di chiusura, applicato al caso del VIV. Per l'analisi di quantificazione, sono state simulate tre diverse velocità di flusso incidente nel regime del ramo inferiore (lower branch) con l'approccio URANS bidimensionale. I risultati ottenuti hanno identificato l'insieme di coefficienti di chiusura che maggiormente contribuiscono all'incertezza nei risultati.
Viene infine presentato un modello multi-frequenza a singolo grado di libertà (*sdof-mf*, single-degree-of-freedom multi-frequency model) per la previsione del fenomeno del VIV. Il modello *sdof-mf* proposto si basa sulla decomposizione della forza idrodinamica totale in una forza di inerzia/resistenza, convenzionalmente associata al movimento del cilindro nel fluido fermo e ad una forza di portanza aggiuntiva associata al distacco di vortici. I parametri di questo modello sono stati identificati usando una procedura di identificazione parametrica (PI, Parameter Identification) applicata ai risultati ottenuti nel dominio del tempo delle forze indotte dal distacco di vortici, ottenute tramite simulazioni CFD. Dai risultati complessivi, il modello mostra capacità promettenti nella riproduzione delle forze di distacco dei vortici e del movimento del cilindro, sia in termini di ampiezze che di frequenze.

Preface

This thesis was submitted to the Department of Engineering and Architecture of the University of Trieste in Italy, as a partial fulfilment of the requirements to obtain the Ph.D. degree. The work presented was carried out during the years 2017-2020 at the HyMOLab (Hydrodynamics and MetOcean Laboratory), a laboratory of the Department of Engineering and Architecture of Trieste under the supervision of Prof. Giorgio Contento and Prof. Mitja Morgut.

Present Contributions

The main objective of the present work is to expand the knowledge concerning the complex phenomenon of Vortex-Induced Vibration (VIV) through numerical studies.
These numerical studies deal with the flow around an elastically mounted rigid circular cylinder free to vibrate in cross flow direction at early subcritical Reynolds numbers. The mechanical system in question is characterised by low mass ratio and low damping ratio. The present work focuses on the simpler problem of only one-degree-of-freedom (1-DOF) with a single rigid circular cylinder in order to validate the CFD procedures and acquire a better assessment of the mesh requirements, turbulence models and computational resource.
The numerical investigation of two-degree-of-freedom (2-DOF) VIV or two or more circular cylinders in tandem arrangement are more relevant from an engineering point of view, but at the same time are complex subjects; the purpose of this work is precisely to be a starting point for the future research regarding more complex VIV problems.
An extensive comparison has been made to both experimental data and numerical simulations using bi-dimensional and three-dimensional URANS simulations and SAS simulations. Particular attention has been given to the study of the wake structures obtained by the different numerical methods considered. The numerical methods considered are appealing for the accuracy of VIV results but with reasonable computational costs.
A quantification of the total uncertainty in the VIV quantity of interest due to uncertainty in the value of closure coefficients of the selected turbulence model is performed. The contribution given to the expansion of the knowledge of these particular closure coefficients have an impact in reducing the parametric uncertainty of results for different flow problems including the VIV on a rigid circular cylinder.
Finally, a novel single-degree-of-freedom multi-frequency model (*sdof-mf*) for the prediction of an elastically mounted circular cylinder in cross flow is presented. The model is assessed considering a wide range of flow regimes, including lock in conditions and a different mass ratio.
The new semi-empirical model provides a new insight of the vortex induced forces and further numerical assessments are aimed at assessing how three dimensionality and tur-

bulence properties affects the numerical estimation of the phenomenon. The proposed *sdof-mf* model can be further exploited using more experimental and/or numerical data to extend its field of application so that it could be used as a simple method for assessing VIV response.

Structure of the Thesis

The thesis is organised as follows.

Ch.1 presents an overview of the complex phenomena of Vortex-Induced Vibration and the motivation behind this research. First of all, the governing and influencing parameters are introduced. After that the linearised equation of self-excited motion is presented.
Then, an introduction of the relevant concept and experimental studies is presented. The role of the mass ratio and mass damping parameter in the cylinder response in terms of peak amplitude of oscillation and oscillation frequency is discussed in detail. The wake of circular cylinder is discussed in the light of data obtained from the free oscillation experiments.
A review of the semi-empirical model with its classifications is presented here. This overview has a fundamental importance in order to better classify the proposed model among the existing ones.
Finally, the previous bi-dimensional and three-dimensional numerical studies on this topic are listed.

Ch.2 is devoted to the numerical results. The first part focuses on the URANS (Unsteady Reynolds-Averaged Navier-Stokes) numerical simulation approach. The sensitivity of the solution to the computational grid, first in the case of bi-dimensional (2D) simulations and then in the case of thee-dimensional (3D) simulations, are evaluated. An extended comparison of the results between the bi-dimensional and three-dimensional mesh models is carried out in order to understand when the bi-dimensional simplification is justified. Some additional simulations with doubled span-wise extension are carried out in order to understand if the selected domain size was sufficient for developing three dimensionality with the URANS approach. The advanced turbulence model Scale Adaptive Simulation (SAS) is used to predict more accurately all the VIV characteristics for all the interested flow regimes. A brief description of the SAS model is given. The improvement in the results of these turbulence models is presented and compared with the previous URANS results.
As the last task, several initial conditions are tested for both turbulence model approaches, 2D/3D URANS and SAS. The final section contains the conclusions.

Ch.3 contains the uncertainty quantification and sensitivity analysis of the SST turbulence model applied to VIV. The first section provides a brief description of the SST Turbulence models with a description of its closure coefficients. Then, the uncertainty quantification (UQ) and sensitivity analysis methodology is presented.

A couple of analytical examples have been performed in order to verify the implemented procedure. In the main section, the results of the UQ study are discussed along with a comparison with the previous UQ work. Major conclusions of these studies are presented at the end.

Ch.4 presents the proposed single-degree-of-fredom multi-frequency model (*sdof-mf*) and the related parameter identification procedure applied to time domain data of vortex force. The numerical data found in Ch.1 is used to obtain the VIV force time-series needed by the proposed model. The results obtained from the *sdof-mf* model are discussed. In particular, selected results are presented to justify/confirm the applicability of the current *sdof-mf* model. Then, the focus on effect of mass ratio, on the response of the cylinder and on the the components of the vortex shedding lift force obtained by the force decomposition adopted in the *sdof-mf* model, is discussed. Conclusions are given at the end of the chapter.

Ch.5 presents conclusions regarding the whole thesis and the proposals for future research are briefly discussed.

Contents

Notation

This section summarises the notation used in this Ph.D. Thesis. In order to avoid departing too much from the conventions normally used in literature a few symbols denote more than one quantity.

Abbreviations

1-DOF	One-Degree-Of-Freedom
CFD	Computational Fluid Dynamics
DES	Detached Eddy Simulations
DNS	Direct Numerical Simulation
DVM	Discrete Vortex Method
FFT	Fast Fourier Transform
GCI	Grid Convergence Index
LES	Large Eddy Simulation
LHS	Latin Hypercube Sampling
NIPC	Non-Intrusive Polynomial Chaos
PC	Polynomial Chaos
PCE	Polynomial chaos expansion
PDF	Probability Density Function
PIMPLE	Merged PISO-SIMPLE
PISO	Pressure Implicit of Split Operations
RANS	Reynolds Averaged Navier Stokes
RDA	Reduced Dimensionality Analysis
RE	Richardson Extrapolation
SAS	Scale-Adaptive Simulation
SIMPLE	Semi-Implicit Method for Pressure Linked Equations
UQ	Uncertainty Quantification

URANS Unsteady Reynolds-Averaged Navier-Stokes

WIV Wake-Induced Vibration

English Symbols

A	Amplitude response of the cylinder
A^*	Amplitude ratio
A^*_{max}	Maximum response amplitude of the cylinder
a_1	Bradshaw's structural parameter
b_1	Constant factor in the turbulent viscosity equation
C	Additive constant in the low of the wall
c_1	Constant factor in the production limiter
C_A	Potential added-mass coefficient
C_D	Drag coefficient
C_{EA}	Effective added mass
C_I	Inertia coefficient
C_L	Lift coefficient
$\overline{C_L}$	Harmonic amplitude for the lift coefficient of the cylinder body in the cross flow direction
$C_L(t)$	Time dependent lift coefficient
$C_{L,\mathrm{rms}}$	Root-mean-square of the non-dimensional total force
$C_{VS,\mathrm{rms}}$	Root-mean-square amplitude of the non-dimensional vortex shedding force
C_μ	Closure coefficient of the $k-\varepsilon$ model
$C_P(t)$	Time dependent potential added mass coefficient
C_R	Reaction coefficient
C_S	Smagorinsky constant
$C_{VS}(t)$	Time dependent vortex shedding coefficient
$CD_{k\omega}$	Positive portion of the cross-diffusion term
Co	Courant number
d	Distance from closest surface

D	Diameter of the cylinder
D^T	Total variance
$D_{i_1,\ldots,i_s}$	Partial variances
Δr	Radial extension of the near-wall layers from the surface of the cylinder
e^a	Approximate relative error
e^{ext}	Extrapolated relative error
f	Frequency of oscillation of a self-excited body
f^*	Frequency ratio
f_0	Natural frequency in water
$f_{0,a}$	Natural frequency in air
f_{0,a_d}	Damped natural frequency in air
F_1, F_2, F_3	Blending functions for shear-stress transport model
$\overline{F_L}$	Harmonic amplitude for the fluid force of the cylinder body in the cross flow direction
$F_L(t)$	Time dependent fluid force acting on cylinder body in the cross flow direction
$F_{L,inviscid}$	Inviscid component of the fluid force of the cylinder body in the cross flow direction
$F_{L,viscous}$	Viscous component of the fluid force of the cylinder body in the cross flow direction
$F_P(t)$	Time dependent potential added mass force acting on cylinder body
F_s	Factor of safety
$F_{SF}(t)$	Time dependent hydrodynamic force in still fluid acting on cylinder body
f_{St}	Vortex shedding frequency of the body at rest (Strouhal frequency)
f_{VS}	Vortex shedding frequency of a body in motion
$F_{VS}(t)$	Time dependent vortex shedding force acting on cylinder body
H	System damping
H_{crit}	System critical damping
k	Turbulent kinetic energy
K	Structural stiffness
$k_{farfield}$	Far-field value of turbulent kinetic energy

L	Length of the computational domain in the inflow direction
L_1	Length of the computational domain at the inflow
L_2	Length of the computational domain at the outflow
$\hat{L}$	Length scale of the modelled turbulence
L_{vK}	von Kármán length scale
Le	Legendre polynomials
M	Mass of the system
m^*	Mass ratio
m^*_{crit}	Critical mass ratio
$m^*\,\zeta$	Mass damping parameter
$(m^* + C_A)\,\zeta$	Modified mass-damping parameter
M_D	Displaced mass
M_A	Added mass
$\mathbf{n}$	Unit vector normal to the boundary
N	Total number of cells
n_c	Number of points along the circumference of the cylinder
n_l	Number of layers in the near-wall region
G	Grid expansion factor in the radial direction (cell size ratio between adjacent cells)
n_p	Oversampling ratio
N_s	Number of samples
n_s	Number of points along the span direction of the cylinder
P	Production of the kinetic energy of turbulence
p	Instantaneous static pressure; Order of convergence accuracy; Order of polynomial
p_0	Reference pressure
P_m	Number of output modes in a full non-intrusive polynomial chaos expansion
$\tilde{P}$	Limiter to prevent the build-up of turbulence stagnation region
Q_{SAS}	SAS source term

Q_{eq}	Equivalent linear drag
R	Convergence ratio
r	Refinement factor
Re	Reynolds number
Re_L	Reynolds number based on length of the computational domain
s	Variable indicating the sign
S	Length of the cylinder
$\hat{S}$	Generic solution
$\hat{S}^{ext}$	Extrapolated solution
$S_{i_1,\ldots,i_s}$	Sobol indices
S_{T_i}	Total Sobol indices
Sc	Scruton number
S_G	Skop-Griffin parameter
St	Strouhal number
t	Time
T_{St}	Strouhal period
$\mathbf{u}$	Instantaneous velocity in vector notation
U	Free stream velocity
U^*	Reduced velocity in water
U_a^*	Reduced velocity in air
u_i	Instantaneous velocity in tensor notation
$\mathbf{u}_\infty$	Instantaneous free stream velocity in vector notation
$\mathbf{u}_{wall}$	Instantaneous moving wall velocity in vector notation
$\mathbf{x}$	Deterministic vector
y	Displacement of the cylinder body in the cross flow direction
y^+	Dimensionless (sub-layer-scaled) distance
y_1	Distance of the first grid point above the wall
$\dot{y}$	Velocity of the cylinder body in the cross flow direction
$\ddot{y}$	Acceleration of the cylinder body in the cross flow direction

y^* Dimensionless displacement of the cylinder body in the cross flow direction

$\overline{y}$ Harmonic amplitude for the displacement of the cylinder body in the cross flow direction

Greek Symbols

α^* Stochastic response function

α_i Deterministic component of α^*

β^* Turbulence-model coefficient

β_1, β_2 Turbulence-model coefficients

χ^2 Merit function

Δ cubic root of the cell volume

δ_{ij} Coefficients involved in log calibration

ε Dissipation per unit mass

$\boldsymbol{\varepsilon}$ Random variable vector

η_2 Coefficient in the SAS equation source term

γ_1, γ_2 Coefficients involved in log calibration

Γ_1, Γ_2 Auxiliary variable in turbulence model

κ von Kármán constant

λ_2 Second eigenvalue of the symmetric tensor $E^2 + \Omega^2$

μ Fluid dynamic viscosity

μ_t Eddy viscosity

μ_t^{eq} Equilibrium eddy viscosity

μ_t^{LES} Eddy viscosity in the LES model by Smagorinsky

$\overline{\mu}$ Mass parameter defined by Skop-Griffin

ν Fluid kinematic viscosity

ν_{sgs} Sub grid scale viscosity

ω Turbulence specific dissipation rate

$\omega_{farfield}$ Far-field value turbulence specific dissipation rate

ϕ Phase angle between the total fluid force and the cylinder displacement

ϕ_R	Phase angle between the reaction and the acceleration of the cylinder
ϕ_{SF}	Phase angle between the force in still fluid force and the cylinder displacement
ϕ_{VS}	Phase angle between the vortex shedding force and the cylinder displacement
Ψ_i	Random variable basis function of α^*
ρ	Fluid density
σ	Turbulent Prandtl number (part of diffusion term)
σ_Φ	Coefficient in the SAS equation source term
ζ	Normalised damping

Chapter 1

Literature review and preliminary discussion

1.1 Preliminary remarks

The problem of Vortex Induced Vibrations (VIV) of cylinders in cross flow conditions arises in many fields of engineering. The prediction of fatigue damages and ultimate strength are final goals. Among others, coastal and marine applications such as riser tubes bringing oil from the seabed to the surface, marine cables for mooring floating offshore structures, sub-sea pipelines used primarily to carry oil or gas, but also for the fresh water transportation, and other situations of practical importance can be taken as examples.

VIV has been studied and adopted also for development of the renewable energy technology, using one or more oscillating cylinders in tandem configuration in a sea current. In particular, an essential research into energy harvesting from the VIV phenomenon is the VIVACE (VortexInduced Vibration Aquatic Clean Energy) converter which was patented by Bernitsas and Raghavan [1] in the University of Michigan.

VIV occurs when vortexes shed by a blunt structure in steady (or unsteady) flow induce an oscillatory force on the structure, mostly in the direction perpendicular to the ambient flow. If the structure is free to move or vibrate in the direction perpendicular to the onset flow or is partially restrained by restoring forces (moorings, structural stiffness, ...), the body starts oscillating. The quasi-synchronisation between vortex shedding frequency and natural frequency - or *lock-in* - may even occur; the structure undergoes near-resonance motions and large displacements are typically observed.

Such vibrations whose amplitude may be of the same order of the size of the body, depend on several parameters, among others the inflow velocity, the diameter of the cylindrical structures, the stiffness of the restoring mechanism, the mechanical damping and the mass of the body related to the displaced mass of fluid. There are also additional features that can affect the cylinder response such as the surface roughness and the incoming flow turbulence.

Much progress has been made during the past two decade, both experimentally and numerically, toward the understanding of the kinematics (vice dynamics) of the Vortex-Induced Vibration (VIV). To explain the complexity of VIV phenomenon I quote a small section of paper written by Sarpkaya [2] which best sums it up in a few words:

VIV is an inherenty nonlinear, self-governed of self-regulated, multi-degree-of-freedom phenomenon. It presents unsteady flow characteristics manifested by existence of large-scale structures, sandwiched between two equally unsteady shear layers

From the experiments and from the numerical studies much is known and understood, but much remains in the empirical/descriptive realm of knowledge. This knowledge is necessarily for the purposes of industrial applications. In particular, the controlling and influencing parameters that influence the dynamic response of fluid structure interaction need to be understood.
The experiments, as well as the numerical studies, try to qualify the relationships between the response of a structure and the governing and influencing parameters. Nevertheless, it remains difficult today to describe nature, identify occurrence and predict the characteristics of bluff bodies self-excited vibrations.

The purpose of this thesis is to try to make a small contribution to the knowledge of Vortex Induced Vibration through the numerical study of the phenomenon, paying particular attention to the industrial requirements of model simplicity and speed of response.

In particular, we want to analyse the amplitude response, the domain response frequency, the range of synchronisation, the variation of phase angle (by which the force leads the displacement), the input of the in-phase and out phase components of the transverse force (lift coefficients), the in-line drag coefficient, the damping coefficient among other influencing parameters.

1.2 Governing and influencing parameters

Before proceeding, it is worthwhile to define those variables considered in this Thesis. With D we define the outer diameter of a circular cylinder, S the length of the cylinder, U is the free stream velocity of fluid flow where ρ and ν are the fluid density and kinematic viscosity respectively.
In addition, there are a number of dimensionless parameters. The *reduced velocity* is defined as $U^* = U/f_0\,D$ where f_0 is the natural frequency of the structure. The VIV literature is rife with too many f symbols used to denote one specific frequency. For reasons of clarity, from here on we will indicate with:

- $f_{0,a}$ the natural frequency in air, obtained from pluck tests in still air;
- f_0 the natural frequency in water which includes the effects of added mass,
- f the frequency of oscillation of a self-excited body;
- f_{VS} the vortex shedding frequency of a body in motion;

- f_{St} the Strouhal frequency corresponding to the vortex shedding frequency of the body at rest. It is uniquely related to the velocity of the flow and the characteristic size of the body through the Strouhal number.

The Strouhal number, defined as $\mathrm{St} = f_{St}D/U$, is a dimensionless number which describes the oscillating flow behaviour. The parameter is named after Vincenc Strouhal, a Czech physicist who first measured in 1878 the frequency of audible tone produced by wires and rods whirled through the air. The variation of St are usually defined in terms of the Reynolds number $\mathrm{Re} = \rho U D/\mu$ a dimensionless parameter which represents the ratio of inertial to viscous force.
The value of St depends on the regime of the flow [3]. $\mathrm{St} - \mathrm{Re}$ relationships can be seen in Fig. 1.1. In the *Laminar periodic regime* the relationship is not linear. After $\mathrm{Re} > 300$ the value of St is constant at the value 0.2, above the value of $Re = 3.5 \times 10^6$, a strong spectral peak appears, well above the turbulence level.

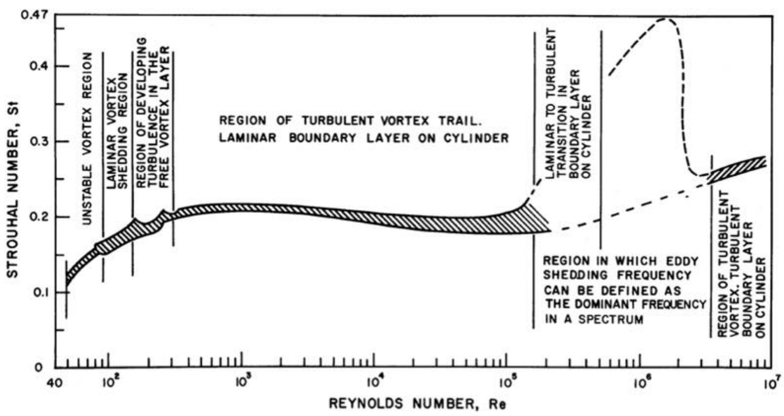

Figure 1.1: After Lienhard [4]. St trend in terms of Re- Transitional-Turbulent regime.

The *mass ratio* m^* is defined as $m^* = M/M_D$ where M_D is the displaced mass defined by $M_D = \pi\, \rho D^2\, S/4$. Different phenomena are seen in structures with high and low structure-fluid mass-ratios m^*. For systems with high-m^*, in the synchronisation range the vortex shedding frequency matches the natural frequency. For systems with low-m^*, it is the fluid oscillation which sets the frequency, the entrainment frequency, instead, tends towards the shedding frequency f_{VS}.

The *normalized damping* is defined as $\zeta = H/2\sqrt{K\,(M + M_A)}$ where H is the system damping, K is the structural stiffness and M_A is the added mass given by $M_A = C_A \cdot M_D$. The coefficient C_A is the potential added-mass coefficient and it can be considered equal to 1 [5] for a circular cylinder.

The *mass damping parameter* $m^* \zeta$ expresses the ratio between the damping force and the excitation force. This parameter, which is proportional to the often used Scruton number ($\mathrm{Sc} = \pi/2\,(m^*\zeta)$), strongly depends on the amplitude response during lock-in and band of fluid velocities over which the lock-in phenomenon exists. As the reduced damping parameter increases, lock-in becomes characterised by a decreasing peak structural amplitude and occurs over a decreasing band of velocities.
Finally, in the graphical representation of the oscillation, amplitude and frequency are plotted using two dimensionless values, respectively the amplitude ratio $A^* = A/D$ where A is the amplitude response of the cylinder, and the frequency ratio $f^* = f/f_0$. The explained nondimensional groups are summarised in Tab. 1.1

Mass ratio	m^*	$\frac{M}{\pi\,\rho D^2 S/4}$
Damping ratio	ζ	$\frac{H}{2\sqrt{k(M+M_A)}}$
Reduced velocity in water	U^*	$\frac{U}{f_0\,D}$
Reduced velocity in air	U^*_a	$\frac{U}{f_{0,a}\,D}$
Amplitude ratio	A^*, y^*	$\frac{A}{D}, \frac{\overline{y}}{D}$
Frequency ratio	f^*	$\frac{f}{f_0}$
Lift coefficient	C_L	$\frac{F_L}{\frac{1}{2}\rho\,D\,L\,U^2}$
Drag coefficient	C_D	$\frac{F_D}{\frac{1}{2}\rho\,D\,L\,U^2}$
Scruton number	Sc	$\frac{\pi}{2}(m^*\zeta)$

Table 1.1: Nondimensional groups.

1.3 Linearised equations of the self-excited motion

Mathematically, the one degree of freedom (1-DOF) dynamic system can be modelled as a rigid two-dimensional cylinder with mass M, supported by a spring with stiffness K and a damper, with damping H as represented in figure 1.2. The one degree of freedom equation of motion for such a mass-spring-damper system can be presented as:

$$M\,\ddot{y} + H\,\dot{y} + K\,y = F_L(t), \tag{1.1}$$

where $F_L(t)$ is the time dependent fluid force acting on a cylinder body in the cross flow direction, which is obtained by integration of pressure and viscous friction on the body surface resulting from the resolution of the Navier-Stokes equation. The symbols y, $\dot{y}$ and $\ddot{y}$ are respectively the displacement, velocity and acceleration of the body.

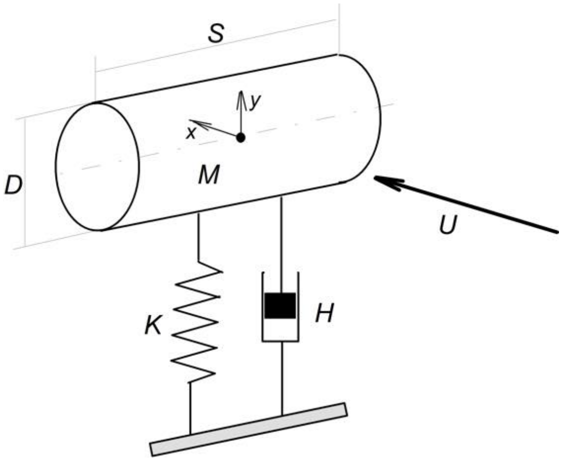

Figure 1.2: Harmonic oscillator model representing an elastically mounted cylinder.

A linear oscillator presents an undamped natural frequency

$$f_{0,a} = \frac{1}{2\pi}\sqrt{\frac{K}{M}}, \tag{1.2}$$

that only takes into account the structural stiffness (K) and the mass of the system (M).
The structural damping is generally expressed by a damping ratio

$$\zeta = \frac{H}{2\sqrt{K\,M}}, \tag{1.3}$$

defined as a fraction of the critical damping $(H_{crit} = 2\sqrt{K\,M})$. If the structural damping is kept sufficiently low, the damped natural frequency $f_{0,a_d} = f_0\sqrt{1-\zeta^2}$ can be considered approximately equal to $f_{0,a}$.
The fluctuating fluid force on the body can be expressed in terms of lift coefficient C_L, where

$$C_L(t) = \frac{F_L(t)}{\frac{1}{2}\rho\,U^2\,D}. \tag{1.4}$$

In order to understand the loading caused by the complex mechanism of vortex shedding, following the analysis proposed by Bearman [6], the equation can be rewritten (1.1) as

$$M\,\ddot{y} + 4\,\pi\,f_0\,\zeta\,M\,\dot{y} + 4\,\pi^2 f_0^2\,M\,y = C_L(t)\frac{1}{2}\rho\,U^2\,D \tag{1.5}$$

where the damping H was written by substituting the value of the stiffness K obtained from equation (1.2) into the equation (1.3). The Eq. (1.5) is a general equation that can be used to describe the response in the transverse or in-line direction, due to approaching turbulence, galloping, or vortex shedding.
For large-amplitude, steady-state and vortex-induced oscillations, the fluid force F_L and the body displacement y oscillate at the same frequency f, which is usually close to $f_{0,a}$. When a bluff body is responding to vortex shedding, the fluid force must lead to the excitation by some phase angle ϕ. Hence, the displacement y and the fluid force F_L can be represented by the expressions

$$y(t) = \overline{y}\sin(2\pi\, f\, t), \tag{1.6}$$

$$F_L(t) = \overline{F_L}\sin(2\pi\, f\, t + \phi_L), \tag{1.7}$$

where $\overline{y}$ and $\overline{F_L}$ represent the harmonic amplitude respectively for the displacement and for the fluid force. The equation of the fluid force (1.7) can be rewritten in terms of the coefficient C_L

$$C_L(t) = \overline{C_L}\sin(2\pi\, f\, t + \phi_L), \tag{1.8}$$

where $\overline{C_L} = \overline{F_L}/(1/2\rho U^2 D)$. With the angle transformation formula, the equation (1.8) can be written as

$$C_L(t) = \overline{C_L}\left(\sin(2\pi\, f\, t)\cos(\phi_L) + \cos(2\,\pi\, f\, t)\sin(\phi_L)\right). \tag{1.9}$$

Differentiating the displacement equation (1.6) $y(t)$ with respect to time gives

$$\begin{aligned} \dot{y} &= (2\,\pi\, f\, t)\,\overline{y}\cos(2\,\pi\, f\, t) \\ \ddot{y} &= -(2\,\pi\, f\, t)\,\overline{y}\sin(2\,\pi\, f\, t) \end{aligned} \tag{1.10}$$

Replacing the equations (1.10) and (1.9) into (1.5) we obtain

$$\begin{aligned} &-M\,(2\,\pi\, f\, t)\,\overline{y}\sin(2\,\pi\, f\, t) + 4\,\pi\, f_0\,\zeta\, M\,(2\,\pi\, f\, t)\,\overline{y}\cos(2\,\pi\, f\, t) + 4\,\pi^2 f_0^2\, M\,\overline{y}\sin(2\pi\, f\, t) \\ &\qquad = \frac{1}{2}\rho\, U^2\, D\,\overline{C_L}\left(\sin(2\pi\, f\, t)\cos(\phi_L) + \cos(2\,\pi\, f\, t)\sin(\phi_L)\right) \end{aligned} \tag{1.11}$$

and equating sine and cosine terms lead to the following relationship

$$\frac{f_{0,a}}{f} = \sqrt{1 - \frac{\overline{C_L}}{4\,\pi^2}\cos(\phi_L)\left(\frac{\rho\, D^2}{2\,M}\right)\left(\frac{U}{f_{0,a}\,D}\right)^2\left(\frac{y}{D}\right)^{-1}} \tag{1.12}$$

$$\frac{\overline{y}}{D} = \frac{\overline{C_L}}{8\,\pi^2}\sin(\phi_L)\left(\frac{\rho\, D^2}{2\,M\,\zeta}\right)\left(\frac{U}{f_{0,a}0\,D}\right)^2\frac{f_{0,a}}{f} \tag{1.13}$$

Taking into consideration the order of magnitude of various terms in equation (1.12), it can be shown that for large-amplitude oscillations of a body in air, where $\rho\, D^2/2\,M$

might be typically of order 10^{-3}, the frequency of body oscillations should be close to its natural frequency. This is confirmed by experiments. In a denser fluid such as water, where $\rho D^2/2M$ may be of order unity, the frequency of oscillation of the body can be appreciably different from its natural frequency. Considering that, the steady-state amplitude response of a bluff body subject to vortex shedding presented in Eq. (1.13) can be rewritten as

$$\frac{\overline{y}}{D} = \frac{\overline{C_L}}{8\,\pi^2}\sin(\phi_L)\left(\frac{\rho\,D^2}{2\,M\,\zeta}\right)\left(\frac{U}{f_{0,a}\,D}\right)^2. \qquad (1.14)$$

It is clear from equations (1.12), (1.13) and (1.14) that the phase angle ϕ_L plays an extremely important role. The response amplitude does not depend on C_L alone but on that part of C_L in phase with the body velocity.

1.4 A brief review of Vortex-Induced Vibration

The subject has received a huge consideration and a large amount of literature is now available, covering many aspects of the problem. Many of the VIV studies are discussed in the comprehensive reviews of Sarpkaya [7][2], Bearman [6], Gabbai and Benaroya [8] and Williamson and Govardhan [9][10], and in the books of Blevins [11] and Summer and Fredsøe [12].

1.4.1 Amplitude and frequency response

Two types of response character for such an elastically mounted system exist, depending on whether the combined mass–damping parameter $(m^*\zeta)$ is high or $(m^*\zeta)$ is low, as pointed out by Khalak and Williamson [5]. A well-known study of the response of an elastically mounted cylinder at high mass–damping parameter $(m^*\zeta) \approx 0.25$ was conducted by Feng [13]. Feng [13] contributed to some important classic measurements of response and pressure for an elastically mounted cylinder. He observed two different branches of amplitude response, which we describe as an "initial branch", corresponding to the highest amplitudes reached, and a "lower branch". In a subsequent experiment at high $(m^*\zeta)$ on a vibrating cable Brika and Laneville [14] also demonstrated the existence of two branches of response. Fig. 1.3 shows the results of the studies on an elastically mounted cylinder at high mass ratio conducted by Feng [13], in terms of amplitudes response and frequency of transverse force vs the "true reduced velocity" (U^*/f^*)St. In the same figure the results from Brika and Laneville [14] are plotted for comparison. It should be noted from Fig. 1.3, that, for both of these experimental results, a hysteretic transition between branches was observed.

Regarding the frequency response, presented in Fig. 1.3(b), the classical definition of lock-in or synchronisation is often perceived as the regime where the frequency of oscillation f, as well as the vortex formation frequency f_{VS}, are close to the natural frequency f_0 of the structure throughout the regime of large-amplitude vibration, so that f/f_0 is close to unity over a range of U^*. In contrast to the cases above, the low-$(m^*\zeta)$

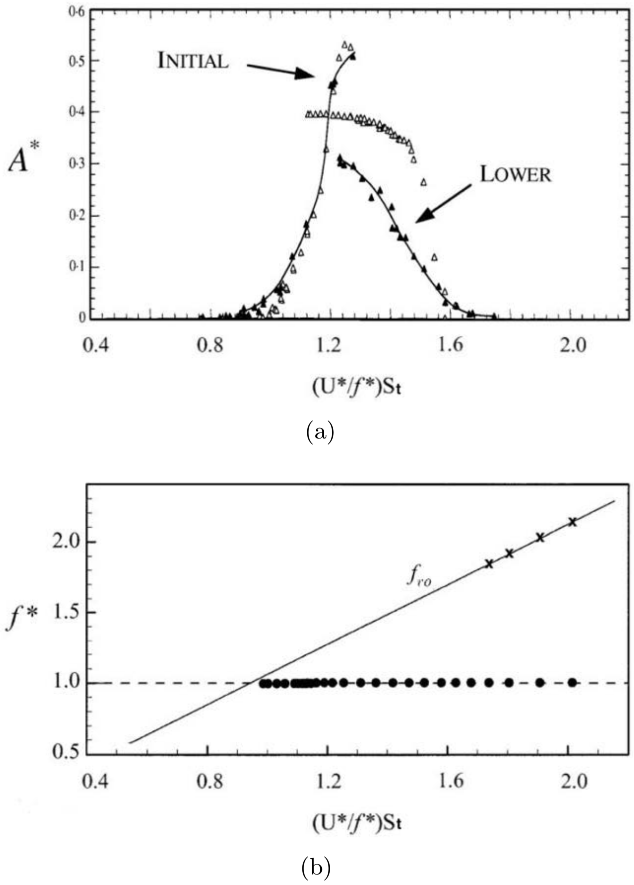

Figure 1.3: After Willamson and Govardhan [9]. Comparison of the experimental results from Feng [13] (▲) with Brika and Laneville [14] (△), both at the same (m^*/ζ), in terms of response amplitude (*Top figure*), vibration frequency (*bottom figure*) of the transverse force vs the non-dimensional parameter (U^*/f^*)St.

experiments of Khalak and Williamson [15] [5] showed the existence of three different branches of response:

i) the initial excitation regime,

ii) the upper branch of response (very high amplitude response),

iii) the lower branch of response (moderate amplitude response).

Fig. 1.4 compare the amplitude A^* and the frequency f^* response, as function of normalized velocity U^*, to the response measured by Feng [13]. Also shown in Fig. 1.4 the desynchronisation region as described in [16]. The amplitude results of Khalak and Willamson (Fig. 1.4(a)) shows much greater value, with nearly twice the maximum amplitude ($A^* \approx 1$) and an increase in range of velocity U^* over which the cylinder is excited. They found the transition between initial and upper branch to be hysteretic, while the transition from upper to lower branch involved an intermittent switching of modes.

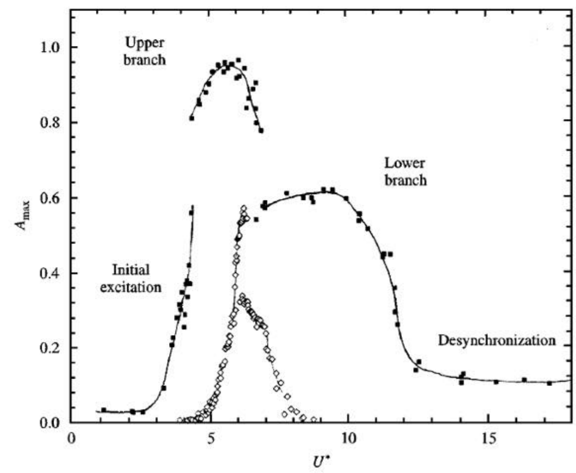

(a)

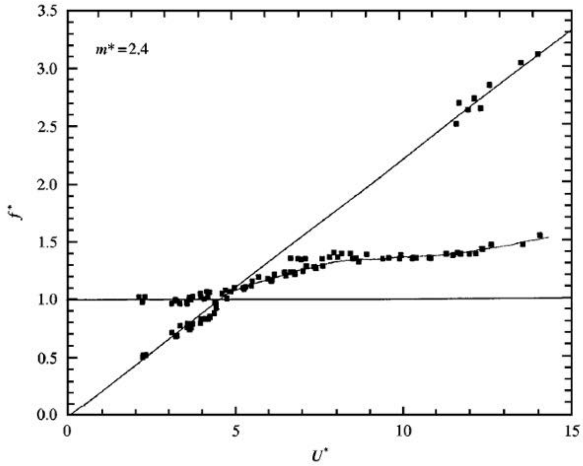

(b)

Figure 1.4: After Khalak and Williamson [16]. Amplitude A^* and frequency f^* response as function of normalised velocity U^*. (a) (■) presents the amplitude responce between the studies from Khalak and Willamson [16] with $m^* = 2.4$ and Feng [13] (⋄) who used $m^* = 248$. In (b) full square the oscillation frequency data from Khalak and Willamson [16] are presented.

Khalak and Willamson highlighted their particularly surprising result of oscillation frequency (fig. 1.4(b)). In fact, the oscillation frequency follows neither the vortex-

shedding frequency (for the stationary cylinder case) f_{St}, nor the structural natural frequency f_0. In classical lock-in from vortex-induced vibrations, the oscillation frequency f locks onto the natural frequency f_0. It is thus clear that the conditions of low mass and damping exhibit quite non-classical phenomena. From these considerations, Khalak and Willamson [5] suggested a more suitable definition of synchronisation as the matching of the frequency of the periodic wake vortex mode with the body oscillation frequency. Correspondingly, the fluid force frequency must match the shedding frequency, which is the useful definition of lock-in used by Sarpkaya [2].
In their experiments, Khalak and Williamson also investigated the effect of mass ratio m^*. The two cases were tested one with low mass ratio ($m^* = 2.4$) and the other with high mass ratio ($m^* = 10.3$), keeping the value of $m^*\zeta$ constant at a very low value.
The results in terms of amplitude of response are reported in Fig. 1.5. To obtain a good collapse of the two different results, Khalak and Williamson plotted the value of amplitude against a "true" reduced velocity U^*/f^* instead of U^*. As reported in Fig. 1.5, the difference in amplitude indicates that the position on the graph of A versus $m^*\zeta$ may not be unique for low $m^*\zeta$ in the lower branch of response. This indicates that m^* plays a role in transitions in the response curve. From these experiments they deduced that the widening of the synchronisation regime (as misused by a range of U^*) is an important effect of m^*. As the m^* decreases, when $m^*\zeta$ remains constant, there is a significant increase in the regime of synchronisation.

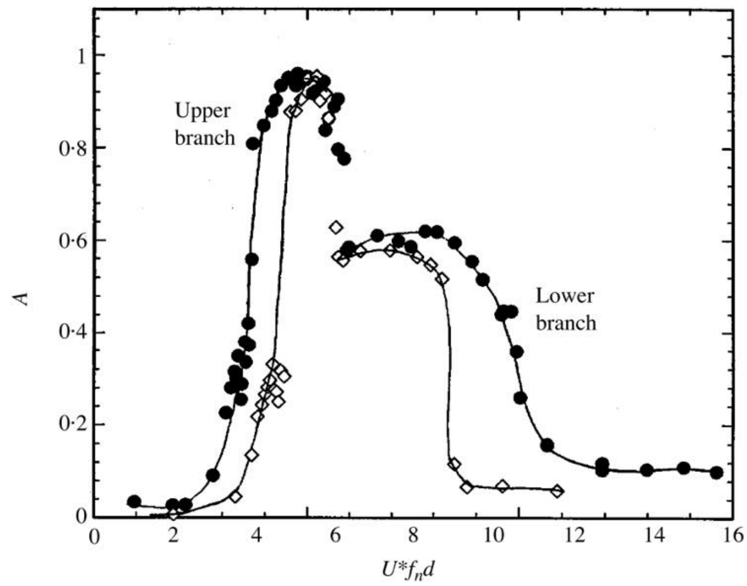

Figure 1.5: After Khalak and Williamson [15]. Response comparison for variation of m^*: $\bullet$ $m^* = 2.4$; $\diamond$ $m^* = 10.3$. The quantity $m^*\zeta$ has been kept constant for these two cases.

To summarise, the character of response for an elastically mounted system depends, among other things, on the combined mass damping parameter ($m^*\zeta$). Fig. 1.6 schematically summarises the two distinct types of amplitude response for high-($m^*\zeta$) and low-($m^*\zeta$). The high-($m^*\zeta$) response exhibits only two branches (initial and lower), while the low-($m^*\zeta$) type of response exhibits three branches (initial, upper and lower). The mode transitions are either hysteretic (H) or involve intermittent switching (I).The range of synchronisation is controlled primary by m^* (when $m^*\zeta$ is constant), whereas the peak amplitude is controlled principally by the product of $m^*\zeta$. For large mass ratios, that is $m^* = O(100)$, the vibration frequency for syncronization lies close to the natural frequency ($f* = f/f_0 \approx 1$), but as mass is reduced to $m^* = O(1)$, f^* can reach remarkably large values.

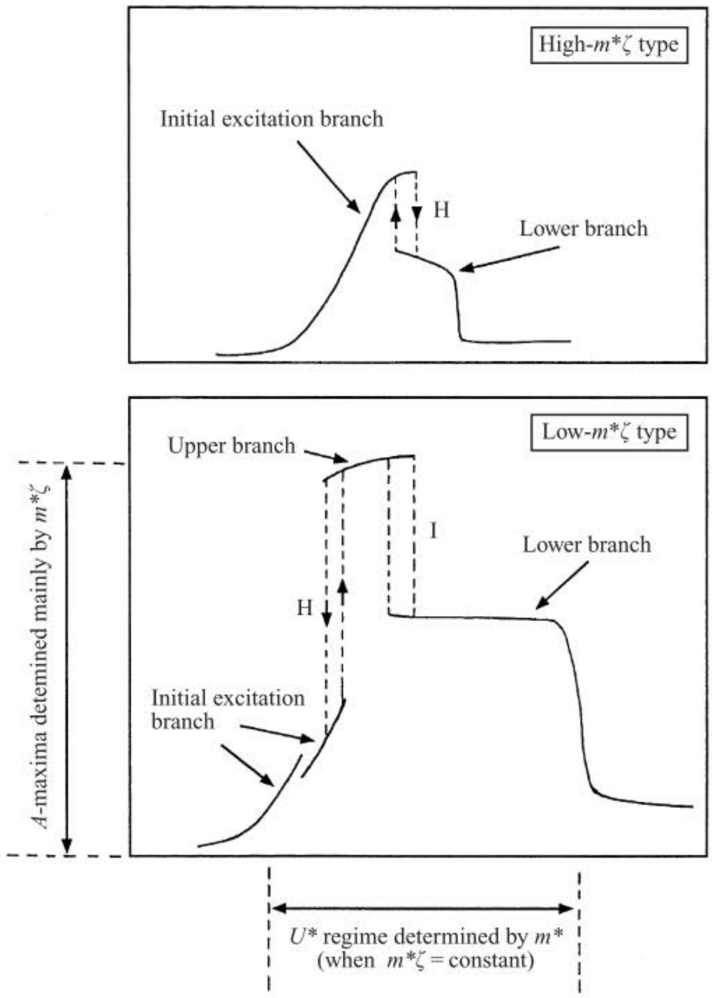

Figure 1.6: After Govardhan and Williamson [17]. The two distinct types of amplitude response are shown here schematically, for type of high-($m^*\zeta$) (top figure) and for low-($m^*\zeta$) (bottom figure). Vertical axis represents A^* and horizontal axis represents U^*.

1.4.2 Linear theory for low mass ratio

Khalak and Williamson developed the traditional linear theory, proposed by Bearman [6] (already presented in section 1.3), often used to describe vortex-induced vibrations, and demonstrated that the parameter $(m^*\zeta)$ does not predict the m^* dependence in the lower branch.
Considering the equation of a second-order linear system under fluid excitation

$$M\,\ddot{y} + H\,\dot{y} + K\,y = F_L, \tag{1.15}$$

For our case of low mass ratio, the inertia of the fluid being accelerated by the cylinder motion is necessary significant. For the theoretically inviscid case, the result is well known as the component of the force due to the added mass [18]. The fluid force can be decomposed into its viscous and inviscid components as follows:

$$M\,\ddot{y} + H\,\dot{y} + K\,y = F_{L,viscous} + F_{L,inviscid}. \tag{1.16}$$

Defining M_A as the inviscid added mass from which the inviscid force may be defined. Also introducing C_L as the instantaneous transverse force coefficient, used to characterize the viscous force:

$$F_{L,inviscid} \cdot n_y = -M_A\ddot{y}, \tag{1.17a}$$
$$F_{L,viscous} \cdot n_y = \frac{1}{2}C_L\rho\,U^2\,D\,S, \tag{1.17b}$$

where U is the flow velocity, ρ is the fluid density, D is the cylinder diameter and S is the length of the cylinder. It is important at this stage to introduce M_D, the mass of displaced fluid, which for a cylinder is $M_D = \pi\rho\,D^2S/4$. This gives

$$(M + M_A)\,\ddot{y} + H\dot{y} + Ky = \frac{2}{\pi D}C_L M_D U^2. \tag{1.18}$$

Using the non-dimensional quantities presented in Tab. 1.1 and defining $C_A = M_A/M_D$ as the added mass coefficient, the non-dimensional form of the equation of motion (1.18) becomes

$$(M + C_A)\left(\frac{1}{f_0}\ddot{y}^* + 4\pi\zeta\dot{y}^* + 4\pi^2 y^*\right) = \frac{2}{\pi}(U^*)^2 C_L, \tag{1.19}$$

where y^* is the non-dimensional position ($y^* = y/D$). In the more complex wake-oscillator models, C_L is described by a nonlinear differential equation which involves constants which must be measured empirically. However, to get an approximation to the resonant response without experimental tuning, the traditional approach is to assume a sinusoidal form for the fluctuating transverse force coefficient and the amplitude [6]:

$$y^* = A\sin(2\pi f t), \tag{1.20a}$$
$$C_L = \overline{C_L}(2\pi f t + \pi), \tag{1.20b}$$

where f is the forcing frequency and the response frequency at resonance (the matching of these two quantity defines resonance) and ϕ_L is the phase difference between the forcing and the response at resonance. Substituting the expression for y^* and C_L, and equating sine and cosine terms, we obtain

$$A\,(m^* + C_A)\,(1-(\frac{f^2}{f_0^2})) = \frac{1}{2\pi^3}(U^*)^2\overline{C_L}\cos\phi_L, \tag{1.21a}$$

$$A\,(m^* + C_A)\,(2\zeta(\frac{f}{f_0})) = \frac{1}{2\pi^3}(U^*)^2\overline{C_L}\sin\phi_L. \tag{1.21b}$$

Bearman [6] then obtained coupled equations for A and (f/f_0) and argued that, in the approximation of high-m^* , (f/f_0) was very close to unity to obtain an expression of A (see 1.3), since having accounted for the added mass, the quantity of (f/f_0) was also be near 1; however, it was more useful to solve explicitly for A. The result is the solution to a quadratic equation,

$$A = \frac{U^*\overline{C_L}\cos\phi_L}{4\pi^3(m^* + C_A)}\left[1 \pm (1 + \zeta^{-2}\tan^2\phi_L)^{1/2}\right] \tag{1.22}$$

In the case of lightly damped systems at resonance , the term $\zeta^{-2}\tan^2\phi_L$ is much greater than unity since ζ is small and ϕ_L is near $1/2\pi$. This gives

$$A = \frac{U^*\overline{C_L}\cos\phi_L}{4\pi^3(m^* + C_A)}\left[1 \pm \frac{|\tan\phi_L|}{\zeta}\right]. \tag{1.23}$$

As said before $\zeta^{-2}\tan^2\phi_L >> 1$, it is possible to extend this for $|\tan\phi_L|/\zeta >> 1$ by the same arguments on the smallness of ζ and closeness of ϕ_L to $1/2\pi$. In fact, this will hold even if $\tan\phi_L$ is order of unity. So, the final solution is

$$A = \frac{1}{4\pi^3}\frac{(U^*)^2\overline{C_L}\sin\phi_L}{(m^* + C_A)\zeta} \tag{1.24}$$

which is the identical result to the approximation for high m^* , except for the fact that it accounts for the inviscid added mass. Note that in Eq. (1.24) no explicit assumption has been made about the magnitude of m^*. The only stipulations are that ζ is small and that ϕ_L is not close to zero, both are not at all stringent for the resonant case.
Finally formulating Eq. (1.24) in terms of adimensional amplitude A^* and frequency ratio f^* follows

$$A^* = \frac{1}{4\pi^3}\frac{\overline{C_L}\sin\phi_L}{(m^* + C_A)\zeta}\left(\frac{U^*}{f^*}\right)f^* \tag{1.25}$$

$$f^* = \sqrt{\frac{m^* + C_A}{m^* + C_{EA}}} \tag{1.26}$$

where C_{EA} is an "effective" added mass coefficent that includes an apparent effect due to the total transverse fluid force in-phase with the body acceleration ($\overline{C_L}\cos\phi_L$):

$$C_{EA} = \frac{1}{2\pi^3}\frac{\overline{C_L}\cos\phi_L}{A^*}\left(\frac{U^*}{f^*}\right)^2. \tag{1.27}$$

The Eq. (1.25) indicates that the proper way to account for the added mass in the linear theory for low m^* is to use, instead of $m^*\zeta$, the quantity (m^*+C_A) a to predict the effects of mass and damping. It could be imagined that , even in the non-linear regime , the response will be non-linearly related to $(m^* + C_A)$.
It should be also noticed that the amplitude A^* is proportional to the transverse force component that is in phase with the body velocity ($\overline{C_L}\sin\phi_L$), and it is well known, from experimental results that, for small mass and damping, the precise value of the phase angle ϕ_L has a large effect on the response amplitude.

1.4.3 The peak response amplitude plot

A fundamental question regarding such an elastically mounted system, is how the maximum response amplitude A^*_{max} will vary as a function of system mass and damping. In literature, the value of A^*_{max} has been plotted as a function of S_G, generally known as 'Skop-Griffin' parameter. S_G is a parameter proportional to the product of mass and damping and is defined as

$$S_G = 2\pi^3\mathrm{St}^2(m^*\zeta). \tag{1.28}$$

Griffin and co-workers in 1970 used the S_G parameter for the first comprehensive compilation of $A*_m ax$ in a log-log plot, today known as "Griffin plot". The logic in choosing a combined parameter involving the product of mass and damping comes from observation of Eq. (1.25) for A^*. As discussed in 1.3, in the case of large mass ratio $m^* >> 1$ the oscillation frequency f at resonance will be close to the vortex shedding frequency for a static cylinder f_{St}, and also close to the system natural frequency f_0 thus leads to $f^* = f/f_0 \approx 1$. One may also notice that in the case of large mass ratio m^*, in the Eq. (1.26) and with C_A,$C_{EA} = O(1)$, $f^* \approx 1$. Hence, at resonance the parameter becomes $(U^*/f^*) = (U/fD) \approx (U/f_{\mathrm{St}}D) = 1/\mathrm{St}$, which is close to 5.0. It is often assumed that both (U^*/f^*) and f^* are constraints under resonance conditions, giving

$$A^*_{max} \propto \frac{\overline{C_L}\sin\phi_L}{(m^* + C_A)\zeta} \tag{1.29}$$

Under this assumption, A^*_{max} is a function of the product of mass and damping $(m^* + C_A)\zeta$. The problems regarding the validity of "Griffin plot" were pointed out clearly by Sarpkaya [7] [2] and Bearman [6]. Criticisms stated by the simple observation of the equation of motion (equivalent to Eq. (1.15)) have led to the conclusion that the dynamic response is governed, among other parameters, by m^* and ζ independently, not just by $(m^*\zeta)$." On the basis of the analysis of three data points, Sarpkaya [7] suggested that one should use the combined parameter S_G only if $S_G > 1.0$, which ruled out most of the plot, as one can see in Fig. 1.7.

On the other hand, Griffin and Ramberg [19] performed two sets of experiments, using the same value of $S_G = 0.5 - 0.6$ for both, but with dissimilar mass ratios, $m^* = 4.8$ and 43. These data demonstrate two points; first, the lower mass ratio leads to a wider synchronisation regime, extending over a larger range of normalized velocity U^*, second, at the same S_G, the peak amplitude is roughly unchanged at $A^*_{max} = 0.5$, despite the fact that $S_G < 1.0$.

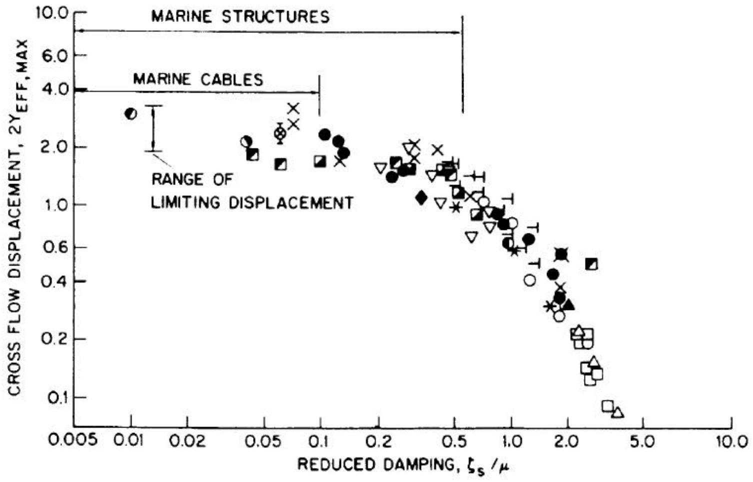

Figure 1.7: After Williamson and Govardhan [9]. One of the original griffin plots, showing maximum cross flow displacement ($A^*_{max} = 2Y_{\mathrm{EFF,MAX}}$ in figure) plotted versus the Skop-Griffin parameter $S_G = \zeta/\overline{\mu}$ where $\overline{\mu} = \rho D^2/8\pi^2\mathrm{St}^2 M$.

If we plot an extension of the "Griffin plot" for a variety of experiments compiled by Skop and Balasubramanian [20] using a linear Y-axis in Fig. 1.8(a), we can see a significant scatter, otherwise masked by the classical log-log format. The collected data from Khalak and Williamson [5] indicated that the maximum attainable amplitude lies anywhere in the range $A^* = 0.8$–1.6. Given this scatter, it does not appear reasonable to collapse data for such different VIV systems (free cylinder, cantilever, pivoted cylinders, etc.) in the same plot.
By removing the data for different vortex-induced systems (forced oscillation, pivoted cylinders, etc.), and therefore taking into consideration only those data corresponding to elastically mounted cylinders, Khalak and Williamson [5] presented an updated version of "Griffin plot. As one can see in Fig. 1.8(b), they also introduced two distinct curves representing the peak amplitudes for both the upper and the lower branches. Fig. 1.8(b) also took into account the added mass, indeed the mass damping parameter $m^*\zeta$ was replaced with the quantity $(m^* + C_A)\zeta$. The approximate functional relationship found, between A^*_{max} and $(m{*}{+}C_A)\zeta$ was applicable for the regime $m{*} > 2$ and $(m{*}{+}C_A)\zeta > 6$ to compare the resulting data from different experimental arrangements. This procedure extended the regime of validity of the Griffin plot to two orders of magnitude lower mass-

damping (down to $S_G \approx 0.01$) rather than the limit ($S_G > 1$) suggested by Sarpkaya and often quoted in the literature. Equations to fit the compiled data in the "Griffin plot" were put forward by several investigators. In particular, Sarpkaya [7] used the assumed equation of motion to derive a simple equation relating A^*_{max} to S_G, as follows

$$A^*_{max} = \frac{B}{\sqrt{C + S_G^2}}. \tag{1.30}$$

This equation fits the data reasonably well as indicated by the curve in Fig. 1.8(a), where $B = 0.385$ and $C = 0.12$. Note that B and C are not strictly constants. In fact, the value of B is proportional to C_L, and C_L in turn depends on A^*. Therefore, one cannot assume that such a formulation will accurately fit the data, a priori. In fact, an even simpler formulation was proposed by Triantafyllou and Grosenbaug [21], where they empirically represented the lift coefficient that is in phase with the velocity $\overline{C_L} \sin \phi_L$ (considering a purely sinusoidal force) as linear function of A^*

$$(\overline{C_L} \sin \phi_L) = D - E\, A^* \tag{1.31}$$

where D and E are curve-fitting constraints, and used it in their new proposed formula

$$A^*_{max} = \frac{D}{E + \frac{1}{2} S_G} \tag{1.32}$$

which also fits the "Griffin plot" data reasonably well.

1.4.4 Vortex-shedding modes

The character of the vortex-shedding is important because it influences the phase of lift force and, consequently, the energy transfer between the fluid and the body. Brika and Laneville [14] were the first to show a change in the pattern of vortex formation, as one varied normalised velocity U^* or the amplitude ratio A^*. Subsequent forced-vibration studies by Williamson and Roshko [22] over a wide range of A^* and U^* (corresponding to $\mathrm{Re} = 300 - 1000$), showed a number of different vortex formation modes. Williamson and Roshko [22] presented a map of vortex synchronisation pattern: in Fig. 1.9 this map of vortex synchronisation patterns near the fundamental lock-in region is reported. The amplitude ratio values were presented in function of the velocity ratio U^* [1] and ratio between the frequency of the forced oscillation in transverse direction f and the frequency of vortex shedding for non oscillating cylinder f_{St}.

Within the fundamental lock-in region ($U^* \approx 5$ or $f/f_{\mathrm{St}} \approx 1$), the acceleration of the cylinder at the start of each half-cycle induces the rolling up of each of the separating shear layers into a new pair of vortices.

Consequently, the cylinder sheds four regions of vorticity in each cycle. The authors found

[1] The original Williamson-Rosko map presents the value of A^* as function of wavelenght ratio, that is equivalent to the reduced velocity, but has the distinct advantage that it introduces the trajectory along which the body travels relative to fluid.

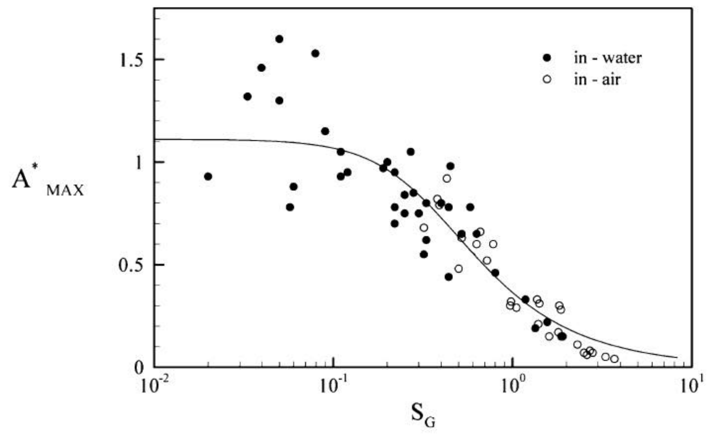

(a)

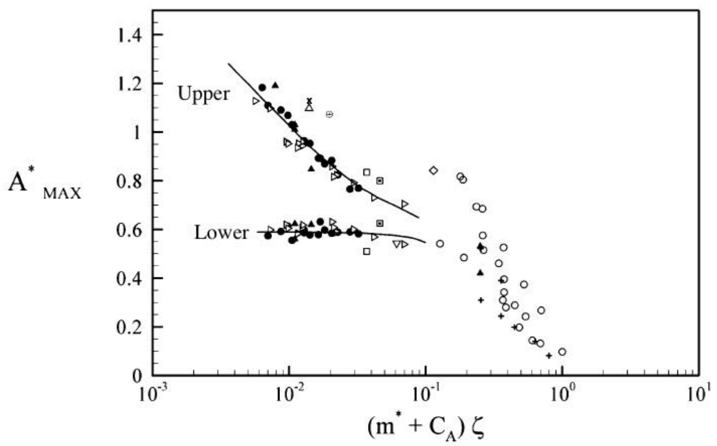

(b)

Figure 1.8: After Williamson and Govardhan[9]. The Griffin plots. (a) Maximum amplitude A^*_{max}, using a linear Y-axis, vs the Skop-Griffin parameter S_G. (b) Maximum amplitude A^*_{max} for upper and lower branches vs the corrected mass-damping parameter $(m^* + C_A)\zeta$, to account for the neglected added mass, as proposed by Khalak and Williamson [15]. In (a) is is the Eq. (1.30) with the best fit $B = 0.385$ and $C = 0.120$. Other symbols and lines refer to [9].

out that, below a critical trajectory wavelength (for a given amplitude ratio A^*), each half-cycle results in the coalescence of a pair of like-signed vortices. Consequently, two regions of opposite vorticity are fed into the downstream wake per cycle. The resulting formation is similar to the classic von Kármán vortex street wake and is called the 2S mode. Above the critical trajectory wavelength, the like sign vortices are found to convect

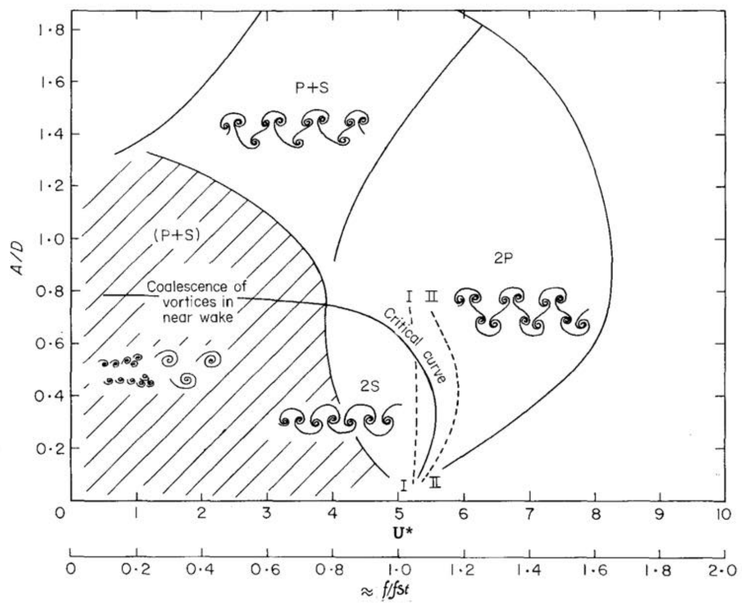

Figure 1.9: After Williamson and Roshko [22]. Map of vortex synchronisation near the fundamental lock-in. The "critical curve" represents the transition from one mode of vortex formation to another. Curves I and II represents where the forces on the body show a sharp jump. I is for U^* decreasing and II is for U^* increasing.

away from each other. Each of these vortices then paired up with a vortex of opposite sign. The resulting formation is two vortex pairs (of opposite signs) convecting laterally away from the centreline. This mode is called the 2P mode.
At exactly the critical wavelength, four regions are no longer formed. Only two vortices are formed in each cycle and the resulting shed vorticity is more concentrated than at other reduced velocity. This condition is called the "resonant" synchronisation. The "resonant" synchronisation is important because it coincides (approximately) with the peak in the lift forces seen in experimental results. The conclusion is that the larger forces are being induced by the shedding of more concentrated vorticity [8].
In a small range of U^* either one or two modes can exist, hysteresis will result. Moving from 2P to 2S mode (decreasing U^*) the jump occurs for a U^* less than that in the passage from 2S to 2P mode (increasing U^*). In Fig. 1.9 these two different critical curves are also reported, I is for decreasing U^* and II is for increasing U^*.
By plotting the experimental amplitude data in the Williamson-Rosko map of different wake modes, Khalak and Willianson [5] noted that the data for the lowest mass ratio ($m = 2.4$ in their experiments) did not follow the expected drop-off in amplitude when U^* exceeds the limit of periodic 2P mode and move into the regime of desynchronisation. They argued that, for low mass ratios, the conventional normalized velocity U^* is not the best parameter to make the response plot. In fact, it is well known that a reduction in mass (e.g. from $m^* = 8.6$ to 1.2) leads to wider synchronisation regime. Hence,

Khalak and Willianson [5] proposed a re-plotting of the data versus an equivalent "true" reduced velocity, defined as (U^*/f^*)St which is equivalent to (f_{St}/f) (inverse of the ratio of the oscillating frequency to the fixed body shedding frequency). As reported in Fig. 1.10, by using the equivalent "true" reduced velocity the data sets collapse very well. It is expected that the wake patterns will be the same when one matches both the amplitude A^* and the equivalent "true" reduced velocity. This is in accordance with the visualisation presented by Khalak and Willamson [5] which is reported in Fig. 1.11. However, the use of the equivalent "true" reduced velocity works well for low-$(m^*\zeta)$. This is because the upper branch frequency $f^* \approx 1$ for a wide number of different m^* gives the same maximum amplitude; it is also the same for the lower branch, because the amplitude saturation level, independent of $(m^*\zeta)$, has been reached for low-$(m^*\zeta)$ (see the Griffin plot Fig. 1.8).

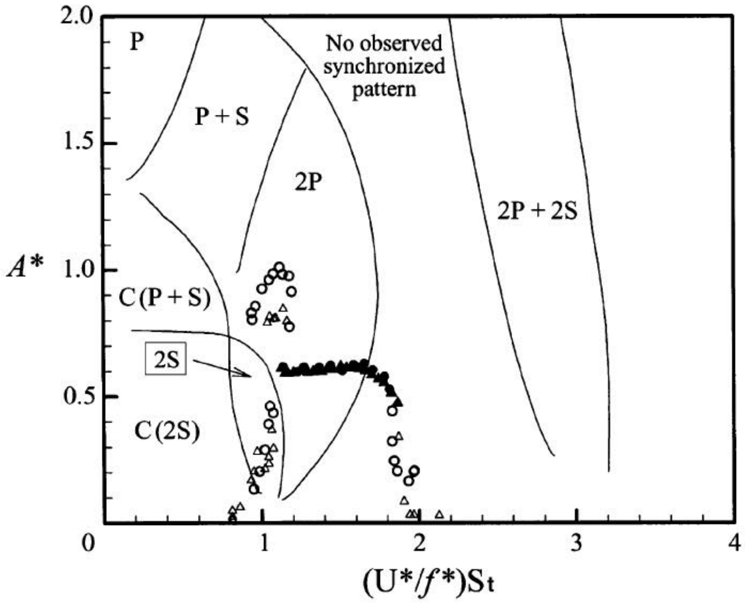

Figure 1.10: After Govardhan and Williamson [17]. Amplitude response for two different mass ratios m^* plotted on the Williamson-Roshko map of wake modes. $\bullet$, $\circ$ $m^* = 1.19$ and $(m^* + C_A)\zeta = 0.0110$; $\blacktriangle$, $\triangle$ $m^* = 8.63$ and $(m^* + C_A)\zeta = 0.0145$. Solid symbols indicate the lower branch regimes.

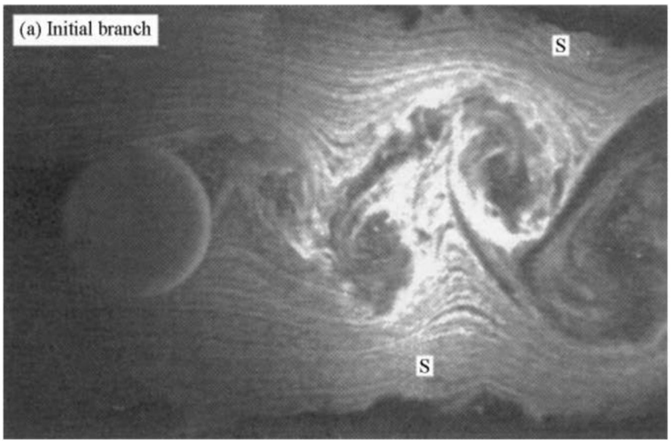

(a) Re = 4500

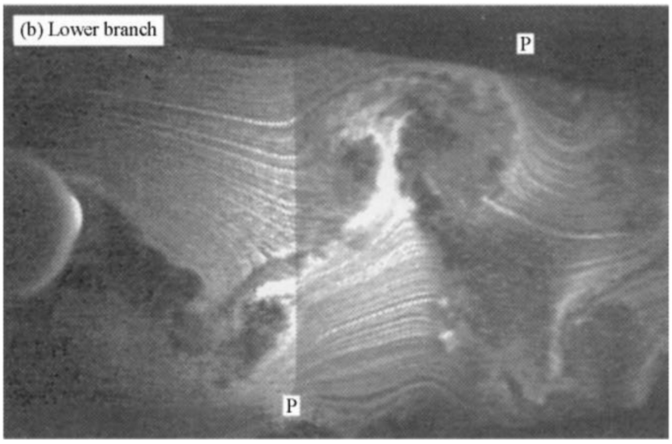

(b) Re = 6000

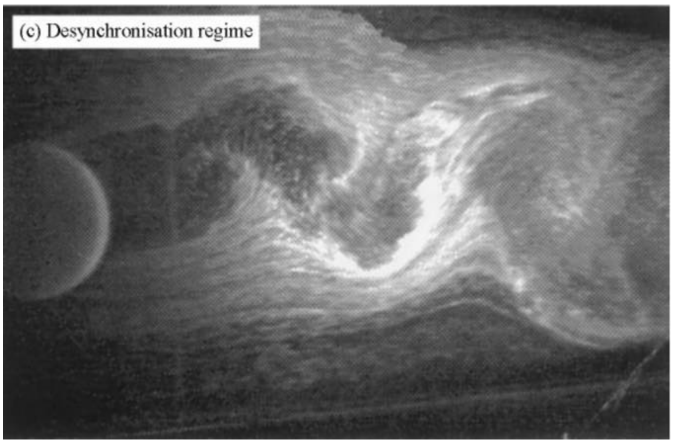

(c) $Re = 9000$

Figure 1.11: After Khalak and Williamson [5]. Hydrogen-bubble flow visualization of (a) the initial branch (2S mode), (b) the lower branch (2P mode)and (c) the desynchronised mode.

1.4.5 Lift force and vortex force phase jump

An important feature of the dynamics of such elastically mounted systems is the jump in phase ϕ_L between the transverse force C_L and the cylinder displacement y that occurs when the response changes modes.
The phase jump was previously inferred by Feng [13]. He saw that the jump of ϕ_L was associated with the oscillation frequency f passing though the natural frequency of the structure in air $f_{0,a}$. The equation of motion used to represent the body dynamics in Eq.(1.33) can be combined with the Eq. (1.7), which assumes harmonic motion:

$$M\,\ddot{y} + H\,\dot{y} + K\,y = \overline{F_L}\sin(2\pi\,f\,t + \phi_L). \tag{1.33}$$

Substituting the Eq. (1.6) into the above equation and balancing $\sin(2\pi f t)$ terms we have

$$\frac{\overline{F_L}\cos\phi_L}{K\overline{y}} = 1 - \left(\frac{f}{f_{0,a}}\right)^2. \tag{1.34}$$

From these simple results one can notice that, as ϕ_L jumps through the value of 90°, then the $(f/f_{0,a})$ passes throughout 1. The "classical" phase jump was associated with a change in timing of vortex shedding. This assumption was denied by the studies of Khalak and Williason [15].
To understand the existence of more than one mode transition for low-$(m^*\zeta)$, Govarhan and Williamson [17] formulated the equation of motion in function of the "vortex force", which is related only to the dynamic of vorticity. They decomposed the total fluid force F_L into a "potential force" F_P, given by the potential added mass force, and a "vortex force" component F_{VS} that is due to the dynamics of what is called "additional vorticity" [2].
The vortex force is related in a definite way to vortex dynamics, and to the convection of vorticity. Any jump in vortex force would necessarily correspond to sharp changes in the process of vortex formation.
The vortex force $F_{VS}(t)$ can be computed from:

$$F_{VS}(t) = F_L(t) - F_P(t). \tag{1.35}$$

Normalizing the force by $F_0 = 1/2\rho U^2 DS$ gives the equation in terms of coefficient:

$$C_{VS}(t) = C_L(t) - C_P(t). \tag{1.36}$$

The instantaneous potential added mass force $F_P(t)$ acting on a cylinder is given by

$$F_P(t) = -C_A M_D \ddot{y}(t) \tag{1.37}$$

[2] "additional vorticity" refers to the entire vorticity in the flow field minus part of the distribution of vorticity attached to the boundary in the form of a vortex sheet, allowing exactly the tangential velocity (slip) associated with the potential flow,' as stated by Lighthill [23]

with the displaced fluid mass given by $M_D = \pi D^2 S/4$. Substituting $y(t) = \overline{y}\sin(t)$ into the Eq. (1.37) and normalizing it, the potential force can be rewritten as $C_P(t)$

$$C_P(t) = 2\pi^3 \frac{y(t)/D}{(U^*/f^*)^2}. \tag{1.38}$$

It can be seen from the Eq. (1.38) that the instantaneous potential added mass force $C_P(t)$ is always in-phase with the cylinder motion $y(t)$, as one might expect. Now, we can rewrite the equation of motion (1.33) in terms of vortex force

$$(M + M_A)\,\ddot{y} + H\,\dot{y} + K\,y = \overline{F_{VS}}\sin(2\pi\,f\,t + \phi_{VS}). \tag{1.39}$$

To clarify, two distinct phases are presented: the total phase ϕ_L between the total force and displacement and the vortex phase ϕ_{VS} between the vortex force and the displacement.
Inspecting the equation of motion using the "vortex force" (Eq. (1.39)), and following the same procedure to achieve the Eq. (1.34), leads to

$$\frac{F_{VS}\cos\phi_{VS}}{K\overline{y}} = 1 - \left(\frac{f}{f_0}\right)^2 \tag{1.40}$$

Therefore, as ϕ_{VS} jumps though 90° then (f/f_0) passes through 1.
From the experimental results Govardhan and Williamson [17] found that there was no jump in vortex phase ϕ_{VS} at the upper-lower branch transition, contrary to what was argued in the previous studies. On the other hand, between the initial and the upper branches, there is a vortex jump. There will necessarily be a switch in timing of the cyclic vortex formation. The overview diagram in Fig. 1.12 shows how there are two distinct jumps between modes for low-$(m^*\zeta)$. In essence, the transition from initial to upper branch is associated with a jump in vortex phase ϕ_{VS} as the response frequency passes through the value $f = f_0$ (natural frequency in the fluid medium; for example, water $f/f_0 = 1$). At this transition there is a switch in the timing of vortex shedding that is associated with the jump from the 2S to the 2P vortex modes.
The second transition from upper to lower branch corresponds to a jump in total phase ϕ_L, as the response frequency passes through the value $f = f_{0,a}$ $(f/f_{0,a} = 1)$, which is not associated with switch in timing of vortex shedding.

Finally, considering the high-$(m^*\zeta)$ experiments from Feng [13], it is apparent that both phases, ϕ_{VS} and ϕ_L, exhibit a large jump at the mode transition from initial to lower branch. Considering the frequency response for high-$(m^*\zeta)$ (Fig. 1.3), it can be noticed that the oscillation frequency jumps through both f_0 and $f_{0,a}$ at the same point, inducing simultaneous jumps in both ϕ_{VS} and ϕ_L. This further identifies the two-mode high-$(m^*\zeta)$ type of responses as being quite distinct from the three-mode low-$(m^*\zeta)$ type of response.

1.4.6 Lower branch frequency and existence of a critical mass ratio

Let's return again to what is stated in the subsection 1.4.1: at high-m^* ($O(100)$) the frequency ratio during the synchronisation regime f^* is close to 1, while for low-m^*

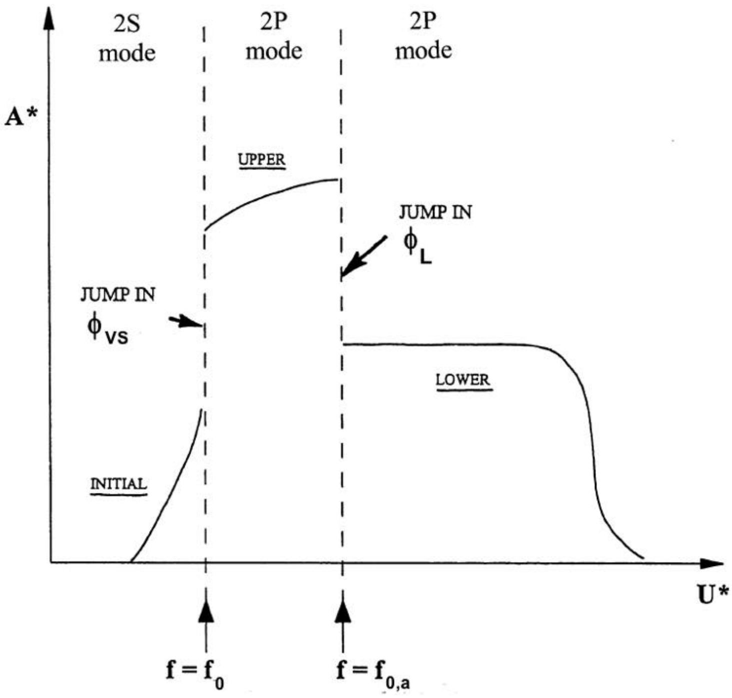

Figure 1.12: After Govardhan and Williamson [17]. Schematic diagram of the low-$(m * \zeta)$ type of response, showing the three principal branches and the corresponding two jump phenomena.

$(O(1))$ the frequency ratio increases dramatically $f^* >> 1$. Khalak and Williamson [5], by using the equation of motion and observing the nature of response amplitude and frequency for the lower branch, derived a simple qualitative expression for the frequency ratio f^*_{lower}, in the lower branch, which permits us to obtain a relation for the regime of synchronisation as a function of mass ratio.
Plotting experimental data for the lower branch frequency f^*_{lower} in function of the mass ratio m^* Fig. 1.13), they found a good collapse of data in a single curve. Therefore, since the response in the lower branch regime is remarkably sinusoidal and periodic, the assumed equation of motion (Eq. (1.33), (1.6) and (1.7)) is an excellent representation of the dynamics. Therefore the equation for frequency takes the form of Eq. (1.26), reported here

$$f^* = \sqrt{\frac{m^* + C_A}{m^* + C_{EA}}}. \tag{1.41}$$

The effective added mass C_{EA} is a function of $\{(U^*/f^*, A^*)\}$ and has a unique value at each point along the lower branch, when plotted in the plane $\{(U^*/f^*, A^*)\}$ as in Fig. 1.10. The Griffin plot results (see Fig. 1.8(b)) show that in the case of $(m^* + C_A)\zeta < 0.05$, the lower branch amplitudes remain (to reasonable accuracy) at a constant level. Therefore it is possible to argue that the lower branch amplitude levels are nearly independent of

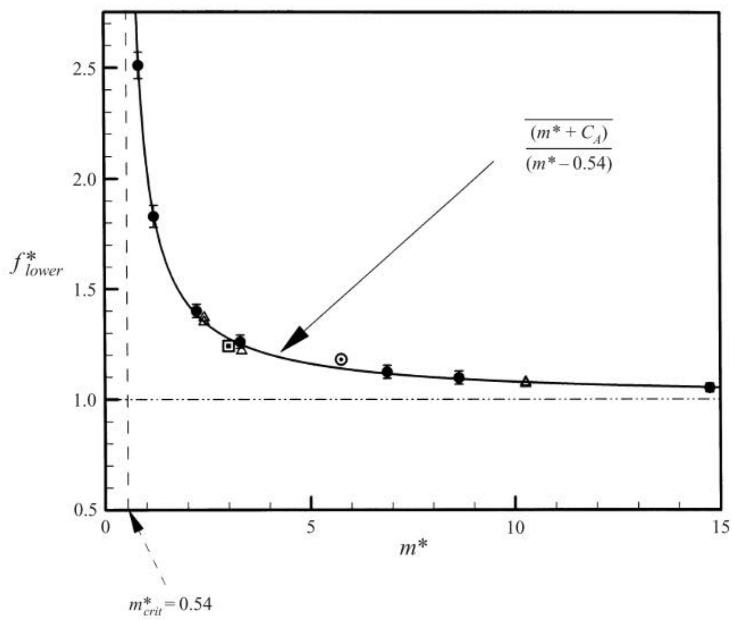

Figure 1.13: After Govardhan and Williamson [17]. Variation of the lower branch frequency f^*_{lower} as function of the mass ratio m^*. The equation for f^*_{lower} indicates a dramatic increase in f^*_{lower} as a approach to the critical mass ratio $m^* = 0.54$. Symbols refer to [17].

mass ratio m^*, so long as $(m^* + C_A)\zeta$ is small.
This means from the Eq. (1.26) that C_{EA} is constant along the lower branch if the mass-damping is small. Hence, C_{EA} is a constant along the lower branch regime and is independent of m^*. The best fit of C_{EA} in the Eq. (1.26), which represents the experimental data of Fig. 1.13, leads to the value of $C_{EA} = -0.54 \pm 0.02$. From this, Khalak and Williamson deduced the lower branch frequency equation:

$$f^*_{lower} = \sqrt{\frac{m^* + C_A}{m^* - 0.54}}. \tag{1.42}$$

Where $C_A = 1$. This curve is drawn through the data in Fig. 1.13, and it represents the data very well. The expression for f^*_{lower} in Eq. (1.42) provides a practical and simple mean to calculate the highest frequency in the synchronisation regime if we are given the mass ratio m^*.
An important consequence of equation Eq. (1.42) is that the frequency becomes large as the mass ratio reduces to a limiting value of 0.54. Therefore, Khalak and Willamson concluded that there exists a critical mass ratio:

$$m^*_{crit} = 0.54. \tag{1.43}$$

As the mass ratio decreases, the value of normalized velocity which defines the start of the lower branch, increases according to the following relation (see Fig. 1.15):

$$\left(\frac{U^*}{f^*}\right)_{start} = 5.75. \tag{1.44}$$

This is consistent with the start of the lower branch in the Williamson-Rosko map of regimes in Fig. 1.10, given by $(U^*/f^*) \approx 1.14$, which (for St = 0.2) yields $(U^*/f^*) = 5.7$. Combining the Eq. (1.42) and Eq. (1.44), it is possible to define the value of reduced velocity at which the lower branch starts:

$$U^*_{start} \approx 5.75\sqrt{\frac{(m^* + C_A)}{m^* - 0.54}}. \tag{1.45}$$

This shows that

$$U^* \to \infty \qquad \text{as} \qquad m^* \to m^*_{crit}. \tag{1.46}$$

Therefore, when mass ratios fall below $m^*_{crit} = 0.54$, the lower branch cannot be reached and ceases to exist. We conclude that the upper branch continues indefinitely and the synchronisation regime extends to infinity.
When the mass ratio is above critical, $m^* > m^*_{crit}$, Govardhan and Willamson also predicted the reduced velocity U^* defining the end of the lower branch in a manner similar to the above simple analysis, to give

$$\left(\frac{U^*}{f^*}\right)_{end} = 9.25, \tag{1.47}$$

giving an equation for U^*_{end} as

$$U^*_{end} \approx 9.25\sqrt{\frac{(m^* + C_A)}{m^* - 0.54}}. \tag{1.48}$$

The above expression yields a quantitative measure of the extent of the synchronisation regime for a given mass ratio m^*. As discussed before, the regime becomes infinitely large when mass ratio falls below the critical value of 0.54. The extent of the complete synchronisation regime, as a function of mass ratio, m^*, is shown as the shaded region in Fig. 1.14. The data marking the end of the synchronisation U^*_{end} is represented well by Eq. (1.48).

1.4.7 Upper-branch frequency

This subsection puts the focus on the frequency f^* of the upper branch and on the transition between the upper and lower branches. A schematic diagram of frequency responses at different mass ratios is given in Fig. 1.15.

Over a large range of mass ratios, the start of the upper branch is found to be close to the point marked as 1, where $U^* \approx 1/\mathrm{St} \approx 5$ and where $f* \approx 1$. The upper-branch frequencies are represented in this diagram as falling on a straight line, from this point up to the point where the lower branch begins. The start of the lower branch satisfies the

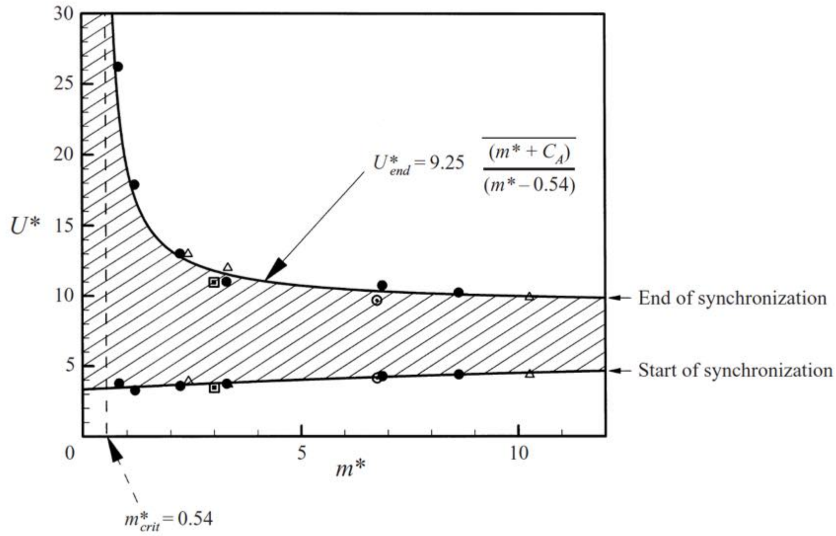

Figure 1.14: After Govardhan and Williamson [17]. The extend of synchronisation (shaded region) as a function of mass ratio m^*. The equation for U^*_{end} fits the data well and indicates a dramatic increase in the extent of the synchronisation regime, determined by U^*_{end}, as we approach the critical mass ratio, $m_{crit} = 054$. For $m < m_{crit}$, the range of synchronisation extends to infinity. Symbols refer to [17]

condition in Eq. (1.44) and it is shown as one of the two dotted lines in the Fig. 1.15. For a given mass ratio m^* the start of the lower branch is defined along this line, where the frequency f^* becomes f^*_{lower} given by Eq. (1.42): in the case of $m^* = 1.05$ for example, is marked as point ②. Then, the lower-branch frequency remains constant until it reaches point ③ situated on the other dotted line which defines the end of the lower branch, given by equation (1.48). As the mass ratio approaches $m^* = 0.54$, the point along the line $(U^*/f^*) = 5.75$, where the lower branch begins, corresponds to a frequency f^* which tends to infinity. Under these conditions ($m^* < 0.54$), the upper-branch frequencies lie along a line which is parallel to $(U^*/f^*) = 5.75$ but shifted to the left by $\delta U^* = 0.75$. This now explains why the frequency line in Fig. 1.15 does not pass through the origin and, instead, has some intercept on the y-axis. The summarising diagram in Fig. 1.15 also explains why the slope of the upper-branch frequency line is always lower than the slope defining the Strouhal frequency line, $f = f_{\mathrm{St}}$.

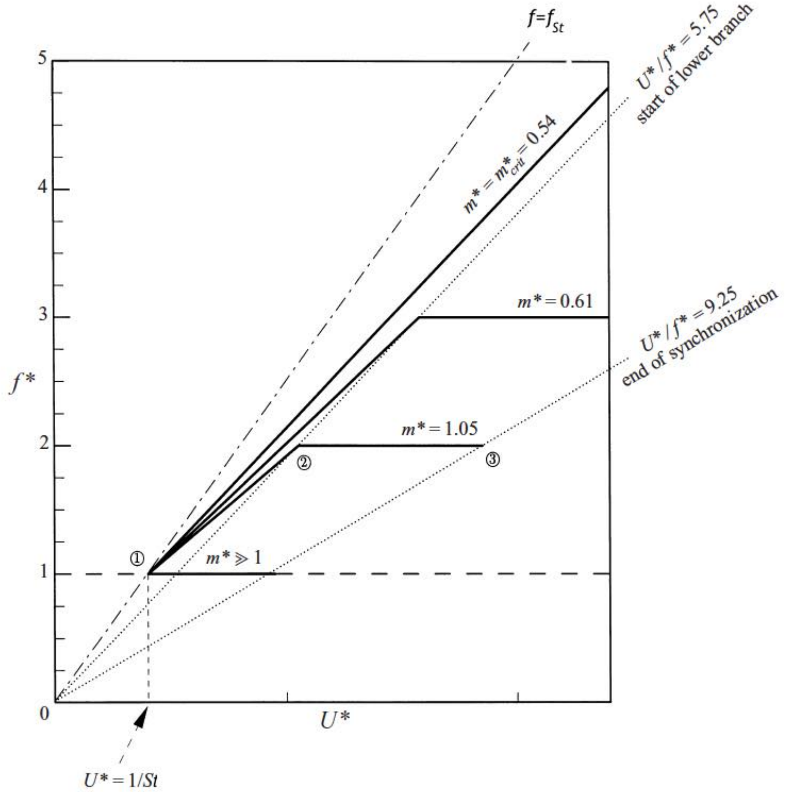

Figure 1.15: After Govardhan and Williamson [17]. Schematic plot of the frequency response for different mass ratios, under conditions for low-$(m^*\zeta)$. The frequency in the lower branch remains constant for each m^*. The condition indicating the start of the lower branch and the end of synchronisation regime, from Eq. (1.44) and Eq. (1.47), are also shown.

1.5 Numerical simulation overview

Given the high demand on computer resource made by three-dimensional (3D) simulation, it is obviously of interest to compare the results for the two-dimensional simulation with the 3D simulations and with the experiments.
The one-degree-of-freedom (1-DOF) vortex-induced vibration (VIV) of a circular cylinder is studied using a bi-dimensional and three-dimensional (3D) computational fluid dynamics (CFD) approach.
Apart from experiments and semi-empirical modelling, there have been an increasing number of studies on VIV based on the Computational Fluid Dynamics (CFD) tools. Due to the continuously increasing capabilities of both hardware and numerical models/-solutions, a considerable number of 2D and 3D CFD results have given a large contribution to the understanding of the VIV problem. Several different models and schemes are adopted to describe the flow field. These include the Discrete Vortex Method (DVM), Large Eddy Simulation (LES), Reynolds Averaged Navier Stokes (RANS) simulations, Direct Numerical Simulation (DNS) or combinations, for example Detached Eddy Simulations (DES). A comprehensive review is given in [8].
The greater part of previous CFD studies on the VIV of a circular cylinder were conducted using two-dimensional (2D) models. Guilmineau and Queutey [24] presented their simulation results of 1-DOF VIV of a circular cylinder. They used a 2D finite volume RANS code with Menter's $k-\omega$ SST turbulence model. Their study included three different initial conditions for the flow velocity, starting from rest or varying the incident flow smoothly and slowly, in both increasing and decreasing directions. With such strategy, both the initial branch and the lower branch of the response amplitude ratio could be examined. Still their numerical results did not correspond with the experimental results.
Pan et al. [25] used the same $k-\omega$ SST turbulence model and carried out a detailed study on the influence of Reynolds-averaging procedure on the features of the upper branch in the cylinder (riser) response. They explained the absence of the upper branch with the disparity in the random behaviour between experiments and the results obtained by RANS codes.
Wanderley et al. [26] used the $k - \epsilon$ turbulence model. The results obtained agreed very well with experimental data and demonstrated the ability of this methodology in predicting amplitudes for a low mass ratio case.
Wu et al. [27] conducted the simulation using the open source CFD tool OpenFOAM with the Spalart-Allmaras turbulence model. Only the *at rest* initial condition were tested. The results of maximum amplitude ratio, frequency ratio, and vortex pattern compared well with experimental data. Transition between VIV branches was predicted successfully, even though the predicted upper branch was not fully satisfying: the amplitude ratio was found 5% lower than the corresponding experimental values.
Kinaci [28] conducted URANS simulations for Reynolds numbers up to 130.000.
The vortex wake of the high-Re number flow around circular cylinders are in general three-dimensional (3D), therefore a series of three-dimensional numerical studies were conducted.

Due to the difficulties, connected with the expensive hardware capacity and extra modelling efforts required to properly describe the fluid flow beyond the laminar region, the vast majority of 3D VIV simulations of the flow around circular cylinders that can be traced in the literature are concerned with low-Re flows. Some of this 3D low-Re research are briefly presented below.

Blackburn et al. [29], presented a comparison between the results from experiments and the corresponding two- and three-dimensional direct numerical simulations of vortex-induced vibration at low Reynolds number. The three-dimensional simulations matched the experiments well, whereas no amplitude branches were observed for the two-dimensional simulations. This also led to the conclusion that two-dimensional simulations were inadequate for modelling high-Re vortex-induced vibration (VIV).

Many operational problems emerged from these studies. The limits of this first comparison between the numerical and the experimental results are related to the difficulties in obtaining high-Re number values in the DNS simulation and low values of Re in the physical experiments. Lucor et al. [30] presented results of a direct numerical simulation (DNS) of 1DOF VIV for three different Reynolds numbers: $\mathrm{Re} = 1000, 2000$ and 3000. First, they noticed the dependence by Re on the location and magnitude of upper branch response. Then, they found that there existed a sharp drop in the spanwise correlation of the wake and forces in the region of U^* around the mode transition between the upper and lower branches and confirmed the existence of a hysteretic region between these two branches.

Leontini et al. [31] investigated the response behaviour of a 1-DOF cylinder subject VIV at low $\mathrm{Re} = 200$. Their numerical study contributed to understanding some of the previous discrepancies about the low-Re VIV and the high-Re VIV behaviour. Two response branches, similar to the upper and lower branches at higher Re, were discovered. Therefore, they concluded that the mechanism that caused the upper and lower branches was not a product of three-dimensionality of the flow (high-Re), although it may be amplified by three-dimensionality. Zhao et al. [32] studied the transition from 2D to 3D for 1-DOF VIV of a circular cylinder at Re ranging from 150 to 1000. In their study, the three-dimensionality of the flow appeared to be strongest in the upper branch and weakest in the initial branch. This was demonstrated through the coexisting presence of 2S and 2P vortex shedding modes in the upper branch which led to the strong variation of the lift coefficient along the span.

However, the greater computational effort for the resolution of 3D equations did not lead to a correct prediction of peak vibration amplitudes on the upper branch. Indeed, the predicited peak vibration amplitudes were around $0.7\,D$ when the referred experiments, conducted with high-Re, produced amplitudes well over $1.0\,D$.

The usefulness of low-Re simulations is arguable, once the flow around marine structures, which presents submerged cylindrical structures, is in general in the range of $10^4 < \mathrm{Re} < 10^6$. Therefore, thanks also to the growing of the computational resources, the numerical study of the VIV phenomenon for high-Re has become of greater interest. Some of the 3D numerical simulation of the VIV phenomenon for high-Re can be found in the works of Dong and Karniadakis [33] and Saltara et al. [34]. In particular, Dong

and Karniadakis presented results of DNS simulations of the flow past a stationary cylinder and a cylinder undergoing forced sinusoidal oscillations in the cross flow direction, using a spectral element method at Re = 10^4. Results of the simulations were in close agreement with the experiments, but the use of the spectral element method to perform DNS required large computational resources. As noted by Sarpkaya [2], there is a huge difference between forced and free oscillation. Forced oscillations offer the advantage of a reduced velocity and amplitude ratios can be independently varied. Indeed, forced oscillations drive external motion by imposing an oscillation frequency and an amplitude to a given Reynolds. This leads to regularizing and idealizing every aspect of vortex induced vibration, leading to nearly pure sinusoidal oscillations, forces and almost wake states. On the other hand, in free oscillation experiments the motion is driven internally by the wake at an average frequency f (dictated by the past and prevailing state of the motion and periodic forcing arising on it) as the Re number increases with the increasing U in $U^* = U/f_{n_w}D$.
The forced oscillations simplifying the problem, can be studied numerically with a lower computational cost, but they lose the ultimate objective of the VIV research which is to predict the kinematics and dynamics of self-excited vibration. This is particularly significant when transient phenomena take place at certain frequencies in practical application (pipe and cables) at high-Re undergoing transverse vibration.
In order to numerically study self-vibrations with high-Re three-dimensional simulations at an acceptable computational cost, nowadays we have therefore moved on to simplified models and schemes to describe the flow field. In this perspective, a first attempt was made by Saltara et al. [34] . Saltara et al. used the Spalart-Allmaras Detached Eddy Simulation (DES) to simulate 1-DOF VIV of a circular cylinder with a low mass-damping parameter at Re = 10^4. In general, their simulation results partially agreed with the experimental results of Khalak and Williamson [15]. The vibration amplitudes and force coefficients followed the three response branches arising in different ranges of the reduced velocity, but they were over predicted for $U^* > 6$. Furthermore, the shift in phase angle between lift coefficient and cylinder displacement, obtained in the simulations, occurred for a different reduced velocity compared to the experimental data.
One of the goals of the present Ph.D. research is to extend the numerical study of the flow around a circular cylinder with 1-DOF via 2D and 3D numerical simulation within an early subcritical Re regime.

1.6 Semi-empirical models

Several semi-empirical models have been proposed in literature which try to describe the kinematics (vice dynamics) of the VIV through simple models.
This short review aims to compare the existing models with what has been proposed in this Ph.D. research in order to understand what the differences and novelties are.
Following the Gabbai and Benaroya [8] classification, these models can be divided into three main categories:

- the *wake-body coupled models* (also referred to wake-oscillator model), in which the body and the wake oscillations are coupled through common terms in equations for both;
- the *single degree-of-freedom (sdof) model*, that uses a single dynamic equation with aeroelastic forcing terms on the right-hand side of the equation;
- the *force decomposition model*, where some components of the forces, acting on a structure, are measured from the experiments.

1.6.1 Wake-body coupled models

The models generally desire to obtain the equations of the cylinder oscillator and the fluid oscillator by independent means and then use them together to predict the response of the combined fluid–elastic system.
These models are based on the fact that the motion of the cylinder strongly affects the lift force, which in turn influences the cylinder motion. The oscillator is self-exciting and self-limiting, the natural frequency of the oscillator is proportional to the free stream velocity so that the Strouhal relationship is satisfied and the cylinder motion interacts with the oscillator. They try to explain and simulate the experimental results without including any analysis of the flow field. The first assumption is that the flow around cylinder is bi-dimensional (i.e, the flow is fully correlated), this limits these models to predict moderate to large response amplitude.
Bishop and Hassan [35] are considered the first to suggest the idea of using a van der Pol type oscillator to represent the time-varying forces on a cylinder due to vortex shedding. Hartlen and Currie [36] formulated the most noteworthy oscillator model. In their model, a Van der Pol soft non-linear oscillator for the lift force is coupled to the cylinder motion by a linear dependence on the cylinder velocity. The cylinder motion is restricited to pure translation in the transverse direction, perpendicular to both the flow direction and the cylinder axis. The cylinder is restrained by linear springs and is linearly damped. The model is given by the pair of coupled non-dimensional differential equations,

$$\ddot{y}^* + 2\zeta\dot{y}^* + y^* = a\,\omega^2\,y^* \tag{1.49}$$

$$\ddot{C}_L - \alpha\omega\dot{C}_L + \frac{\gamma}{\omega}(\dot{C}_L)^3 + \omega^2 C_L = b\,y^* \tag{1.50}$$

where y^* is a dimensionless displacement of the cylinder and C_L defines the instantaneous lift coefficient. This dimensionless displacement, y^*, is related to the actual displacement, y, by $y^* = y/D$ where D is the diameter of the cylinder. The dots represent differentiation with respect to time t.
Eq. (1.49) represents a dimensionless dynamic equation of motion for the cylinder in which $+2\zeta\dot{y}^*$ represents the viscous damping force, y^* the spring force, and $a\,\omega^2\,y^*$ the pressure force due to vortex shedding.
The second Eq. (1.50) represents a van der Pol type equation in which the lift coefficient C_L is linearly affected by the cylinder velocity.
The parameters in Eq. (1.49) and Eq. (1.50) are the damping factor ζ, the dimensionless flow velocity ω, the van der Pol coefficients α and γ, the dimensionless constant a and the interaction parameter b. The dimensionless flow velocity $\omega = \mathrm{St}U/D\,f_0$ where St is the Strouhal number, U the flow velocity and f_0 is the natural frequency of the cylinder. It is worth noting that the second term on the left-hand side of Eq. (1.50) provides the growth of the lift coefficient C_L; while the third term on the left-hand side of the same equation prevents its unlimited growth. These terms are important to the success of the model because the large-amplitude oscillations, characteristic of VIV, are accompanied by a significant (yet finite) increase in the lift coefficient.
As successfully shown by Ng et al. [37] with the appropriate choice of parameters, the Hartlen and Currie model qualitatively captures many of the features seen in experimental results.
Fig.1.16 shows the amplitude and frequency responses of the Hartlen and Currie model using the parameter $\zeta = 0.0015$, $\alpha = 0.02$,$\gamma = 2/3$,$a = 0.002$ and $b = 0.4$. In Fig.1.16, arrows, show jumps in amplitude and frequency occurring in response to sweeps of parameter co (proportional to flow velocity), resulting in hysteresis. These jumps occur because of changes in stability and are associated to bifurcations of periodic motions. The asymmetry in the amplitude response is a direct result of the velocity coupling term $b\,y^*$ used in Eq. (1.50).

Skop and Griffin [38] developed a model to resolve what they felt were the inadequacies of the Hartlen and Currie model, including the fact that the model parameters are not related to any physical parameters of the system. A modified Van der Pol equation is again employed as the governing equation of the lift and an equation is presented for the oscillatory motion of the body.
The two cited models, Hartlen and Currie model and the Skop and Griffin models, have several contradictions compared to the experimental studies of Feng [13]. The main differences with the Feng researches are the position of the maximum lift, maximum cylinder displacement and the region of synchronisation. In particular, Feng found that the maximum lift and maximum cylinder displacement occurred at the same value of flow speed and that the cylinder continued to oscillate at its natural frequency outside the lock-in range.
Other wake-body coupled models were presented by Iwan and Blevins [39] and by Landl [40]. They arrived at fluid oscillator equation respectively by considering the fluid mechanics of vortex street (introducing a hidden fluid variable) and by including a non-linear

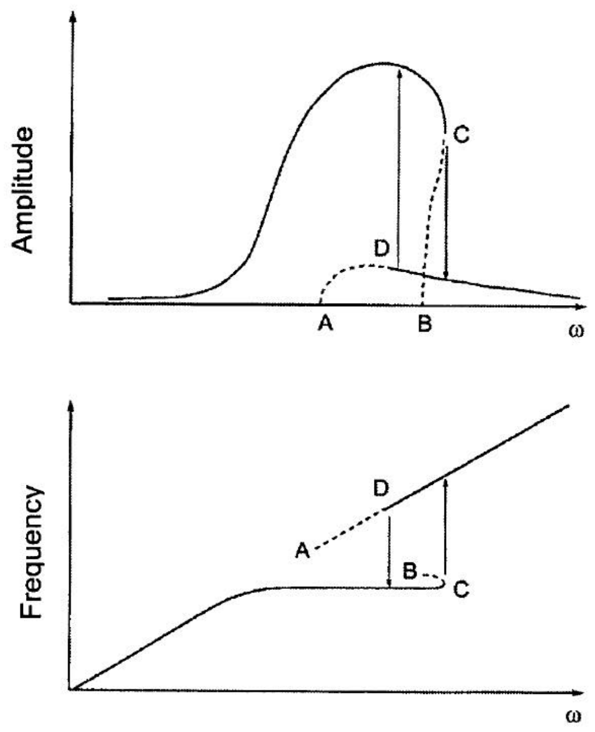

Figure 1.16: After Ng et al. [37]. Amplitude and frequency response of wake oscillator model (Horizontal axis is dimensionless flow velocity. Vertical arrows represent jumps in response to slow sweeps in flow velocity and result in hysteresis. Solid lines represent stable branches of periodic motions and dotted lines represent unstable branches).

aerodynamic damping term of fifth order in the two-equation model. A comprehensive review of the dynamics of the wake oscillator models for 2D VIV can be found in the research of Facchinetti et al. [41]. The authors examined three different types of linear coupling terms modelling for the fluid–structure interaction and compared them with the experimental data in literature. More specifically, the considered coupling terms, used in the right-hand side of the given fluid-oscillator equation, were the velocity coupling, the displacement coupling and the acceleration coupling. It was found that the displacement and velocity couplings failed to predict the lift phase seen in experimental results of vortex shedding from cylinders forced to oscillate, while the acceleration coupling succeeded in qualitatively modelling the features of VIV.

1.6.2 Single degree-of-freedom models

Single degree-of-freedom (*sdof*) models use a single ordinary differential equation to describe the behaviour of the structural oscillator. The general form of such models is given by:

$$M(\ddot{y} + 2\zeta f_0 \dot{y} + f_0^2\, y) = F(y, \dot{y}, \ddot{y}, f_{\mathrm{St}} t) \tag{1.51}$$

where M is the mass of the cylinder, y is the transverse (lift direction) displacement, f_{St} is the Strouhal frequency and F is an aeroelastic forcing function. The influence of the wake dynamics is incorporated into Eq. (1.51) via the appropriate choice of the function F.

Some of the proposed models can be found in Simiu and Scanlan [42], Blasu and Vickery [43], Goswami et al. [44][45] and Chen et al. [46].

Belonging to this category is also the model proposed by Bearman [6] previously presented in the section 1.3. Recalling the Eq. (1.12) and Eq. (1.13) the authors exposed the dependency of the frequency ratio $f_{0,a}/f$ and of the amplitude ratio $\overline{y}/D$ on the mass ratio. In particular, from the Eq. (1.12) it can be noted that a large value of the mass ratio means that the frequency of oscillation of the cylinder is appreciably different from its natural frequency, only for small value of mass ratio that $f_{0,a} \approx f$. Eq. (1.13) shows that the amplitude ratio is affecited only by the part of the fluctuating lift coefficient that is in-phase with the cylinder velocity.

1.6.3 Force-decomposition models

In the force–decomposition model, introducted by Sarpkaya [7], the lift force on an elastically mounted rigid cylinder is decomposed into a fluid inertia force related to the cylinder displacement and a fluid damping force related to the cylinder velocity. The lift coefficient, C_L is expressed as

$$C_L = C_I \sin(2\pi f\, t) - C_D \cos(2\pi f\, t) \tag{1.52}$$

where C_I is the inertia coefficient and C_D is the drag coefficient, f is the transverse oscillation frequency of the cylinder. These components are related to Sarpkaya's generalised force coefficients $\overline{C_I}$ and $\overline{C_D}$ by

$$C_I = \pi^2 \overline{C_I} \left(2\pi \frac{y}{D}\right)^2 (U^*)^{-2} \tag{1.53a}$$

$$C_D = \frac{8}{3\pi} \overline{C_D} \left(2\pi \frac{y}{D}\right)^2 (U^*)^{-2} \tag{1.53b}$$

Eq. (1.52) can then be incorporated into the equation of motion for elastically mounted, linearly damped and periodically forced cylinder, yielding

$$\ddot{y}^* + 2\zeta \dot{y}^* + y^* = \overline{\mu} \left(\frac{f_{\mathrm{St}}}{f_0}\right)^2 \left(C_I \sin(2\pi f\, t) - C_D \cos(2\pi f\, t)\right). \tag{1.54}$$

In Eq. (1.54) $\overline{\mu}$ is a mass parameter defined by $\overline{\mu} = \rho\, D^2/8\pi^2 \mathrm{St}^2 M$ which results from the normalization of the force coefficients and $y^* = y/D$ is the dimensionless displacement. Here St is the Strouhal number for a stationary cylinder. If the values of $\overline{C_I}$ and $\overline{C_D}$ corresponding to the U^* value at perfect synchronisation can be determined from

experiments, then Eq. (1.54) can be solved and the response of the cylinder in the synchronisation region ascertained.
Sarpkaya shows through a parametric study that the maximum response of the cylinder is governed by a single parameter, the stability (mass-damping) parameter $S_G = \zeta/\overline{\mu}$; in case of values of this parameter larger than about unity. This stability parameter, can be recognized in literature as the Skop–Griffin parameter ($S_G = 8\pi^2\zeta S^2\,M/\rho D$) and it corresponds to the the ratio of the material damping and a mass ratio. For low values of the stability parameter, the mass ratio and damping affect the response separately.
Another force-decomposition model was presented by Griffin and Koopman [47]. The fluid force was slitted in two components: an excitation part and a reaction part that included all the motion-dependent force components. In non-dimensional form, the equation of motion for an elastically mounted rigid cylinder is written as:

$$\ddot{y}^* + 4\pi\zeta\dot{y}^* + y^* = \overline{\mu}\left(\frac{f_{\mathrm{St}}}{f_0}\right)^2 (C_L - C_R) \tag{1.55}$$

where C_L is the lift coefficient and C_R is the reaction coefficient. Since the fluid lift and reaction forces have the same frequency as the structural vibrations, they can be written in the respective forms:

$$C_L = \overline{C_L}\sin(2\pi f + \phi_L), \tag{1.56a}$$

$$C_R = \overline{C_R}\sin(2\pi f + \phi_R). \tag{1.56b}$$

Here ϕ_L and ϕ_R are the phase angles between the lift and the displacement and between the reaction and the acceleration, respectively.
The two forces represented by C_L and C_R are orthogonal. The new systems decomposition proposed, allows the fluid and structural forces to be completely separated. The various fluid forces, then, can be measured individually or deduced from the total measured force.
The lift component in phase with the cylinder velocity, by which energy is transferred to the system, was measured and was in agreement with analogous measurements in water. The non-linear dependence of the lift force on the cylinder amplitude confirms the "wake-oscillator" hypothesis put forward by several previous investigators.
In a following paper, Griffin [48] showed that the two presented approaches were identical when

$$C_L\sin\phi_L = -C_D\cos\epsilon, \qquad \text{Excitation,} \tag{1.57a}$$

$$C_L\cos\phi_L = C_D\sin\epsilon, \qquad \text{Fluid inertia,} \tag{1.57b}$$

$$C_R\sin\phi_R = -C_I\sin\epsilon, \qquad \text{Fluid reaction (damping),} \tag{1.57c}$$

$$C_R\cos\phi_R = -C_I\cos\epsilon, \qquad \text{Added mass} \tag{1.57d}$$

where ϵ is an undefined phase angle. These relations (Eq.(1.57)) can be used to compare recent measurements of the various force components. When the force coefficients are assumed to be known, as from experiments, these analytical models can be used to predict the cylinder displacement and vice versa.

Conclusion of the chapter

Through this review we want to highlight both the experimental and the numerical studies which have been already presented in literature, as results of these studies, several semi-empirical models have been suggested.
Nevertheless, we found out that so far there is no simplified and reliable model which analyses the effect of several parameters (*e.g.* mass ratio m^*, mass-damping parameter $m^*\zeta$, Reynolds number Re, ...) on the response of a cylinder subject to VIV.
All things considered, one of the purposes of this thesis is to search for a new semi-empirical model which is capable of analysing the governing and influencing parameters. Therefore, in order to find this model, detailed numerical studies have been be carried out. The numerical studies, presented in the next chapter, are presented following the time-line of the studies undertaken during the doctoral period. The numerical study of VIV on 1-DOF elastically mounted circular cylinder has first dealt with a simplified numerical treatment (bi-dimensional and three-dimensional URANS model), then the same study has been carried out using a more computational demanding one (the Scale-Adaptive simulations SAS model).

Chapter 2

Numerical VIV analysis

In this chapter an in-depth numerical study of 1-DOF VIV in cross-flow direction is extensively investigated. The selected self-excited oscillation test case is the experiment of Khalak and Wilamson [15], characterised by low mass and damping ratios.
This chapter is divided in six main sections. In the first section an overview of the numerical set-up are presented. For all of the CFD simulations the same numerical scheme, mesh morphing, boundary and initial condition of the section are applied.
In the second section a grid sensitivity study is shown. This study was made with the URANS-based CFD simulations for both bi- and three-dimensional grids.
The third section aims to demonstrate the differences between the use of 2D and 3D meshes in the case of URANS simulations and to understand if the 2D simplification can be accepted or even considered in the case of VIV.
The fourth section takes into consideration a possible span-wise dependence of the URANS solution. The span-wise length of the cylinder has been doubled keeping the grid span-wise resolution unchanged.
In the fifth section, the Scale-Adaptive Simulation (SAS) model for turbulent flow predictions is considered. The use of the SAS is evaluated and compared to the standard SST-URANS for the selected VIV test case.
Finally, several initial conditions are tested for both types of simulations URANS and SAS, in order to investigate the transition between branches.

2.1 Numerical approach and validation

2.1.1 Governing equation

In this study, the numerical simulation has been performed using OpenFOAM (release 2.4). an open source finite volume based CFD toolbox. The finite volume method is employed to discretise the momentum (Navier-Stokes equations) and mass conservations of an incompressible Newtonian fluid, read as follows

$$\frac{\partial u_i}{\partial t} + u_j \frac{\partial u_i}{\partial x_j} = -\frac{1}{\rho}\frac{\partial p}{\partial x_i} + \nu \frac{\partial^2 u_i}{\partial x_j \partial x_i} + F_i \tag{2.1}$$

$$\frac{\partial u_i}{\partial x_i} = 0 \tag{2.2}$$

where u_i is a velocity component, p is the pressure, F_i are the body forces (if any), t and x_i are time and space independent variables.
In Reynolds-Averaged Navier-Stokes (RANS) method, the turbulent flow is divided into two parts, one is time averaged flow and the other is the transient pulsating flow. And any turbulence varable can be written as:

$$\phi = \overline{\phi} + \phi' \tag{2.3}$$

where $\overline{\phi}$ represents the average value of the variable ϕ over time and ϕ' is the pulsating value. Then, the incompressible continuty equation and momentum equations are rewritten as:

$$\frac{\partial \overline{u_i}}{\partial t} + \overline{u_j}\frac{\partial(\overline{u_i})}{\partial x_j} = -\frac{1}{\rho}\frac{\partial \overline{p}}{\partial x_i} + \nu\frac{\partial^2 \overline{u_i}}{\partial x_j \partial x_i} - \frac{\partial \overline{u_i' u_j'}}{\partial x_i} + \overline{F_i} \tag{2.4}$$

$$\frac{\partial \overline{u_i}}{\partial x_i} = 0 \tag{2.5}$$

2.1.2 Turbulence model

In order to solve the time-averaged continuity equation (2.5) and the three momentum equation (2.4) the ten unknowns, the four usual ones ($\overline{u_i}$, $\overline{p}$) plus six turbulent stresses $\overline{u_i' u_j'}$ must be found. This is called the "closure problem". Therefore some new equations for the turbulent stresses must be found. The additional equations, namely turbulence model, devise approximations for the unknowns terms.
In this study, the $k-\omega$ Shear Stress Transport model (SST) turbulence model is used for modelling the turbulence[49, 50, 51]. This chioice is related to a number of studies that shows a good prediction of the adverse pressure gradient flows, such as flow around a cylindrical bluff body [52, 53], with the use of the $k-\omega$ SST. This model approximates the eddy viscosity using transport equations for the kinetic energy (k) and its specific dissipation rate (ω).

2.1.3 Equation of motion

The VIV response system of a cylinder to move with 1-DOF in the cross flow direction can be regarded as a mass-spring-damper system. The dynamic equation of an oscillatory cylinder system is given as follows:

$$M\,\ddot{y} + H\,\dot{y} + K\,y = F_L(t), \tag{2.6}$$

where $F_L(t)$ is the time dependent fluid force acting on cylinder body in the cross flow direction, which is obtained by integration of pressure and viscous friction on the body surface resulting from the resolution of the momentum equation (2.1). The symbols y, $\dot{y}$ and $\ddot{y}$ are respectively the displacement, velocity and acceleration of the body. M is the mass of the system with stiffness K and damping H.

2.1.4 Experimental validation

Before moving on to the presentation of computational domain, numerical schemes, initial and boundary conditions, the selected experimental test case, used as a benchmark in evaluating the validity of the computational studies, must be introduced.
The experimental setup of Khalak and Williamson [15] where a circular cylinder, mounted on a linear spring and working in uniform cross flow of velocity U, is considered.
Khalak and Williamson [15] conducted the experiments at the Cornell-ONR free-surface water channel with a vertical surface-piercing cylinder. Fig. 2.1 presents a sketch of the facility. The experiment of Khalak and Williamson [15] is widely used as benchmark for evaluating in the CFD results in case of bi-dimensional simulation for the particular care of the cylinder end conditions. Thus, we have assumed that those data can be considered 2D. Indeed, in the experimental facility a fixed flat horizontal plate was installed at a $0.04D$ from the bottom of the cylinder in order to minimize 3D effects at the bottom end of the cylinder. Morse et al. [54] studied the effect of the end conditions (with or without end plates at the far end or small gaps with a fixed bottom) concluding that, unless the gap exceeds a given threshold, the results in terms of peak amplitude response are almost comparable.

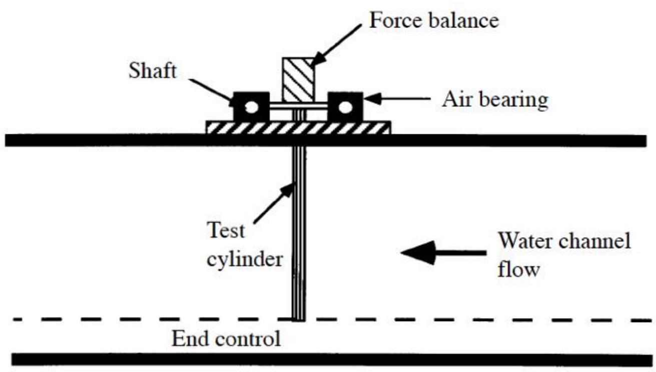

Figure 2.1: Schematic of experimental facility. Taken from [15]

A wide range of flow regimes, characterised by reduced velocity $U^* = U/(f_0\, D)$, is taken into consideration. f_0 is the natural frequency of the system in fluid at rest. The reduced velocity U^* is varied between 2 and 16 approximately, corresponding to sub-critical Reynolds numbers in the range $2.0 \cdot 10^3$ to $1.3 \cdot 10^4$. The entire set of velocities of the onset flow at a given U^* is obtained with smooth continuous increment of the relative incident flow velocity, from the lowest to the highest.
It is worth noting that in the work of [15] U^* is defined according to the natural frequency

in air $f_{0,a}$, where the added mass is three orders of magnitude smaller than in water. Their U^* values have been recomputed here for fresh water.
The value of the stiffness is found from the value of the frequency in the air

$$f_{0,a} = \frac{1}{2\,\pi}\sqrt{\frac{K}{M}}.$$

In order to find the reduced velocity in water, we need the system natural frequency in air. Considering the added mass $M_A = C_A\,M_d$ we can find the system natural frequency in water from the equation

$$f_0 = \frac{1}{2\,\pi}\sqrt{\frac{K}{(M + M_A)}}$$

and then the reduced velocity in water $U^* = U/(f_0\,D)$.
In order to find the value of the damping H, the following equation has been used:

$$H = \zeta\,2\,\sqrt{K\,(M + M_A)}.$$

The mass/damping data used in the experiments and in the present simulations are such that the problem is characterised by low mass ratio $m^* = 2.4$ and low damping $\zeta = H/H_{crit} \approx 0.0054$ ratios. The study is performed using fresh water.

2.1.5 Computational domain

The shape of the computational domain in the plane $O(x, y)$, used in the current simulations, is sketched in Fig. 2.2, with names of the boundary patches.

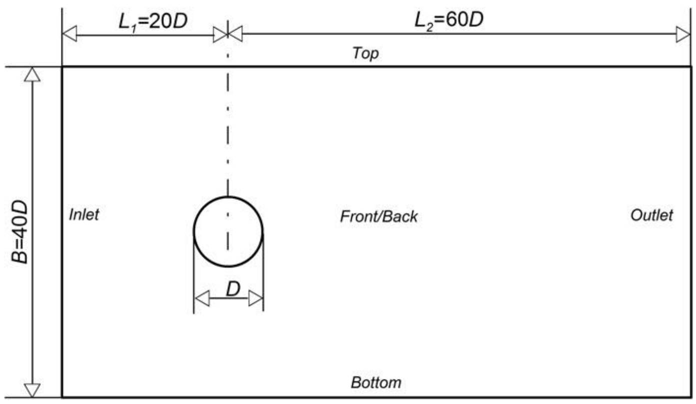

Figure 2.2: Computational domain.

The dimension of this domain is $40D$ (width B) in the cross-flow direction and $20D$ (L_1) at the inflow and $60D$ (L_2) at the outflow from the cylinder centre. The domain size was determined by a preliminary domain independence study conducted for a smooth stationary cylinder presented in the Master Thesis of Martini [55]. With this computational set-up the blockage ratio is 0.025. Other studies showed that the domain width has a little effect on cylinder response if the blockage ratio is less than 0.05 [32]. Therefore, the selected domain width is satisfactory to enable detailed study at a wide parametric space and at affordable computational time.

2.1.6 Grid structure

The mesh generation utility, `snappyHexMesh`, supplied with OpenFOAM is used in setting up the grid system. The `snappyHexMesh` utility provides a flexible solution during the meshing process thanks to the specification of specific mesh refinement region inside the domain.
The centre of cylinder is taken as origin. The near-wall grid spacing is designed to ensure the first cell in the viscous sub-layer, the dimensionless parameter y^+, which is related to the wall shear stress, is fixed to the order of 1. For the off-wall region, grids have two concentric levels of higher resolution. An additional refinement box, spanning from the centre of cylinder to the outlet boundary of the domain, has been added in order to correctly resolve the wake field. Finally, to avoid a big change in grid spacing between two neighbour cells, the number of buffer layers between different refinement levels has been set to 4. The main characteristics of the grid used for the Master Thesis of Martini [55], here referred as 2D BASE, are summarised in Tab. 2.1. Fig. 2.3 shows the mesh refinement close to the cylinder surface.

2D BASE	Value
Cells	38468
Faces	154723
Points	78638
Add layer set-up	
Number of surface layers	40
Minimum thickness	6.214e-05
Final layer thickness	1.677e-03
Expansion ratio	1.088
Mesh quality	
Maximum cell aspect ratio	13.066
Maximum mesh non-orthogonality	44.890
Maximum skewness	0.544

Table 2.1: Grid information

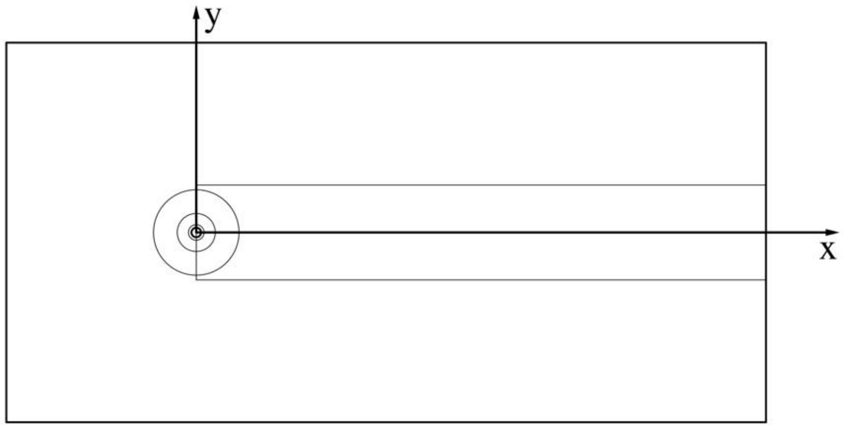

(a)

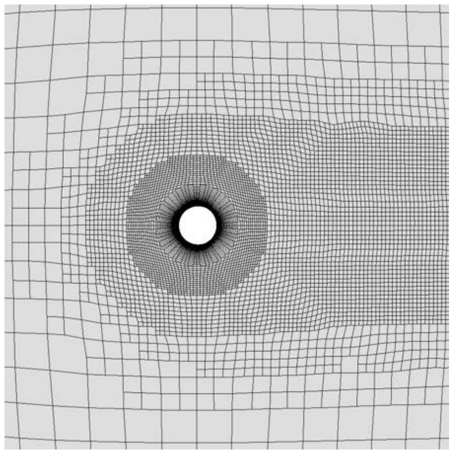

(b)

Figure 2.3: 2D BASE grid structure and its detail.

2.1.7 Boundary and initial conditions

In Tables 2.2 to 2.4, the boundary and initial conditions used for the velocity, pressure, turbulent kinetic energy k and the turbulence specific dissipation rate ω are listed along with their mathematical formulations. Bold symbols refer to vectors, "**n**" is the unit vector normal to the boundary.
As for the initial conditions, a uniform flow field is imposed on the whole domain, including boundaries. A uniform static pressure is set to zero on the whole domain. For k and ω, uniform values are also set across the domain; their values have been computed following Menter's approach [49]. In Tab. 2.4 L is the approximate length of the computational domain, Re_L is the Reynolds number associated with the approximate length of the computational domain, y_1 is the distance of the first grid point above the wall.

To enforce the two-dimensional flow the "empty" condition of OpenFOAM is applied on the *Front* and *Back* patches for both velocity and pressure.This condition specifies that the field equations are not solved in the direction normal to these patches.

Domain / Boundaries		Equation	
	Boundary condition		
Top/Bottom	zeroGradient	$(\mathbf{n} \cdot \nabla \mathbf{u}) = 0$	
Inlet	fixedValue	$\mathbf{u} = \mathbf{u}_\infty$	
Outlet	inletOutlet	$(\mathbf{n} \cdot \nabla \mathbf{u}) = 0$	if: $\mathbf{u} \cdot \mathbf{n} > 0$
		$\mathbf{u} = 0$	if: $\mathbf{u} \cdot \mathbf{n} < 0$
Cylinder wall	movingWallVelocity	$\mathbf{u} = \mathbf{u}_{wall}$	
	Initial condition		
Inner domain & Inlet		$\mathbf{u}_\infty = (U, 0, 0)$	

Table 2.2: Boundary and initial conditions - *Velocity*

Domain / Boundaries		Equation
	Boundary condition	
Top/Bottom	zeroGradient	$(\mathbf{n} \cdot \nabla p) = 0$
Inlet	zeroGradient	$(\mathbf{n} \cdot \nabla p) = 0$
Outlet	fixedValue	$p = p_0$
Cylinder wall	zeroGradient	$(\mathbf{n} \cdot \nabla p) = 0$
	Initial condition	
Inner domain & Outlet		$p_0 = 0$

Table 2.3: Boundary and initial conditions - *Pressure*

2.1.8 Mesh morphing and numerical schemes

As far as the body motion is concerned, the ALE method, available in OpenFOAM, has been used to follow the mesh motion [56], where the displacement of the internal nodes is computed from the boundary motion by means of the Laplace equation with variable diffusivity based on inverse distance [56].
The time dependent simulations have been carried out using the first order implicit Euler scheme coupled with the dynamically adjustable stepping technique [57]. This choice has proved to be a good compromise for having a stable solution at an affordable computational cost. In detail, the implicit scheme of the first order ensures us an adequate

Domain / Boundaries		Equation	
	Boundary condition		
Top/Bottom	zeroGradient	$(\mathbf{n} \cdot \nabla k) = 0$	
		$(\mathbf{n} \cdot \nabla \omega) = 0$	
Inlet	fixedValue	$k = k_{farfield}$	
		$\omega = \omega_{farfield}$	
Outlet	inletOutlet	$(\mathbf{n} \cdot \nabla k) = 0$	if: $\mathbf{u} \cdot \mathbf{n} > 0$
		$k = k_{farfield}$	if: $\mathbf{u} \cdot \mathbf{n} < 0$
		$(\mathbf{n} \cdot \nabla \omega) = 0$	if: $\mathbf{u} \cdot \mathbf{n} > 0$
		$\omega = \omega_{farfield}$	if: $\mathbf{u} \cdot \mathbf{n} < 0$
Cylinder wall	fixedValue	$k = 0$	
		$\omega = \frac{60\,\nu}{0.075\,y_1^2}$	
	Initial condition		
Inner domain & Inlet		$k_{farfield} = 0.1\,\frac{U^2}{Re_L}$	
		$\omega_{farfield} = 10\frac{U}{L}$	

Table 2.4: Boundary and initial conditions - $(k - \omega)$

stability while the adaptive time step helps to satisfy the accuracy of the solution. The pressure-velocity coupling is obtained thought PIMPLE algorithm, and is a combination of the SIMPLE and PISO algorithms [58]. Two outer correctors (SIMPLE loop) and two correctors (PISO loop) are selected.
To achieve stable and convergent calculations for every time step, a Courant number Co less than 0.9 was adopted as well as an accuracy of 10^{-5} for velocity, 10^{-6} for pressure and 10^{-7} for the other dependent variables.
The other discretisation schemes employed in this study are collected in Table 2.5. We point out that the choice of second order spatial discretisation scheme has resulted in improved accuracy with respect to first order schemes. Yet, with the present numerical set-up, no relevant stability problems have been encountered.

Operator	Symbol	Scheme	Order
Time derivative	$\partial/\partial t$	Backward Euler	1^{st}
Gradient	∇	linear	2^{nd}
Divergence	$\nabla \cdot (\phi, V)$	linear upwind	2^{nd}
Laplacian	∇^2	linear limited	2^{nd}

Table 2.5: Schemes in use

2.2 Grid sensitivity studies

To determine the overall grid resolution required to have a grid independent solution, a grid sensitivity study is conducted for a circular cylinder free to move with 1-DOF in the cross flow direction. It can be noted that the 2D BASE mesh used for the Master Thesis of Martini [55], presented in chapter 2.1, was obtained after a study on the mesh carried out on a smooth stationary cylinder. This is a common strategy to get the grid independent solution with a lower computational cost [27] compared to the same case with the cylinder free to move, but the effects due to the mesh morphing are neglected.

The grid sensitivity studies are performed in three stages. The first two stages construct bi-dimensional meshes varying the grid density and the near-wall layer treatment respectively. In this stage, the new 2D meshes will be compared with the previous presented 2D BASE mesh.
The findings from these stages are used as a guide for further three-dimensional meshes. In particular, the reference 3D mesh is generated extending the slice of the 2D meshes in the span direction of the cylinder. Therefore, both 2D and 3D computational meshes share the same construction in the XY plane, i.e. any 3D mesh XY slice corresponds to the 2D mesh. The length of the 3D domain in the spanwise direction is defined according to the experiment dimension[15]. The level of grid convergence for the three-dimensional meshes is evaluated using the Grid Convergence Index (GCI).
A wide range of reduced velocity U^* is taken into consideration to evaluate, also, the grid sensitivity with different flow regimes. The results are presented in the usual way; dimensionless amplitude $A^* = A/D$ and dimensionless frequency $f^* = f/f_0$ as a function of reduced speed $U^* = U/(D \cdot f_0)$.
This section is organized as follows. The first bi-dimensional refinement study, where only the density of the cylinder will be modified (leaving the near-wall area unchanged), is presented. It follows the presentation of the second bi-dimensional refinement study, where the the near-wall area is changed. Finally, the three-dimensional grid refinement study is then described and the level of grid convergence is evaluated using the GCI. The conclusions with the final mesh selection for the further studies are given in the last subsection.

2.2.1 Grid density analysis

In this initial study, a set of four different 2D meshes are presented. OpenFOAM by default only works with 3D mesh elements, so in order to create a 2D mesh a single cell perpendicular to the plane $O(x, y)$ must be created. The thickness of $S = 2.50 \times 10^{-2}$ is used for all the 2D simulations. Tab. 2.6 summarizes the system properties of 2D simulations.

Tab. 2.7 summarizes the main characteristics of the meshes. In Tab. 2.7, n_c represents the number of points along the circumference of the cylinder. The number of cells has been varied reducing the cell size at the boundaries of the domain (background hex mesh), consequently all other refined zones scaled accordingly. The cell thickness of the

Cylinder diameter	D	(m)	3.81×10^{-2}
Cylinder length	S	(m)	2.50×10^{-2}
Cylinder mass	M	(kg)	6.83×10^{-2}
Spring stiffness	K	(N/m)	1.6609
Structural damping	H	(N/(m/s))	4.344×10^{-3}
Mass ratio	m^*	$(-)$	2.4
Damping Ratio	ζ	$(-)$	0.0054
Added mass coeff.	C_A	$(-)$	1.0
Mass-damping parameter	$m^* \zeta$	$(-)$	13.00×10^{-3}
Natural frequency in air	$f_{0,a}$	(Hz)	0.7846
Natural frequency in water	f_0	(Hz)	0.6592

Table 2.6: System properties of the 2D simulations.

layer adjacent to the cylinder, where a specific refinement has been applied, remaining unchanged.

The circumferential subdivision varies as external subdivision is modified. Therefore, for the cells near the cylinder wall, the cells aspect ratio varies accordingly with the background grid.

Fig. 2.4 shows an overlap of the different computational grids, used for the grid density analysis, with the base 2D OLD grid.

The four meshes are tested for all the interested flow regimes $2.5 \leqslant U^* \leqslant 17$. The choice to carry out the study on such a wide range of reduced velocity U^* is linked to the complex nature of the VIV phenomenon, in fact, as it was shown in the introductory chapter 1, the response characteristics of the cylinder varies a lot as the reduced velocity varies.

Fig. 2.5 shows the comparison between the four different meshes in terms of dimensionless oscillation amplitude $A^* = A/D$ (Fig. 2.5(a)) and frequency ratio $f^* = f/f_0$ (Fig. 2.5(b)) in function of the number of cells. To better identify the discrepancy between the meshes, the results presented in Fig. 2.5 are divided into the corresponding branches.

Grid name	2D COARSE	2D BASE	2D BASEFINE	2D BASESFINE
Cells	25066 (65.16%)	38468 (100.00%)	54062 (140.54%)	96606 (251.13%)
Faces	100913	154723	217225	387724
Points	51430	78638	110078	195812
Background grid	(80,40,1)	(100,50,1)	(120,60,1)	(160,80,1)
Circumference points n_c	44	56	68	88
Max non-orthogonality	40.704	44.899	50.713	47.231
Max skewness	0.473	0.544	0.541	0.586
Max aspect ratio	12.557	13.067	15.116	13.902

Table 2.7: Comparison of the mesh characteristics of the grid density analysis.

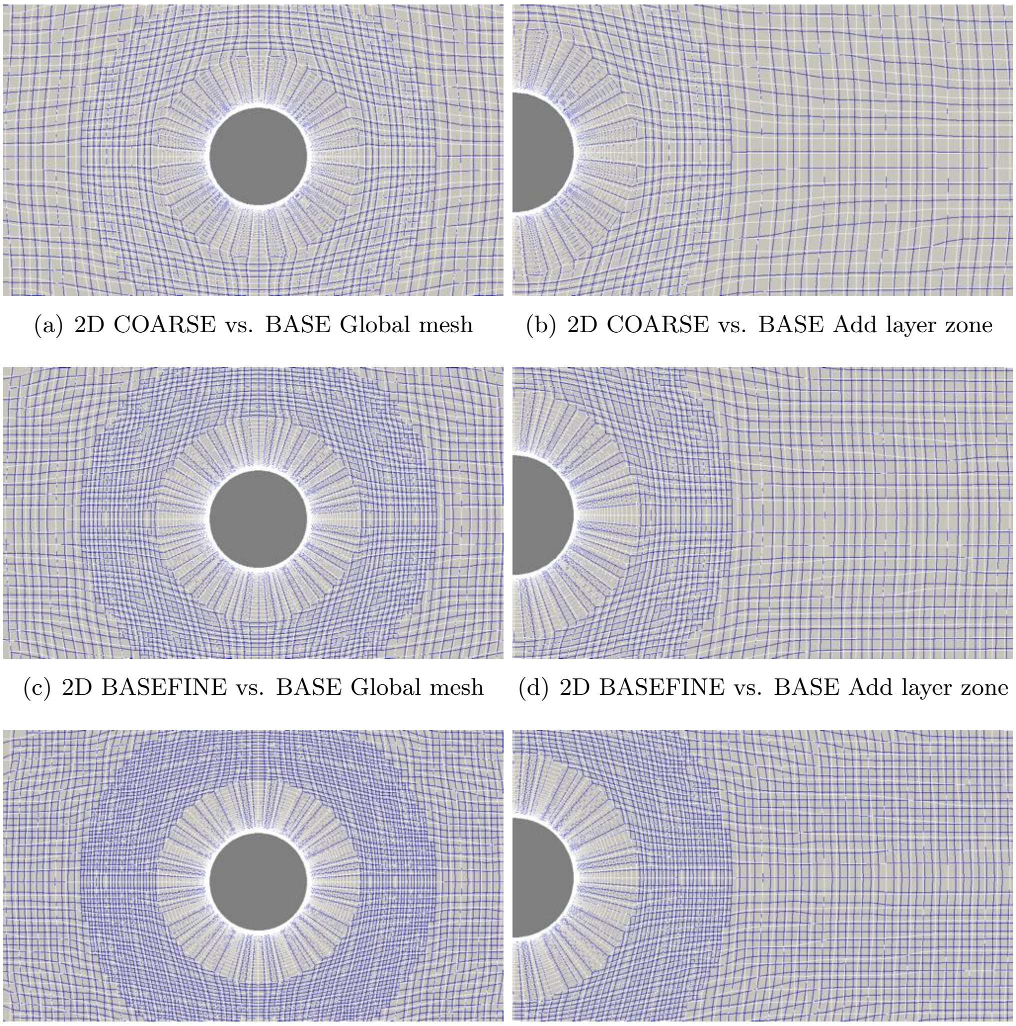

(a) 2D COARSE vs. BASE Global mesh (b) 2D COARSE vs. BASE Add layer zone

(c) 2D BASEFINE vs. BASE Global mesh (d) 2D BASEFINE vs. BASE Add layer zone

(e) 2D BASESFINE vs. BASE Global mesh (f) 2D BASESFINE vs. BASE Add layer zone

Figure 2.4: Overlap of the various mesh details. In all figures the white lines represent the 2D BASE mesh.

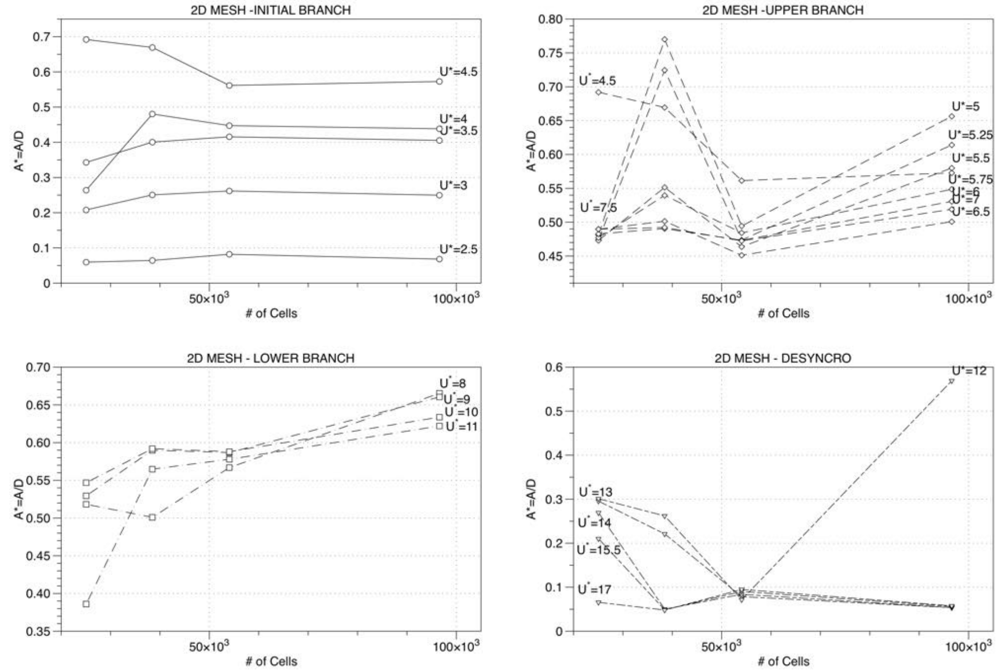

(a)

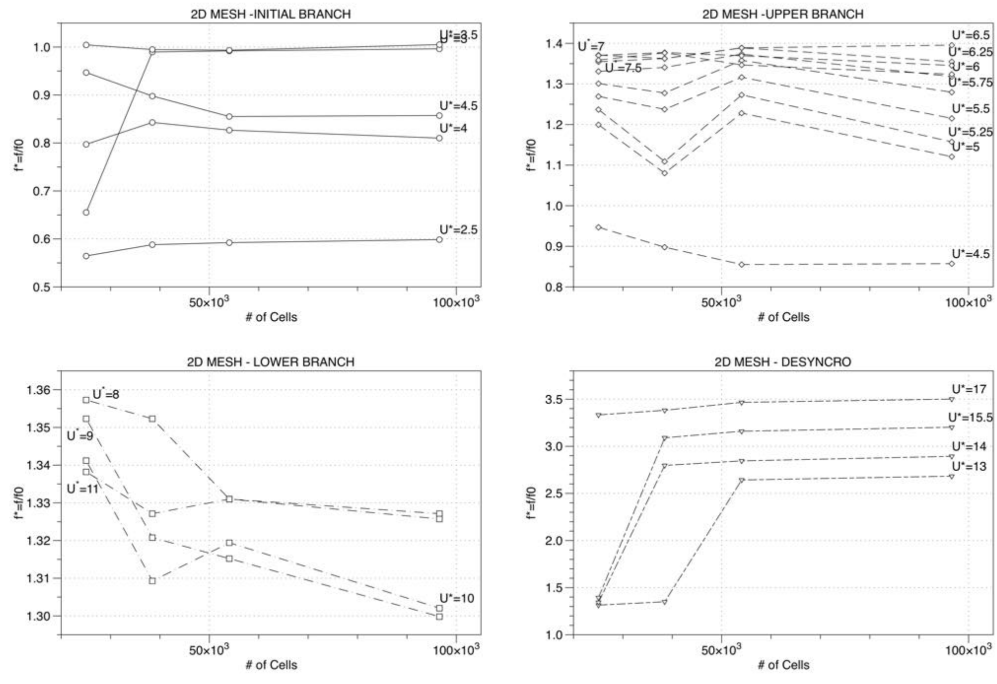

(b)

Figure 2.5: Effect of varying grid density. Amplitude ratio A^* (a) and frequency ratio f^* (b) versus the number of cells. The results are divided into the corresponding branches.

The maximum differences occur for the amplitude ratio in the upper branch region. In this region, any clear convergence has been found towards a unique value. It can be noted that, in the upper branch and in the desynchronisation region the value obtained with the 2D BASE mesh and 2D BASESFINE shows similar trends as the background grid is refined from $(100, 60, 1)$ to $(160, 80, 1)$. As regards the frequency ratio, the predicted values are identical to the tested meshes except for the 2D COARSE. In other words, the coarser grid is certainly inadequate to get the correct value of the oscillation frequency. The unsteady variation in both amplitude and frequency is therefore thought to be highly dependent on the grid density.
The time histories of the response displacement of the cylinder and the lift coefficient based on the four different meshes are compared in Fig. 2.6 for three representative flow regimes ($U^* = 3.5, 5.5$ and 7.5). The cylinder displacements, calculated from the four meshes, oscillate regularly at almost the same frequency in the case of $U^* = 3.5$ and $U^* = 7.5$ while, in the case of $U^* = 5.5$, the different time dependent lift force between the four meshes, leads to a worse correspondence of the obtained cylinder displacements.

It is worth noting that attaining grid independence numerical value does not mean getting the experimental value. Indeed, a grid independent solution only means the spatial discretisation errors have been eliminated and the asymptotic value may still have errors causing it to converge to a value different from the true experimental value. However, as exposed in the studies of Zhao et al. [32], Guilmineau and Queutey [24], Pan et al. [25] and Wu et al. [27], the 2D URANS simulations are not able to predict the experimental response amplitude in the upper and desynchronisation regimes. This is mainly due to the strong three-dimensional wake flow in these regimes.

2.2.2 Conclusions

The mesh density of $(100, 60, 1)$, used in the 2D BASE mesh, is considered to be adequate for further studies, as the differences between 2D BASE and 2D BASESFINE are minimal (5% for the A^* and 3% for f^*) in the two regimes where the bi-dimensional approach is in good agreement with the experimental results (see [24],[25] and [27] for reference).

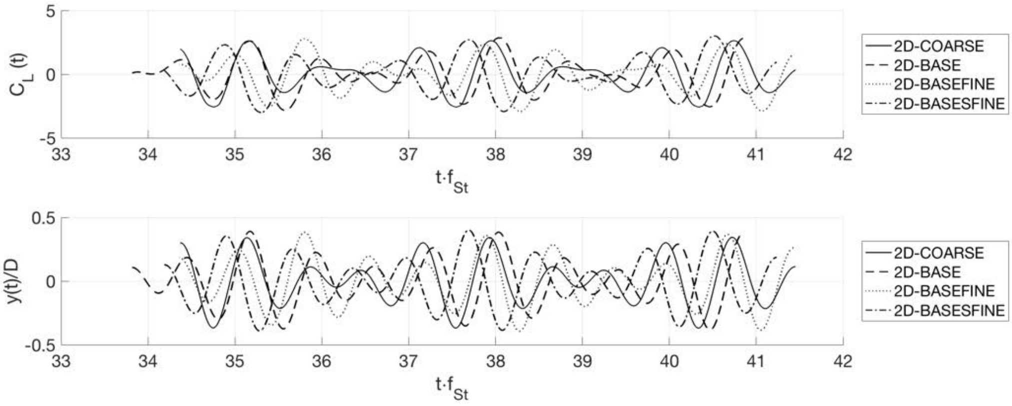

(a) Re=2941, U^*=3.50

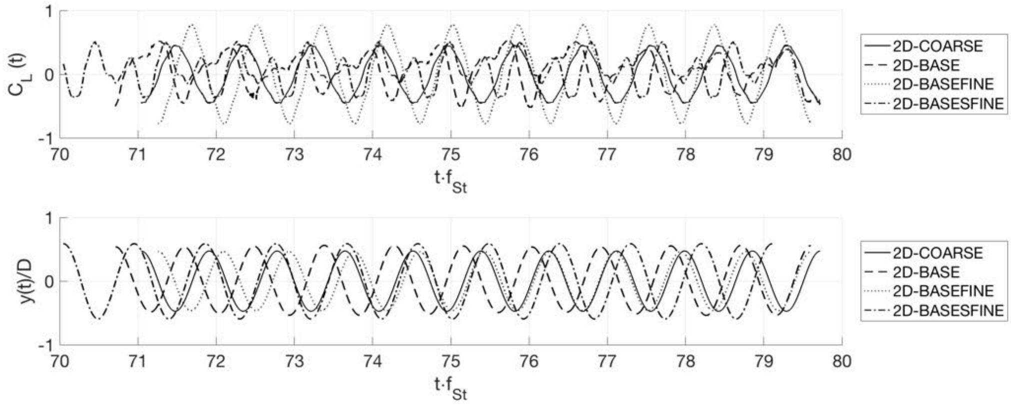

(b) Re=4622, U^*=5.50

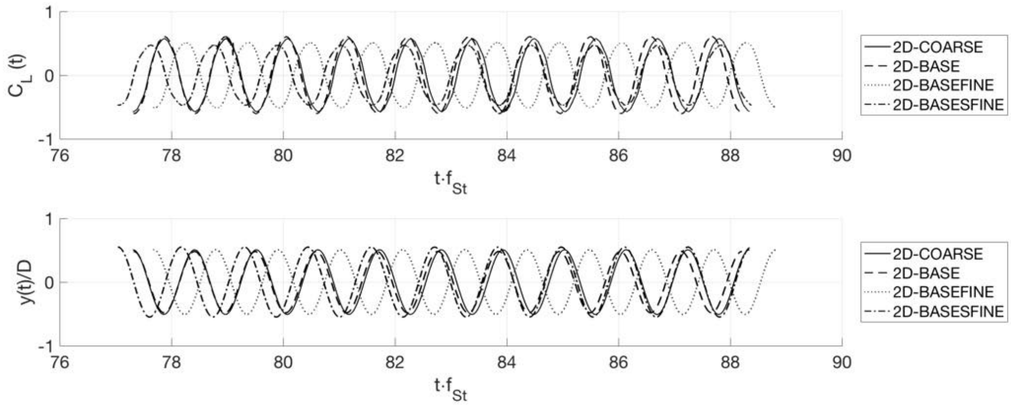

(c) Re=6303, U^*=7.50

Figure 2.6: A comparison between time-domain non-dimensional total force C_L (top plots) and the non-dimensional cylinder displacement $y(t)/D$ (bottom plots), obtained varying the grid density.

2.2.3 Near-wall layer treatment

The characteristics of the boundary layer play an important role in the overall flow structure (i.e. flow separation), therefore it is necessary to accurately capture the boundary layer profile. To achieve this for all meshes discussed until now, we must have the y^+ set equal to 1, doing so, the first cell of the mesh in radial direction from the cylinder wall will be inside the viscous sub-layer [59]. In order to investigate if the created near-wall layer treatment properly resolves the large velocity gradient close to the cylinder surface, a new set of meshes have been created.

The new meshes are obtained starting from the 2D BASE mesh with some changes only in the near-wall zone of the cylinder. In other words, the density of the meshes has been kept constant.

The different mesh characteristics are summarised in Tab. 2.8. The tables also report the 2D BASE mesh characteristics as reference. In Tab 2.8, Δr represents the radial extension of the near-wall layers from the surface of the cylinder, n_l the number of layers in the near-wall region and G is the grid expansion factor in the radial direction (cell size ratio between adjacent cells). The 2D NEW mesh is created by a reduction of the near-wall layer area in order to have the same aspect ratio of the cells after the circular refining zone. In the 2D NEW2 the near-wall layer area has been further reduced. Finally the 2D NEW3 has the same radial near-wall layer treatment of the 2D NEW2 grid but a further degree of cylindrical external refinement has been added. This is done in order to avoid the occurrence of numerical inaccuracies due to unfavourable cell aspect ratios inside the near-wall layer area.

Fig. 2.7 shows an overlap of the different computational grids, used for the near-wall treatment analysis, with the base 2D BASE grid. It can be seen, from the Fig. 2.7, that the grids near the cylinder are only stretched in the radial direction.

Grid name	2D BASE	2D NEW	2D NEW2	2D NEW3
Cells	38468 (100.00%)	38188 (99.27%)	37796 (98.25%)	40939 (106.42%)
Faces	154723	153603	152035	164688
Points	78638	78078	77294	83742
Background grid	(100,50,1)	(100,50,1)	(100,50,1)	(100,50,1)
Number of near-wall layers n_l	40	35	28	28
Circumference points n_c	56	56	56	108
Layers radial extension $\Delta r/D$	0.052	0.026	0.013	0.013
Grid expansion factor G	1.088	1.078	1.080	1.080
Max non-orthogonality	44.899	33.804	33.600	31.360
Max skewness	0.544	0.444	0.392	0.412
Max aspect ratio	13.067	13.285	14.263	15.167

Table 2.8: A comparison among the mesh characteristics of the near-wall layer treatments analysis.

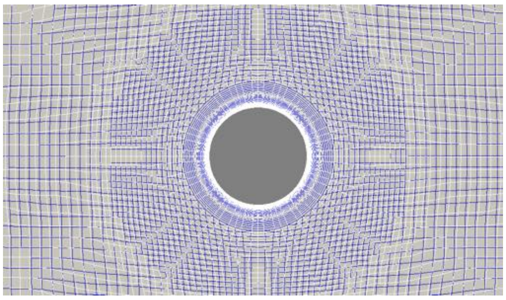

(a) 2D NEW vs. BASE Global mesh

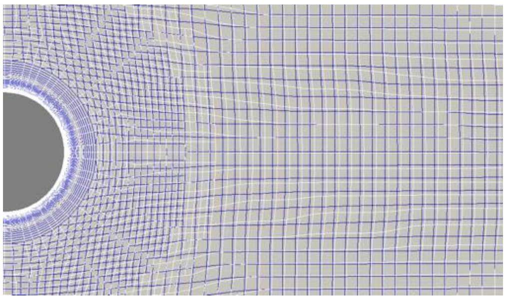

(b) 2D NEW vs. BASE Add layer zone

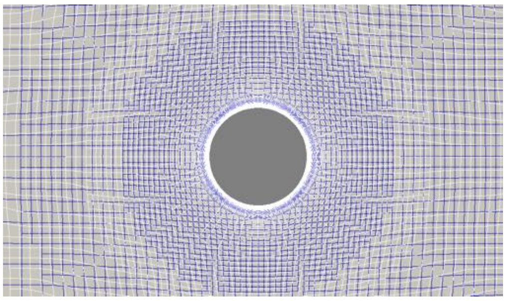

(c) 2D NEW2 vs. BASE Global mesh

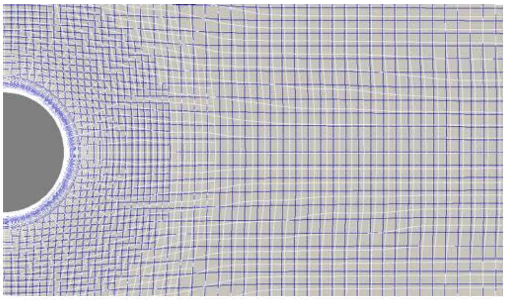

(d) 2D NEW2 vs. BASE Add layer zone

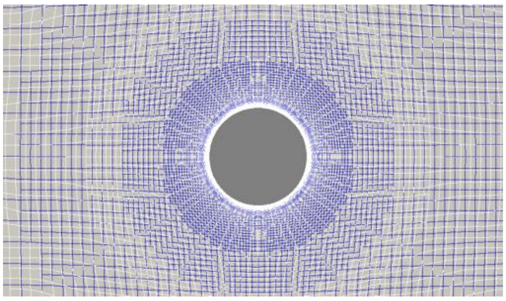

(e) 2D NEW3 vs. BASE Global mesh

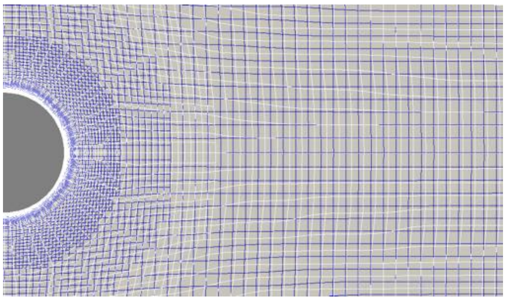

(f) 2D NEW3 vs. BASE Add layer zone

Figure 2.7: Overlap of the various mesh details. In all figures the white lines represent the 2D BASE mesh.

Fig. 2.8 shows the comparison among the four different meshes, made for the near-wall refinement studies, in terms of dimensionless oscillation amplitude $A^* = A/D$ (Fig. 2.8(a)) and frequency ratio $f^* = f/f_0$ (Fig. 2.8(b)). To better identify the discrepancy between the meshes, the results presented in Fig. 2.8 are divided into the corresponding branches.

The results found in terms of A^* are very sensitive to the different near-wall resolution, while the difference of the results in terms of f^* are negligible for almost all the U^*.

By reducing the near-wall layer area from $\Delta r/D = 0.052$ of the 2D BASE mesh, to $\Delta r/D = 0.026$ of the 2D NEW mesh, there are significant differences in the amplitude of cylinder response, while the further reduction of near-wall layer area, from $\Delta r/D = 0.026$

to $\Delta r/D = 0.013$ seems to have less influence in the A^* response. The error estimated by comparing the solutions between the meshes 2D BASE and the 2D NEW, shows a difference of 37% for some values in the upper branch region and more than 50% for the value in the desynchronisation region. A possible reason is related to the high grading ratio ($G = 1.088$) used to stretch the grid in radial direction in case 2D BASE. This ratio creates a large discrepancy element size among adjacent cells. Thus, case 2D BASE presents large cells close to the cylinder wall. Then, the simulation is unable to resolve accurately the high velocity gradient near-wall area.
The difference between the 2D NEW and the 2D NEW3 meshes shows an error higher than 50% for the results in terms of A^* and $\approx 30\%$ in the results in terms of f^* for a few U^*.
Now taking into account the considerations made at the end of the subsection 2.2.1 and considering only the initial and lower branch, where the bi-dimensional approach predicts correctly the experimental value, the different results between the 2D NEW and the 2D NEW3 are greatly reduced to 12% for A^* and 4% for f^*.
Note that the $U^* = 3$ and $U^* = 14$ are two particular cases because a double peak behaviour of the frequency is found. As reported by Pigazzini et al. [60], the lower frequency is the Strouhal frequency, the upper frequency is the natural frequency in still water. Therefore, in order to compare the differences between the meshes in terms of frequency, both main peaks of the amplitude spectrum must be compared. In the two cases $U^* = 3$ and $U^* = 14$, there is indeed a dominant frequency exchange, this leads to a wrong estimation of the error having considered only the dominant peak.

Fig. 2.9 reports the comparison between the time histories of the cylinder response displacement and the lift coefficient based on the four different near-wall treatments for the same three representative flow regimes ($U^* = 3.5, 5.5$ and 7.5) reported in the previous subsection 2.2.1. The same considerations made in the previous subsection 2.2.1 can be made here. In particular, in case of $U^* = 5.5$ (Fig. 2.9(b)), the complex time dependent lift force $C_L(t)$ leads to a worse correspondence of the cylinder response $y(t)/D$ between the meshes.

2.2.4 Conclusions

Based on the detailed mesh sensitivity study described here, the 2D NEW mesh configuration are selected as baseline mesh for the following thee-dimensional study. The 2D NEW grid has been retained better than the 2D BASE thanks to the more gradual change in cell/element size (smoothness) in the near-wall region. Moreover, the maximum mesh non-orthogonality and the maximum skewness has been reduced in the 2D NEW mesh compared to the 2D BASE. The 2D NEW grid has been retained since it offers similar accuracy to the 2D NEW3 mesh with fewer cells, due to its extra circumferential refinement, but with the same quality mesh control (non-orthogonality, skewness and aspect ratio).

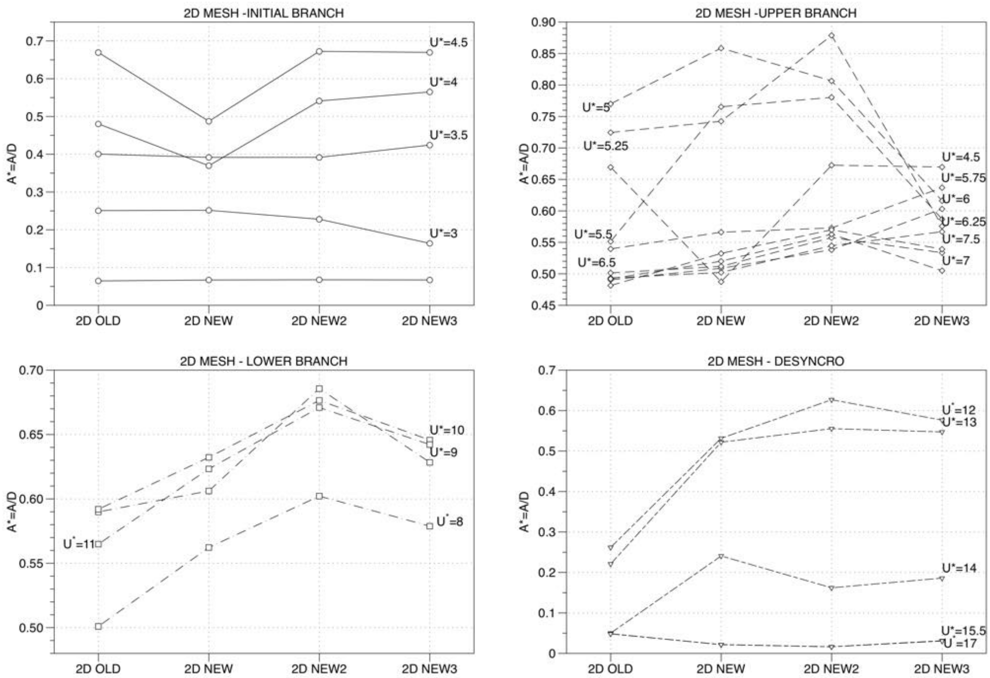

(a)

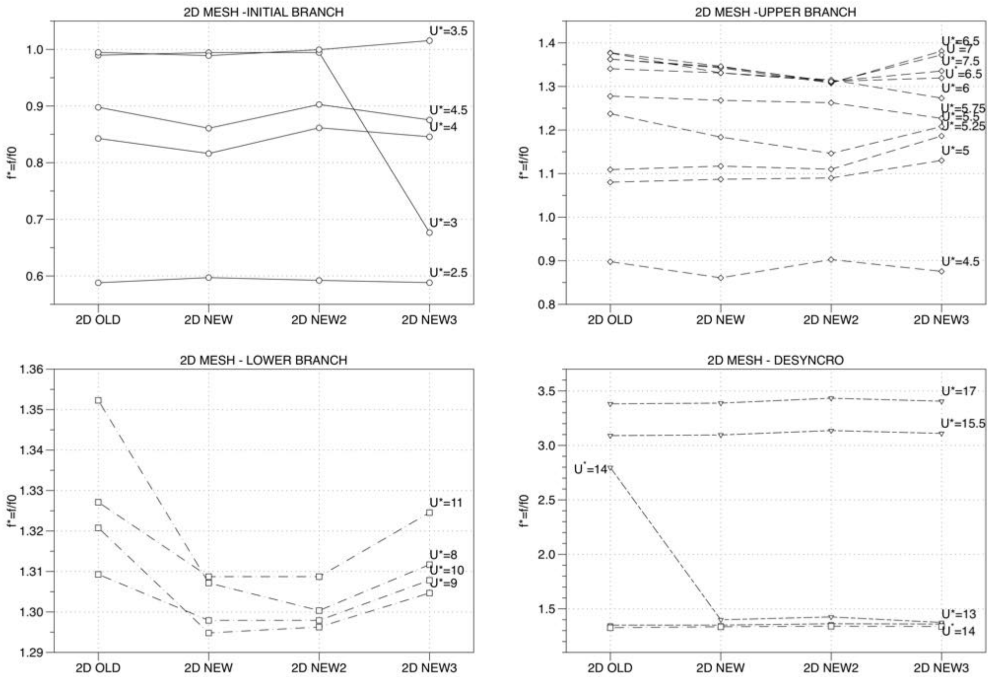

(b)

Figure 2.8: Effects of varying grid density. Amplitude ratio A^* (a) and frequency ratio f^* (b) versus the number of cells. The results are divided into the corresponding branches.

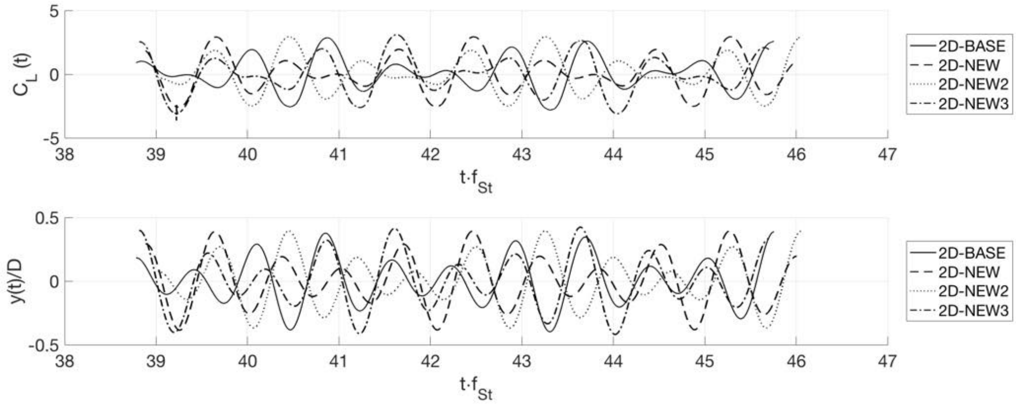

(a) Re=2941, U^{*}=3.50

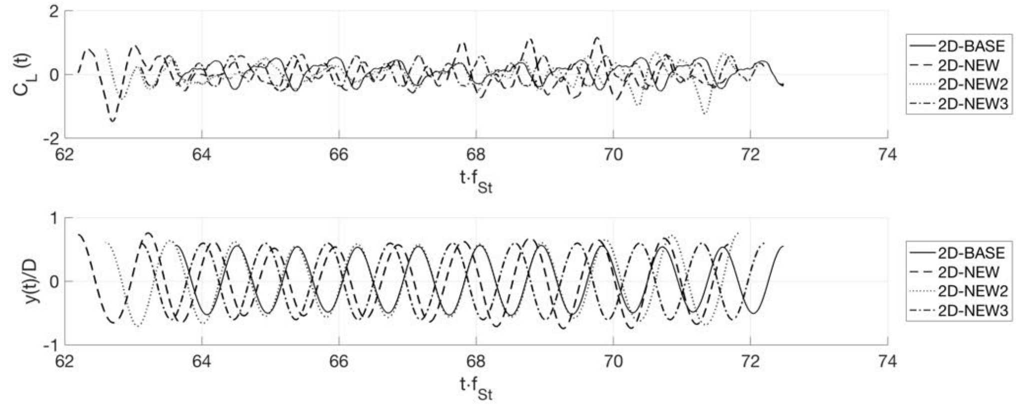

(b) Re=4622, U^{*}=5.50

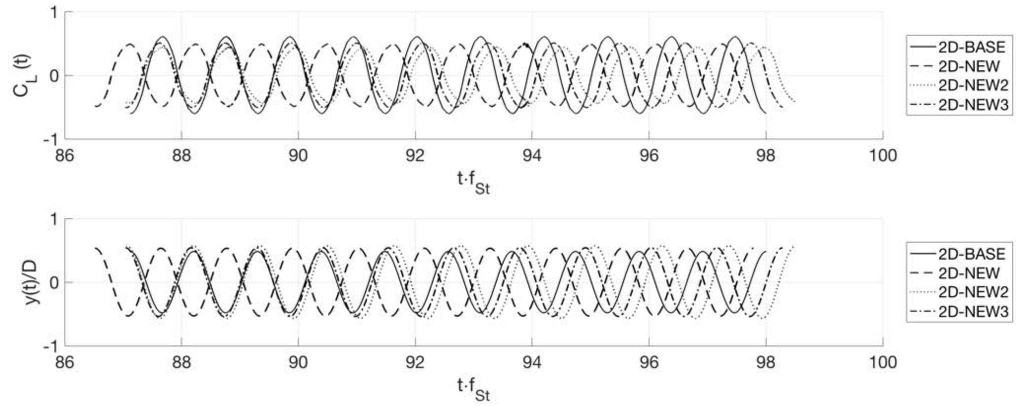

(c) Re=6303, U^{*}=7.50

Figure 2.9: A comparison between time-domain non-dimensional total force C_L (top plots) and the non-dimensional cylinder displacement $y(t)/D$ (bottom plots) obtained varying the near wall treatment.

2.2.5 Three-dimensional grids

In order to quantify the dependency of the numerical results on the mesh density, 3D numerical simulations of 1-DOF VIV of a circular cylinder are performed using three different meshes as summarized in Tab. 2.10 in which n_s represents the number of points along the span direction of the cylinder.
The length of the 3D domain in the span direction is defined according to the experimental dimension of Khalack and Willamson $S \approx 10 \cdot D$ [15]. In Tab. 2.9 the system properties of the 3D simulations are summarized.

Cylinder diameter	D	(m)	3.81×10^{-2}
Cylinder span	S	(m)	0.38
Cylinder mass	M	(kg)	1.0388
Spring stiffness	K	(N/m)	25.2465
Structural damping	H	(N/(m/s))	0.0660
Mass ratio	m^*	$(-)$	2.4
Damping Ratio	ζ	$(-)$	0.0054
Added mass coeff.	C_A	$(-)$	1.0
Mass-damping parameter	$m^* \zeta$	$(-)$	13.00×10^{-3}
Natural frequency in air	$f_{0,a}$	(Hz)	0.7846
Natural frequency in water	f_0	(Hz)	0.6592

Table 2.9: System properties of the 3D simulations.

The 3D NEW grid is created starting from the same slice of the 2D NEW grid and maintaining the same cell aspect ratio also in the span-wise directions. The final span-wise resolution of the three meshes, respect guidelines suggested by D'Alessandro et al.[61]. D'Alessandro et al. suggested a minimum number of 48 cells every πD to capture the stream-wise vortex structures.
The 3D COARSE mesh shares the same features on the plane normal to the cylinder's axis with the 2D COARSE mesh. While the 3D FINE has the same grid density of the 2D FINE mesh but with the near-wall treatment of the 2D NEW3. It can be noted that

the three grids also have a different span-wise resolution in order to maintain the same cell aspect ratio of the surface mesh.
Five representative reduced velocity $U^* = 3.5, 5, 5.5, 10$ and 14 are selected in order to investigate the difference between the meshes for all the branches.
The time step employed in the simulation is dynamically adjusted to achieve a Courant number less than 0.9 for every time step.

Grid name	3D COARSE	3D NEW	3D FINE
Cells	1961860 (56.38%)	3479859 (100.00%)	8046472 (231.23%)
Faces	5966356	10563538	24380112
Points	2043288	3604422	8288241
Background grid	(80,40,10)	(100,50,12)	(120,60,14)
Circumference points n_c	44	56	132
Span points n_s	192	256	512
Max non-orthogonality	43.439	35.925	34.022
Max skewness	0.457	0.417	0.3725
Max aspect ratio	38.300	32.948	16.232

Table 2.10: Comparison of the mesh characteristics of the 3D grid sensitivity study.

Quantitative comparisons of the non-dimensional oscillation amplitudes A^* and frequency ratio f^* calculated from the different meshes are provided in Tab. 2.11.

The comparison of Tab. 2.11 among the results from different meshes suggests that the mesh density has a greater influence on the amplitude value than on the frequency. In detail, Tab. 2.11 shows that the amplitude ratio of the 3D NEW is more than 23% different from the 3D FINE mesh for the value of $U^* = 3.5$ and 14. For the other three considered reduced velocity the difference is less than 7%. The comparison among the results in term of frequency ratio shows that the difference between the 3D FINE mesh and the other considered meshes are less than 8% for all the considered velocity fields.

Grid Convergence Index

The Grid Convergence Index (GCI) provides a uniform measure of convergence for grid refinement studies [62]. It is based on estimated fractional error derived from the gener-

	Grid name	U^*				
		3.5	5.0	5.5	10.0	14.0
A^*	3D COARSE	0.382	0.830	0.900	0.474	0.161
	3D NEW	0.390	0.859	0.957	0.635	0.270
	3D FINE	0.317	0.879	0.983	0.688	0.218
f^*	3D COARSE	0.988	0.926	0.970	1.317	1.447
	3D NEW	0.989	0.961	0.926	1.306	1.528
	3D FINE	0.990	0.979	1.010	1.312	1.455

Table 2.11: Comparison of the results from the three different 3D meshes.

alisation of Richardson Extrapolation (RE)[63]. The GCI value represents the resolution level and how much the solution approaches the asymptotic value.
The recomended procedure for estimation of the discretisation error based on GCI, as reported by the Fluids Engineering Division of ASME [64], can be summarized with the following steps:

1. Convergence studies for parameters are performed following a systematic refinement process to create multiple solutions (at least 3) for parameters under investigations, holding all parameters constant. Defining r as refinement factor, in the case of unstructured grid it can be calculated in terms of total number of cells N_i used in the grids with the following formula:

$$r_{21} = \left(\frac{N_1}{N_2}\right)^{1/d}, \qquad r_{32} = \left(\frac{N_2}{N_2}\right)^{1/d}, \tag{2.7}$$

   where d is the dimensionality of the problem (for 3D simulations is 3) and $N_1 > N_2 > N_3$ are the total number of cells of the three selected sets of grids.

2. Select three different solutions $\hat{S}_{i,1}, \hat{S}_{i,2}$ and $\hat{S}_{i,3}$ with fine, medium and coarse for the i input parameters. Then, changes between medium-fine and coarse-medium input are represented by $\epsilon_{i,21} = \hat{S}_{i,2} - \hat{S}_{i,1}$ and $\epsilon_{i,32} = \hat{S}_{i,3} - \hat{S}_{i,2}$. So the convergence ratio for the input parameter is defined as:

$$R_i = \frac{\epsilon_{i,21}}{\epsilon_{i,32}}. \tag{2.8}$$

   Depending on the sign and magnitude of R_i, three convergence conditions are possible:

   - $0 < R_i < 1$ monotonic convergence,
   - $R_i < 0$ oscillatory convergence,

- $R_i > 1$ divergence.

For monotonic convergence, generalized RE is used to estimate the aproximate relative error e^a, the extrapolated relative error e^{ext} and the GCI. For oscillatory convergence, the solution exhibits oscillations, which may be erroneously identified as monotonic or divergence conditions in function of the relationship of the chosen grid size to the unknown period(s) of oscillation(s) (as shows by Coleman et al. [65]). In the case of oscillatory convergence, more than 3 solutions are required. In the case of divergence the solutions diverge and the errors cannot be estimated.

3. After the convergence study the order of convergence or accuracy p_i is estimated using the expression:

$$p_i = \left| \frac{\ln |\epsilon_{i,32}/\epsilon_{i,21}|}{r_2 1} + q(p) \right|, \tag{2.9}$$

$$q(p) = \ln \left(\frac{r_{21}^p - s}{r_{21}^p - s} \right), \tag{2.10}$$

$$s = 1 \cdot \mathrm{sgn}(\epsilon_{32}/\epsilon_{21}). \tag{2.11}$$

Note that $q(p) = 0$ for $r = const.$ Eq. (2.9) can be solved using fixed-point iteration, with the initial guess equal to the first term.

4. Calculate extrapolated values from

$$\hat{S}_{i,21}^{ext} = \left(r_{21}^{p_i} \hat{S}_{i,1} - \hat{S}_{i,2} \right) / \left(r_{21}^{p_i} - 1 \right), \tag{2.12}$$

similarly calculate $\hat{S}_{i,32}^{ext}$.

5. Finally, calculate and report the following error estimate along with the apparent order p_i. In approximate relative error:

$$e_{21}^a = \left| \frac{\epsilon_{i,21}}{\epsilon_{i,32}} \right|. \tag{2.13}$$

In extrapolated relative error:

$$e_{21}^{ext} = \left| \frac{\hat{S}_{i,21}^{ext} - \hat{S}_{i,1}}{\hat{S}_{i,21}^{ext}} \right|. \tag{2.14}$$

In the GCI:

$$GCI_{fine}^{21} = \frac{F_s e_{21}^a}{r_{21}^{p_i}}. \tag{2.15}$$

Thus, GCI is defined to be a multiple of Richardson normalised discretisation error by F_s (factor of safety), suggested to be 1.25 in the case of symmetric parameter refinement study with at least three inputs.

Tab. 2.12 and Tab. 2.13 illustrates the calculation procedure for the three 3D meshes in terms of A^* and f^* for the selected U^*. The results only show monotonous or oscillatory convergence.

As listed in Tab. 2.12 and Tab. 2.13, there is a reduction of GCI value for the successive grid refinements ($GCI^{21}_{fine} < GCI^{32}_{fine}$) about each of the two variables for all the selected U^*. The only exception is the case $U^* = 3.5$ for the variable A^* and $U^* = 5.5$ for the variable f^* where the GCI value grows from 0.4% to 1.2% and from 14.1% to 15.4% respectively. This is probably due to the oscillatory convergence, in fact, as shown by Coleman et al. [65], in the case of oscillatory convergence more than 3 grids are required in order to get them correctly diagnose as either monotonic convergence or divergence.

$A^* = A/D$	$U^* = 3.5$	$U^* = 5$	$U^* = 5.5$	$U^* = 10$	$U^* = 14$
1) 3D FINE	0.317	0.879	0.983	0.688	0.218
2) 3D NEW	0.390	0.859	0.957	0.635	0.270
3) 3D COARSE	0.382	0.830	0.900	0.474	0.161
r_{21}	1.322	1.322	1.322	1.322	1.322
r_{32}	1.210	1.210	1.210	1.210	1.210
ϵ_{21}	0.073	-0.020	-0.025	-0.053	0.051
ϵ_{32}	-0.008	-0.029	-0.058	-0.161	-0.108
R	-9.513	0.717	0.439	0.328	-0.474
s	-1	1	1	1	-1
p	7.497	1.255	3.137	4.263	2.835
$\hat{S}^{ext}_{21}$	0.306	0.928	1.001	0.711	0.176
$\hat{S}^{ext}_{32}$	0.392	0.964	1.028	0.764	0.420
e^a_{21}	23.2%	2.3%	2.6%	7.7%	23.5%
e^a_{32}	2.0%	3.3%	6.0%	25.4%	40.2%
e^{ext}_{21}	3.4%	5.2%	1.8%	3.2%	24.2%
e^{ext}_{32}	0.6%	10.9%	6.8%	16.8%	35.9%
GCI^{21}_{fine}	4.1%	6.9%	2.3%	4.2%	24.4%
GCI^{32}_{fine}	0.8%	15.3%	9.2%	25.2%	69.9%

Table 2.12: Calculation of the discretisation error for A^*

For all the other cases the GCI for finer grid (GCI^{21}_{fine}) is relatively low if compared to the coarser grid (GCI^{32}_{fine}), this indicating that the dependency of the numerical simulation on the cell size has been reduced. The value of GCI^{21}_{fine} still remains high, further refinement probably will improve the results of the simulation. The study of an even finer grid remains outside our computational possibilities for now. Nevertheless, considering that the reduction from the coarser grid to the finer grid is relatively high, the grid independent solution can be said to have been nearly achieved. Comparison between the extrapolated value ($\hat{S}^{ext}_{21}, \hat{S}^{ext}_{32}$) calculated from Richardson extrapolation Eq. (2.12)

$f^* = f/f_0$	$U^* = 3.5$	$U^* = 5$	$U^* = 5.5$	$U^* = 10$	$U^* = 14$
1) 3D FINE	0.990	0.979	1.010	1.312	1.455
2) 3D NEW	0.989	0.961	0.926	1.306	1.528
3) 3D COARSE	0.988	0.926	0.970	1.317	1.447
r_{21}	1.322	1.322	1.322	1.322	1.322
r_{32}	1.210	1.210	1.210	1.210	1.210
ϵ_{21}	-0.001	-0.019	-0.084	-0.006	0.073
ϵ_{32}	-0.001	-0.035	0.044	0.010	-0.081
R	0.896	0.538	-1.909	-0.533	-0.898
s	1	1	-1	-1	-1
p	0.808	2.729	1.846	2.765	0.802
$\hat{S}_{21}^{ext}$	0.993	0.996	1.135	1.316	1.165
$\hat{S}_{32}^{ext}$	0.994	1.011	0.822	1.291	2.017
e_{21}^{a}	0.1%	1.9%	8.3%	0.4%	5.0%
e_{32}^{a}	0.1%	3.6%	4.8%	0.8%	5.3%
e_{21}^{ext}	0.3%	1.6%	11.0%	0.4%	24.9%
e_{32}^{ext}	0.5%	5.0%	12.7%	1.1%	24.3%
GCI_{fine}^{21}	0.4%	2.1%	15.4%	0.5%	24.9%
GCI_{fine}^{32}	0.6%	6.6%	14.1%	1.4%	40.0%

Table 2.13: Calculation of the discretization error for f^*

and the simulation values shows that the successive grid refinements nearly achieve the asymptotic values at the finest grid resolution. The extrapolated relative error e_{21}^{ext} is less than 5.2% for all the monotonically convergent cases. This indicates that the specific VIV case has been adequately resolved.

Final Mesh selection

The computational expense of the study turned out to be considerable, primarily due to the necessity of simulating a very large number of time steps for statistical convergence. With the GCI method, it is shown that the solution has converged with refinement from the coarser grid to the finer grid.
Since the 3D FINE mesh shows significant variations in terms of amplitude for some U^* considered, it has been discharged due to the exaggerated computational cost. Considering the results shown in Tab. 2.11 for the reduced velocity U^*, the 3D NEW mesh shows $\approx 2\%$ of difference in both frequency and amplitude from the 3D FINE mesh, while the 3D COARSE mesh shows more than 5% of difference. This confirms the adequacy of the mesh 3D NEW in computing accurate results in the upper branch where maximum response amplitude occurs. Therefore, even knowing that high spatial discretisation errors exist in the initial branch and in the desynchronisation regime regarding the non-dimensional amplitude, it can be concluded that the 3D NEW mesh is chosen for the further three-dimensional research.

2.3 Comparison between 2D and 3D URANS simulations

The present study aims to access the adequacy of the often made bi-dimensional mesh simplification in Vortex-Induced Vibrations studies. The use of the bi-dimensional approach may easily reduce the computational time by a few orders of magnitude, but for long unsteady calculations the 3D simulations seem to be the only reasonable way to simulate [66]. However, understanding whether this simplification can be accepted or even considered for a case of VIV, is one of the key tasks of this study.
Therefore, through the use of a case study, we want to explore in detail the differences between 2D and 3D mesh models in order to compare their results with the selected experimental case. Furthermore, we want to understand the limits of URANS simulation in VIV specific aspect.

This section is organised as follows. The results of the CFD simulations are firstly discussed. Then, the differences between the bi-dimensional and three-dimensional URANS simulations are highlighted. In particular, the cylinder VIV response is presented in terms of motion amplitude and frequency, then the analysis of total and vortex forces and their phases with respect to the cylinder motion are discussed. In this study the three-dimensional character of the wake field is illustrated using different plots and evaluated using the correlation coefficient. Finally the vortex flow patterns are compared to the well known Roshko map. Computational costs and facilities are then briefly summarized.

2.3.1 Cylinder response

The 3D results of VIV for a circular cylinder are compared with the 2D results and with the the experimental data by Khalak and Williamson [15]. The non-dimensional amplitude of the motion of the cylinder $A^* = A/D$ and the non-dimensional dominant frequency of the motion $f^* = f/f_0$ are shown in Fig. 2.10(a) and Fig. 2.10(b) respectively. The vertical dashed line in Fig. 2.10 defines the different branch regions according to the 3D simulations.

The 2D and the 3D results are identical in some parts of the interested regimes. The greatest discrepancies between CFD and experimental results are found in the upper branch and in the transition zone between lower branch and desyncronization regime. Otherwise, the oscillation amplitudes are in reasonable agreement with experimental results. The difference in the upper-lower branch transition location between CFD ($U^* = 6$) and experimental results ($U^* \approx 7$), may be due to the distinction of velocity initial conditions between the two methods. Indeed, the velocity initial condition for the CFD simulation was fixed at the target value for every case, while in the experiments, the velocity was gradually incremented. Lower branch amplitudes are slightly underestimated between $U^* = 6$ and $U^* = 8$. This effect has been also observed by Morse et al. [**morse2008effect**] in the case of attached endplate (as in the simulations) compared to experimental data from Khalak and Williamson [5].
Comparing 2D and 3D results in Fig. 2.10(a), the most important difference lies in the

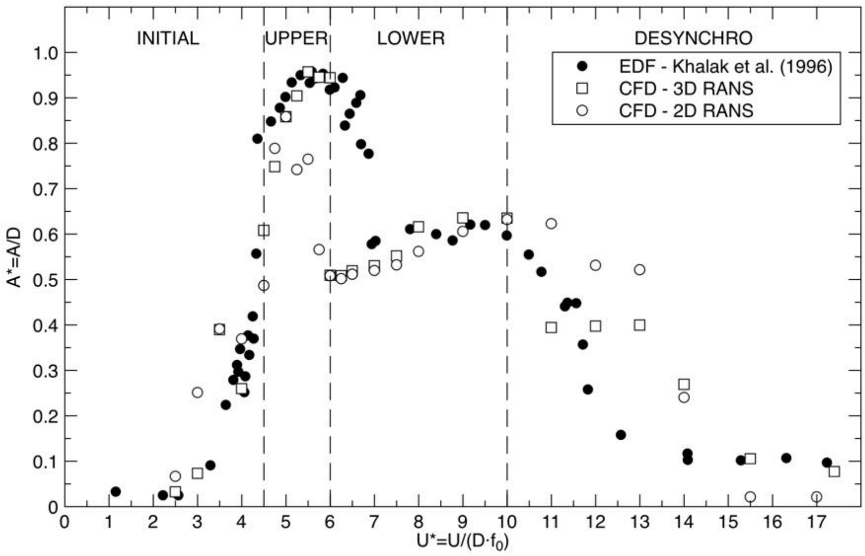

(a) Amplitude ratio A^* Vs reduced velocity U^*

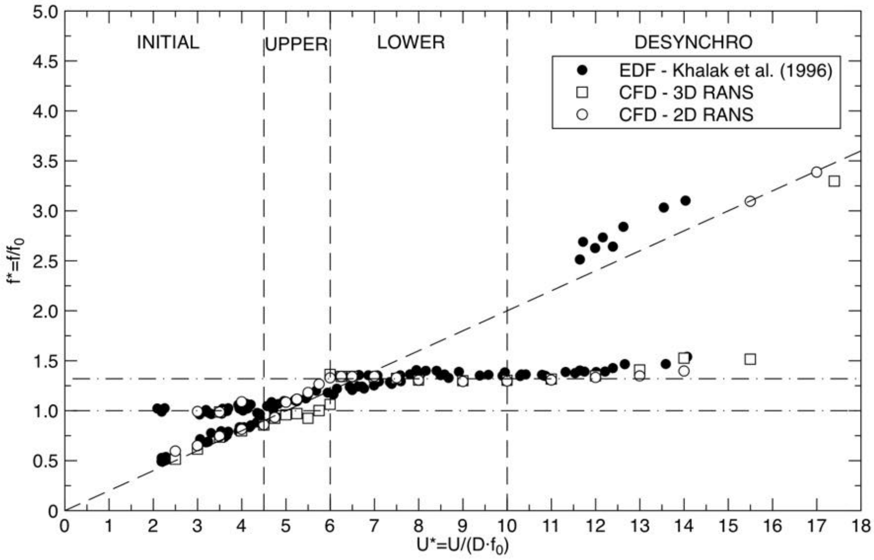

(b) Frequency ratio f^* Vs reduced velocity U^*

Figure 2.10: Comparison between experimental data by Khalak and Williamson [15] (solid circles), present 2D CFD results (empty circles) and present 3D CFD results (empty squares). The oblique dashed line in (b) corresponds to the Strouhal frequency (St = 0.20).

better estimation of maximum oscillation amplitudes in the upper branch using the 3D URANS approach, as well as in the desyncronization range for $U^* \geqslant 15$. Notable differences are also observed in the initial part of desyncronization range.

The cylinder frequency response of 2D and 3D simulations compares very well with experimental data in Fig. 2.10(b). In particular, also some double-peaked behaviour in the initial branch has been successfully simulated. The frequency response of the 3D simulations in the upper branch shows slightly lower frequencies with respect to experimental results, otherwise a good agreement with experimental data is found. In Fig. 2.10(b), it can also be seen that the dominant frequency of 2D simulations and experiments increases throughout the upper branch, where in the case of 3D simulation, the frequency stays near the natural frequency instead. This particular aspect is commented in the next section.

2.3.2 Force coefficient and phase

In an attempt to further investigate the vortex shedding modes obtained with the numerical simulations, an additional analysis has been made on the phase lag between the motion of the cylinder and the forcing term. In that respect, Godvardhan and Williamson [9] suggest considering not only the total force F_L but also the "vortex shedding" (VS) force F_{VS} thus, following the decomposition used by Govardhan and Williamson [**govardhan2000modes**] the vortex shedding force can be computed by

$$F_{VS}(t) = F_L(t) - F_{POT}(t) \tag{2.16}$$

F_{POT} is the potential force component (POT), given by the potential added-mass force:

$$F_{POT}(t) = -M_A \ddot{y} \tag{2.17}$$

with $M_A = C_A \rho \frac{\pi D^2}{4} S$ is the added mass, C_A the added mass coefficient.
In non-dimensional form, F_L,F_{VS} and F_{POT} can be written conveniently as:

$$C_L(t) = \frac{F_L}{F_0}, \qquad C_{VS}(t) = \frac{F_{VS}}{F_0}, \qquad C_{POT}(t) = \frac{F_{POT}}{F_0}, \tag{2.18}$$

where $F_0 = \frac{1}{2}\rho D S U^2$ is a reference force.

The root mean square (rms) of the total force C_L amplitude and phase ϕ between the total force and the displacement are presented in Fig.2.11(a) with respect to the reduced velocity U^* for both 2D and 3D simulations.

The total force shows a rapid increase in its amplitude between the initial and upper branch, where it peaks. A sharp drop is shown in the upper-lower transition zone as expected (see [**govardhan2000modes**]). The total force further decreases along the lower branch and desynchronisation regime.

Differences between 2D and 3D are most visible in the initial and upper branches: in the early stages of initial branch, 2D simulations show higher total force, where in the

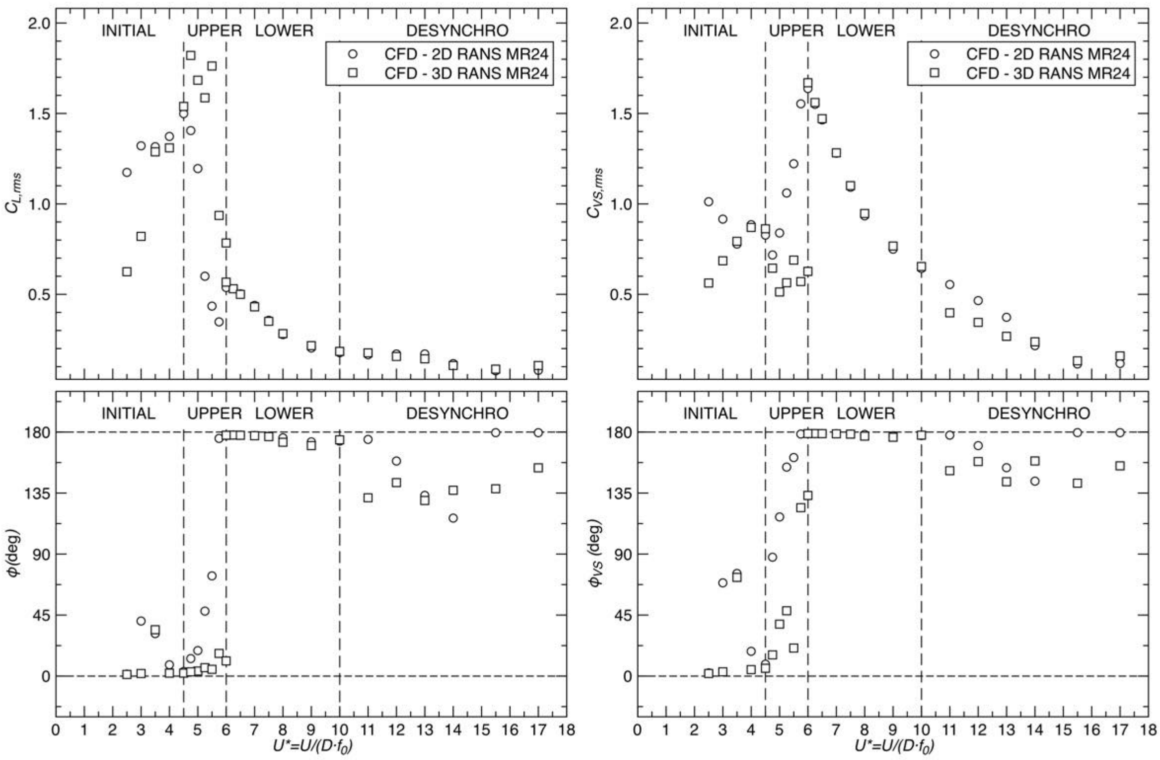

(a) Total force.

(b) Vortex Shedding force.

Figure 2.11: Force and phase angle variation with U^*.

upper branch it drops rapidly, where the 3D case shows higher and more steady values. In general, the 3D case shows higher total force in the upper branch with respect to the 2D case, allowing for larger amplitudes. No significant differences are present both in the lower branch and desynchronisation regime as 2D and 3D results overlap.

The total force phase ϕ comparison shows that the 3D case exhibits a sharp jump of the total force phase jump between upper and lower branch, from 0 to 180 deg as observed, and reported in [5]. The 2D results show instead that during the upper branch, the phase rises gradually before reaching 180 deg a little earlier than the 3D case. Total force phases of both cases remain almost identical in the lower branch.

The value of the vortex shedding force, C_{VS}, and phase, ϕ_{VS}, between the vortex shedding force and the displacement are presented in Fig. 2.11(b). Also for the case of the vortex shedding force, the main differences between the two cases are found in the upper branch. Differently from what is observed in the case of the total force, the vortex shedding force of the 3D case is lower and more constant compared to the 2D case. Also, the vortex shedding force in the 2D case rises in the upper branch peaking at the upper-lower transition. For the 3D case, vortex shedding force in the upper branch is lower than the total force. The 2D case instead shows values of the vortex shedding forces that are higher than the total force towards the end of the upper branch. For $U^* \geqslant 5$, the vortex shedding force is almost identical for both cases in the lower branch, the 3D case shows slightly lower values once in the desynchronisation range.

The vortex shedding force ϕ_{VS} phase shows that in both 2D and 3D cases in the upper branch there are intermediate values between 0 and 180 deg. No large phase jump is present between upper and lower branch, both cases show increasing phase angle, and as in the case for the total force, the 2D case reaches 180 deg phase slightly earlier than the 3D case. Also in this case, phases in the lower branch are identical.

Fig. 2.11 shows the non-dimensional time domain vortex shedding force C_{VS} and the non-dimensional total force C_L, obtained through the 2D and the 3D CFD simulations respectively, for eight representative flow regimes ($U^* = 3.5, 4.5, 5, 5.5, 5.75, 6, 6.25, 12$). In the same figures, the non-dimensional cylinder displacement $y(t)/D$ time series are also shown. The bottom plot of Fig. 2.11 shows also the phase $\phi(t)$ as function of time computed using the Hilbert transform [9].

As noted by Govardhan and Williamson [9] the initial excitation regime can be marked by two sub-regimes. The first sub-regime denoted as "quasi-periodic" (QP) exhibits "slipping" of the phase angle $\phi(t)$ periodically through 360°. As shown in Fig. 2.12(a), the QP sub-regime is well captured by both 2D and 3D URANS simulations.
The second sub-regime denoted as "periodic" (P) instead, shows a constant phase angle $\phi(t)$ which remains close to 0°. In this initial branch the vortex shedding phase ϕ_{VS} follows the trend of the total phase angle $\phi(t)$. Again there is a perfect correspondence between the 2D and 3D simulation and the experimental data (see Fig. 2.12(b)).
The main observation as regards the upper branch is that the 2D time series appear to be less stable. It can be seen in Fig. 2.12(c) and Fig. 2.12(d) that the instantaneous phase and frequency ratios of the left plots are unsteady whereas on the right plots a steady value has been achieved. The frequency response unsteadiness for such low mass ratio m^* was observed by Govardhan and Williamson during experiments [**govardhan2000modes**]. It is worth noting that as the phase of the 2D results tends to zero for some time (see Fig. 2.12(c) left plot around $80 \cdot t_{St}$), also frequency ratio tends to the same values observed in 3D results, and the maximum 2D motion amplitude occurs.

The fact that the frequency for the 2D case during the upper branch is not steady means that the value of the frequency ratio plotted in Fig. 2.10(b) (obtained using spectral peak analysis) is an average value, that is never steadily achieved by the simulations. Differently, the frequency ratio of 3D simulations obtained using the Hilbert transform is equal to the spectral peak frequency through the entire window.
As noted above, the change of vortex shedding mode is associated with the start of the synchronisation phase $U^* = 6$. The jump of the total phase $\phi(t)$ is clearly visible in the 2D case already at $U^* = 5.75$ (Fig. 2.12(e) left), while the 3D case remains in the upper branch. Intermittent behaviour is observed only in the 3D case for $U^* = 6$ (Fig. 2.12(f) right). The intermittent switching is shown using the Hilbert transform (Fig. 2.12(f) bottom right), where the upper branch region is characterised by lower frequencies, while higher frequencies are associated to the lower branch. The switching between upper and lower branches is highlighted by the total phase ϕ jump between 0

and 180 deg. In the lower branch, the total phase ϕ and the vortex phase ϕ_{VS} remains at 180 deg.

From $U^* = 6.25$ (Fig. 2.12(g)), the correspondence between 2D and 3D cases is restored until the start of the desynchronisation regime. From the comparison of the 2D and the 3D results for $U^* = 12$, shown in Fig. 2.12(h), it can be seen that the 2D solution is periodical, while the 3D case show non-periodic behaviour.

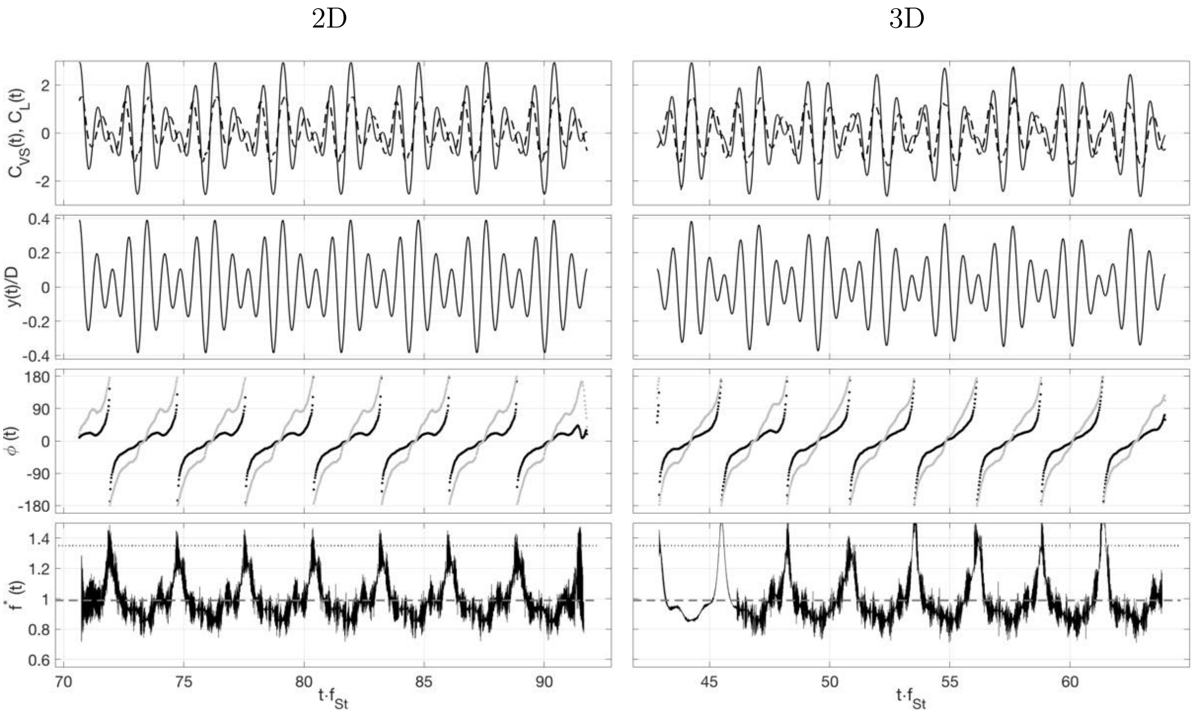

(a) Initial branch, Re=2941, U^*=3.50

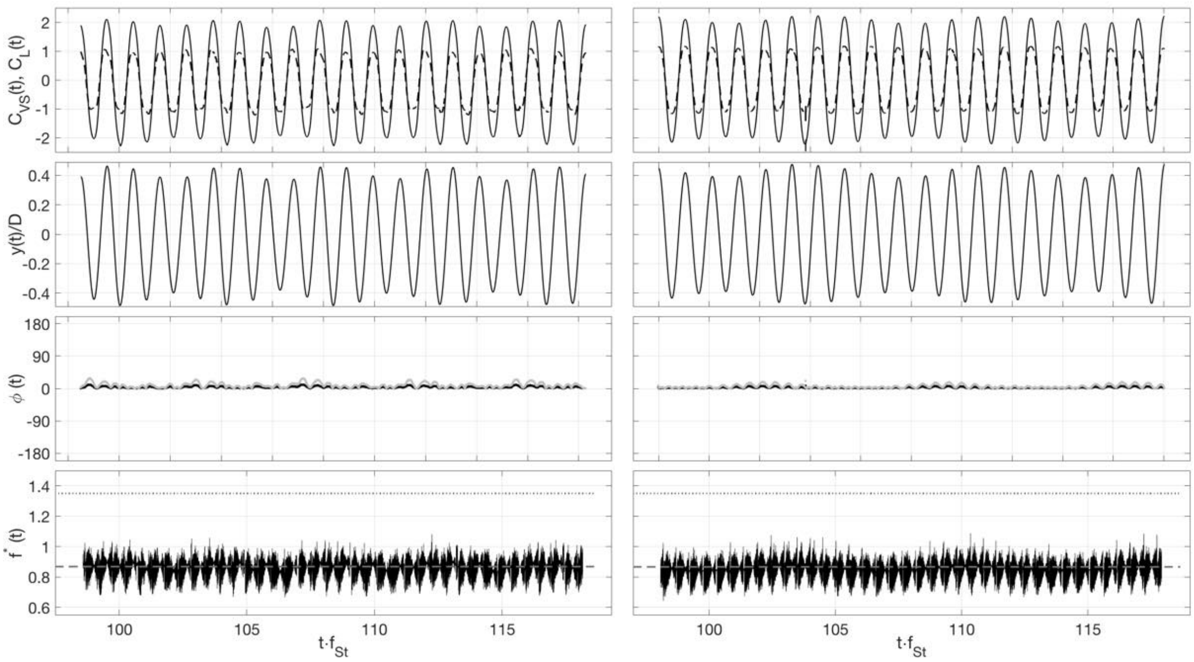

(b) Initial branch, Re=3781, U^*=4.50

Figure 2.12: First plot: total $C_L(t)$ (solid line) and vortex shedding force coefficient $C_{VS}(t)$ (dashed line). Second plot: non-dimensional cylinder displacement $y(t)$. Third plot: phase angle ϕ between C_L and $y(t)$ (black points) and phase angle ϕ_{VS} between C_{VS} and $y(t)$ (grey points). Fourth plot: frequency ratio $f^*(t)$ (using Hilbert transform), dashed line shows the main oscillation frequency (from analysis of spectral peaks) and dotted line shows the synchronisation frequency at lower branch.

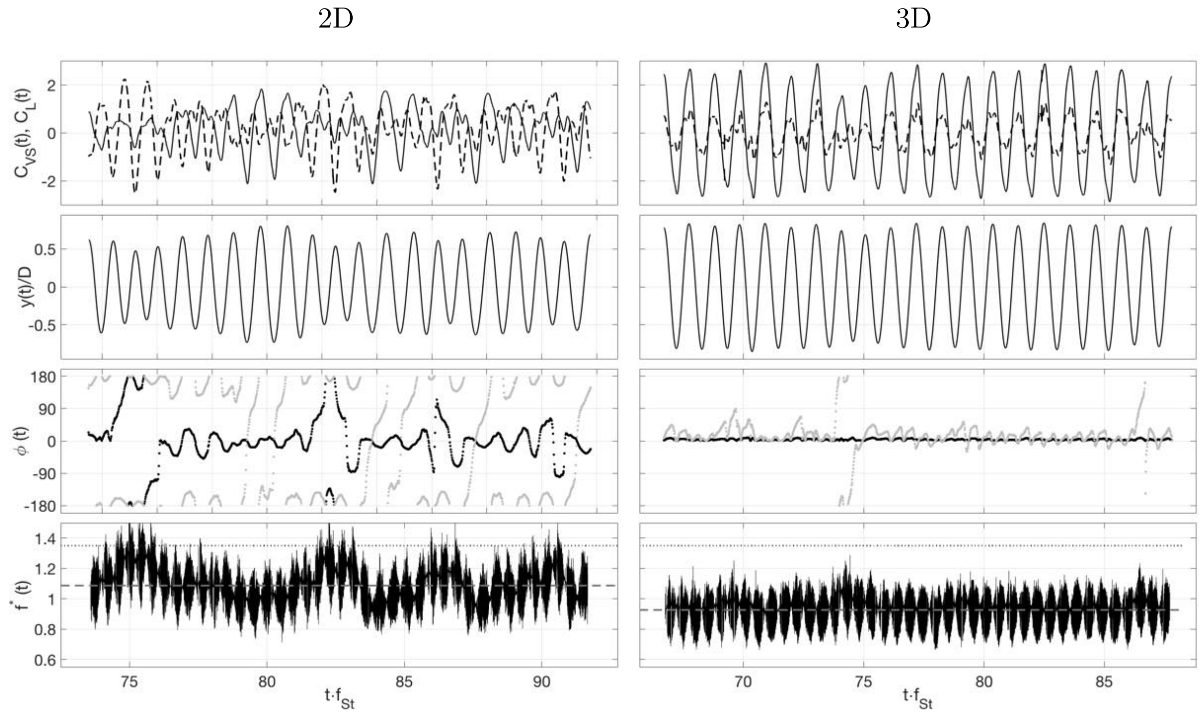

(c) Upper branch, Re=4202, U^*=5.00

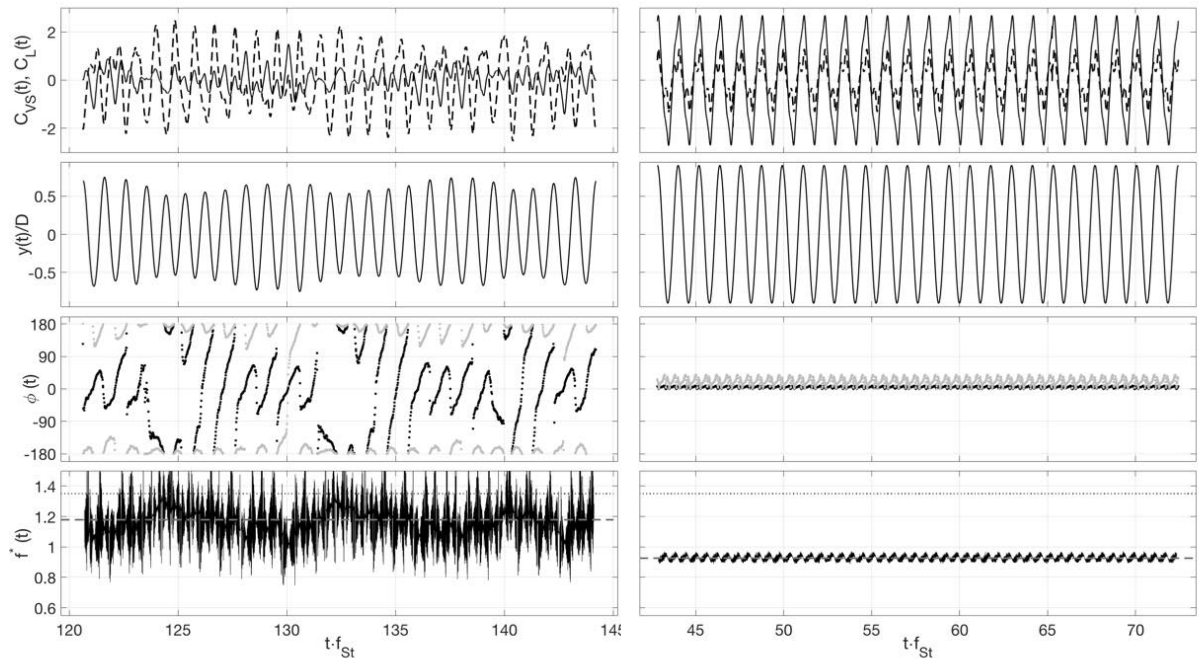

(d) Transition upper/lower branch, Re=4622, U^*=5.50

Figure 2.12: (*Cont.*) First plot: total $C_L(t)$ (solid line) and vortex shedding force coefficient $C_{VS}(t)$ (dashed line). Second plot: non-dimensional cylinder displacement $y(t)$. Third plot: phase angle ϕ between C_L and $y(t)$ (black points) and phase angle ϕ_{VS} between C_{VS} and $y(t)$ (grey points). Fourth plot: frequency ratio $f^*(t)$(using Hilbert transform), dashed line shows the main oscillation frequency (from analysis of spectral peaks) and dotted line shows the synchronisation frequency at lower branch.

2D 3D

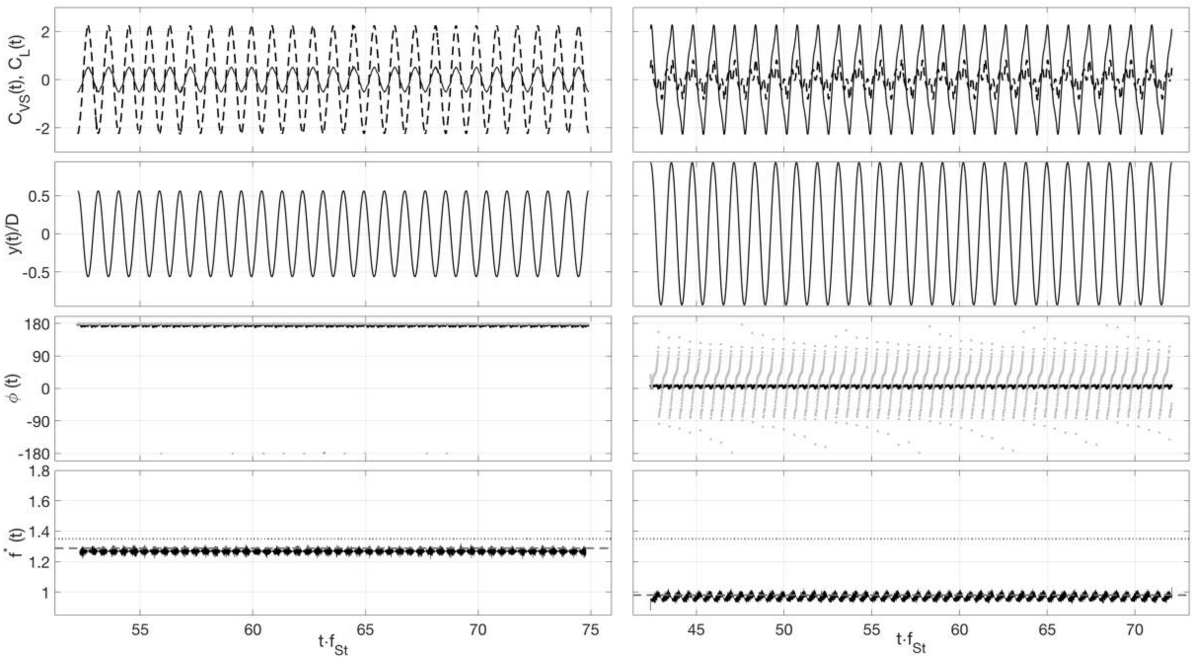

(e) Upper branch, Re=4832, U^*=5.75

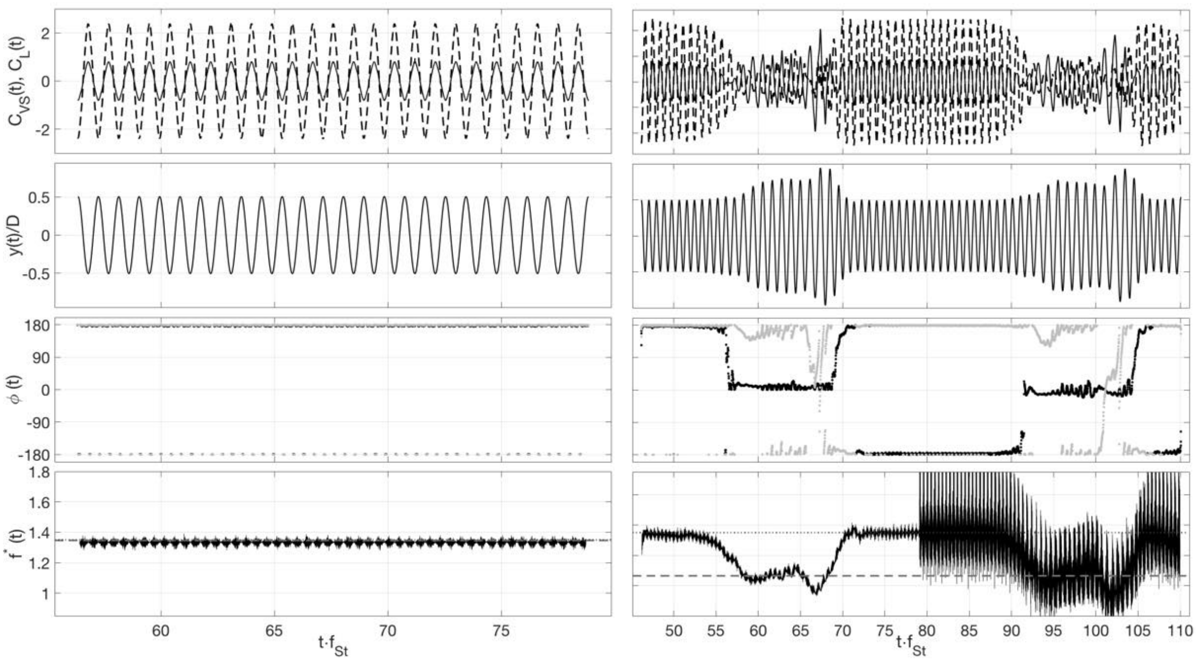

(f) Transition upper/lower branch, Re=5042, U^*=6.00

Figure 2.12: (*Cont.*) First plot: total $C_L(t)$ (solid line) and vortex shedding force coefficient $C_{VS}(t)$ (dashed line). Second plot: non-dimensional cylinder displacement $y(t)$. Third plot: phase angle ϕ between C_L and $y(t)$ (black points) and phase angle ϕ_{VS} between C_{VS} and $y(t)$ (grey points). Fourth plot: frequency ratio $f^*(t)$ (using Hilbert transform), dashed line shows the main oscillation frequency (from analysis of spectral peaks) and dotted line shows the synchronisation frequency at lower branch.

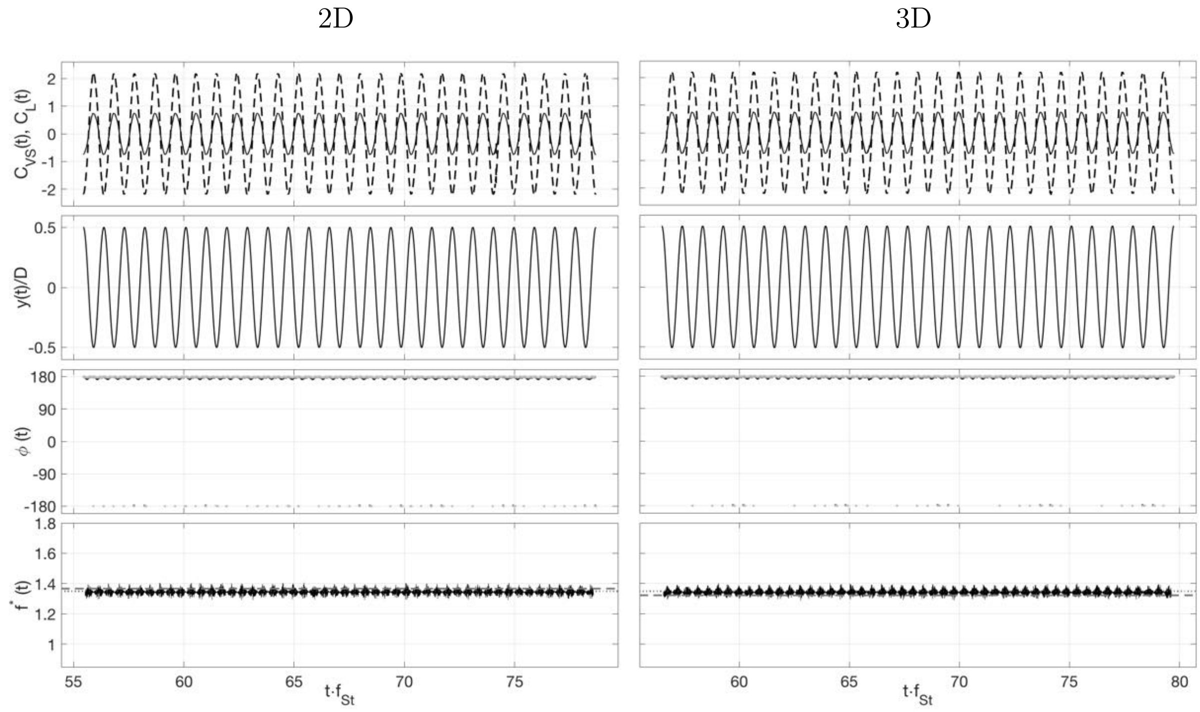

(g) Lower branch, Re=5252, U^*=6.25

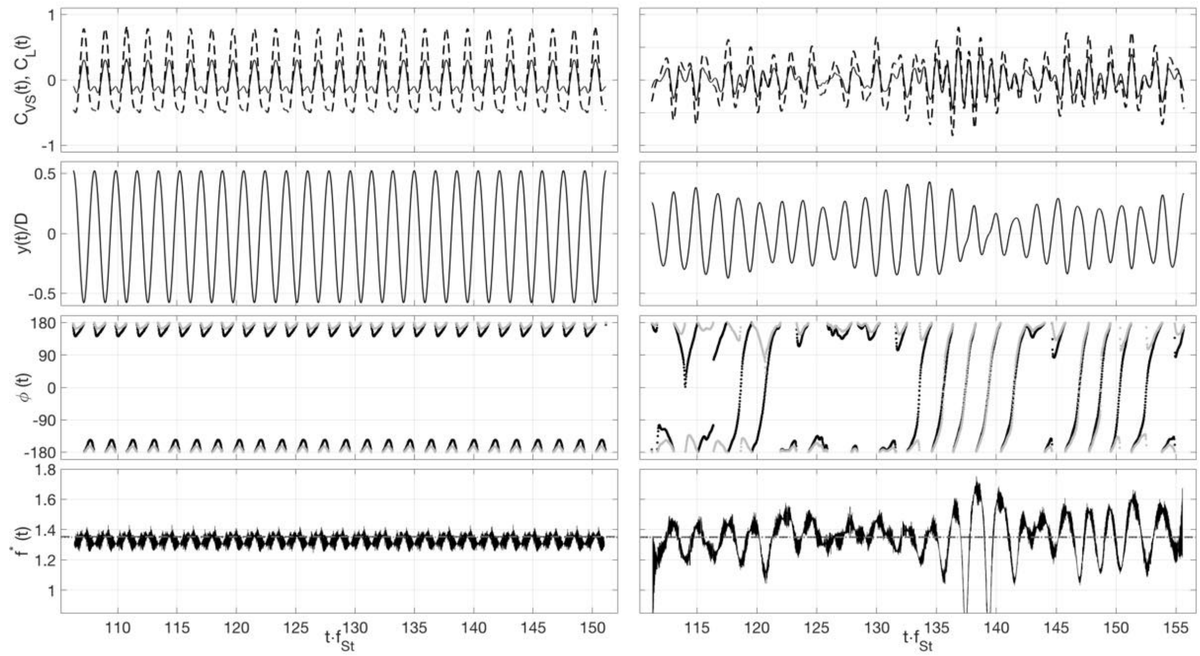

(h) Desynchronisation regime, Re=10084, U^*=12.00

Figure 2.11: (*Cont.*) First plot: total $C_L(t)$ (solid line) and vortex shedding force coefficient $C_{VS}(t)$ (dashed line). Second plot: non-dimensional cylinder displacement $y(t)$. Third plot: phase angle ϕ between C_L and $y(t)$ (black points) and phase angle ϕ_{VS} between C_{VS} and $y(t)$ (grey points). Fourth plot: frequency ratio $f^*(t)$ (using Hilbert transform), dashed line shows the main oscillation frequency (from analysis of spectral peaks) and dotted line shows the synchronisation frequency at lower branch.

2.3.3 Wake flow three-dimensionality

Fig. 2.11 shows the variation of lift force along the cylinder span direction in time for different response branches. The strongest variation of the sectional lift force along the span direction occurs in the transition zones. For example, at $U^* = 5$ and 6 (shown in Fig. 2.12(j) ad Fig. 2.12(l) respectively) the sectional lift force shows considerable variation along the cylinder span.
For $U^* > 11$, the three-dimensionality of the flow is well developed. For example, in the case of $U^* = 12$ (Fig. 2.12(n)) the forces are not synchronized along the span, leading to a more irregular cylinder motion. The strong three-dimensionality in the wake produces smaller excitation forces with respect to the cases with lower inflow velocities, this leads to a consequent reduced oscillation amplitudes of the cylinder. The wake flow is found to be almost bi-dimensional in the initial branch (Fig. 2.12(i)), at resonance in the upper branch (Fig. 2.12(k)) and in the lower branch (Fig. 2.12(m)).
Fig. 2.12 shows the three-dimensional representations of the lift coefficient C_L as a function of time and space for 5 significant periods of the time series. The surface representation of the lift force coefficient is plotted in order to give a more detailed picture of its span-wise distribution. It may be noted that for the $U^* = 3.5$ case (Fig. 2.12(o)), although the wake flow in the initial branch is considered bi-dimensional, small span-wise variations of the forcing term are present.
In the upper branch area where peak amplitude response are observed (Fig. 2.12(q)), 3D effects are not visible in the lift force distribution. The lower branch also shows no variation of the lift coefficient along the cylinder span, e.g. $U^* = 7.50$ (Fig. 2.12(r)). This results are in contrast with the previous findings of Zhao et al. [32], where the three-dimensionality of the flow were found to be the strong both in the upper branch and in the lower branch. One of the possible reasons behind this discrepancy could be that in the simulations made by Zhao et al. the Reynolds number was kept at a constant value of 1000, and the mechanical parameters were changed in order to obtain increasing reduced velocities. When the desynchronisation regime starts at $U^* \approx 10$, the three-dimensional disturbances in the wake flow heavily impact on the lift coefficient distribution (Fig. 2.12(t)), as expected.

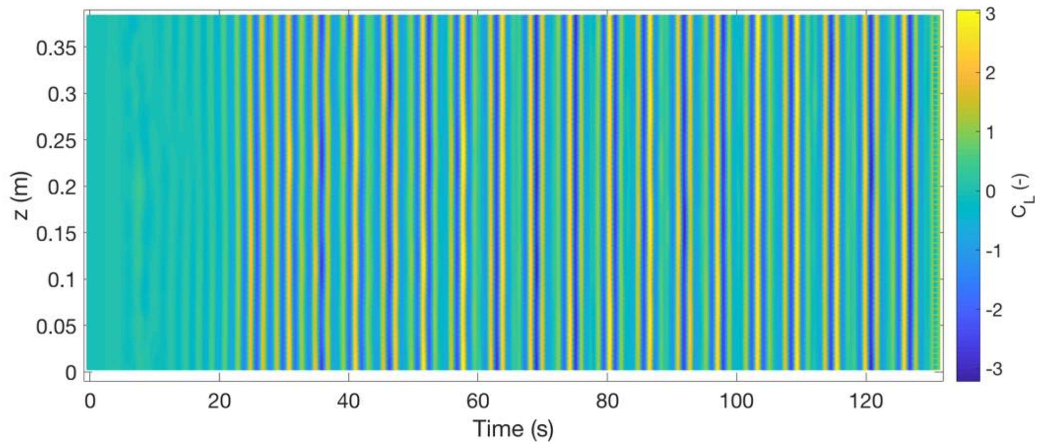

(i) Initial branch, Re=2941, U^{*}=3.50

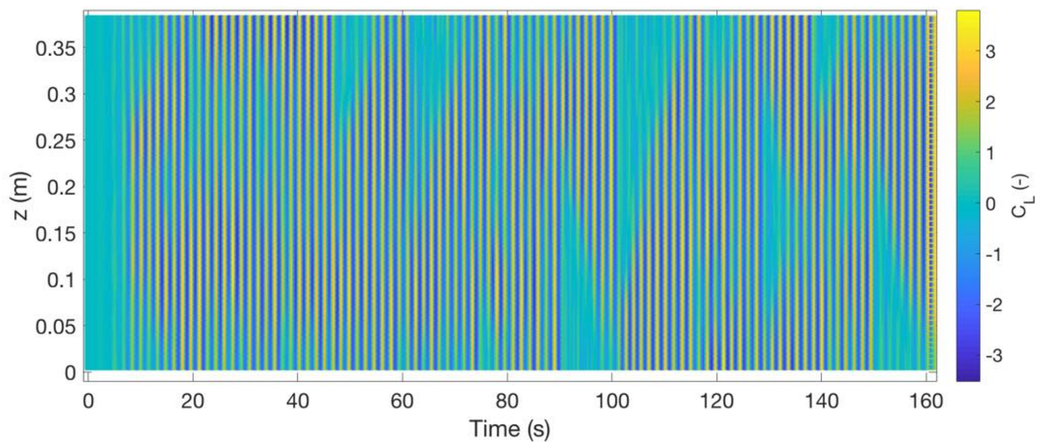

(j) Upper branch, Re=4202, U^{*}=5.00

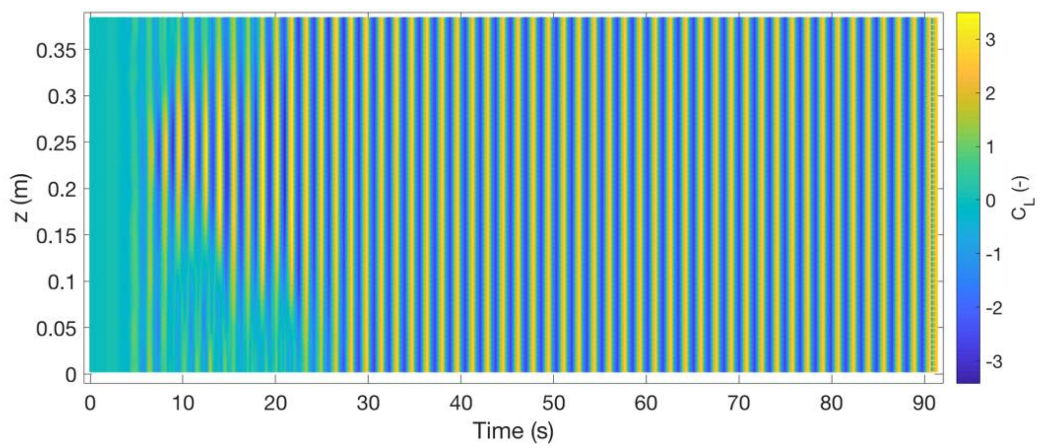

(k) Upper branch, Re=4622, U^{*}=5.50

Figure 2.12: Contours of the lift coefficient on the z-t plane for the 3D URANS cases.

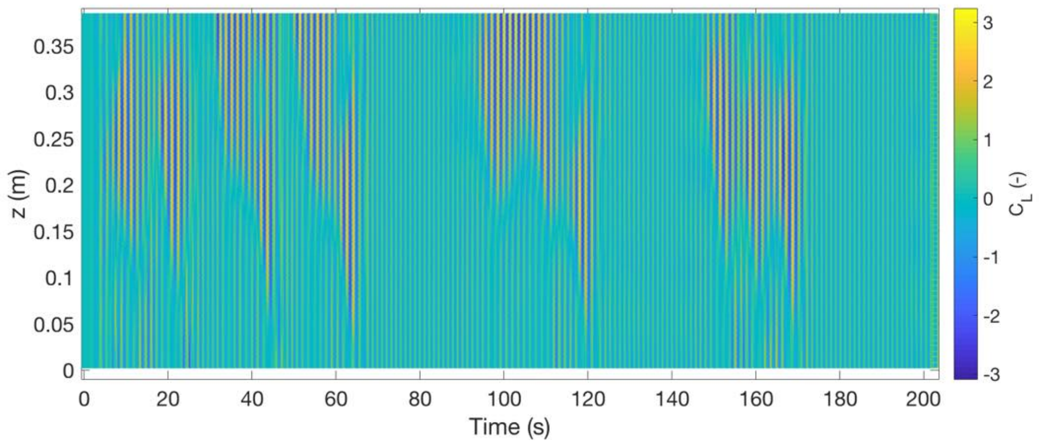

(l) Transition upper/lower branch, Re=5042, U^{*}=6.00

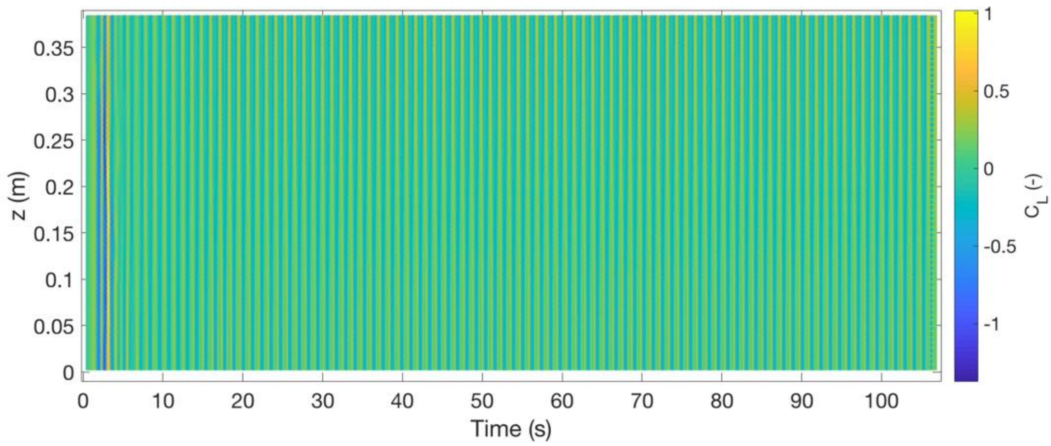

(m) Lower branch, Re=8404, U^{*}=10.00

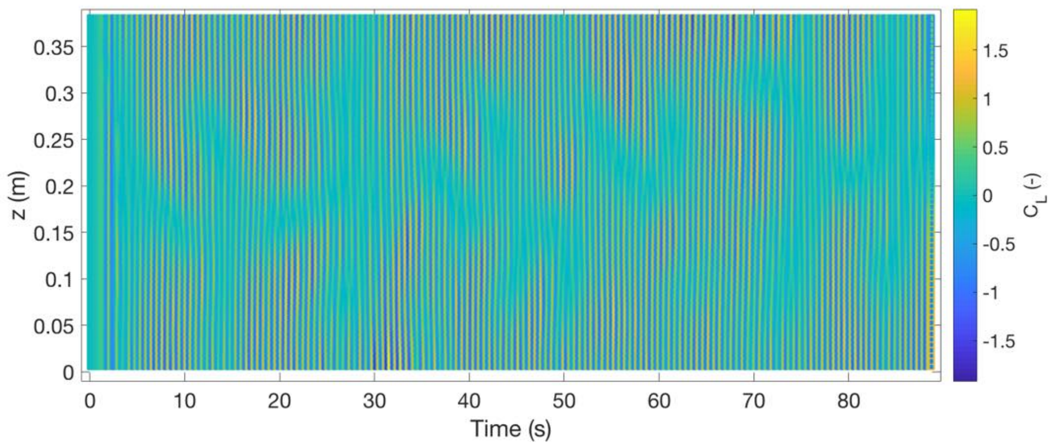

(n) Desynchronisation regime, Re=10084, U^{*}=12.00

Figure 2.11: (*Cont.*) Contours of the lift coefficient on the z-t plane for the 3D URANS cases.

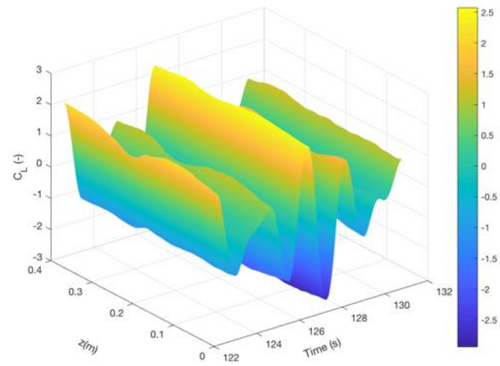

(o) Initial branch, Re=2941, U^{*}=3.50

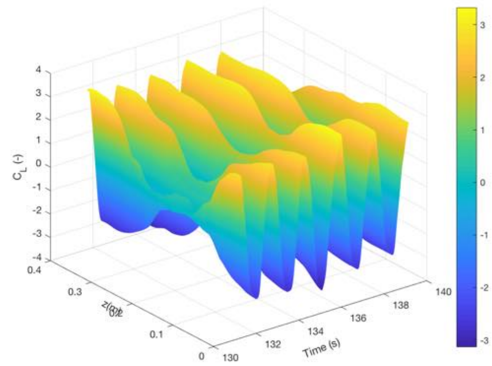

(p) Upper branch, Re=4202, U^{*}=5.00

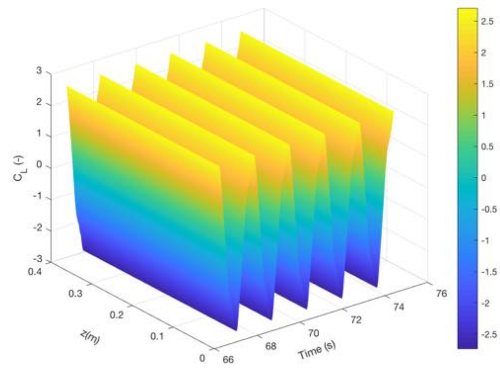

(q) Upper branch, Re=4622, U^{*}=5.5

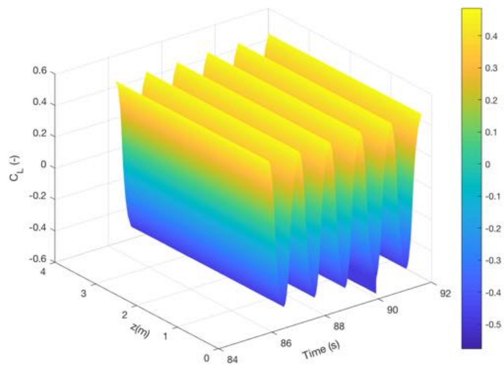

(r) Lower branch, Re=6303, U^{*}=7.50

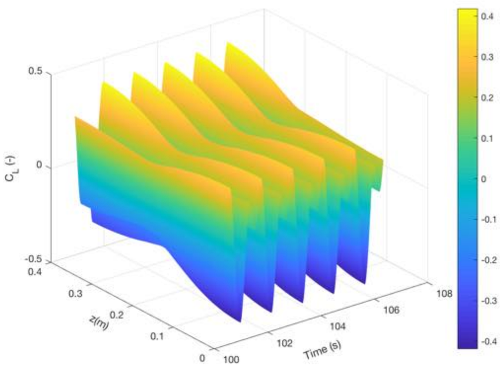

(s) Lower branch, Re=8404, U^{*}=10.00

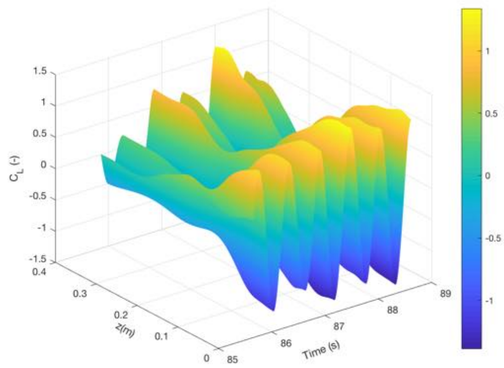

(t) Desynchronisation regime, Re=10084, U^{*}=12.00

Figure 2.12: 3D plot of the span-wise distribution of the lift coefficient for the 3D URANS cases.

As suggested by Zhao et al. [32] the variation of the lift coefficient along the cylinder span can be quantified by the *correlation coefficient* between two locations at z_1 and z_2 along the cylinder span, which is defined by

$$R(z_1, z_2) = \frac{\overline{C_L(z_1)C_L(z_2)}}{[C_{L,\mathrm{rms}}(z_1)C_{L,\mathrm{rms}}(z_2)]},$$

where the over-bar stands for averaging over the time. Fig. 2.13 shows the variations of the correlation coefficient R(0,z) of the sectional lift coefficient with z. R(0,z) represents the correlation coefficient of the lift coefficient between one end of the cylinder at $z = 0$ and the considered section. It is evaluated considering the last 10 oscillations of the cylinder. It can be seen that the correlation of the lift coefficient stays close to 1 in the upper and lower branch. This indicates that there are no three-dimensional effects. Even if slight variations are present, the cases in the initial branch can also be considered bi-dimensional.

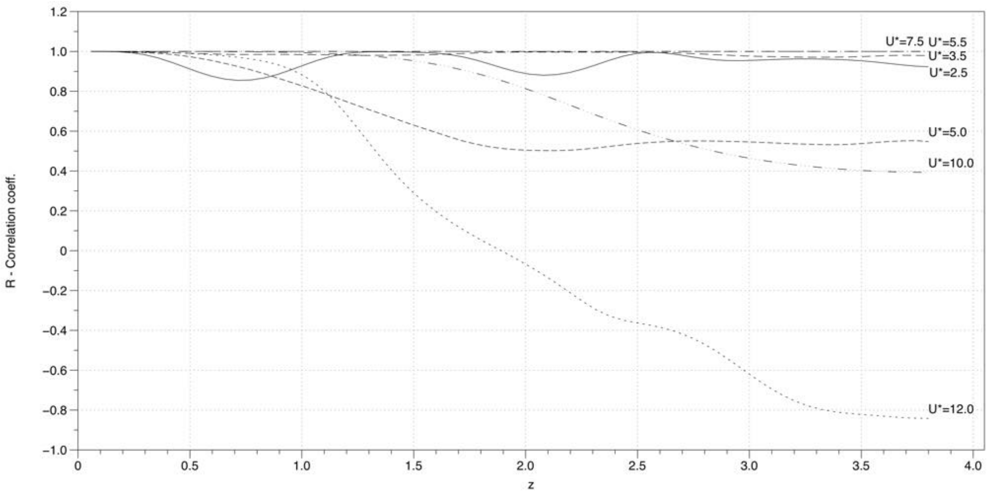

Figure 2.13: Correlation coefficient $\overline{R}(0, z/D)$ of the sectional lift coefficient.

The three-dimensional character of the wake field can be visualized in more detail using the λ_2 method proposed bu Jeong and Hussain [67] in which λ_2 is the second eigenvalue of the symmetric tensor $E^2 + \Omega^2$. Here E and Ω are the symmetric and anti-symmetric parts of the velocity gradient tensor $\nabla\mathbf{u}$.

Fig. 2.13 and Fig. 2.13 show the $\lambda_2 = -0.2$ iso-surfaces. The iso-surfaces are coloured according to the spanwise components of vorticity $W_z = \partial u_y/\partial x - \partial u_x/\partial y$ and the streamwise component of vorticity $W_x = \partial u_z/\partial y - \partial u_y/\partial z$ respectively.
In Fig. 2.14(a)-2.27(a), the three-dimensional distortion of the vortex tubes in the initial branch ($2 < U^* < 4$) can be seen.
This is due to the presence of pairs of counter-rotating, rib-like structures of streamwise vorticity braided together with the span-wise vortices. However, the intensity of the rib vortices is too weak to influence the primary mode of vortex shedding for the case

$U^* = 2.5$ and $U^* = 3.5$ (Fig. 2.27(a)). Consequently, also the cylinder motion response is not altered and remains essentially identical to that obtained from the bi-dimensional computations. On the contrary, in the case $U^* = 3.0$ (Fig. 2.14(a)), the rib structures close to the cylinder disrupt the wake. This causes a variation in the response of the cylinder both in terms of motion amplitude and its dominant frequency (Fig. 2.10(a) and Fig. 2.10(b)).
The intensity of the three-dimensional structures are also evident during the transition between initial and upper branch (Fig. 2.14(c)).
In the upper branch region, the wake vortex formations appear to be bi-dimensional (Fig. 2.14(d)). In the lower branch, the three-dimensionality of the flow is very weak and is restricted to the initial transitory. This is clearly evident in figures Fig. 2.14(e) and Fig. 2.14(l), for instance, by the fact that the stream-wise vorticity W_x disappears. Therefore, the lower branch exhibits mostly bi-dimensional mode characteristics.
For $U^* > 10$ (Fig. 2.14(f) and Fig. 2.14(g)), the three-dimensional distortion of the vortex tubes becomes important. This, in turn, forms a complex vortex structure generated from the interaction between the von Karman street vortexes and longitudinal rib vortexes.

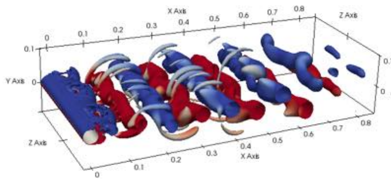

(a) Initial branch, Re=2521, U^*=3.00

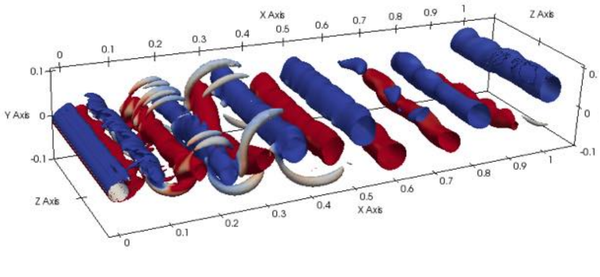

(b) Initial branch, Re=2941, U^*=3.50

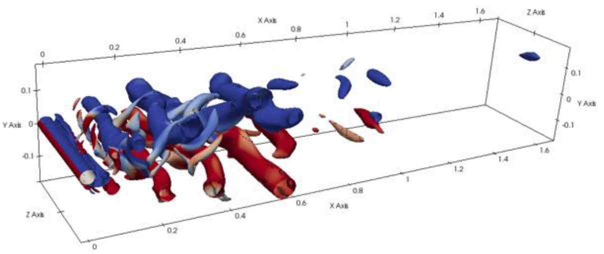

(c) Upper branch, Re=4202, U^*=5.00

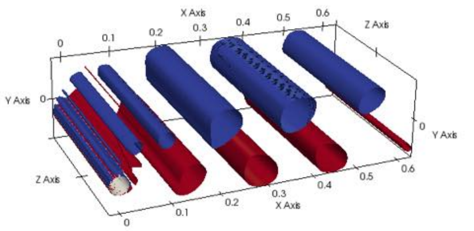

(d) Upper branch,Re=4622, U^*=5.50

Figure 2.14: Iso-surface of the eigenvalue $\lambda_2 = -0.2$ and the contours of span-wise vorticity W_z for the 3D URANS cases (blue: clockwise, red: anti-clockwise).

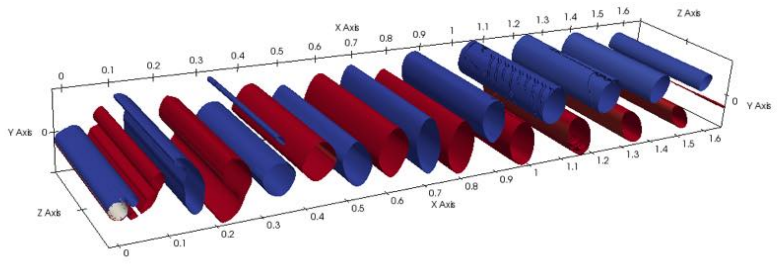

(e) Lower branch, Re=5882, U^*=7.00

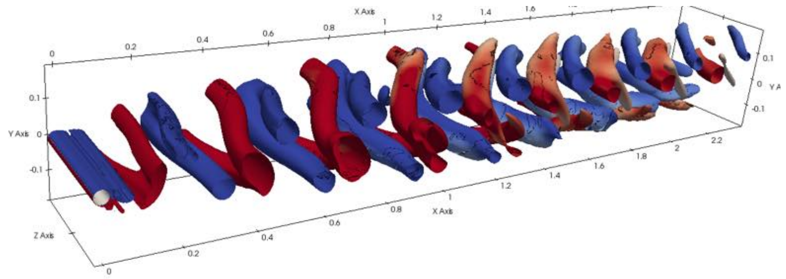

(f) Lower branch, Re=8404, U^*=10.00

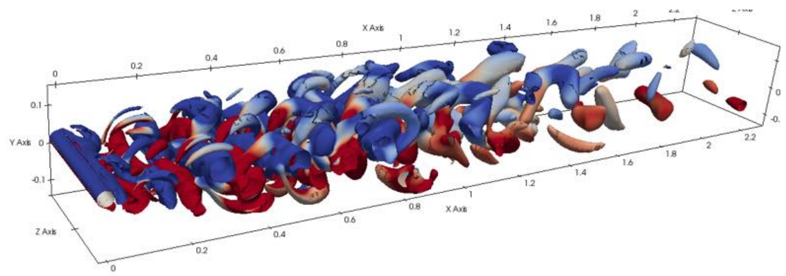

(g) Desynchronisation regime, Re=10084, U^*=12.00

Figure 2.13: *(Cont.)* Iso-surface of the eigenvalue $\lambda_2 = -0.2$ and the contours of spanwise vorticity W_z for the 3D URANS cases (blue: clockwise, red: anti-clockwise).

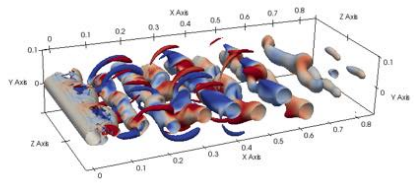

(h) Initial branch, Re=2521, U^{*}=3.00

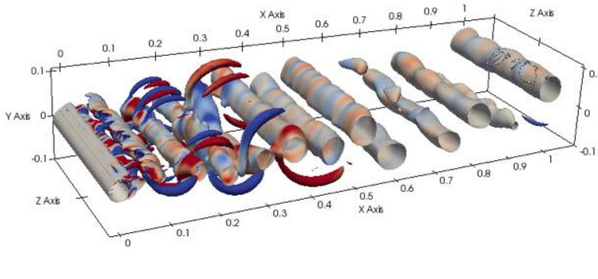

(i) Initial branch, Re=2941, U^{*}=3.50

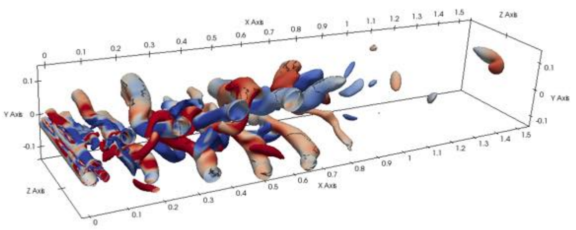

(j) Upper branch, Re=4202, U^{*}=5.00

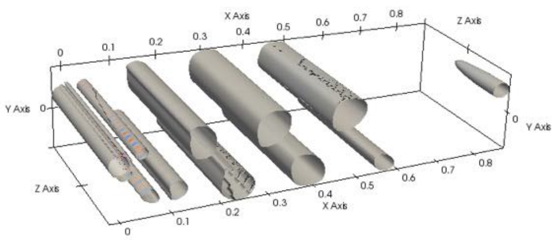

(k) Upper branch,Re=4622, U^{*}=5.50

Figure 2.14: Iso-surface of the eigenvalue $\lambda_2 = -0.2$ and the contours of the stream-wise vorticity W_x for the 3D URANS cases (blue: clockwise, red: anti-clockwise).

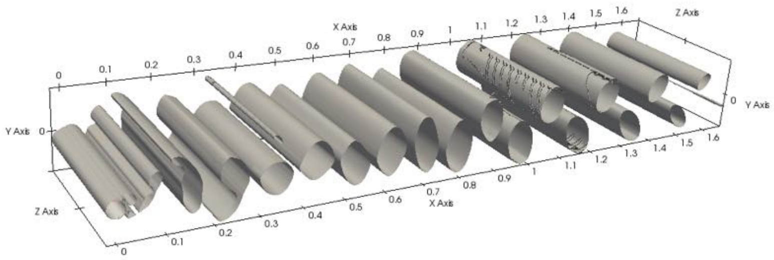

(l) Lower branch, Re=5882, U^{*}=7.00

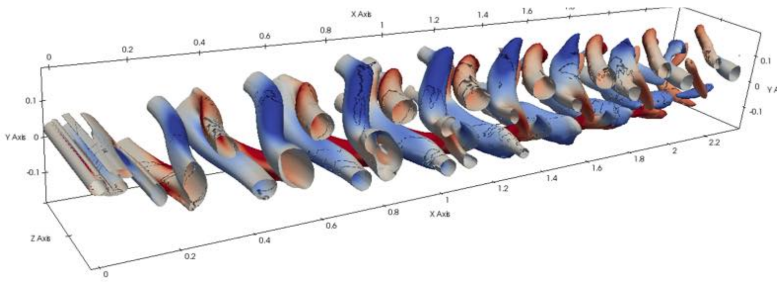

(m) Lower branch, Re=8404, U^{*}=10.00

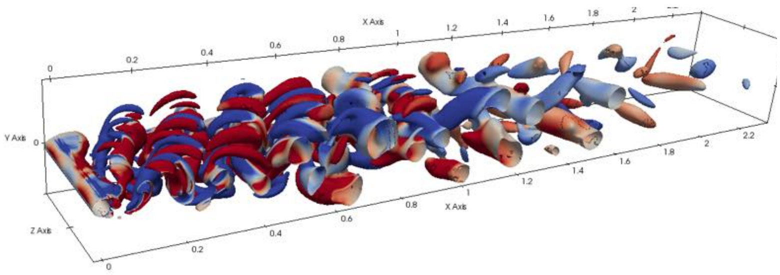

(n) Desynchronisation regime, Re=10084, U^{*}=12.00

Figure 2.13: (*Cont.*) Iso-surface of the eigenvalue $\lambda_2 = -0.2$ and the contours of the stream-wise vorticity W_x for the 3D URANS cases (blue: clockwise, red: anti-clockwise).

2.3.4 Vortex Shedding modes

Vortex shedding modes, defined by the vortex pattern observed in cylinder wake flow are also investigated in the present work. The axial vorticity field W_z is plotted for the three branches of cylinder response in Fig. 2.14 and Fig. 2.14 for the 2D and the 3D cases, respectively. The vorticity plots in Fig. 2.14 and Fig. 2.14 are relative to the lowest position of the cylinder trajectory. In order to better observe the pattern variations along the axial direction of the cylinder, the figures referring to the 3D RANS simulations (Fig. 2.14) show three different sections of cylinder. In order to provide a comparison with literature, the CFD results are plotted against the Williamson-Roshko map [22].

As suggested by Khalak and Williamson [5], the adimensional amplitudes A^* are plotted as a function of the so called "true" reduced velocity (U^*/f^*)St (Fig. 2.15), where St is the Strouhal number (St = 0.2). In general, the vortex shedding modes are similar between the 2D and the 3D cases, however, there are some exceptions. The vortex shedding modes are in good agreement with the Williamson-Rosko map. The 2S vortex shedding mode, that is two single vortices of opposite circulation are shed from the cylinder, is observed in the initial branch (Von karman vortex street) for both 2D (Fig. 2.14(o)) and 3D (2.15(a)) simulations.
The 2P mode, that is the formation of vortex pairs which convect laterally outwards from the wake centreline, is observed in the upper branch for all cases and in some part of the lower branch. Good agreement has been found between Williamson-Rosko map and the 3D case in the upper branch, e.g. Fig. 2.15(b) for the case of $U^* = 5.75$. On the other hand, even if the 2D case shows the same vortex pattern as the 3D case (2P), it is barely outside 2P region of the Williamson-Rosko map (Fig. 2.14(p)). Since the 2P/2S transition is subject to histeretic effects, both states are possible near the boundary line, as shown in [22], this could easily be the case. The transition from upper to lower branches is also characterised by the vortex shedding mode transition, from 2P to 2S. In both 2D (Fig. 2.14(q)-2.14(r)) and 3D Fig. 2.15(c)-2.15(d)), a change in the vortex pattern can be observed. This is also shown when the data points are plotted on the Williamson-Rosko map (Fig. 2.15). As the inflow velocity increases, the vortex pattern again change from 2S to 2P. This transition is clearly observed by comparing Fig. 2.14(r)-2.15(d) for the case of $U^* = 6.25$ and Fig. 2.14(s)-2.15(e) for the case of $U^* = 9$. This vortex pattern change is again in accordance with the Williamson-Rosko map. Finally, when U^* exceeds the limit of the periodic 2P mode, the numerical solution follows the expected drop in amplitude ratio A^* going into the desynchronisation regime. This final region is identified with "no observed synchronisation pattern" in Fig. 2.15, meaning that no wake pattern having the same period as the oscillation has been observed. Wake flow of both 2D (Fig. 2.14(t)) and 3D cases (Fig. 2.15(f)) show the absence of a recognisable pattern.

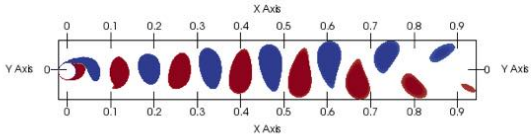

(o) Initial branch, Re=2101, U^*=2.50, (U^*/f^*)St = 0.837

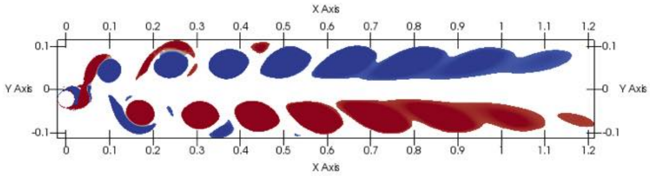

(p) Upper branch, Re=4832, U^*=5.75, (U^*/f^*)St = 0.907

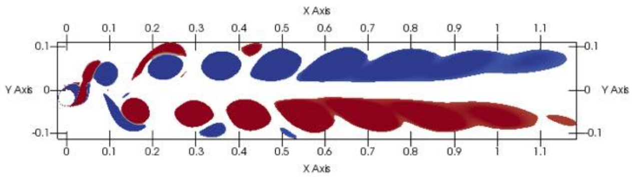

(q) Transition upper/lower branch, Re=5042, U^*=6.00, (U^*/f^*)St = 0.902

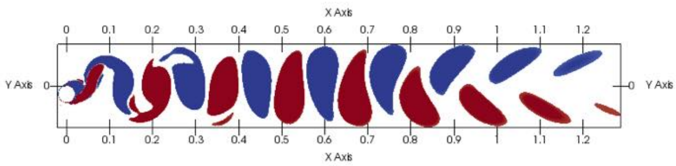

(r) Lower branch, Re=5252, U^*=6.25, (U^*/f^*)St = 0.930

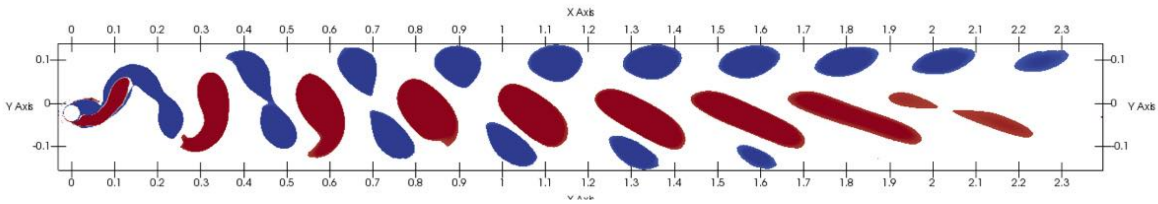

(s) Lower branch, Re=7563, U^*=9.00, (U^*/f^*)St = 1.390

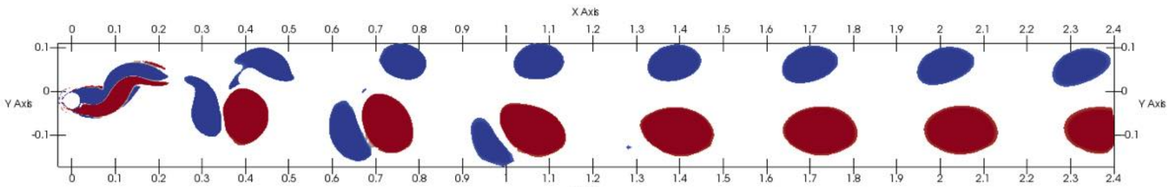

(t) Desynchronisation regime, Re=10084, U^*=12.00, (U^*/f^*)St = 1.797

Figure 2.14: Contour of the axial vorticity W_z for the 2D URANS cases (blue: clockwise, red: anti-clockwise).

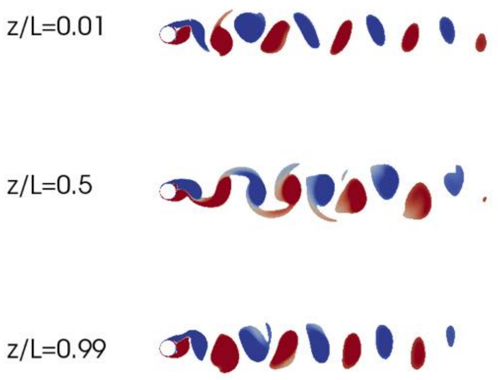

(a) Initial branch, Re=2101, U^{*}=2.50, (U^{*}/f^{*})St = 0.969

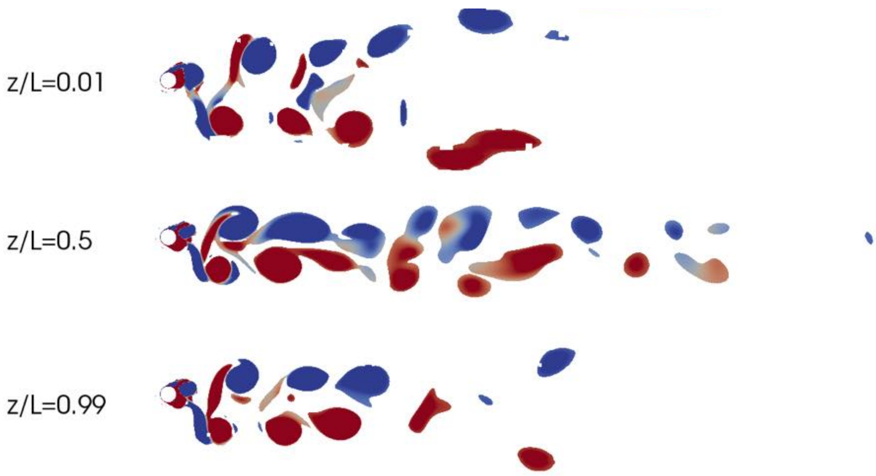

(b) Upper branch, Re=4832, U^{*}=5.75, (U^{*}/f^{*})St = 1.146

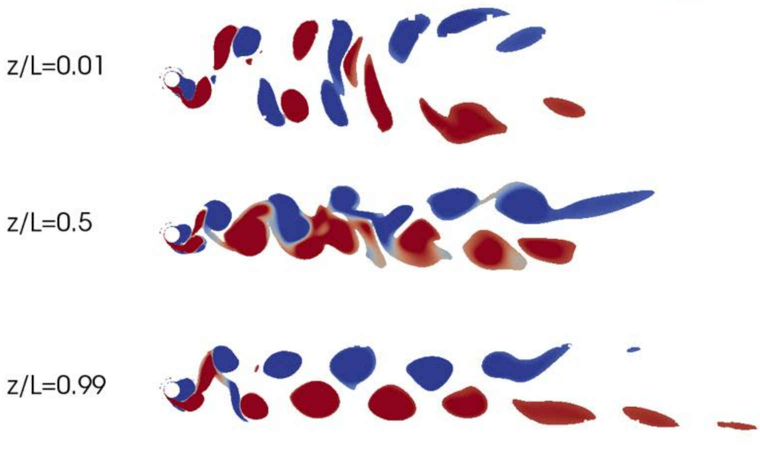

(c) Transition upper/lower branch, Re=5042, U^{*}=6.00, (U^{*}/f^{*})St = 1.127

Figure 2.15: Contour of the axial vorticity W_z at three section along the cylinder span for the 3D URANS cases (blue: clockwise, red: anti-clockwise).

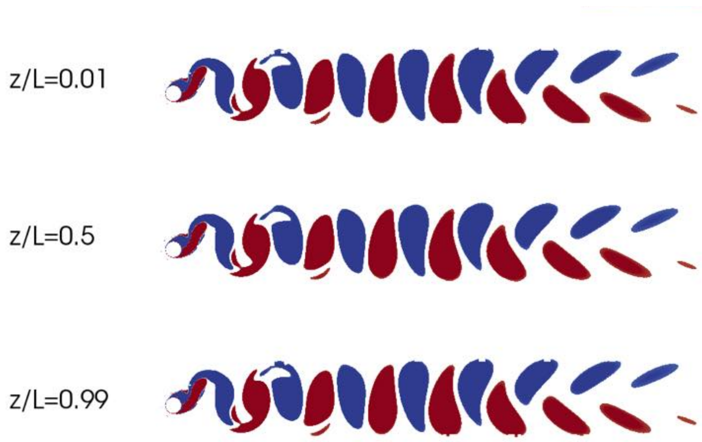

(d) Lower branch, Re=5252, U^*=6.25, (U^*/f^*)St = 0.930

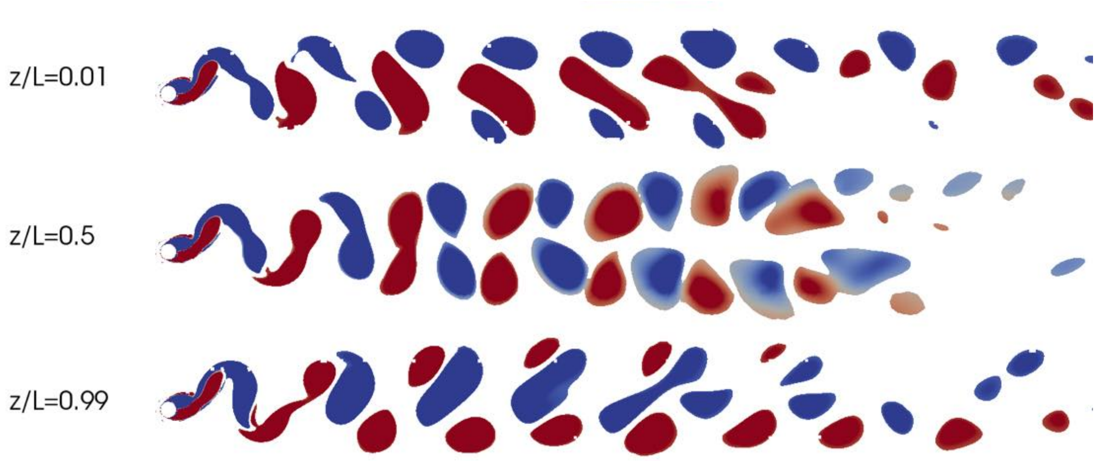

(e) Lower branch, Re=7563, U^*=9.00, (U^*/f^*)St = 1.382

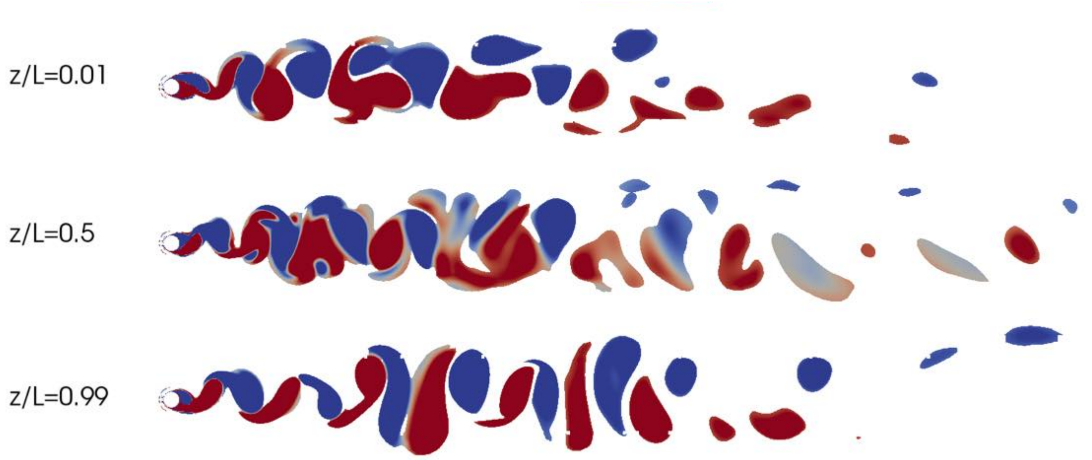

(f) Desynchronisation regime, Re=10084, U^*=12.00, (U^*/f^*)St = 1.777

Figure 2.14: (*Cont.*) Contour of the axial vorticity W_z at three section along the cylinder span for the 3D URANS cases (blue: clockwise, red: anti-clockwise).

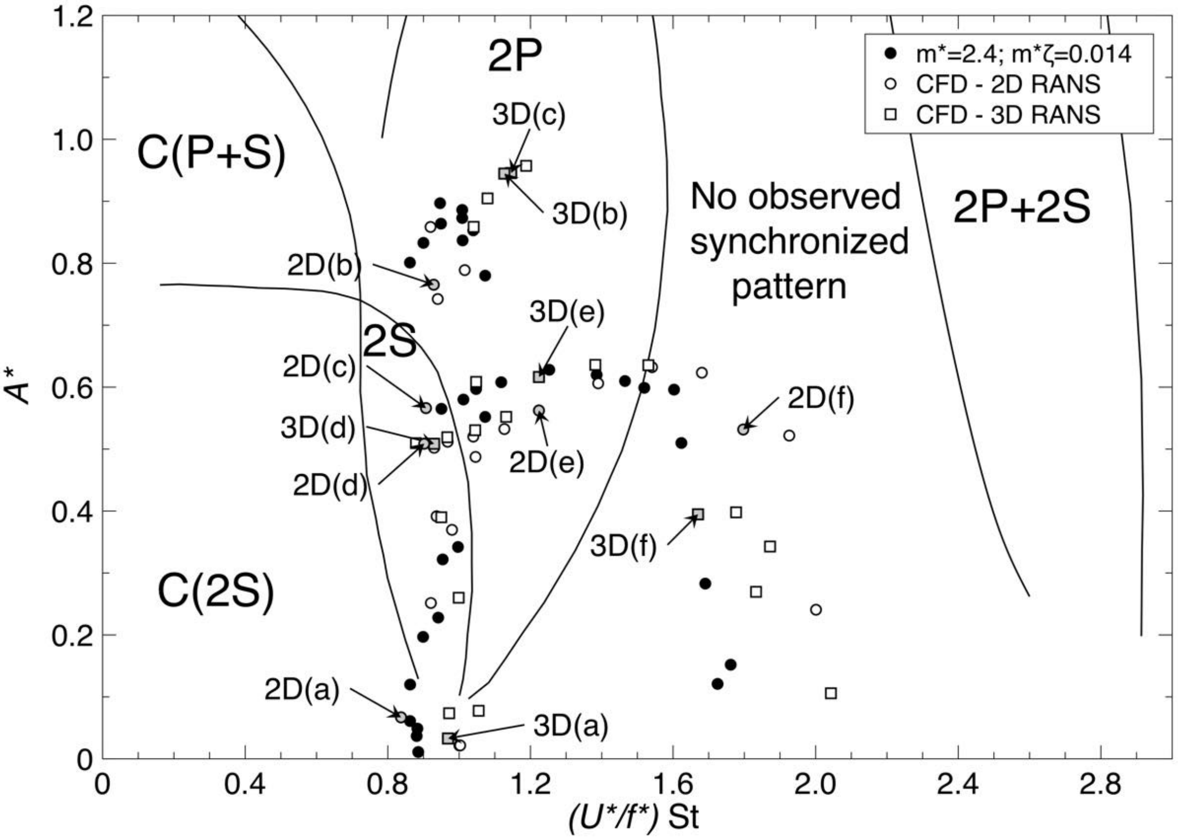

Figure 2.15: After Williamson and Govardhan [9]. Amplitude response is plotted against the "true" normalised velocity (U^*/f^*)St of all CFD cases plotted in the Williamson-Roshko (1988) map of the vortex shedding modes. The grey points refer to Fig. 2.14 for the 2D URANS cases and Fig. 2.14 for the 3D URANS cases.

2.3.5 Computational costs

Every simulation, has been carried out on the same workstation, a Tier-1 Linux Cluster (Intel® Xeon® E5-2680 v2 CPU).
The cluster is based on IBM Dataplex dx360 M4 servers made by 224 nodes and 4480 cores. The total RAM of the cluster is 12TB with 2GB per core for most of the nodes, 8GB per core for 24 nodes and 16GB per core for 8 special nodes. The interconnection between the nodes is provided by an Infiniband QDR (40Gbit/s) network.
The execution time of a 2D case, parallelised via Open Message Passing Interface (MPI) in 8 different processes in the same computing node, is 2 hour and 19 min for 200 s of simulated time for $U^* = 6$. The same case with a three-dimensional mesh, parallelised in 120 processes divided in 6 different computing nodes, takes 6 days 11h and 16 min for the same simulated time.
At higher reduced velocities, the execution time grows in proportion to the decrease in the time step, requiring an even larger number of steps to compute the same amount of simulated time. Therefore, despite a considerable increase in computational resources, the three-dimensional numerical simulation of a single case is not practical for engineering design purposes.

2.3.6 Conclusions

The results found in this section are briefly summarized here. The results of 2D and 3D numerical simulations of Vortex Induced Vibrations (VIV) of an elastically-mounted circular cylinder, with low mass ratio and damping ratio, have been compared successfully to experimental data from the literature.
The aim of the study has been to investigate the difference between the 2D and 3D numerical simulations in the case of 1-DOF VIV using a simple URANS approach in order to investigate the limits of the simpler approach. It has been found that the bi-dimensional simulations does not show important discrepancies with the experiments except for the non-dimensional amplitude of the cylinder motion in the upper branch region. In order to overcome such issues, more computationally expensive three-dimensional simulations have been carried out. The analysis of the phase between the cylinder response and the fluid forces confirms that the transition between the upper and lower is associated with the phase jump ϕ between the cylinder motion and the total force.
On the other hand, it is not clear if the phase jump ϕ_{VS} between the cylinder oscillation and the vortex shedding force could be the cause of the transition between the initial branch and the upper branch as it is not shown in our 3D simulations results.
The main difference between the 2D and 3D simulation in the upper branch region are due to the different phase between the vortex shedding force and the cylinder motion and are not related to three-dimensional flow structures.
From the analysis of the wake flow in span-wise direction it has been found that the three-dimensionality of the flow is stronger in the transition zones. The best comparison with the bi-dimensional case is found in the lower branch where three-dimensional flow effects are absent. The visualization of the wake velocity field agrees with the vortex

shedding modes of the Willamson-Rosko map.

The main differences between the presented results and the experiments could be due to the inability of $k - \omega$ SST URANS simulation of developing sufficient three-dimensional structures along the cylinder span, as already highlighted by Shur et al.[66]. In this regard,in the next section the effect of span-wise end conditions on vortex-induced vibrations will be explored.

2.4 Span-wise dependence study

It is well known from the literature that if the span-wise domain is not sufficiently extended the URANS method fails to sustain the three dimensionality of the flow [66]. This leads to a loss of interest in three-dimensional URANS for bi-dimensional or slender geometries. This attitude is consistent with a belief that classical URANS turbulence models are not meant to allow the intrinsic incoherent three dimensionality that is typical of real turbulent flows even when the geometry is two dimensional.
This motivates an investigation to explore the effect of span-wise conditiion for 3D URANS simulations applied to the VIV case. The effect of span-wise length has been evaluated doubling the length of computational domain in span-wise direction and then doubling the cylinder length. In order to respect guidelines suggested by D'Alessandro et al.[61], who suggested a minimum number of 48 cells every πD, the span-wise grid resolution has been kept constant. Thus, the computational grid created, called "3D LONG", is equivalent to the mesh "3D NEW" but doubled in span-wise length. Tab 2.14 summarised the "3D LONG" mesh characteristics. Tab. 2.14 n_c represents the number of points along the circumference of the cylinder, n_s represents the number of points along the span direction of the cylinder, Δr represents the radial extension of the near-wall layers from the surface of the cylinder, n_l the number of layers in the near-wall region and G is the grid expansion factor in the radial direction.

The value of the cylinder mass M, stiffness K and structural damping H have been found considering the same test case, characterised by low mass ratio $m^* = 2.4$ and low damping $\zeta = 0.0054$ ratios, with the procedure explained in Sec. 2.1.4. Tab. 2.15 summarised the system properties for the 3D simulations with the extended span-wise length.

2.4.1 Cylinder response and phase jump

Fig. 2.16 shows a direct comparison of the cylinder response characteristics obtained in these doubled span-wise length simulations, with the previous presented 3D simulations. The numerical results obtained show a very similar, though not completely identical behaviour. The only difference has been found for the reduced velocity $U^* = 6$ for the maximum adimensional amplitude found A^*. As highlighted in the previous sec. 2.3, at this velocity the transition between the upper and the lower branches occurs. This transition shows an intermittent behaviour. This intermittent behaviour is not properly captured by the doubled span-wise length simulations, although, as can be seen from Fig. 2.17, an oscillation of the cylinder response as a function of time still exists. The reason why this happens is not completely clear. One of the reasons could be intrinsically connected with the span-wise extension. As shown by the experiment of Khalak and Willamson [5], the extension of the transition region is related to the initial conditions which in the case of double-length cylinders could lead to a different response from that found in the case of a cylinder of length equal to the experimental one. Fig. 2.16(b) illustrates how the oscillation frequency is quite insensitive to the span size extensions of the domain.

Grid name	3D LONG
Cells	6960145 (180.93%)
Faces	21089383
Points	3658462
Background grid	(100,50,24)
Circumference points n_c	56
Span points n_s	512
Number of near-wall layers n_l	35
Layers radial extension $\Delta r/D$	0.026
Grid expansion factor G	1.078
Max non-orthogonality	35.925
Max skewness	0.417
Max aspect ratio	32.948

Table 2.14: 3D LONG mesh characteristics.

Cylinder diameter	D	(m)	3.81×10^{-2}
Cylinder span	S	(m)	0.76
Cylinder mass	M	(kg)	2.0776
Spring stiffness	K	(N/m)	50.4930
Structural damping	H	(N/(m/s))	0.1320
Mass ratio	m^*	$(-)$	2.4
Damping Ratio	ζ	$(-)$	0.0054
Added mass coeff.	C_A	$(-)$	1.0
Mass-damping parameter	$m^* \zeta$	$(-)$	13.00×10^{-3}
Natural frequency in air	$f_{0,a}$	(Hz)	0.7846
Natural frequency in water	f_0	(Hz)	0.6592

Table 2.15: System properties of the 3D simulations with the extended span-wise length.

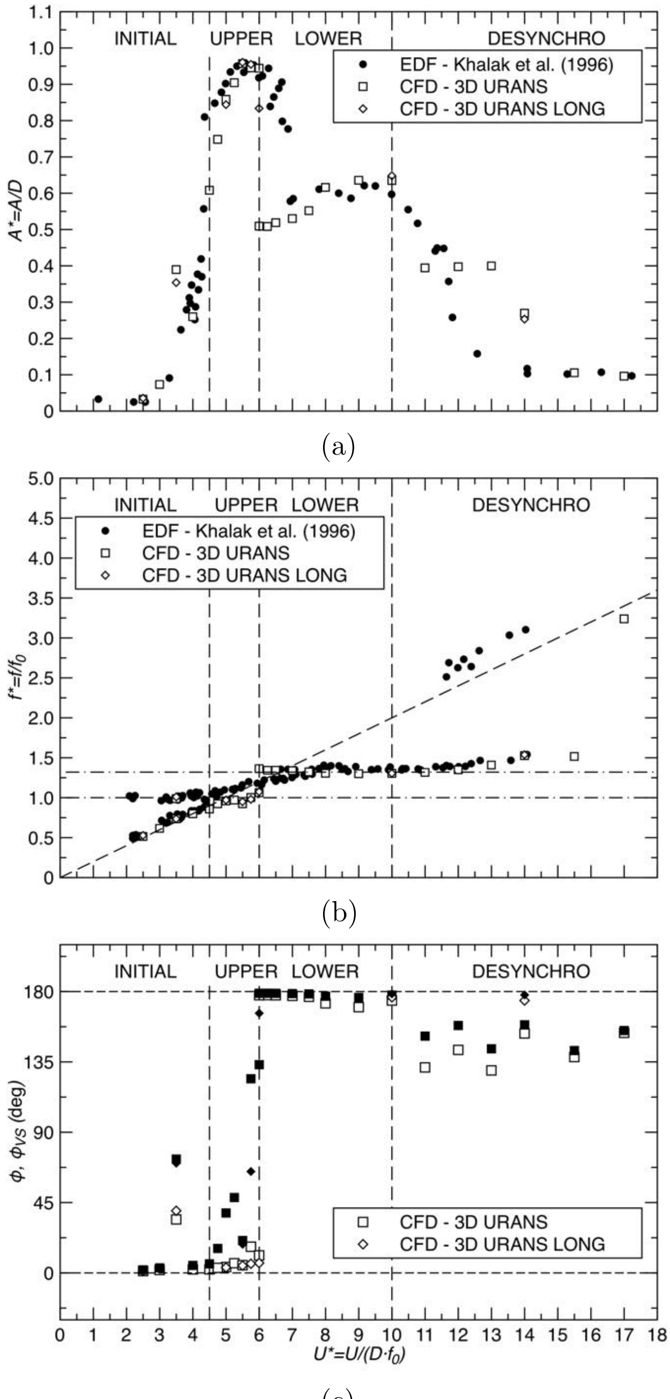

Figure 2.16: Amplitude ratio A^* (a), frequency ratio f^* (b) and phase lag ϕ (c) Vs reduced velocity U^*. Comparison between experimental data by Khalak and Williamson [15] (solid circles), present 3D URANS results (empty squares) and 3D URANS with extended span-wise length (empty diamonds). In (c) empty symbols correspond to the phase between the cylinder response and $y(t)$ and the total force $F_L(t)$, full symbols corresponds to the phase between the cylinder response and the vortex shedding lift force $F_{VS}(t)$.

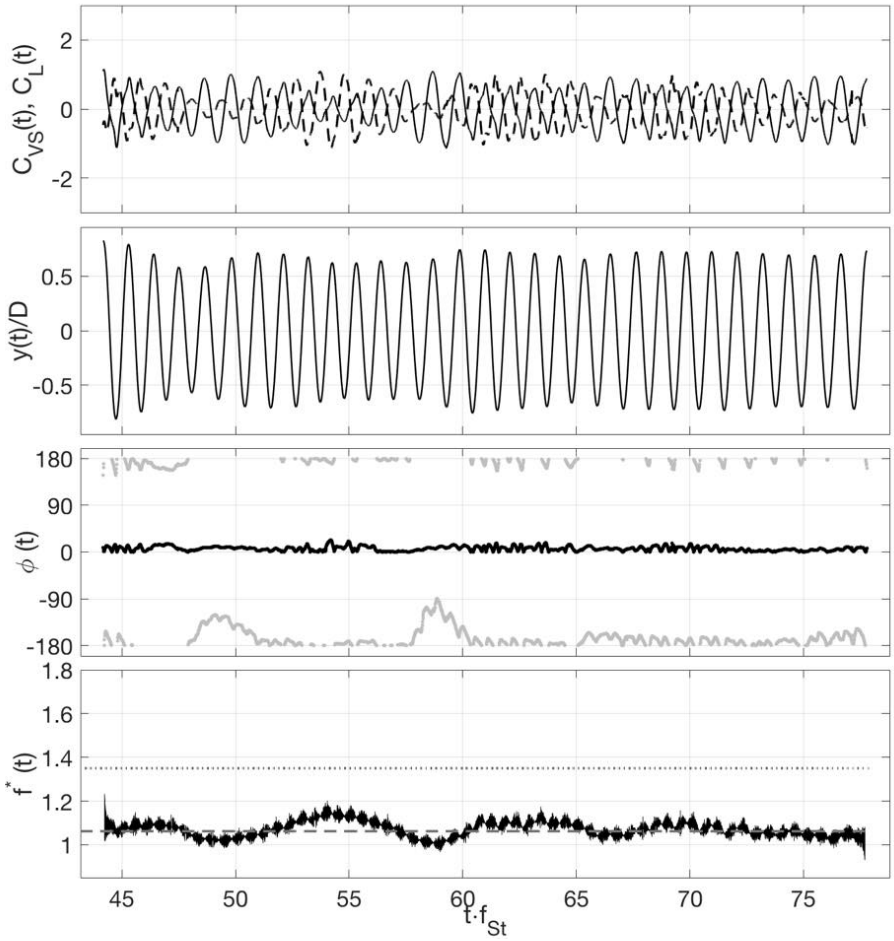

Figure 2.17: Time trace at $U^* = 6.00$ for the 3D URANS LONG case. First plot: total $C_L(t)$ (solid line) and vortex shedding force coefficient $C_{VS}(t)$ (dashed line). Second plot: non-dimensional cylinder displacement $y(t)$. Third plot: phase angle ϕ between C_L and $y(t)$ (black points) and phase angle ϕ_{VS} between C_{VS} and $y(t)$ (grey points). Fourth plot: frequency ratio $f^*(t)$ (using Hilbert transform), dashed line shows the main oscillation frequency (from analysis of spectral peaks) and dotted line shows the synchronisation frequency at lower branch.

The value of phase lag ϕ is summarised in Fig. 2.16(c) as a function of the reduced velocity. According with the definition of the subsection 2.3.2, ϕ represents the phase angle between the non-dimensional total force C_L and the non-dimensional cylinder displacement $y(t)/D$, ϕ_{VS} the phase angle between the non-dimensional vortex shedding force C_{VS} and the non-dimensional cylinder displacement $y(t)/D$. All of the defined phase angles follow the reported trend of the 3D URANS simulation with the experimental span-wise length (Fig. 2.11).

2.4.2 Force coefficient and flow visualisation

Fig.2.18 illustrates the effect of the span size of the domain on the time behaviour of the cylinder lift. The lift force is virtually identical to the simulation with the experimental span-wise length (Fig. 2.11). This conclusion is supported also by the Fig. 2.19 and Fig. 2.20, where the state of three-dimensionality of the wake is visualised using the λ_2 method [67] and coloured by the span-wise W_z and stream-wise W_x vorticity contours respectively.

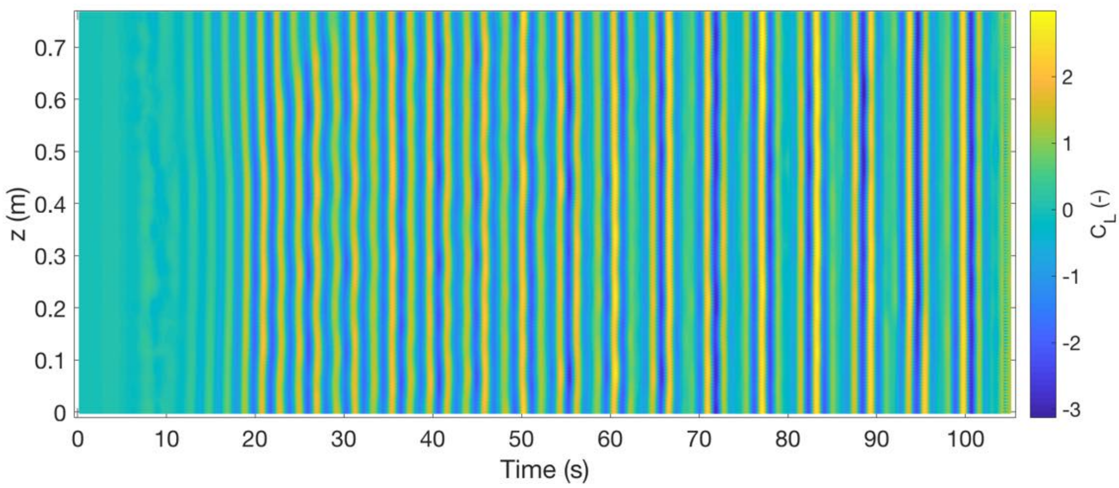

(a) Initial branch, Re=2941, U^{*}=3.50

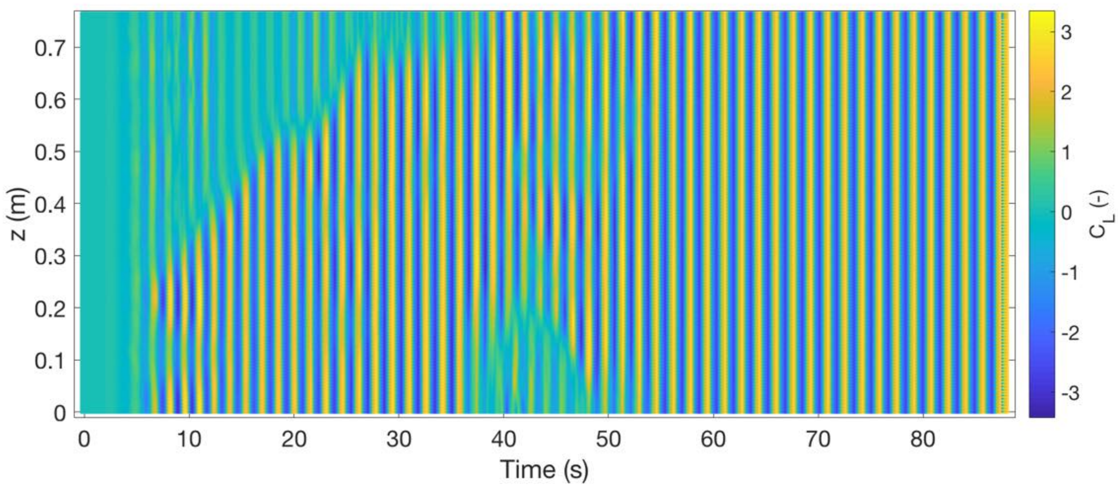

(b) Upper branch, Re=4622, U^{*}=5.50

Figure 2.18: Contours of the lift coefficient on the z-t plane for the 3D URANS LONG cases.

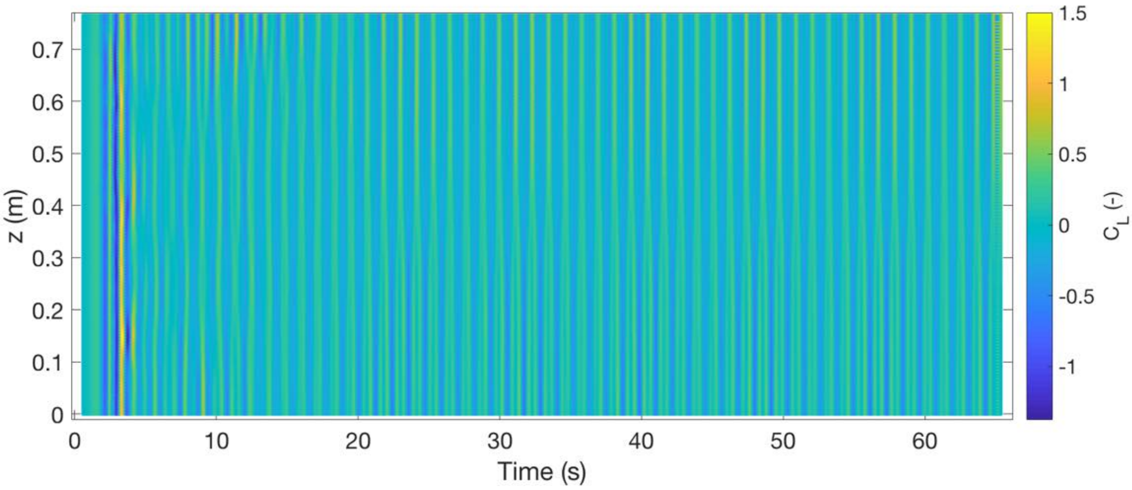

(c) Lower branch, Re=8404, U^*=10.00

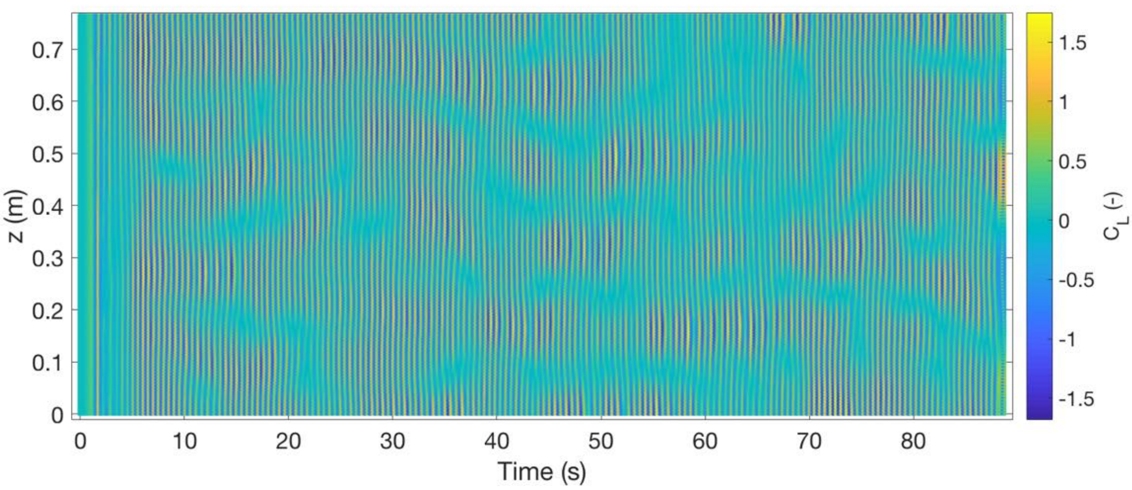

(d) Desynchronisation regime, Re=11765, U^*=14.00

Figure 2.18: (*Cont.*) Contours of the lift coefficient on the z-t plane for the 3D URANS LONG cases.

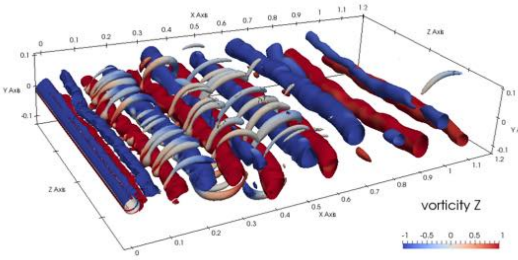

(a) Initial branch, Re=2941, U^{*}=3.50

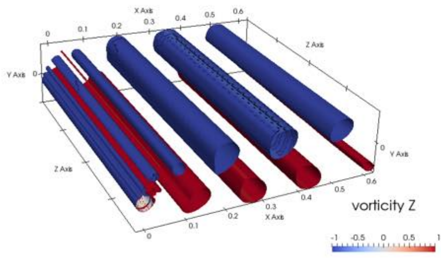

(b) Upper branch, Re=4622, U^{*}=5.50

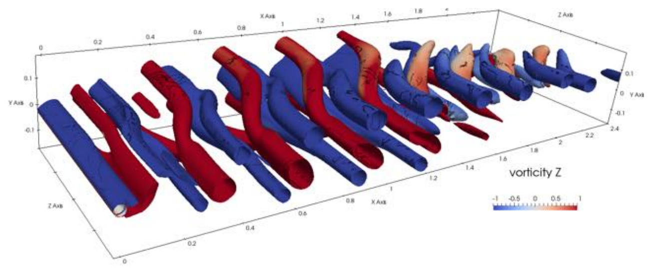

(c) Lower branch, Re=8404, U^{*}=10.00

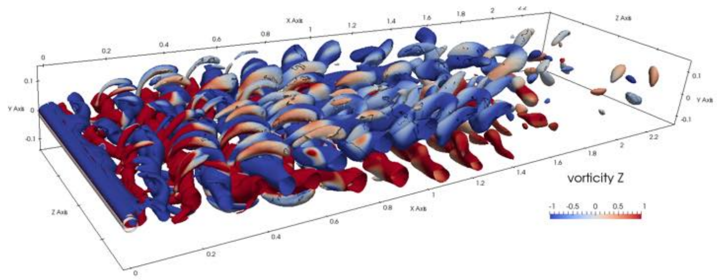

(d) Desynchronisation regime, Re=11765, U^{*}=14.00

Figure 2.19: Iso-surface of the eigenvalue $\lambda_2 = -0.2$ and the contours of the span-wise vorticity W_z (blue: clockwise, red: anti-clockwise) for the 3D URANS LONG cases.

2.4.3 Conclusions

In conclusion, the three-dimensional URANS simulations are quite insensitive to the extension of the span-wise dimension. Therefore, three-dimensional URANS simulations, with a span-wise size selected according to the experimental case $(10 \cdot D)$, have a span extension sufficient to capture correctly the existence of span periods for this particular case of bi-dimensional bluff body.

In next section, in order to avoid the limits of the URANS model to properly solve

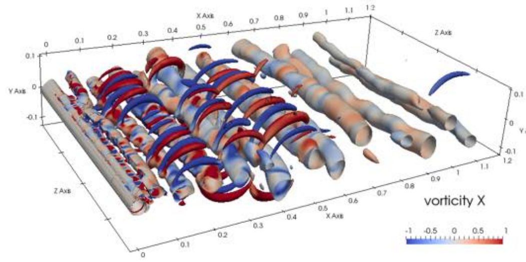

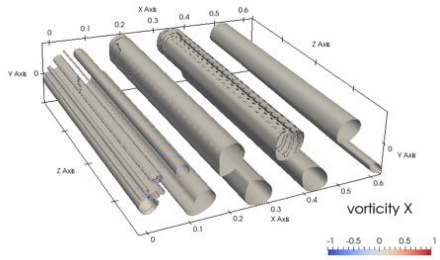

(a) Initial branch, Re=2941, U^{*}=3.5

(b) Upper branch, Re=4622, U^{*}=5.5

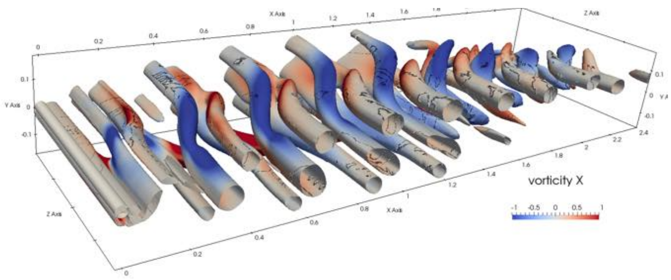

(c) Lower branch, Re=8404, U^{*}=10.0

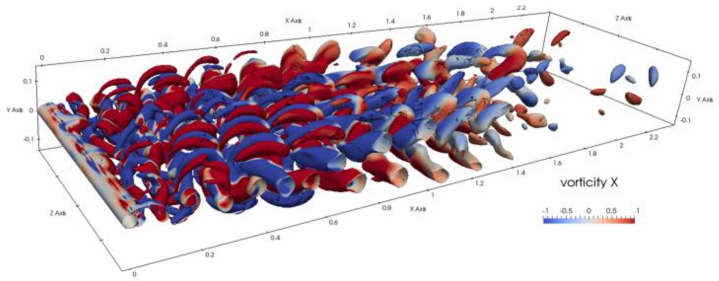

(d) Desynchronisation regime, Re=11765, U^{*}=14.0

Figure 2.20: Iso-surface of the eigenvalue $\lambda_2 = -0.2$ and the contours of the stream-wise vorticity W_x (blue: clockwise, red: anti-clockwise) for the 3D URANS LONG cases.

the VIV behaviour, the more advanced SAS model will be tested. The choice of this model with respect to the other hybrid RANS-LES (DES, DDES,...) model is mainly related to the simplicity of use of the SAS model, indeed the other models require the application of strict rules for grid generation to obtain a consistent solution. The choice of the SAS model, therefore, gives us the possibility to use the same mesh used on the 3D URANS simulations.

2.5 Scale-Adaptive Simulation Model

The previous sections have proven that the URANS does not solve properly the VIV behaviour for all of the interested flow regimes. This is probably due to the overlay dissipative character of standard URANS methods, which prevents the formulation of a turbulence cascade starting from the large URANS structures. From a practical standpoint, the URANS alternatives, such as LES or the hybrid RANS-LES (DES, DDES,...), require the application of strict rules for grid generation to obtain a consistent solution. From an industrial CFD perspective, it is difficult to ensure that all the users of a general purpose CFD codes can be informed about all the grids and time step guidelines avoiding this simulation. Furthermore, this technique doesn't provide the saving of computational cost required in today's CFD simulations.
These reasons have led to a new formulation of turbulence-resolving models, with a standard URANS base, capable of predicting the turbulent cascade up to the grid resolution limit without an explicit grid dependency in the model.
From a fundamental standpoint, all the currently used two-equation models suffer from the lack of an underlying exact transport equation, which can serve as a guide for the model development on a term by term basis. The reason for this deficiency lies in the fact that the exact equation for ε doesn't describe the large scales but the dissipative scales. The goal of a two-equation model is however the modelling of the influence of the large scale motions on the mean flow. Due to the lack of an exact equation, the ε- and the ω-equations are modelled in analogy with the equation for the turbulent kinetic energy k, using purely heuristic arguments.
The Scale-Adaptive Simulation (SAS) model was invented by Menter and coworkers [68]. The SAS is an improved URANS formulation, which allows the resolution of the turbulent spectrum in unstable flow conditions. Compared to the original $k-\omega$ turbulent model, the von Kármán length-scale L_{vK} has been introduced into the turbulence scale equation. The information provided by the von Kármán length-scale allows SAS models to dynamically adjust to resolved structures in a URANS simulation, which results in a LES-like behaviour in unsteady regions of the flowfield. At the same time, the model provides standard RANS capabilities in stable flow regions. The introduction of the von Kármán length-scale is based on the reformulation of Rottas's equation for the integral length-scale [68]. Instead of using purely heuristic and dimensional arguments, Rotta formulated an exact transport equation for turbulent kinetic energy times length scale kL. Rotta's equation represents the large scales of turbulence and can therefore serve as a basis for term-by-term modeling. The transport equations for the SST-SAS model as implemented in OpenFOAM (v.2.4), are based on transforming Rotta's approach to $k-\omega$ SST as presented by Ergov and Menter [69].
The governing equation of the SST-SAS model differs from those of the $k-\omega$ SST model by the additional SAS source term Q_{SAS} in the transport equation for the turbulence eddy frequency ω. A complete description of the $k-\omega$ SST model and its constants will be given in the following chapter 3.0.1. Here only the governing transport equations with an extended description of the Q_{SAS} source terms are reported.

The model transport equation for the turbulent kinetic energy k, used in the SST-SAS model, is defined as:

$$\frac{D\rho k}{Dt} = P - \beta^* \rho k \omega + \frac{\partial}{\partial x_j}\left[(\mu + \sigma_k \mu_T)\frac{\partial k}{\partial x_j}\right], \tag{2.19}$$

and the transport equation for the turbulence eddy frequency ω:

$$\frac{D\rho\omega}{Dt} = \frac{\gamma\rho}{\mu_t}P - \beta\rho\omega^2 + Q_{SAS} + \frac{\partial}{\partial x_j}\left[(\mu + \sigma_\omega \mu_T)\frac{\partial \omega}{\partial x_j}\right] + 2\rho\frac{(1-F_1)\sigma_{\omega_2}}{\omega}\frac{\partial k}{\partial x_j}\frac{\partial \omega}{\partial x_j}. \tag{2.20}$$

The additional source term Q_{SAS} reads [69]:

$$Q_{SAS} = max\left[\rho\eta_2\kappa(|E_{ij}|)^2\left(\frac{\hat{L}}{L_{vK}}\right)^2 - C\frac{2\rho k}{\sigma_\Phi}max\left(\frac{|\nabla\omega|^2}{\omega^2}, \frac{|\nabla k|^2}{k^2}\right), 0\right] \tag{2.21}$$

where $|\nabla\omega|^2 = \frac{\partial\omega}{\partial x_j}\frac{\partial\omega}{\partial x_j}$ and $|\nabla k|^2 = \frac{\partial k}{\partial x_j}\frac{\partial k}{\partial x_j}$. This SAS source term originate from a second order derivative term in Rotta's transport equation. For detailed derivations see Ergov and Menter [69]. The model parameters in SAS source term are:

$$\eta_2 = 3.51, \qquad \sigma_\Phi = 2/3, \qquad C = 2. \tag{2.22}$$

The Q_{SAS} term is essentially zero for boundary layer flows (due to $C = 2$) while it activates the term with L_{vK} in the unsteady situation.
The value of $\hat{L}$ in the SAS source term (2.21) is the length scale of the modelled turbulence

$$\hat{L} = \frac{\sqrt{k}}{\left(C_\mu^{1/4} \cdot \omega\right)}, \tag{2.23}$$

here $C_\mu = 0.09$ is a constant taken from the $k - \varepsilon$ model and the von Kármán length scale L_{vK} is a three-dimensional generalisation of the classic boundary layer definition

$$L_{vK,BC} = \kappa\frac{\dfrac{\partial \mathbf{u}}{\partial y}}{\dfrac{\partial^2 \mathbf{u}}{\partial y^2}}. \tag{2.24}$$

The first velocity derivative $\partial\mathbf{u}/\partial y$ is represented in L_{vK} by $|E_{ij}|$ a scalar invariant of the strain rate tensor E_{ij}, while the second velocity derivative $\partial^2\mathbf{u}/\partial y$ is generalised to 3D using the magnitude velocity of the Laplacian $|\nabla^2\mathbf{u}|$. So the von Kármán length scale can be rewritten in the following more suitable form

$$L_{vK} = \kappa\left|\frac{\dfrac{\partial u_i}{\partial x_j}\dfrac{\partial u_i}{\partial x_j}}{\dfrac{\partial^2 u_i}{\partial x_k^2}\dfrac{\partial^2 u_i}{\partial x_j^2}}\right|. \tag{2.25}$$

So defined $\hat{L}$ and L_{vK} are both equal to (κy) in the logarithmic part of the boundary layer, where $\kappa = 0.41$ is the von Kármán constant.
The model also provides a direct control of the high wave number damping. This is realized by a lower constraint on the L_{vK} value in the following way:

$$\tilde{L}_{vK} = \left(L_{vK}, C_S \sqrt{\frac{\kappa \eta_2}{(\beta / C_\mu) - \gamma}} \cdot \Delta \right) \tag{2.26}$$

where Δ is the cubic root of the cell volume. The purpose of this limiter is to control the damping of the finest resolved turbulent fluctuation. The structure of the limiter is derived from analysing the equilibrium eddy viscosity of the SST-SAS model. Assuming the source term equilibrium (balance between production and destruction of the kinetic energy turbulence) in both transport equations, one can derive the following relation between the equilibrium eddy viscosity μ_t^{eq}, L_{vK} and $|E_{ij}|$:

$$\mu_T^{eq} = \rho \cdot \left(\sqrt{\frac{((\beta / C_\mu) - \gamma)}{\kappa \eta_2}} \cdot L_{vK} \right)^2 |E_{ij}| \tag{2.27}$$

This formula has a similar structure to the subgrid scale eddy viscosity in the LES model by Smagorinsky: $\mu_T^{LES} = \rho \cdot (C_S \cdot \Delta)^2 \cdot |E_{ij}|$. Therefore, it is natural to adopt the Smagorinsky LES model as a reference, when formulating the high wave number damping limiter for the SST-SAS model. The limiter, imposed on the L_{vK} value, must prevent the SAS eddy viscosity from decreasing lower than the LES subgrid-scale eddy viscosity:

$$\mu_T^{eq} \geqslant \mu_T^{LES} \tag{2.28}$$

Substitutions of μ_T^{eq} and μ_t^{LES} in condition (2.28) result in the L_{vK} limiter value used in Eq. (2.26). Similar to LES, the high wave number damping is a cumulative effect of the dissipation and the modelled eddy viscosity. Therefore, the model parameter C_S must be calibrated for each particular discretisation scheme. The SST-SAS model calibrated for the OpenFOAM solver has a C_S value of 0.11. This provides the same energy spectrum, as the Smagorinsky LES model in OpenFOAM. Summarising, the formulation of the SST-SAS model differs from the pure SST model by the additional source term Q_{SAS} in the ω equation. This new source term enables the smooth variation of the flow mode from URANS to LES-like mode. Moreover, when in the stable region, $\hat{L} < L_{vK}$ and $Q_{SAS} = 0$ returns a pure URANS mode, while when in the unstable region, $\hat{L} > L_{vK}$, $Q_{SAS} > 0$ and the mode turns to LES-like mode.

2.5.1 Overview of the SAS simulation

In this study, the results of the SAS simulations are given and compared with the previously presented 3D URANS simulations. The computational grid used for the SAS simuations are the 3D NEW presented in Tab. 2.10.
As the SAS model is based on the turbulence model $k-\omega$ SST, the used numerical scheme, mesh morphing, boundary and initial condition for the SAS simulations are always the same as URANS simulations (shown in section 2.1). The only difference is in the boundary turbulent kinetic energy k. Because the SST-SAS model includes division of k in the transport equations it is better practice to choose $k \neq 0$ on the cylinder wall. The value of $k = 1 \cdot 10^{-10}$ is sleeted to avoid zero. The SST-SAS model requires us to define the initial and boundary conditions for the sub grid scale viscosity ν_{sgs}. On the cylinder, the turbulence goes to zero and hence any shear stress caused by turbulence should be zero as well. Therefore, the sub grid scale viscosity is set to zero at the wall. For all other boundaries, the calculated boundary condition is applied. This means that no special boundary condition is assigned to turbulent viscosity, but it is assumed to have been assigned using other fields. This is appropriate since k and ω determine ν_{sgs}. Adaptive-time stepping technique [57] with Co < 0.9 is used for the time integration.

2.5.2 Cylinder response

Fig. 2.21 presents the results obtained by SAS numerical simulations and the comparison with experimental data by Khalak and Willamson [15]. The results from the 3D URANS simulation are also reported in Fig. 2.21 in order to better appreciate the difference between the two models. Fig. 2.21(a) shows the variation of the non-dimensional amplitude of cylinder motion A^* as a function of the reduced velocity U^*. From the results in terms of A^*, we can see that the SAS numerical results follow exactly the experiments. The only overprediction of the amplitude values are for $U^* > 13$. The main discrepancies between the 3D URANS and SAS where for some velocities of the initial branch, $U^* = 3.5$ and $U^* = 4.75$, and especially in the desyhcronisation region.
Fig. 2.21(b) shows the frequency ratio f^* as a function of the reduced velocity U^*, according to the FFT analysis of the cylinder displacement. The SAS and the 3D URANS are identical in almost everything in the interested regime. Some discrepancies have been found for the value higher than $U^* > 14$. As for the 3D URANS, the SAS simulations fail to predict the experimental oscillation frequency in the upper branch region.
As a final note, the region identification is consistent between the two numerical models. The only discrepancy has been revealed for the value $U^* = 4.75$ which in the case of SAS is still in the initial branch while for 3D URANS it is already in the upper branch.

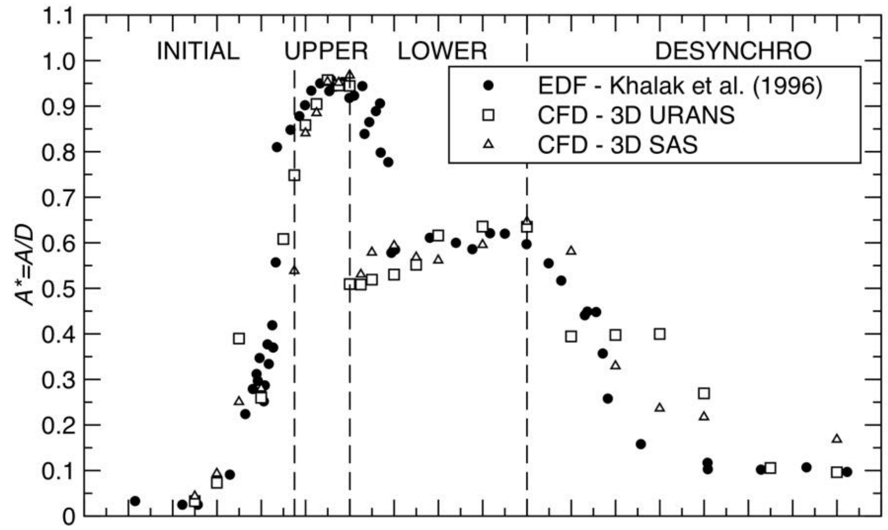

(a) Amplitude ratio A^* Vs reduced velocity U^*

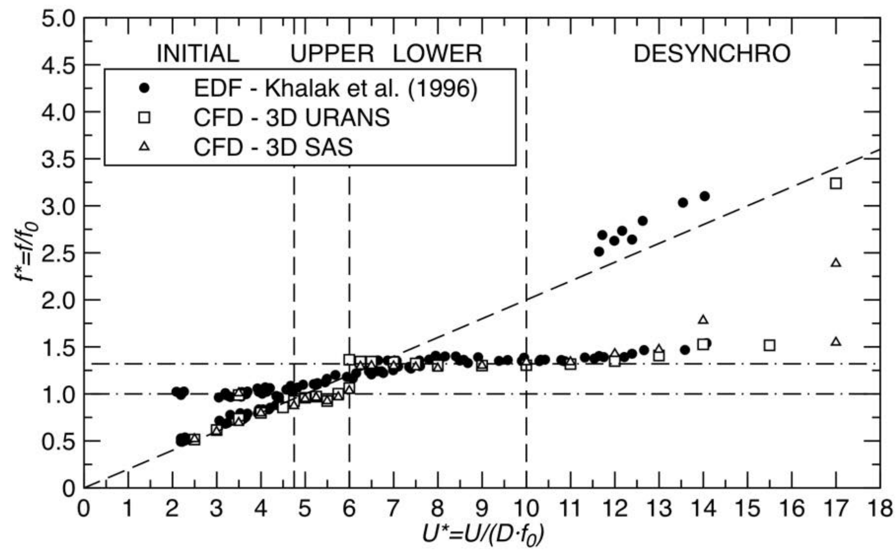

(b) Frequency ratio f^* Vs reduced velocity U^*

Figure 2.21: Comparison between experimental data by Khalak and Williamson [15] (solid circles), present 3D URANS results (empty squares) and SAS results (empty triangles). Vertical dashed lines marks the boundaries of branches in accordance with the CFD results. The oblique dashed line in (b) corresponds to the Strouhal frequency (St = 0.20).

2.5.3 Force coefficient and phase

The value of the root mean square (rms) of the total force $C_{L,\mathrm{rms}}$ and its phase ϕ with respect to the displacement of the cylinder is shown in Fig. 2.22(a) as a function of the reduced velocity U^* for 3D URANS and SAS simulations. Fig. 2.22(b) shows the root mean square (rms) of the non-dimensional shedding force $C_{VS,\mathrm{rms}}$ of the vortex shedding force and its phase ϕ_{VS} with respect to the displacement of the cylinder and the non-dimensional shedding force C_{VS}.

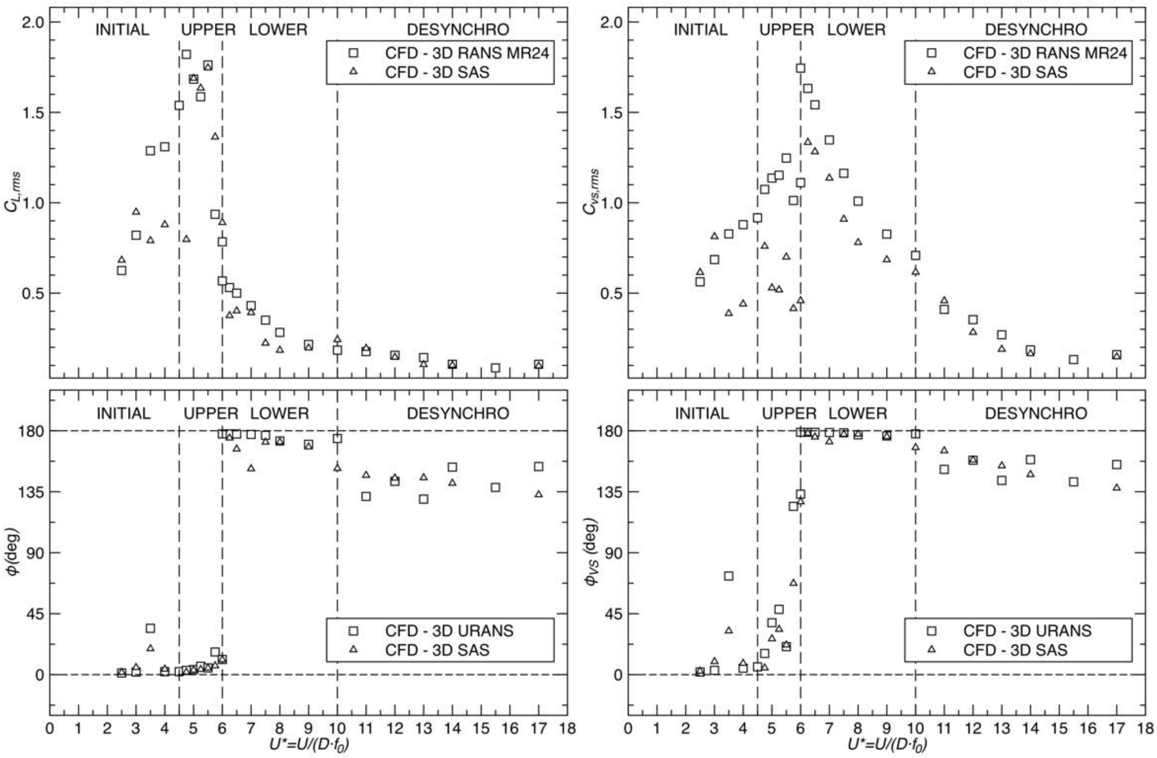

(a) Total force.

(b) Vortex Shedding force.

Figure 2.22: Force and phase angle variation with U^* for the case 3D SAS.

Considering as first the total force, the difference between 3D URANS and SAS are most visible in the initial branch. The 3D URANS shows a rapid increase of $C_{L,rms}$ as U^* increases, instead the SAS model shows a constant value of $C_{L,rms} \approx 0.85$. A small discrepancy is also found for some values in the lower branch region. In the other two branches, upper branch and in the desynchronisation region, the values of the total force are almost comparable.

The value of the root mean square (rms) of the non-dimensional shedding force shows the most visible differences between the two models. Instead of a constant increase of

$C_{VS,rms}$ as the U^* increases until the peak value, as shows by the 3D URANS simulations, the SAS model shown an almost constant value in the initial and upper branches and then a drop to the peak value.

The values of phases ϕ and ϕ_{VS} are almost comparable for all the branches.

Again the results from SAS are in contrast with the experimental observation of Khalak and Williamson [5]. In their experimental studies they found that the transition between the initial and the upper branch is associated with the ϕ_{VS} jump. Here in the case of SAS simulation the ϕ_{VS} jump, although present, is not clearly visible in Fig. 2.22(b). One of the reasons can be related to the different oscillation frequency between the SAS results and the experiments of Khalak and Williamson. In the experimental results the oscillation frequency increases as the U^* increases along the upper branch region (fig. 2.21(b)), while in the SAS solution the oscillation frequency remains very close to the natural frequency through the same U^* (as for the 3D URANS cases). Khalak and Williamson also argue that the first transition initial-upper occurs when the frequency ratio $f^* = f/f_0$ passes though 1.0. Hence, the ϕ_{VS} jump occurs also when frequency ratio $f^* = f/f_0$ passes though 1.0. This assumption is confirmed by the SAS results. Indeed, at $U^* = 6$ in the case of SAS simulation the frequency ratio passes from the value of 1.0 to the synchronisation value ≈ 1.3 and at the same the ϕ_{VS} jump occurs. For this reduced velocity $U^* = 6$, as for the 3D URANS simulation, the transition from upper to lower occurs as the velocity occurs. The previously presented Fig.2.12(f) shows that the system, for the 3D URANS case, switches between these branches intermittently. This complex mode transition is surprisingly captured by the 3D URANS simulations. Instead, as shown in Fig. 2.22 for the SAS case, the intermittent switch between the two regions is not observed. However an oscillation of the cylinder response as a function of time still exists.

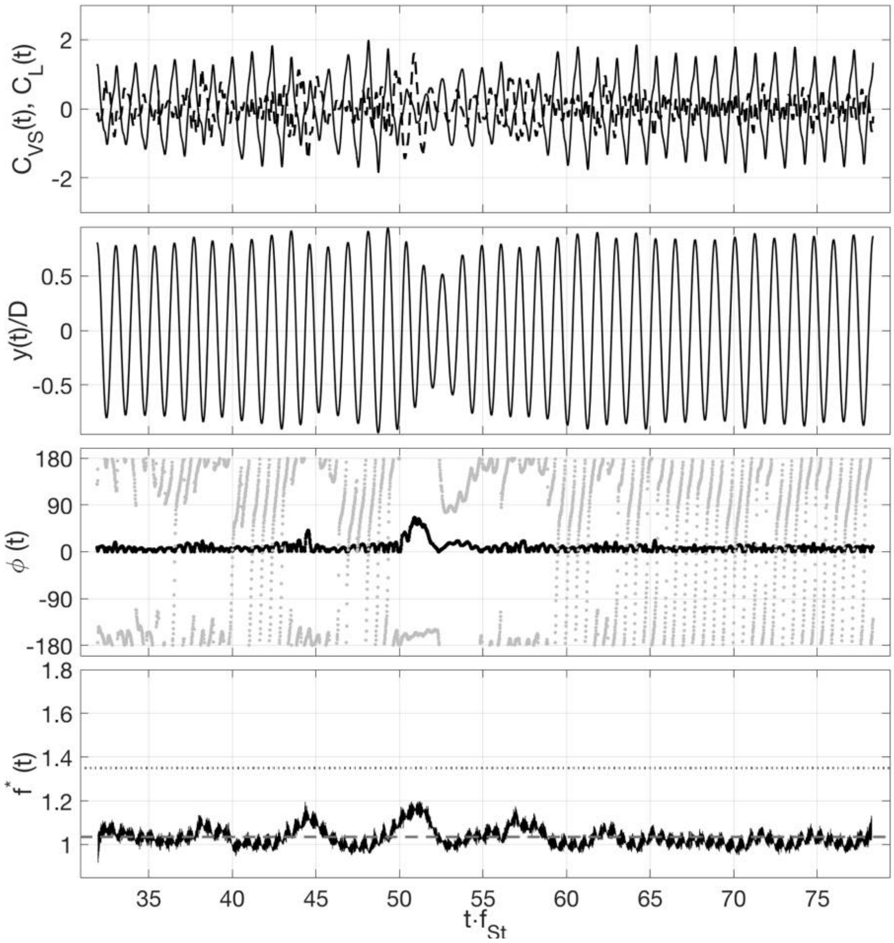

Figure 2.22: Time trace at $U^* = 6.00$ for the 3D SAS simulations. First plot: total $C_L(t)$ (solid line) and vortex shedding force coefficient $C_{VS}(t)$ (dashed line). Second plot: non-dimensional cylinder displacement $y(t)$. Third plot: phase angle ϕ between C_L and $y(t)$ (black points) and phase angle ϕ_{VS} between C_{VS} and $y(t)$ (grey points). Fourth plot: frequency ratio $f^*(t)$ (using Hilbert transform), dashed line shows the main oscillation frequency (from analysis of spectral peaks) and dotted line shows the synchronisation frequency at lower branch.

2.5.4 Wake flow three-dimensionality

The sensitivity of the solution to the SAS model is illustrated in Fig. 2.24, in which the time dependent force is presented in the z-t plane. The same variation of the lift force coefficients along the cylinder span discovered by the 3D URANS simulations are also found with the SAS model. The strongest variation occurs in the tradition zone ($4.5 < U^* < 5$ and $5.75 < U^* < 6.25$) and in the desynchronisation region $U^* > 10$. Again the lift coefficient acquires a quasi bi-dimensional characteristic in the initial branch and in the lower branch (Fig. 2.24(c)). Even if small oscillations are detected along the span direction of the cylinder. These span oscillations are more visible through the three-dimensional representation of the lift coefficient C_L in the time and space presented in Fig. 2.25. Graphically comparing the two numerical solutions in terms of lift coefficients for the reduced velocity $U^* = 7.5$, it can be seen that the SAS solution (Fig. 2.25(c)) presents span-wise variation, while in the 3D URANS solution (Fig. 2.12(r)) these variations are totally absent.
The quantification of these variations can be done by using the correlation coefficient (already presented in 2.3.3). The correlation $\overline{R}(0, z/D)$ represents the correlation coefficient of the lift coefficient between one end of the cylinder at $z/D = 0$ and with z. Fig. 2.23 shows the variations of the correlation $\overline{R}(0, z/D)$ of the sectional lift coefficient with z adimensionalised by the diameter. It can be seen that the correlation of the lift coefficient stays between 0.8 and 1 in the initial and lower branch. This indicates that the span-wise variation shown in Fig. 2.25 for those two regions are still low. This result confirms that the three-dimensionality of the flow is weak in the initial and in the lower branch.

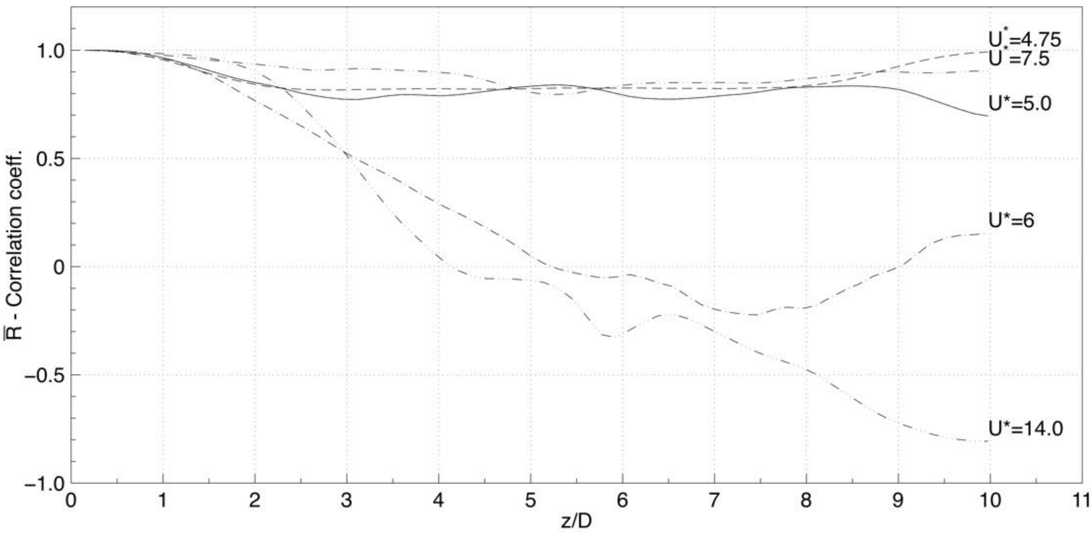

Figure 2.23: Correlation coefficent $\overline{R}(0, z/D)$ of the sectional lift coefficient for the SAS simulations.

The capabilities of the SAS model in reproducing the turbulent unsteadiness are displayed in Fig. 2.26 and Fig. 2.27, which shows the istantaneous turbulent structures identified by the λ_2-criterion [67] iso-surface and coloured by the span- and steam-wise component of vorticity respectively.
The three-dimensional flow pattern, with both span- and stream-wise vortices ("rollers and ribs"), are clearly visible for all the reduced velocity in Fig. 2.26 and Fig. 2.27. Through closer inspection, the SAS solution differs drastically from that of 3D URANS solution (previously shown in Fig. 2.13 and Fig. 2.13) in terms of the size of the flow structures resolved by the two approaches: SAS produces much finer vortices than 3D URANS.
As first note, the changes of span-wise vorticity agree with the variation of the lift coefficient as shown in Fig. 2.24. The clearly identifiable span-wise vortices in the initial branch $U^* < 4.75$ (Fig. 2.26(a) and 2.26(b)) indicate the strong bi-dimensionality of the flow at low U^*. The variation of the flow in the upper branch region $4.75 < U^* < 6$ are stronger but the span-wise vortices can still be identified at $U^* = 4.75$ (Fig. 2.26(b)). In the lower branch region the presence of pairs of counter-rotating rib-like structures of stream-wise becomes stronger. As shown in Fig. 2.25(c), the presence of these structures has a marginal effect on the variation of the lift coefficient along the span direction. In the remaining cases $U^* > 10$ it is difficult to identify the span-wise vortices (Fig. 2.27(e)).

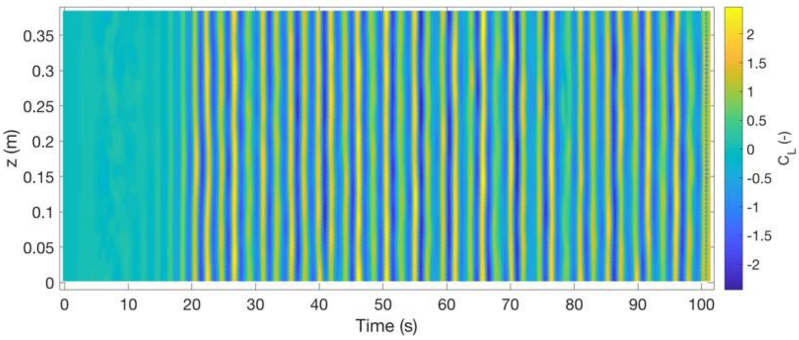

(a) Initial branch, Re=2941, U^*=3.50

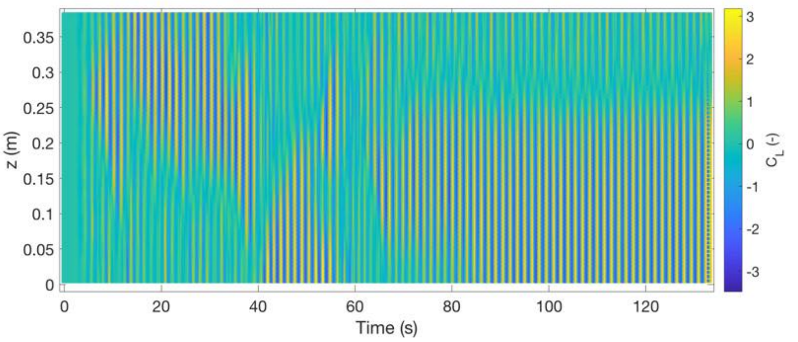

(b) Transition upper/lower branch, Re=5042, U^*=6.00

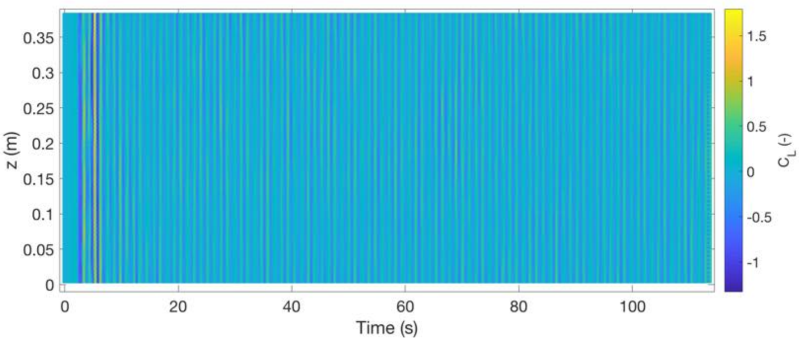

(c) Lower branch, Re=6303, U^*=7.50

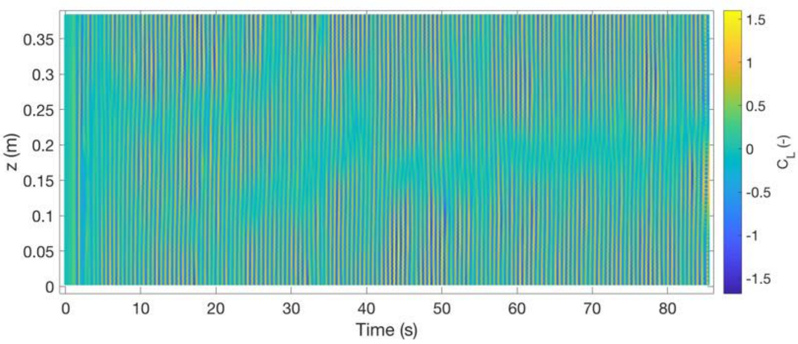

(d) Desynchronisation regime, Re=10925, U^*=14.00

Figure 2.24: Contours of the lift coefficient on the z-t plane for the 3D SAS cases.

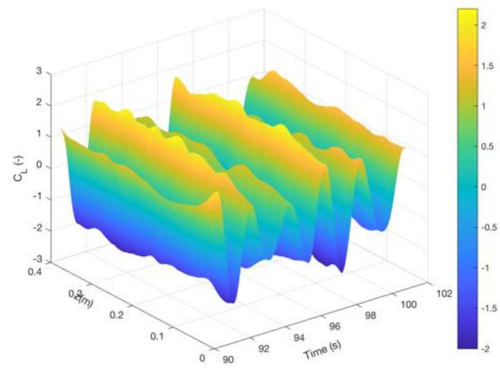

(a) Initial branch, Re=2941, U^{*}=3.50

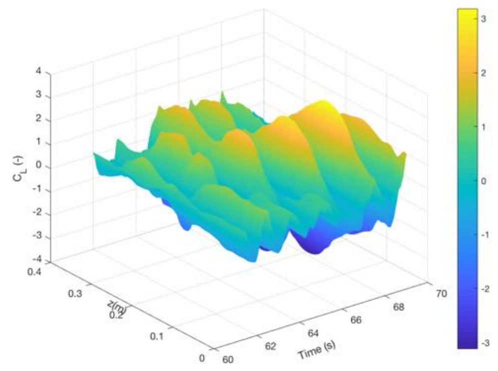

(b) Transition upper/lower branch, Re=5042, U^{*}=6.00

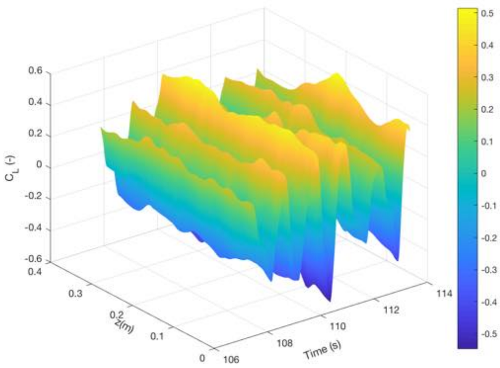

(c) Lower branch, Re=8404, U^{*}=7.50

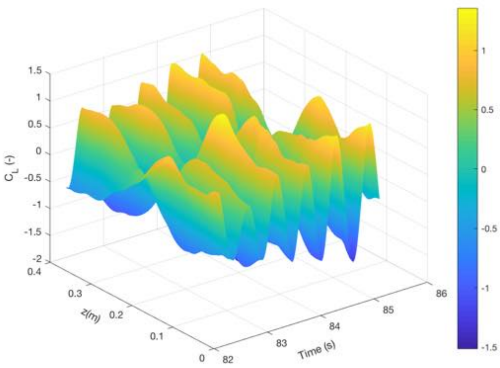

(d) Desynchronisation regime, Re=10084, U^{*}=14.00

Figure 2.25: 3D plot of the lift coefficient as function of time and z-axis for the 3D SAS cases.

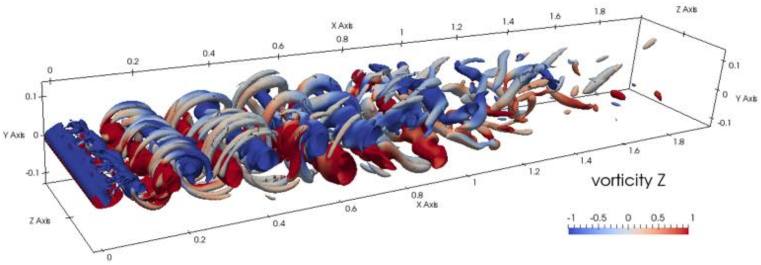

(a) Initial branch, Re=2941, U^{*}=3.50

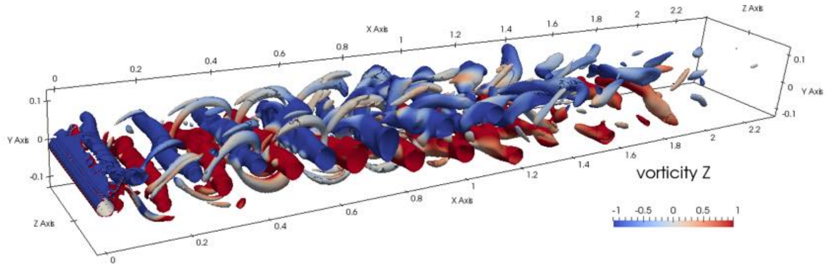

(b) Upper branch, Re=3991, U^{*}=4.75

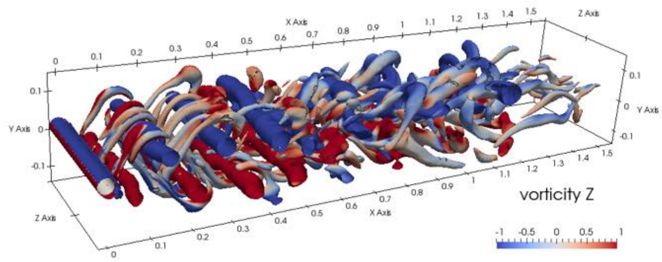

(c) Upper branch, Re=4622, U^{*}=5.5

Figure 2.26: Iso-surface of the eigenvalue $\lambda_2 = -0.2$ and the contours of the span-wise vorticity W_z (blue: clockwise, red: anti-clockwise) for the 3D SAS cases.

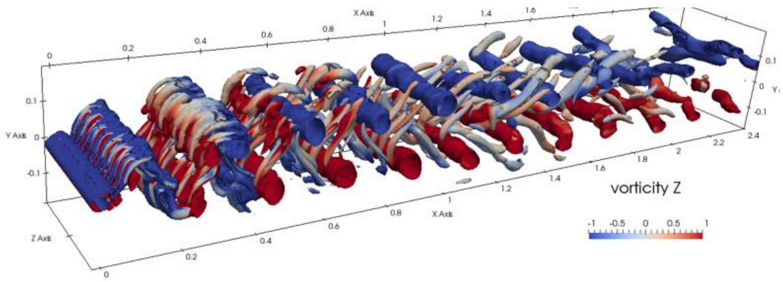

(d) Lower branch, Re=6303, U^{*}=7.50

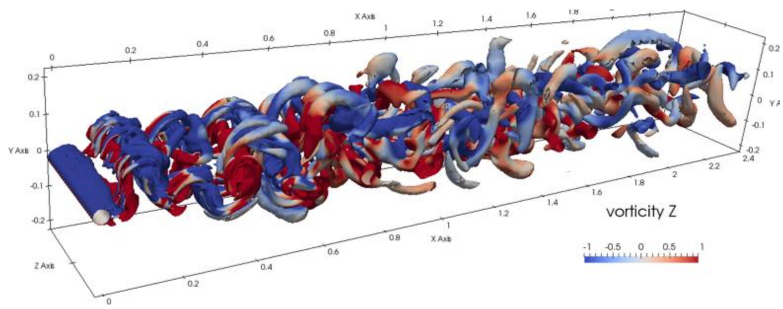

(e) Desynchronisation regime, Re=8404, U^{*}=10.00

Figure 2.26: (*Cont.*) Iso-surface of the eigenvalue $\lambda_2 = -0.2$ and the contours of the span-wise vorticity W_z (blue: clockwise, red: anti-clockwise) for the 3D SAS cases.

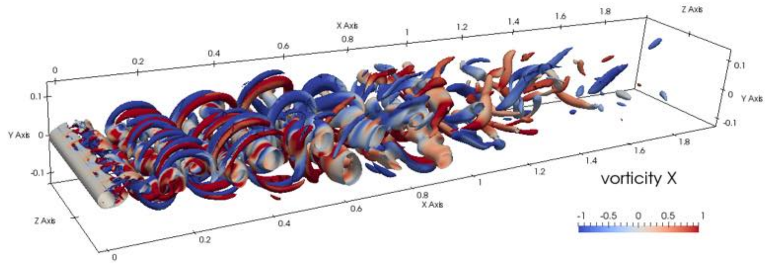

(a) Initial branch, Re=2941, U^{*}=3.50

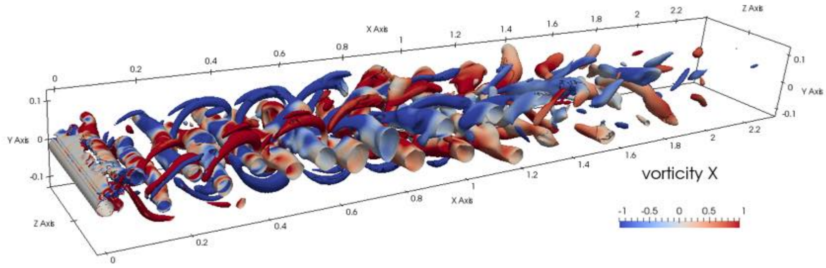

(b) Upper branch, Re=3991, U^{*}=4.75

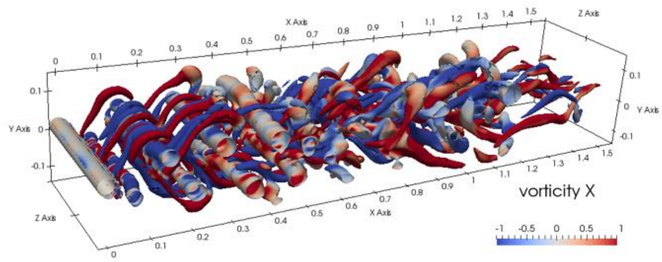

(c) Upper branch, Re=4622, U^{*}=5.5

Figure 2.27: Iso-surface of the eigenvalue $\lambda_2 = -0.2$ and the contours of the stream-wise vorticity W_x (blue: clockwise, red: anti-clockwise).

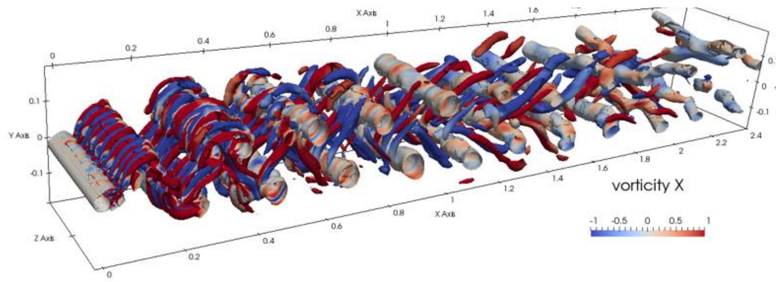

(d) Lower branch, Re=6303, U^{*}=7.50

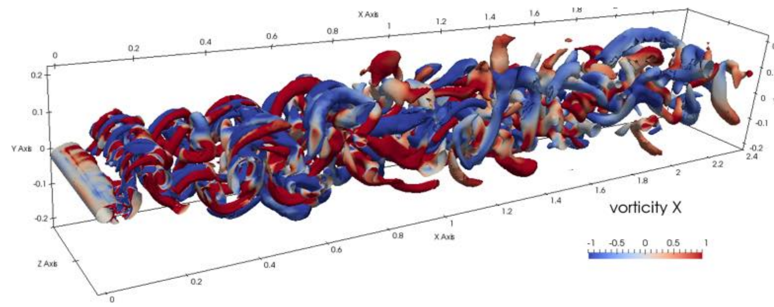

(e) Desynchronisation regime, Re=8404, U^{*}=10.00

Figure 2.27: Iso-surface of the eigenvalue $\lambda_2 = -0.2$ and the contours of the stream-wise vorticity W_x (blue: clockwise, red: anti-clockwise) for the 3D SAS cases.

2.5.5 Vortex Shedding mode

Contours of span-wise vorticity W_z at the lowest cylinder y-position on three cross sections along the cylinder are presented in Fig. 2.28. It can be seen from Fig. 2.28(a) that the vortex shedding for $U^* = 3.5$ exhibits a 2S mode where two single vortices of opposite circulation are shed from the cylinder. A 2P vortex mode, two pairs of vortices are shed in one oscillation cycle, appears at the upper branch (Fig. 2.28(b)). At the beginning of the lower branch the evidence of a 2P mode is not clearly visible. In the case of the reduced velocity $U^* = 6.5$ (Fig. 2.28(d)) a quasi-2S mode is visible close to the cylinder. However, when the vortex progress downstream, they split in a couple of small vortices similar to the 2P vortex pattern. As the reduced velocity increases $U^* = 7$ (Fig. 2.28(e)) the 2P vortex mode it becomes clearly visible again. In the desynchronisation region (Fig. 2.28(f)) the vortex shedding structures along the cylinder becames noticeably different.

To compare the vortex pattern observed in the cylinder wake flow with the literature reference the Williamson-Rosko map is used. In the Williamson-Rosko map the experimental results in terms of A^* are plotted as a function of the "true reduced velocity" (U^*/f^*)St. Fig. 2.29 shows the SAS results plotted on the Williamson-Rosko map. In the same figure the 3D URANS value are also reported for comparison. As observed in the Fig. 2.29, the discovered vortex shedding mode is in good agreement with the Williamson-Rosko map. In particular the non-clear vortex shedding pattern at the beginning of the lower branch (Fig. 2.28(d)) is consistent with the plot of the amplitude results in the map. Indeed, the two reduced velocity $U^* = 6.25$ and $U^* = 6.5$ are close to the boundary region between the 2S and 2P modes. This result confirms again the quality of the Williamson-Rosko map with the "true reduced velocity" on the abscissa, as proposed by Khalak and Williamson [5], in predicting the vortex pattern.

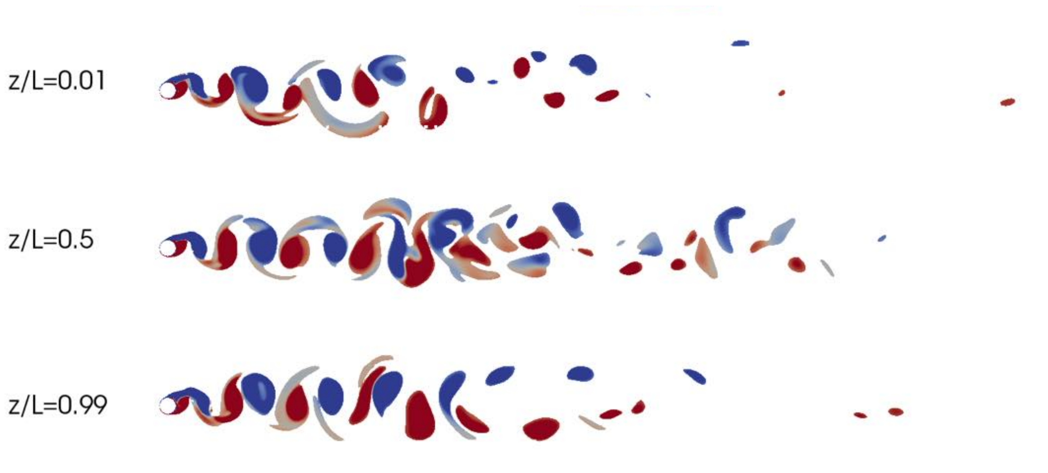

(a) Initial branch, Re=2941, U^*=3.50, (U^*/f^*)St = 1.008

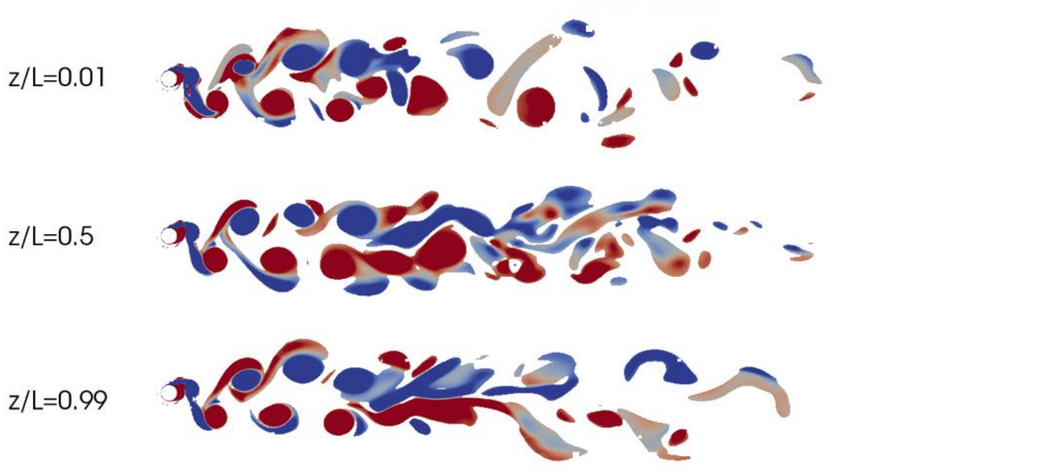

(b) Upper branch, Re=4832, U^*=5.75, (U^*/f^*)St = 1.190

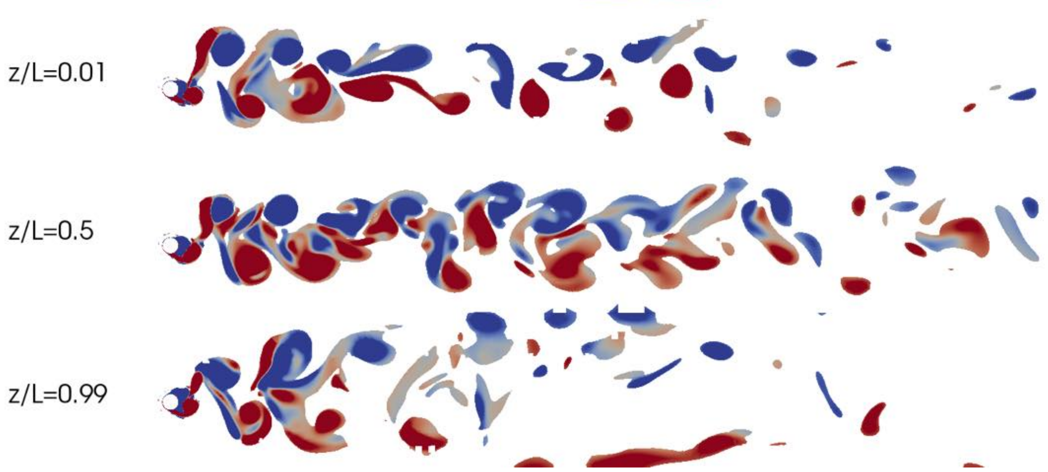

(c) Transition upper/lower branch Re=5042, U^*=6.00, (U^*/f^*)St = 1.160

Figure 2.28: Contour of the axial vorticity W_z at three section along the cylinder span (blue: clockwise, red: anti-clockwise) for the 3D SAS cases.

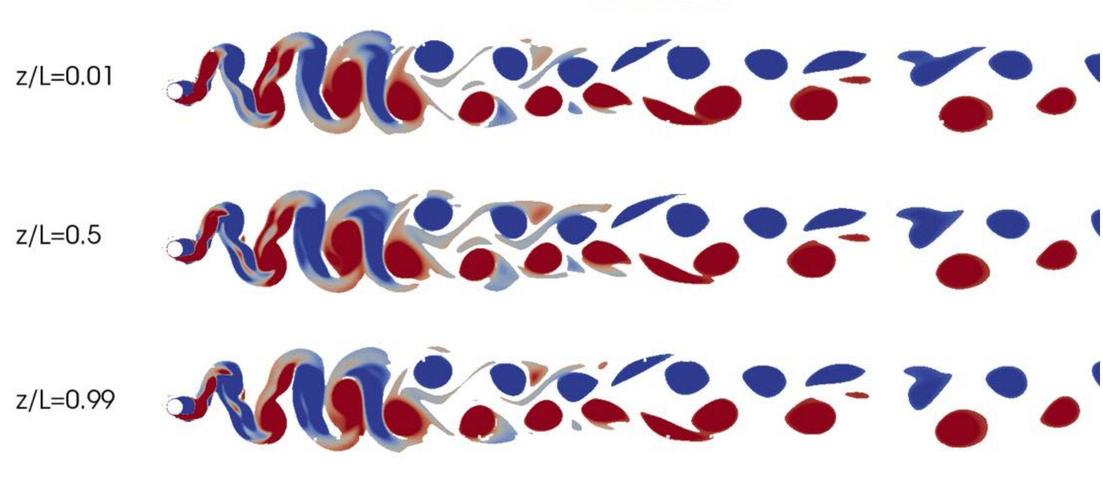

(d) Lower branch, Re=5462, U^*=6.5, (U^*/f^*)St = 0.999

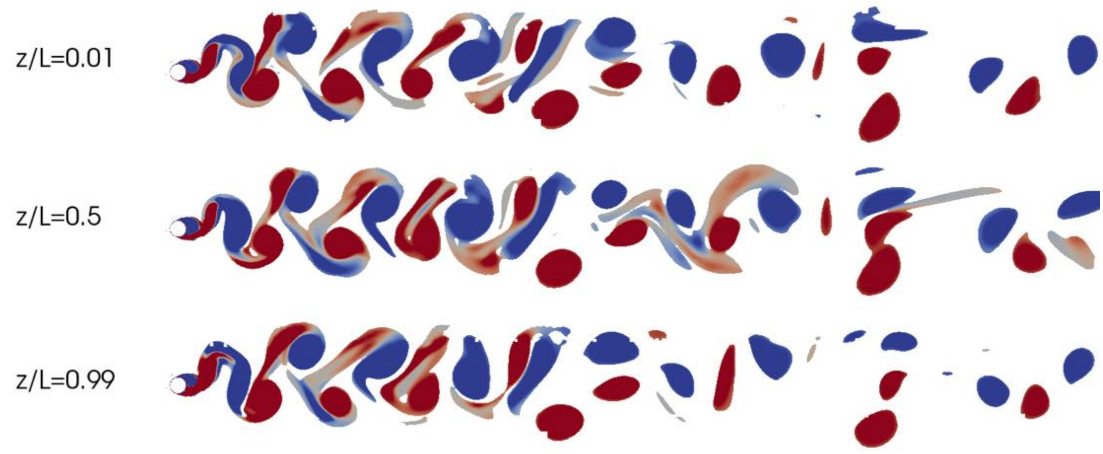

(e) Lower branch, Re=5882, U^*=7.00, (U^*/f^*)St = 1.08

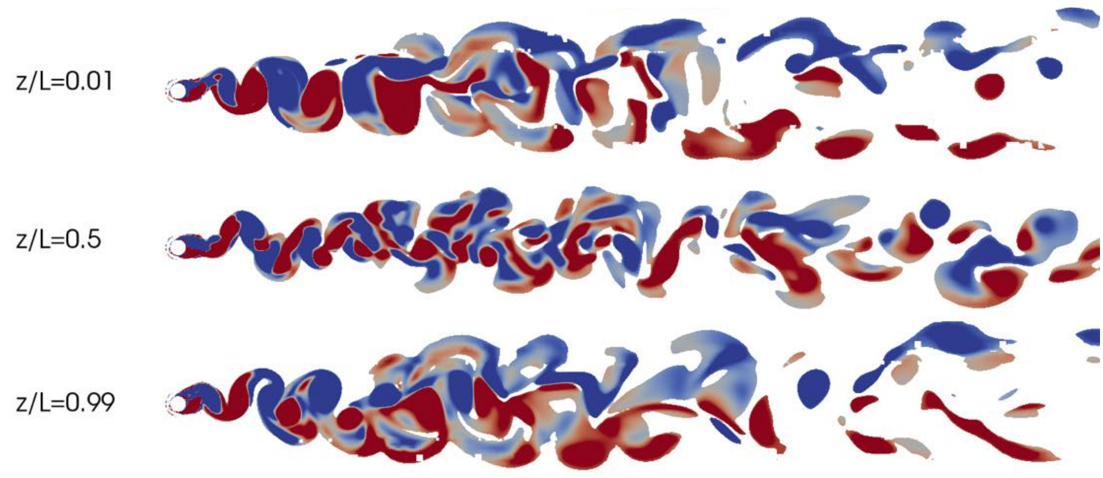

(f) Desynchronisation regime, Re=10084, U^*=12.00, (U^*/f^*)St = 1.681

Figure 2.28: (*Cont.*) Contour of the axial vorticity W_z at three section along the cylinder span (blue: clockwise, red: anti-clockwise) for the 3D SAS cases.

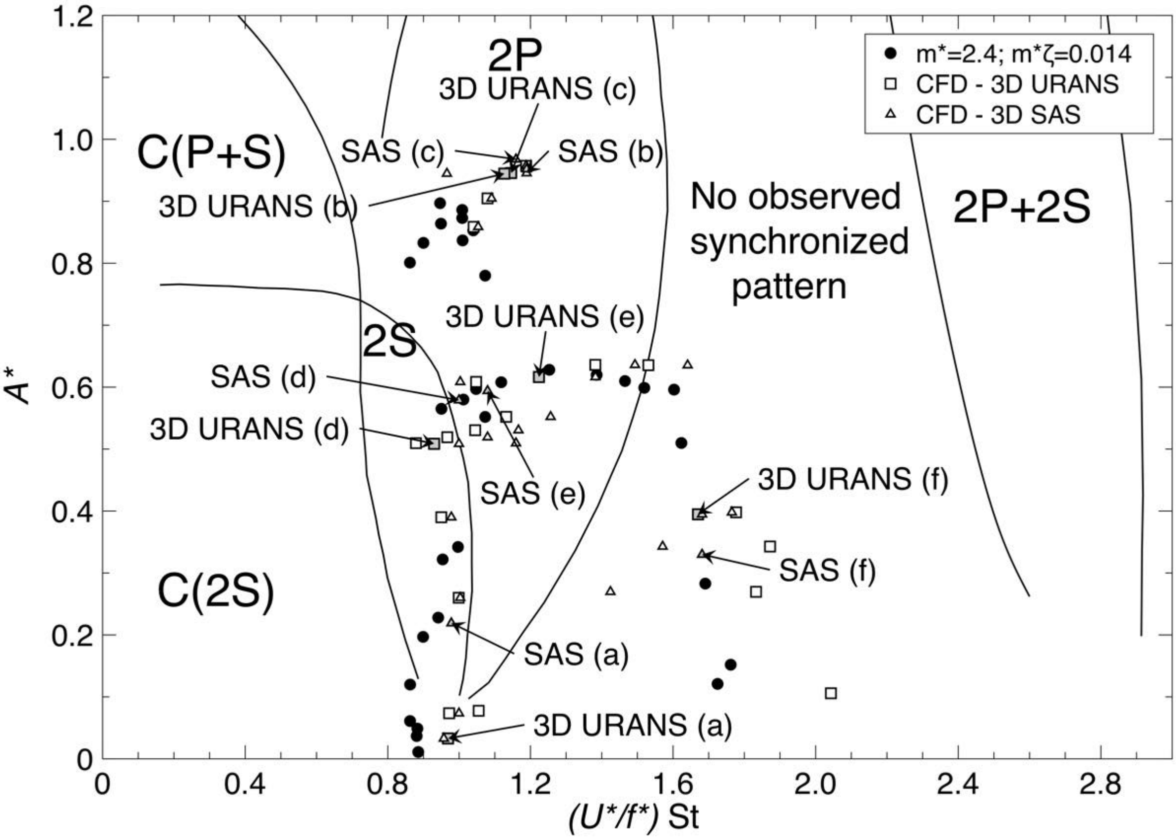

Figure 2.29: After Williamson and Govardhan [9]. Amplitude response is plotted against the "true" normalised velocity (U^*/f^*)St of all CFD cases plotted in the Williamson-Roshko (1988) map of the vortex shedding modes. The grey points refer to Fig. 2.28 for the SAS cases and Fig. 2.14 for the 3D URANS cases.

2.5.6 Computational cost

To compare different models also in terms of computational efficiency, all the simulations are performed in the same workstation with 120 cores divided in 6 different nodes. The workstation is the same used in the previous study a Tier-1 Linux Cluster (Intel(R) Xeon(R) CPU E5-2680 v2) (see the subsection 2.3.5 for a complete description).
It should be emphasised that all the simulations used the same computational grids, the same boundary and initial conditions and the iteration in every time step ensured convergence; thus, the model efficiency just depends on the solving speed of the turbulent equations.
The computational efficiency of the 3D URANS and SAS methods is shown in Fig. 2.30 for the case of $U^* = 7.5$, in which the simulated time is in seconds while the transverse axis is the clock time in seconds. As shown, the relations between the simulated time and clock time appear to be oblique lines with different slopes. The efficiency of SAS appears very close to 3D URANS during the first part of the simulated time, this means that the computational cost of the initial transitory is equivalent for the two methods. As the solution becomes periodic, the work mechanism using the additional source term Q_{SAS} in SST-SAS is more complex than that only using the original $k - \omega$ SST formulation, which means the SAS equations are more expensive to be solved. It should be noted that the Speedup of the 3D URANS metod, as shown in Fig. 2.30, is linked to the stability of the simulation itself, in fact having used the dynamically adjustable stepping technique, the URANS method as the solution becomes periodic a higher time step is automatically selected, keeping the Courant number less than 0.9.
However, the increase in computational cost seems to be low, compared to a considerable improvement in the numerical results.

2.5.7 Conclusions

In this section the advanced SAS model is briefly introduced and tested for the selected VIV case. The results have been successfully compared with the experimental data and with the 3D URANS simulations, presented in the section 2.3.
From the analysis of the results, it can be argues that the SAS models are able to capture finer turbulent structures than 3D URANS. This improved flow resolution leads to a better prediction of the amplitude response in the region where the three-dimensional effect is higher. In the other regions the results of 3D URANS and the SAS are very close. The more advanced SAS model confirms that in the lower branch region the effects of three dimensionality disappear. The increase of computational cost of SAS model compared to the 3D URANS are almost negligible.

In the next section the study of different initial conditions will be considered in order to investigate on the sensibility of the CFD simulation on the hysteresis and/or intermittent effect in the transition zones. In particular the value of the incident flow velocity will be increased or decreased until the final velocity will be reached.

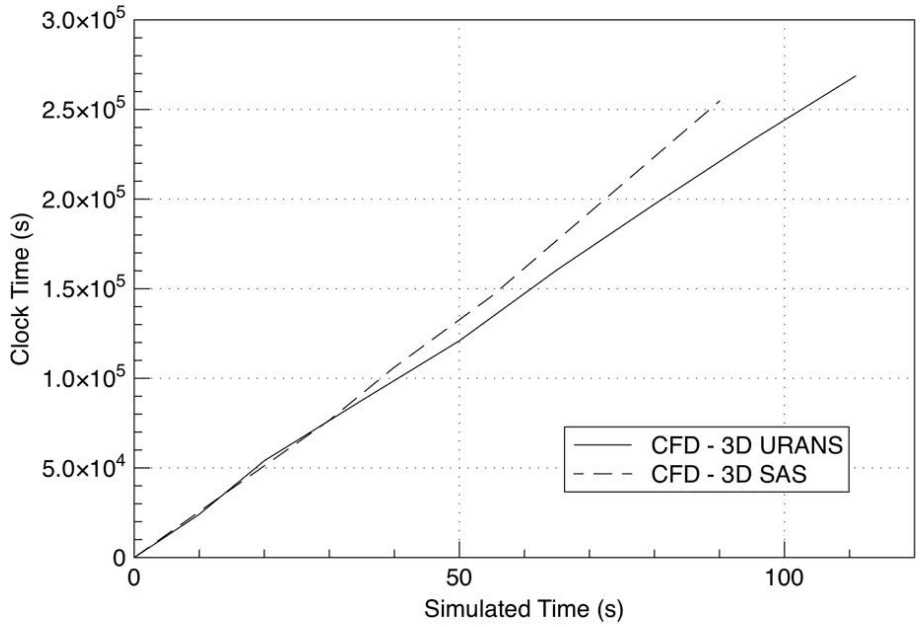

Figure 2.30: Computational efficiency of 3D URANS and SAS simulations.

2.6 Different initial condition

It is of particular interest to investigate the manner in which a vibrating cylinder can transition between one mode of response to another. This transition is instigated here with two different initial conditions.

i) The first condition is called *increasing velocity* that is to say with the cylinder still oscillating at the selected U^*_{START}, the inflow velocity is increased until the final $U^*_{FINAL} > U^*_{START}$ is reached.

ii) The second condition is called *decreasing velocity* that is to say with the cylinder still oscillating at the selected U^*_{START}, the inflow velocity is decreased until the final $U^*_{FINAL} < U^*_{START}$ is reached.

All the computation has been initialised with a fully developed solution at each selected starting point U^*_{START}. The increment or decrement of the inflow velocity are carried out in order to have a variation of 0.125 U^* every 30 seconds of simulated time. The sampling of the results is instead done every 30 seconds of simulated time in order to sample the possible variations of the solution in detail.
This numerical investigation has been carried out for both transitions: from initial to upper and from upper to lower. The simulations are carried out with the same numerical models and same computational grid already presented in this chapter. In particular for the 2D URANS simulation the mesh "2D NEW" is selected while for the three-dimensional cases, 3D URANS and SAS, the mesh "3D NEW" is used.

2.6.1 Transition from initial to lower branch

Here we focus on the transition from the initial excitation branch to the upper branch. The selected starting velocity for the increasing condition is $U^*_{START} = 2.5$ while for the decreasing condition $U^*_{START} = 5$. The final velocity for the increasing condition is $U^*_{FINAL} = 5$ while for the decreasing condition $U^*_{FINAL} = 2.5$, these values are reached after 600 seconds of simulated time.

2D URANS

In this subsection the results obtained from the 2D URANS simulations are summarised. Fig. 2.31 shows the variation of normalized maximum amplitude of transverse oscillation with U^*. From the response amplitude data, we find only a small presence of hysteresis. In general, the decreasing velocity condition follows the trend of the results from rest. The drop down to the initial excitation regime occurs close to $U^* = 4.6$ for the decreasing velocity condition, while the jump from the upper branch occurs at $U^* = 4.75$ for the increasing velocity condition. The quasi-periodic regime (QP) is evident from the value $U^* = 3.75$ to $U^* = 4.75$. In this region the increasing velocity condition over-predicts the experimental data. In the form $U^* = 2.5$ to $U^* = 3.75$ an over-prediction of the amplitude data is present for both conditions.

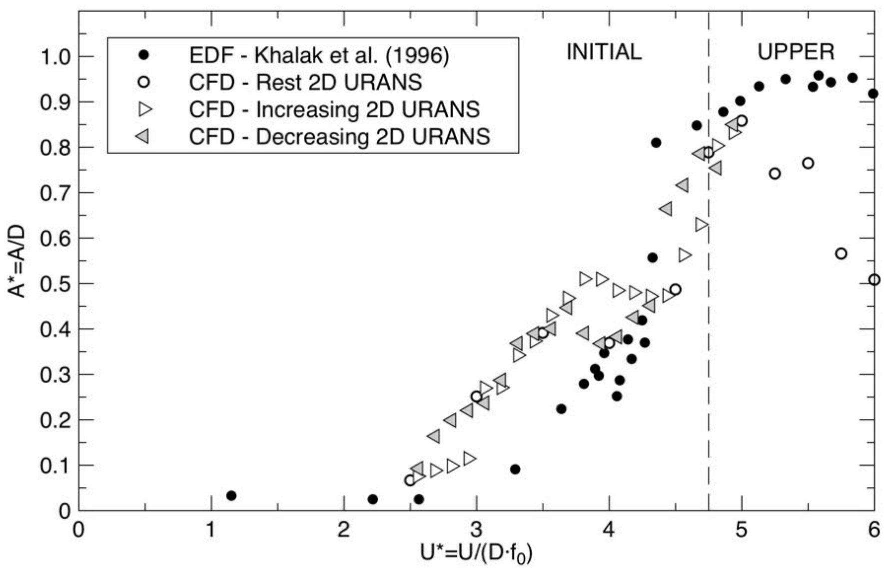

Figure 2.31: Amplitude ratio A^* Vs reduced velocity U^*. Comparison between experimental data by Khalak and Williamson [15] (solid circles), present 2D CFD results from rest (empty circles), increasing velocity (empty right triangles) and decreasing velocity (grey left triangles).

Fig. 2.32 shows the variation of frequency ratio f^* with U^*. The two different initial conditions are presented in two separate plots, Fig. 2.32(a) and Fig. 2.32(b) for increasing and decreasing velocity condition respectively, in order to show the two distinct peaks of displacement spectra. As the velocity U^* is increased, the frequency changes as follows. In the quasi-periodic initial branch, the spectra of displacement shows two distinct peaks, one corresponding to the vortex shedding frequency of nonoscillanting body f_St (Strouhal frequency), and one corresponding to the natural frequency f_0. As as one entries in the upper branch region $U^* = 4.75$ only a single value of frequency is found, which is f_St. For decreasing U^* the same cylinder dynamic, in terms of oscillation frequencies, of the increasing conditions is found.

Interestingly, the phase lag between the motion of the cylinder and the forcing term is analysed. Fig. 2.33 shows the non-dimensional time domain vortex shedding force C_{VS} and the non-dimensional total force C_L as function of the reduced velocity U^*. In the same figure is also shown the non-dimensional cylinder displacement $y(t)/D$ as function of the reduced velocity U^*. The bottom plot of Fig. 2.33 shows the phase lag ϕ and ϕ_{VS} as function of U^* computed using the Hilbert transform. From the Fig. 2.33 it can be observed how the QP regime, where the phase "slips" periodically through 360°, starts and finishes in two different locations for the two different initial conditions. For the increasing velocity condition the QP regime is identified between $3.1 < U^* < 3.85$, while for the decreasing is sifted to lower value of U^* ($2.75 < U^* < 3.75$). After the QP regime the phase angle ϕ and ϕ_{VS} remains close to 0°, for this reason this region is denoted as "periodic" (P). As the value of the reduced velocity reaches 4.75, for increasing condition, or 4.6, for decreasing condition, the jump of the ϕ_{VS} occurs corresponding to the start of the upper branch.

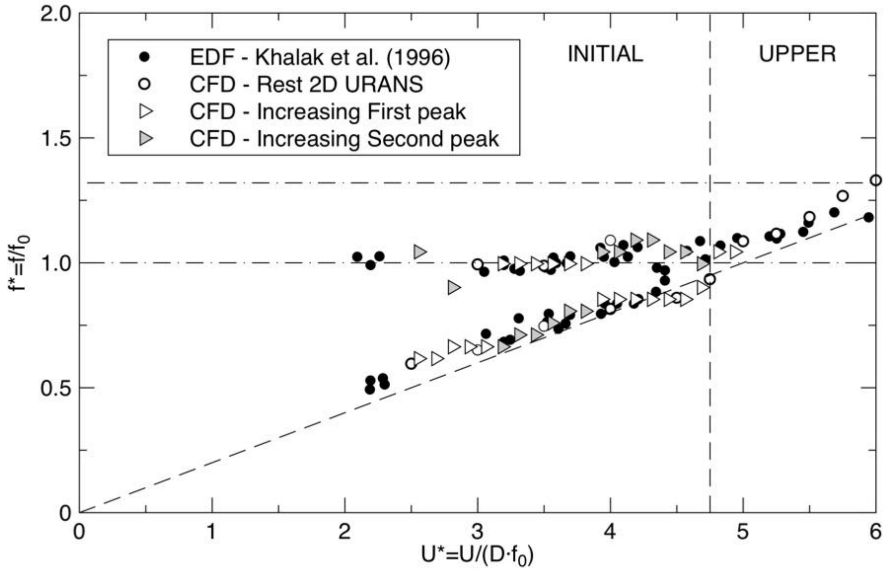

(a) Increasing velocity.

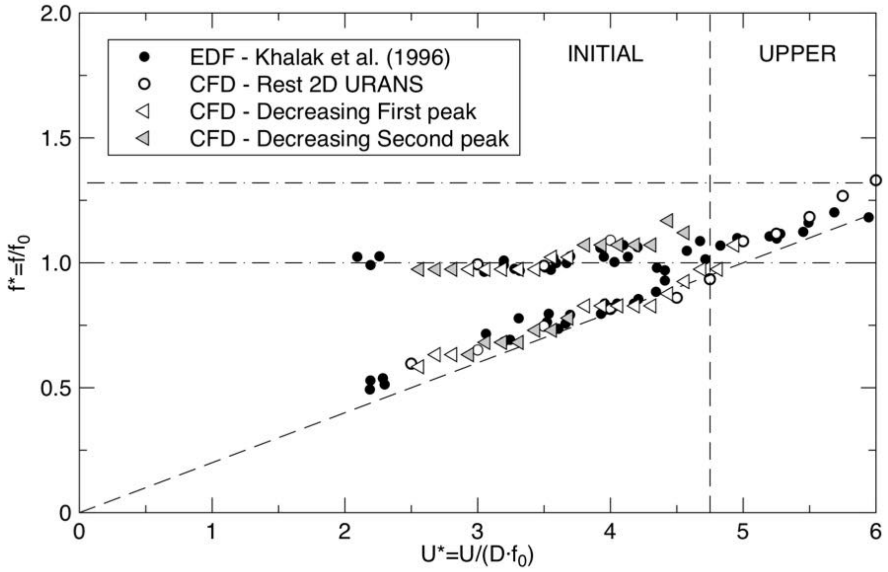

(b) Decreasing velocity.

Figure 2.32: Frequency ratio f^*Vs reduced velocity U^*. Comparison between experimental data by Khalak and Williamson [15] (solid circles), present 2D CFD results (empty circles) and present first peak (empty triangles) and second peak of displacement spectra (grey triangles). The oblique dashed line corresponds to the Strouhal frequency.

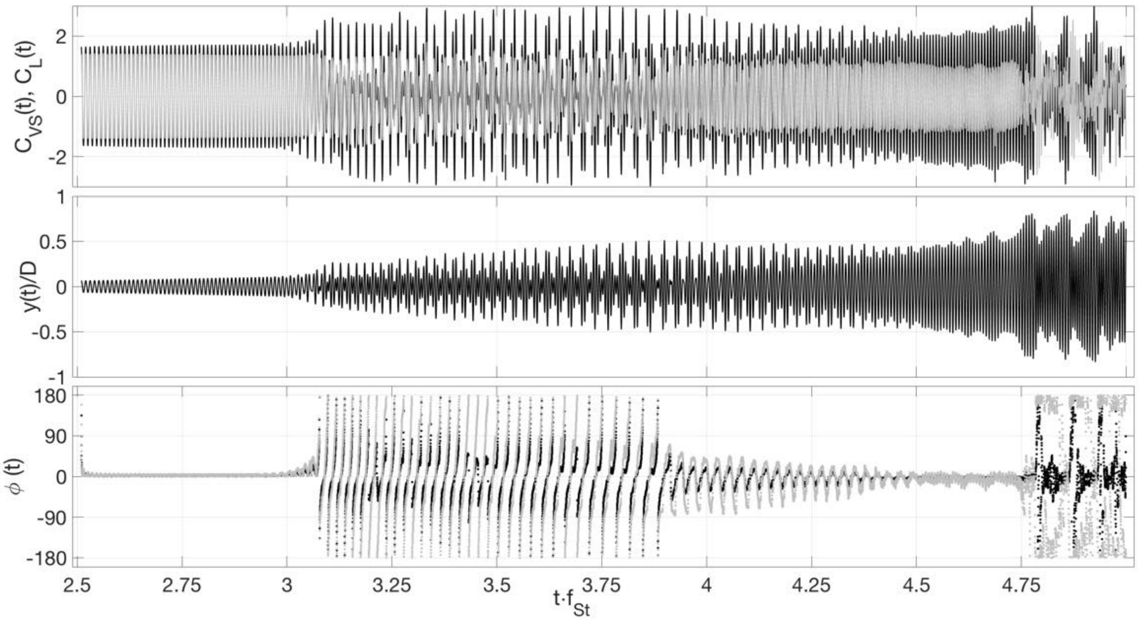

(a) 2D URANS, Increasing velocity.

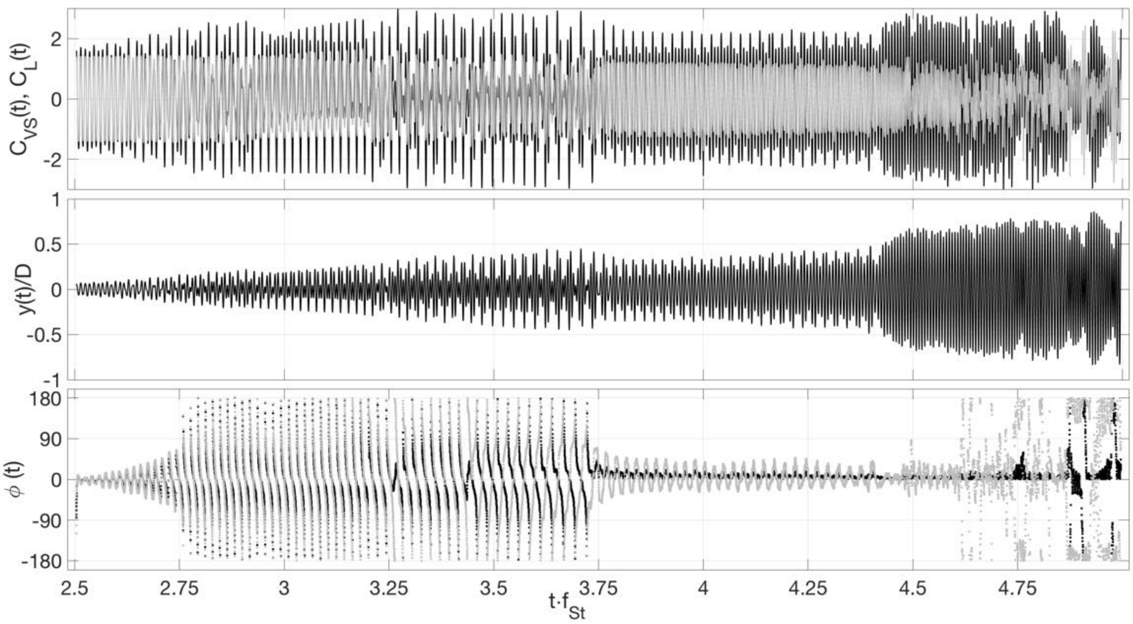

(b) 2D URANS, Decreasing velocity.

Figure 2.33: First plot: non-dimensional total $C_L(t)$ (black line) and vortex shedding force $C_{VS}(t)$ (grey line). Middle plot: time series of the non-dimensional cylinder motion . Lower plot: phase angle ϕ between the non-dimensional total force C_L and the non-dimensional cylinder displacement $y(t)/D$ (black points) and phase angle ϕ_{VS} between the non-dimensional vortex shedding force C_{VS} and the non-dimensional cylinder displacement $y(t)/D$ (grey points).

3D URANS

In this subsection the results obtained from the 2D URANS simulations are summarised. Fig. 2.34 shows the variation of normalized maximum amplitude of transverse oscillation with U^*. As for the 2D case we have found an hysteresys between the initial branch to the upper branch, as evidence from the response amplitude data. The decreasing condition well agrees with the experimental data for all the interested reduced velocity reactions, except in the range of U^* from 3 to 3.5 where an over-prediction of the amplitude data has been found. For the increasing velocity condition the over-prediction of the amplitude data is shifted into the QP region. This result is in agreement with the 2D results.

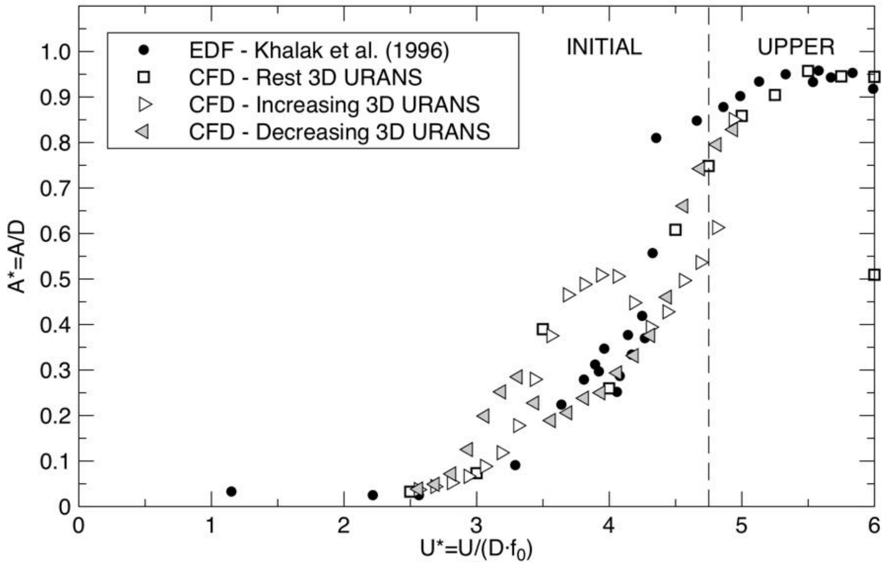

Figure 2.34: Amplitude ratio A^* Vs reduced velocity U^*. Comparison between experimental data by Khalak and Williamson [15] (solid circles), present 3D URANS results from rest (empty squares), increasing velocity (empty right triangles) and decreasing velocity (grey left triangles).

Fig. 2.35 shows the variation of frequency ratio f^* with U^* for the two simulated different initial conditions, Fig. 2.35(a) and Fig. 2.35(b) for increasing and decreasing velocity condition respectively. In the initial branch region the results in terms of frequency ratio f^* correspond with those found in the 2D URANS case, the only difference has been found for values less than $U^* < 3$ where only a single value of frequency is found. In the upper branch region the frequency ratio follows the trend of the rest of the initial condition results where the oscillation frequency corresponds to the natural frequency f_0.

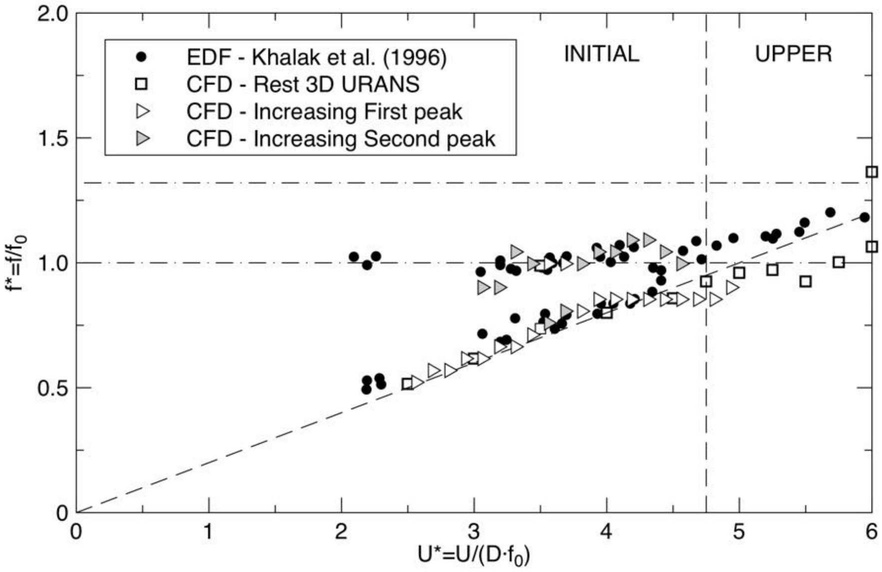

(a) Increasing velocity.

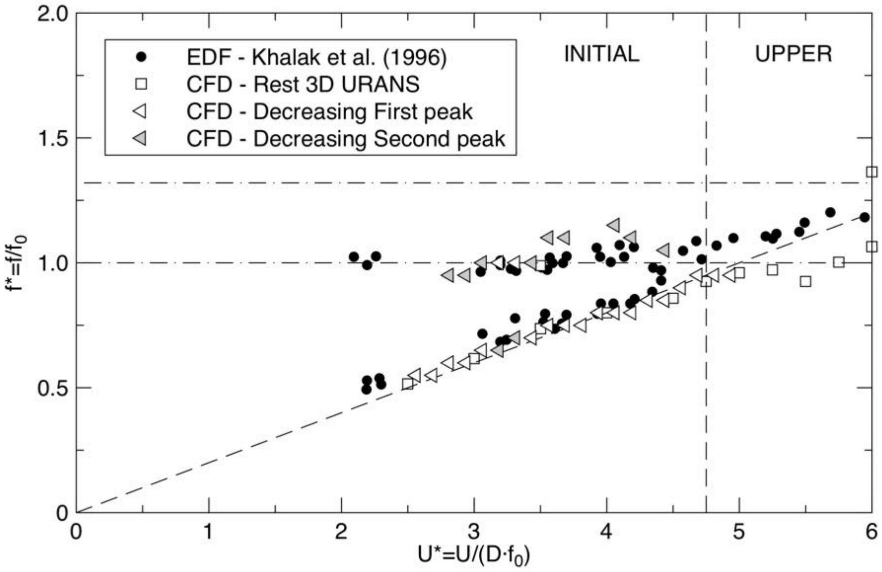

(b) Decreasing velocity.

Figure 2.35: Frequency ratio f^* Vs reduced velocity U^*. Comparison between experimental data by Khalak and Williamson [15] (solid circles), present 3D URANS results (empty squares) and present first peak (empty triangles) and second peak of displacement spectra (grey triangles). The oblique dashed line corresponds to the Strouhal frequency.

From the analysis of the time domain non dimensional forces (C_L and $C_{VS}(t)$), cylinder displacement ($y(t)/D$) and phase angles (ϕ and ϕ_{VS}) for increasing (Fig. 2.36(a)) and decreasing velocity (Fig. 2.36(b)) conditions it can be noted that, as for the 2D URANS, the QP region is shifted between the two different initial conditions. Compared to the 2D case, the range of reduced velocity in which the QP occurs is considerably reduced. The beginning of the upper branch region is marked by the variation of phase angle ϕ_{VS}. This happens for $U^* = 5$ in the case of increasing velocity and for $U^* = 4.75$ for decreasing velocity.

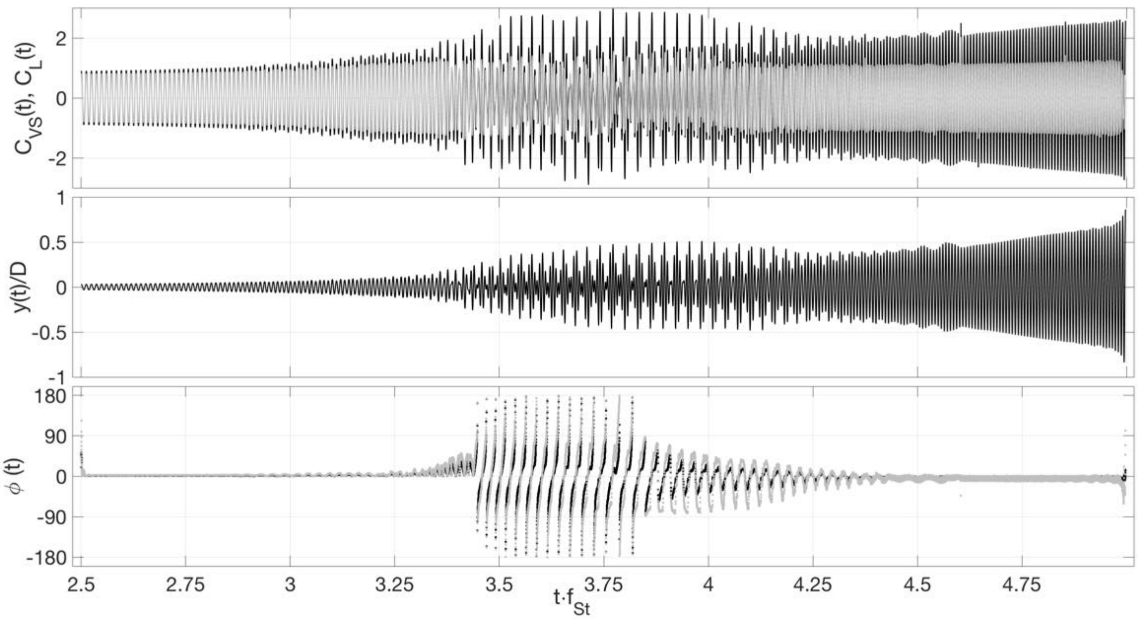

(a) 3D URANS, Increasing velocity.

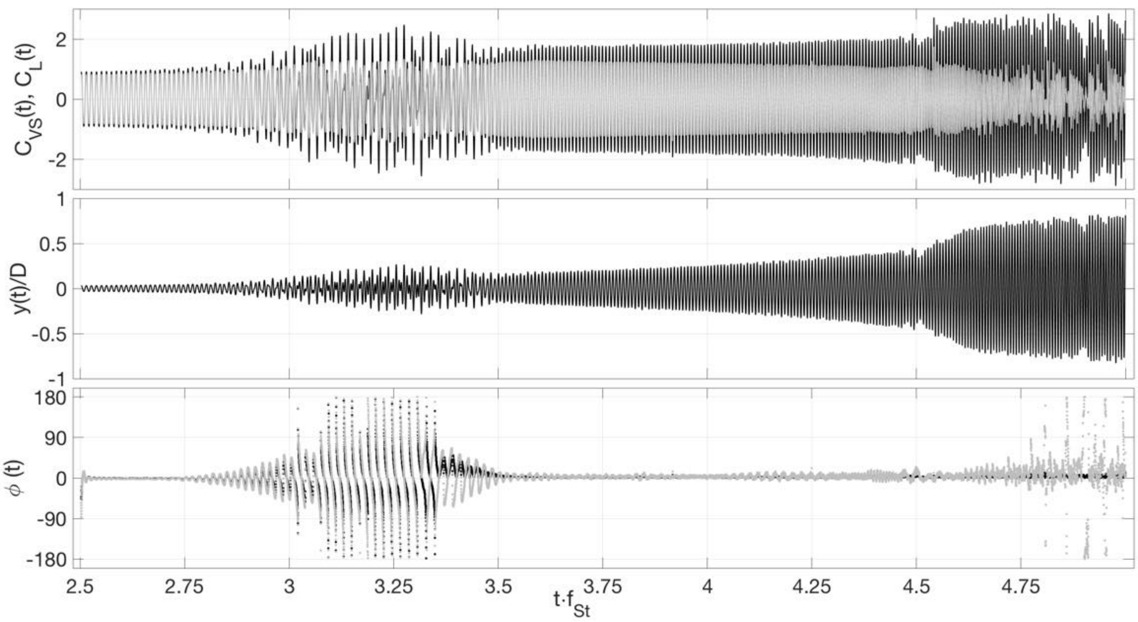

(b) 3D URANS, Decreasing velocity.

Figure 2.36: First plot: non-dimensional total $C_L(t)$ (black line) and vortex shedding force $C_{VS}(t)$ (grey line). Middle plot: time series of the non-dimensional cylinder motion . Lower plot: phase angle ϕ between the non-dimensional total force C_L and the non-dimensional cylinder displacement $y(t)/D$ (black points) and phase angle ϕ_{VS} between the non-dimensional vortex shedding force C_{VS} and the non-dimensional cylinder displacement $y(t)/D$ (grey points).

3D SAS

In this subsection the results obtained from the 2D URANS simulations are summarised. Fig. 2.37 shows the variation of normalised maximum amplitude of transverse oscillation with U^*. The results obtained from the SAS model are still closer to the measurements. Only a small hysteretic behaviour has been found in the QP region, while in the transition from initial to upper branch the hysteresis region is absent.
From the results of the frequency ratio, presented in Fig. 2.38, we can see how both for the increasing and for the decreasing initial condition the dominant frequency peak is the one corresponding to the vortex shedding frequency of non-oscillating body (f_{St}). Moreover for the case with decreasing U^* the beats are not observed in the time histories of cylinder response and fluid forces within the initial branch (fig. 2.39(b)). Looking at the time histories of cylinder response and fluid forces plotted against U^*, it can be concluded that the SAS model is the most sensitive, as far as the oscillation frequency is concerned, to the initial conditions.

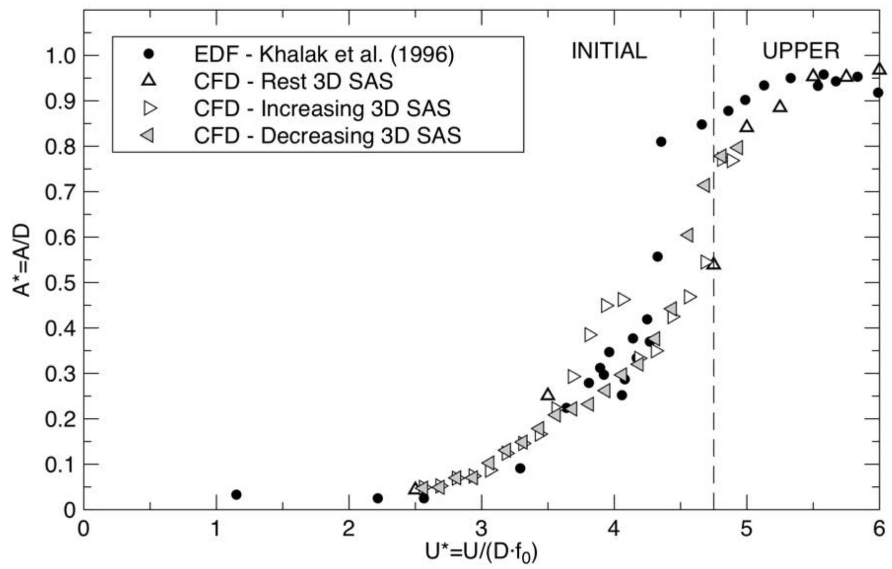

Figure 2.37: Amplitude ratio A^* Vs reduced velocity U^*. Comparison between experimental data by Khalak and Williamson [15] (solid circles), present SAS CFD results from rest (empty upside triangles), increasing velocity (empty right triangles) and decreasing velocity (grey left triangles).

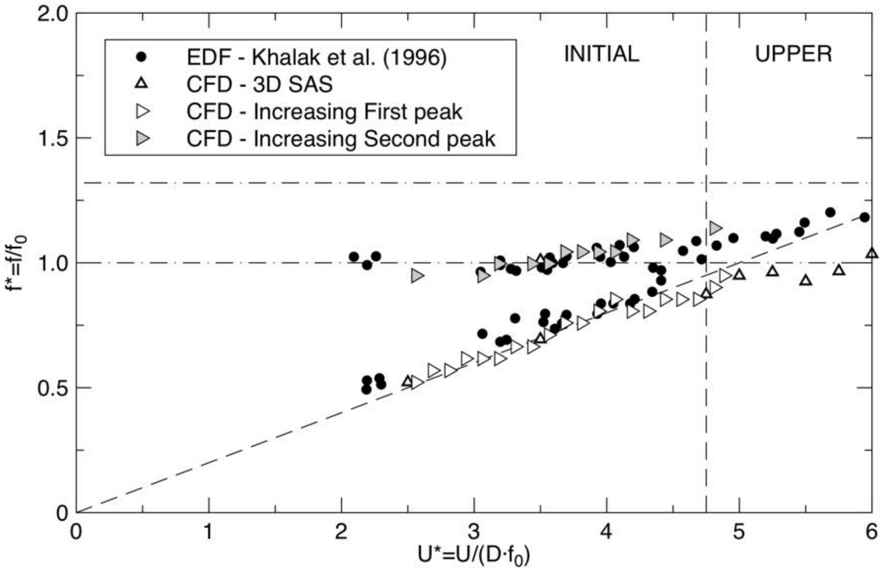

(a) Increasing velocity.

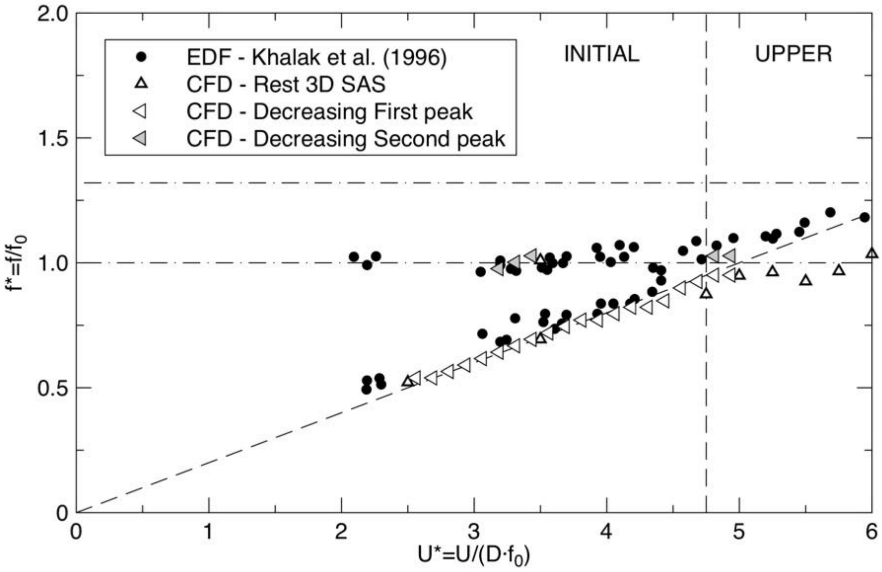

(b) Decreasing velocity.

Figure 2.38: Frequency ratio f^* Vs reduced velocity U^*. Comparison between experimental data by Khalak and Williamson [15] (solid circles), present SAS results (empty upside triangles) and present first peak (empty triangles) and second peak of displacement spectra (grey triangles). The oblique dashed line corresponds to the Strouhal frequency.

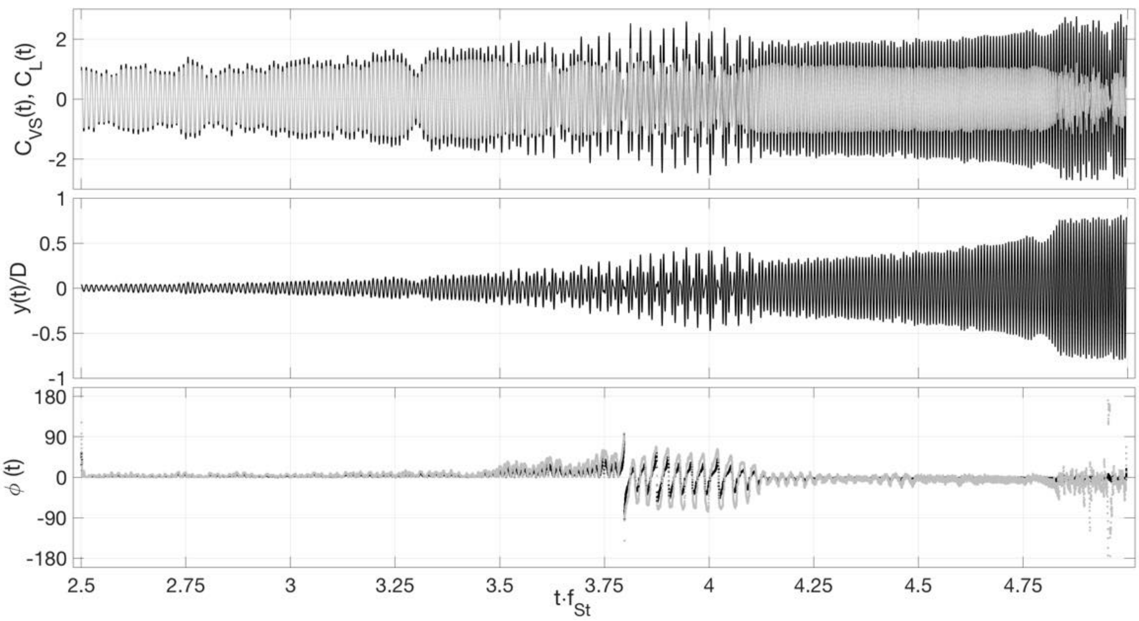

(a) SAS, Increasing velocity.

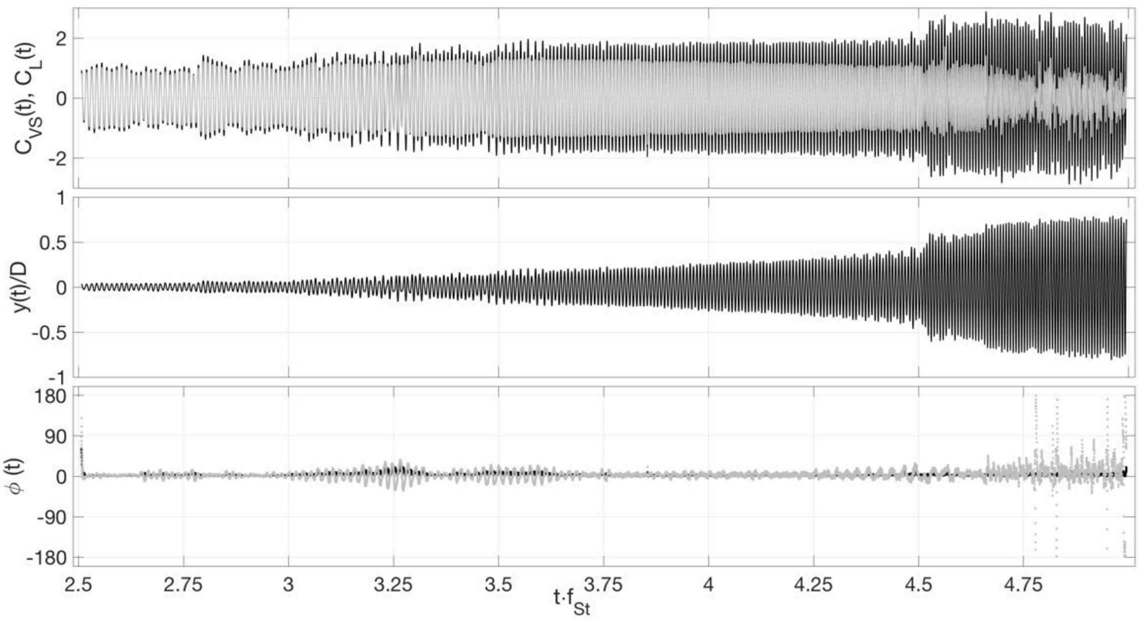

(b) SAS, Decreasing velocity.

Figure 2.39: First plot: non-dimensional total $C_L(t)$ (black line) and vortex shedding force $C_{VS}(t)$ (grey line). Middle plot: time series of the non-dimensional cylinder motion. Lower plot: phase angle ϕ between the non-dimensional total force C_L and the non-dimensional cylinder displacement $y(t)/D$ (black points) and phase angle ϕ_{VS} between the non-dimensional vortex shedding force C_{VS} and the non-dimensional cylinder displacement $y(t)/D$ (grey points).

2.6.2 Transition from upper to lower branch

Here we focus on the second transition from lower branch to the upper branch. For the 2D URANS cases the selected starting velocity for the increasing condition is $U^*_{START} = 4.5$ while for the decreasing condition $U^*_{START} = 7$. The final velocity for the increasing condition is $U^*_{FINAL} = 7$ while for the decreasing condition $U^*_{FINAL} = 4.5$, these values are reached after 600 seconds of simulated time.
For the 3D cases the selected starting velocity for the increasing condition is $U^*_{START} = 5.75$ while for the decreasing condition $U^*_{START} = 7$. The final velocity for the increasing condition is $U^*_{FINAL} = 7$ while for the decreasing condition $U^*_{FINAL} = 5.25$, these values are reached after 300 seconds of simulated time for the increasing velocity condition and in 420 seconds for the decreasing condition.

2D URANS

In this subsection the results obtained from the 2D URANS simulations in the transition region between the upper and lower branch are here summarised. The non-dimensional amplitude of the motion of the cylinder A^* and the non-dimensional dominant frequency of the motion f^* are shown in Fig. 2.40. Khalack and Williason [5], from the results of their measurements, defined this mode transition as intermittent. In this region the system switches between the upper and the lower branch intermittently. In the intermittent region the system seems only weekly "locked" into one or another mode.
From the 2D URANS results the intermittent zone is not captured at all. When maximum amplitude values are reached a drop of the amplitude value occurs. Both the two initial conditioned tested follow the trend of the results obtained in the conditions from rest. The f^* values found with the two initial conditions tested are comparable except at the beginning of the upper branch where in the increasing condition they are locked-in with the natural frequency in water.
What is of great interest is to understand what occurs when you have the phase jump of C_L and C_{VS}. Considering the Fig. 2.41 where the time domain non dimensional forces ($C_L(t)$ and $C_{VS}(t)$), cylinder displacement ($y(t)/D$) and phase angles (ϕ and ϕ_{VS}) are shown as a function of U^*. It is shown that the vortex shedding jump ϕ_{VS} is associated with the change from the initial excitation regime to the upper branch, while the total phase jump ϕ is associated with the drop from the upper to the lower branch. This behaviour is perfectly found in 2D URANS simulations. For the increasing condition the jump of ϕ_{VS} occurs at $U^* \approx 5.125$, the jump of ϕ occurs $U^* \approx 5.85$. For the decreasing condition the jump of ϕ_{VS} occurs at $U^* \approx 4.75$, the jump of ϕ occurs $U^* \approx 5.6$. The different jump of ϕ_{VS} for the two different conditions is a consequence of the hysteretic nature of the transition mode from the initial to the upper branch. The different U^* at which the transition from the upper to the lower occurs (denoted by the jump of ϕ) shows that an hysteretic response is also present in this second transition. With a careful comparison of the frequency condition (Fig. 2.40(b)) and the phase jump it can be noted that the ϕ jump is associated with the change of the oscillation frequency from the value

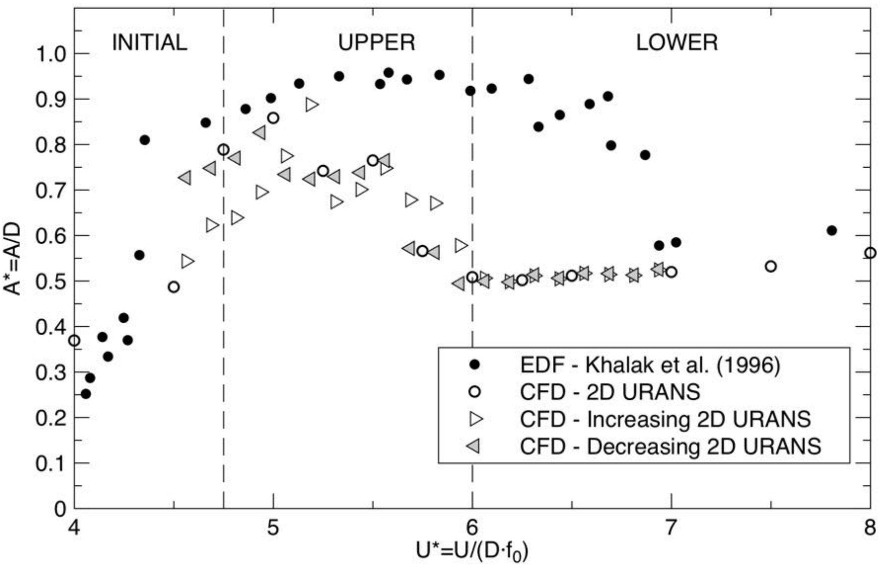

(a) Amplitude ratio A^* reduced velocity U^*

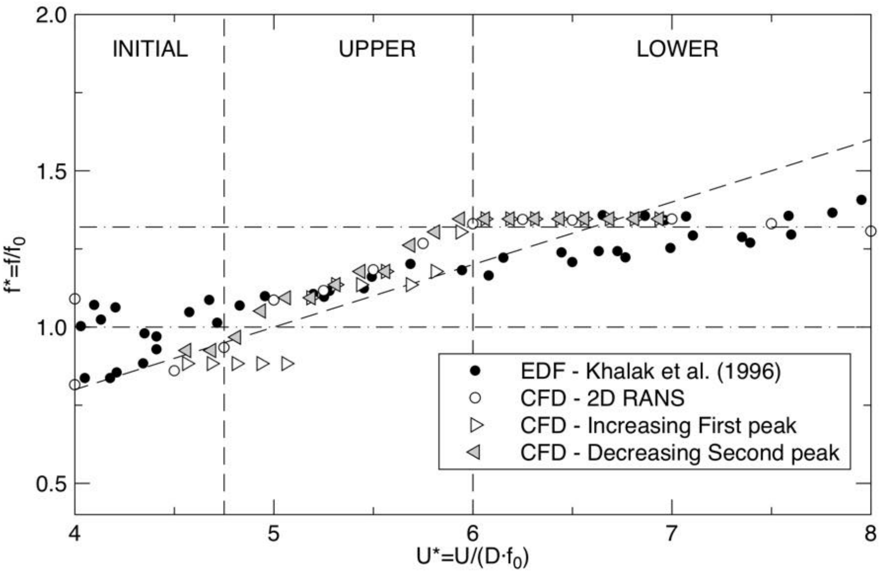

(b) Frequency ratio f^* Vs reduced velocity U^*

Figure 2.40: Comparison between experimental data by Khalak and Williamson [15] (solid circles), present 2D CFD results from rest (empty circles), increasing velocity (empty right triangles) and decreasing velocity (grey left triangles). The oblique dashed line in (b) corresponds to the Strouhal frequency (St = 0.20).

corresponding to the Strouhal frequency to the synchronisation frequency.

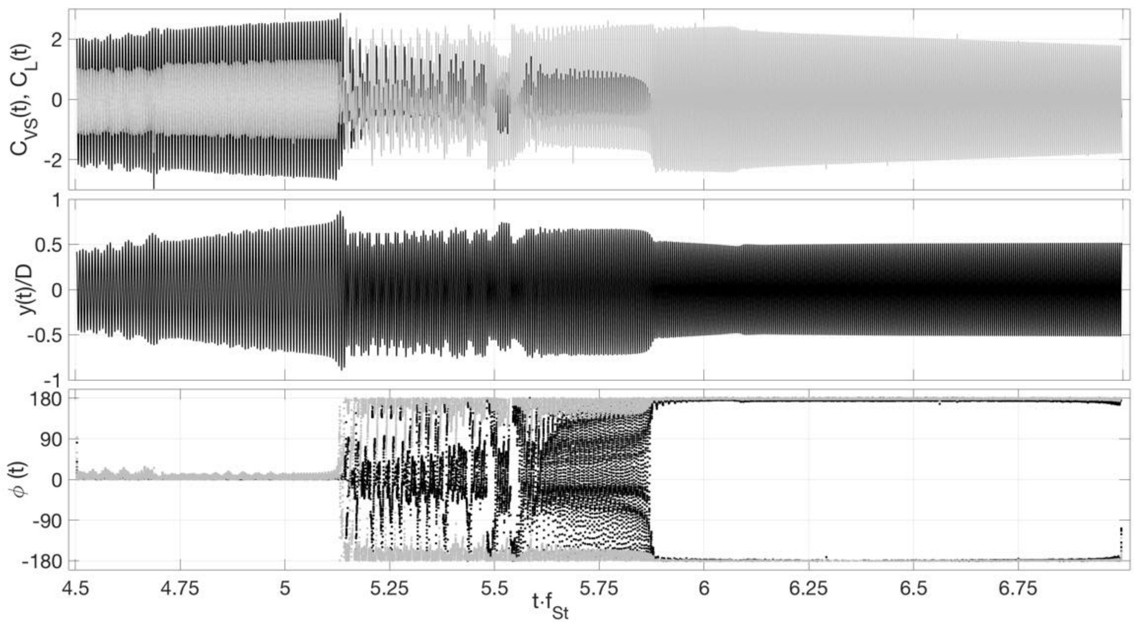

(a) 2D URANS, Increasing velocity.

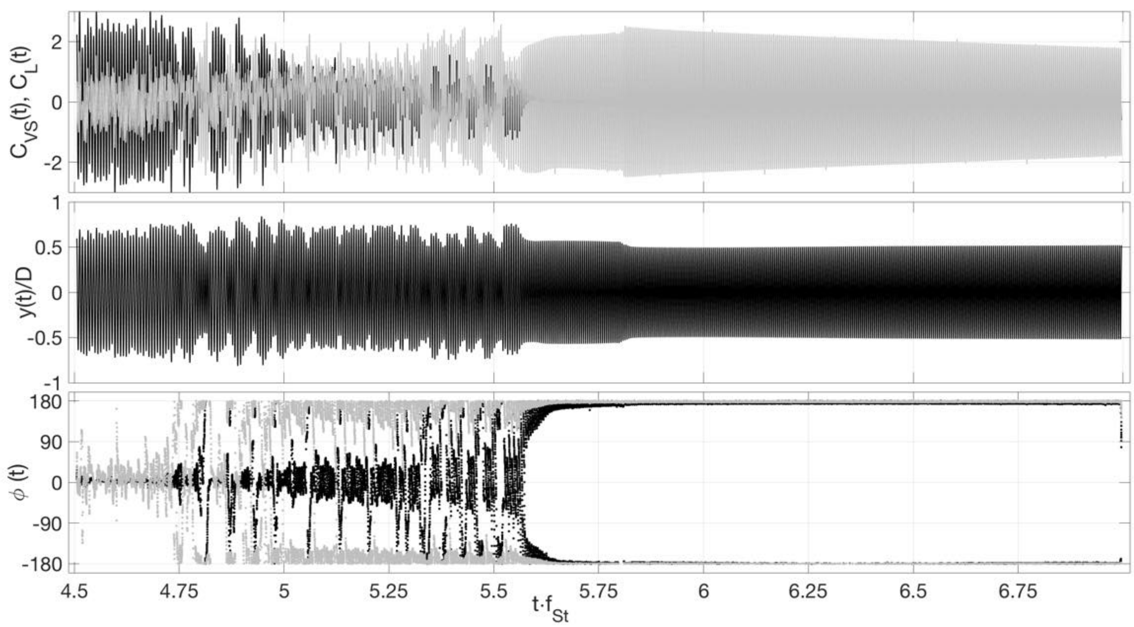

(b) 2D URANS, Decreasing velocity.

Figure 2.41: First plot: non-dimensional total $C_L(t)$ (black line) and vortex shedding force $C_{VS}(t)$ (grey line). Middle plot: time series of the non-dimensional cylinder motion. Lower plot: phase angle ϕ between the non-dimensional total force C_L and the non-dimensional cylinder displacement $y(t)/D$ (black points) and phase angle ϕ_{VS} between the non-dimensional vortex shedding force C_{VS} and the non-dimensional cylinder displacement $y(t)/D$ (grey points).

3D RANS

In this subsection the results obtained from the 3D URANS simulations in the transition region between upper and lower branch are here summarised. The main results relevant here are shown in Fig. 2.42. A hysteretic response is observed for $5.8 < U^* < 6.4$. Computation for increasing U^* the cylinder amplitude response stays in the upper branch for this range of U^*. Unlike for decreasing U^* the cylinder amplitude response stays in the lower branch.
In the present computations, with two different initial condition, the intermittency transition has not been found. However, in the "from rest" computation intermittent behaviour is observed for $U^* = 6$ (Fig. 2.12(f)). This suggests that although the intermittent behaviour is not seen with this new initial condition it could be present in the range identified as hysteretic. Understanding if intermittency is present the range $5.8 < U^* < 6.4$ is one of the future tasks of this research. The idea is to carry out the simulation increasing/decreasing the inflow velocity up to a value of U^* corresponding to the selected range, then the inflow velocity will be kept constant long enough to reach a fully developed unsteady state.

As for the 2D URANS case the total phase jump ϕ occurs when the oscillation frequency reaches the synchronisation frequency, while the vortex shedding jump ϕ_{VS} occurs when the oscillation frequency is equal to the natural frequency in water ($f^* = 1$) (fig. 2.43). In the case of 3D URANS simulations, there is no congruence between the jump of ϕ_{VS} and the transition between the initial and upper branch.

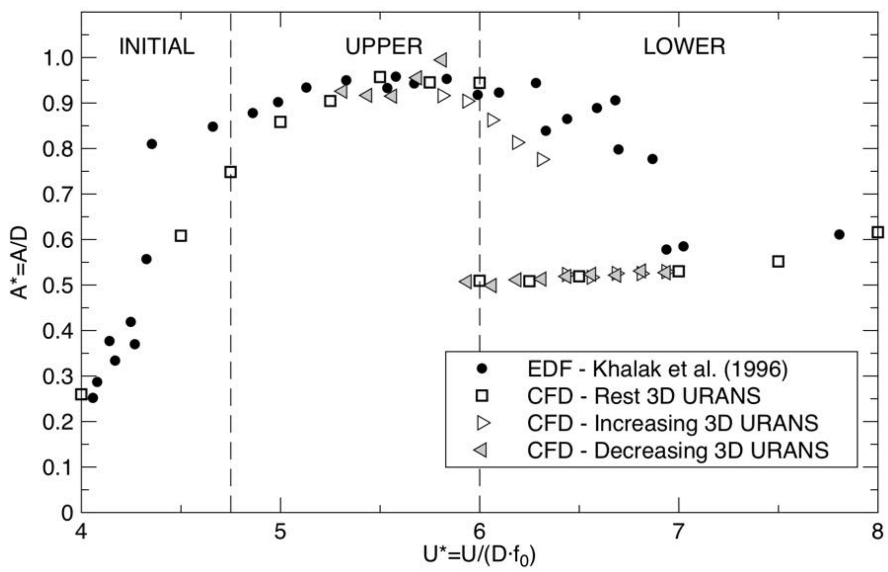

(a) Amplitude ratio A^* Vs reduced velocity U^*

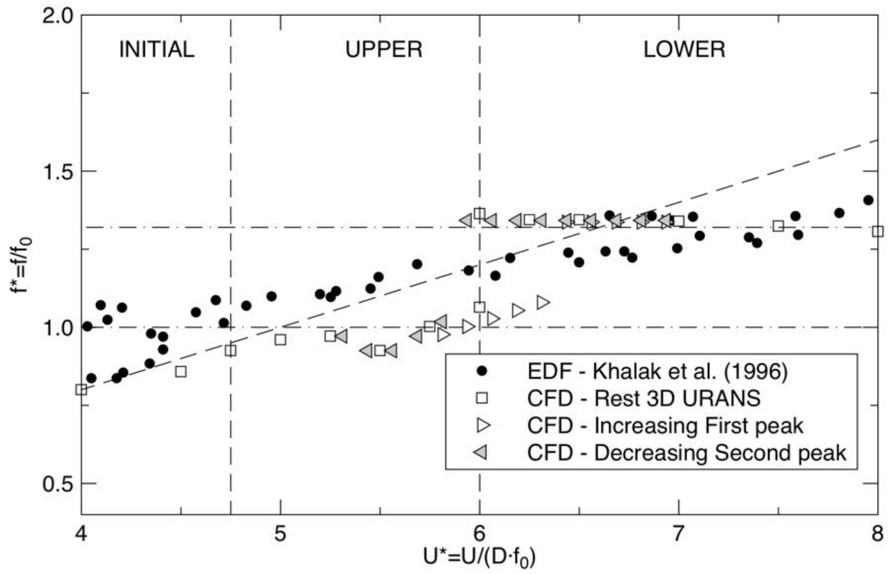

(b) Frequency ratio f^* Vs reduced velocity U^*

Figure 2.42: Comparison between experimental data by Khalak and Williamson [15] (solid circles), present 3D URANS results from rest (empty squares), increasing velocity (empty right triangles) and decreasing velocity (grey left triangles). The oblique dashed line in (b) corresponds to the Strouhal frequency.

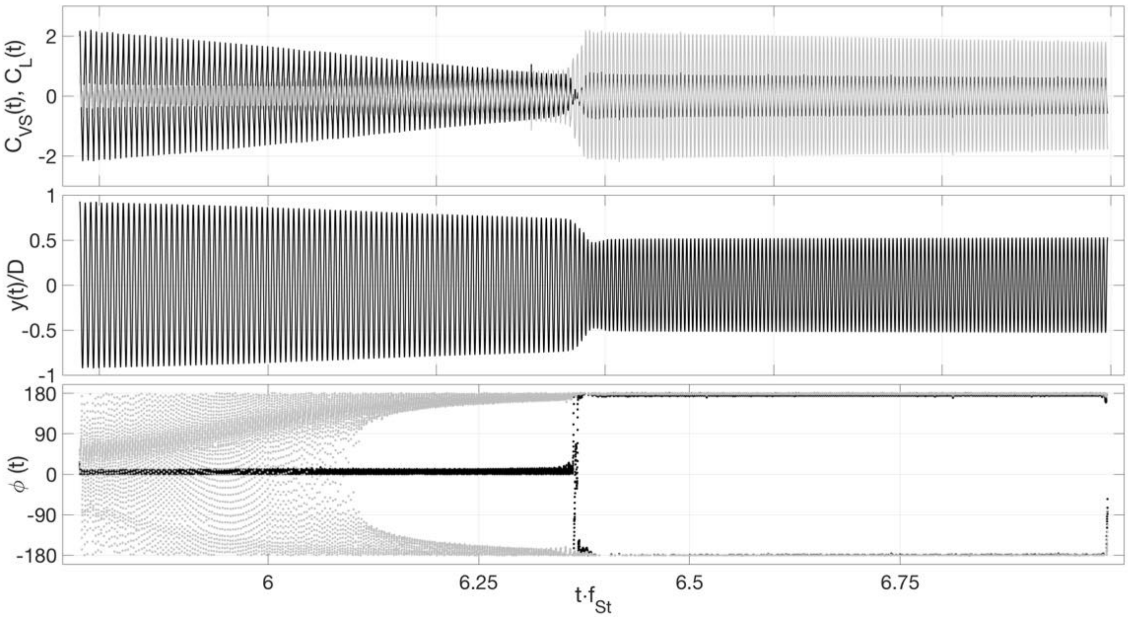

(a) 3D URANS, Increasing velocity.

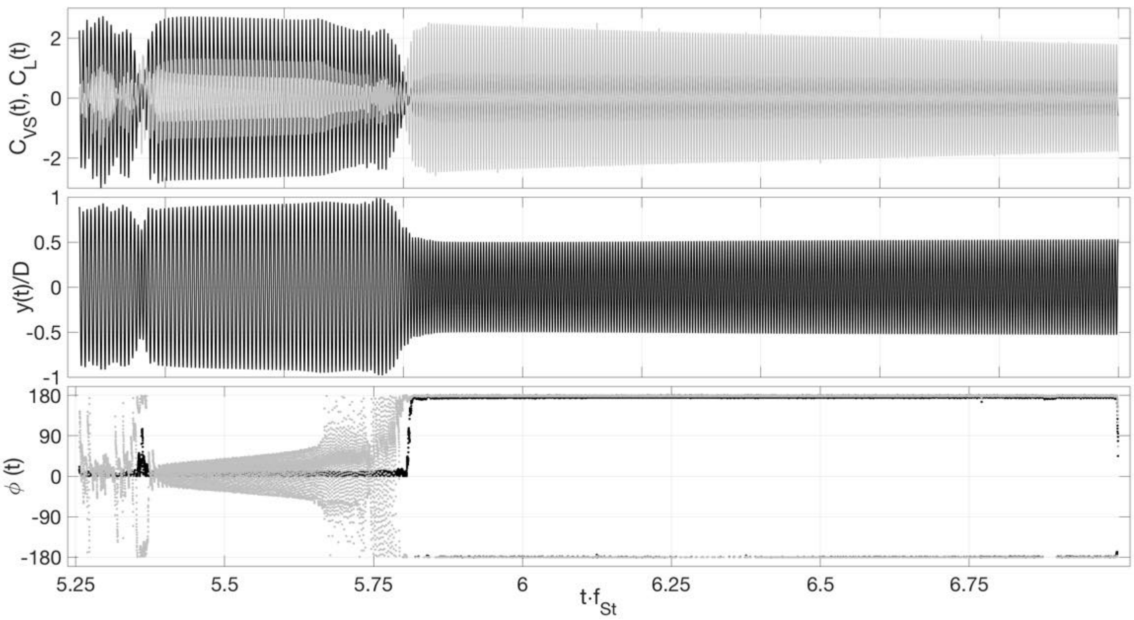

(b) 3D URANS, Decreasing velocity.

Figure 2.43: First plot: non-dimensional total $C_L(t)$ (black line) and vortex shedding force $C_{VS}(t)$ (grey line). Middle plot: time series of the non-dimensional cylinder motion . Lower plot: phase angle ϕ between the non-dimensional total force C_L and the non-dimensional cylinder displacement $y(t)/D$ (black points) and phase angle ϕ_{VS} between the non-dimensional vortex shedding force C_{VS} and the non-dimensional cylinder displacement $y(t)/D$ (grey points).

3D SAS

In this subsection the results obtained from the 3D SAS simulations in the transition region between upper and lower branch are here summarised. Fig. 2.44(a) shows the variation of normalised maximum amplitude A^* of transverse oscillation with U^*. The computation with increasing U^* follows the experimental measurement until the value of $U^* \approx 6.6$ where the transition from the upper to the lower branch occurs. Instead in the computation for the decreasing U^* the cylinder response stays at a value of $A* \approx 0.5$ as the U^* decreases until the transition occurs for a value of $U^* \approx 5.9$. Therefore, as for the 3D URANS case a hysteretic response is observed.
Fig. 2.44(b) shows the variation of frequency ratio f^* with U^*. The hysteresis region is delimited by the variation of the oscillation frequency. In the upper branch region both of the tested initial conditions agree with the results "from rest". In this region the computational results of oscillation frequency stay close to one, unlike the experimentally measured value that follows the frequency Strouhal.

The time domain non dimensional forces (C_L and $C_{VS}(t)$), cylinder displacement ($y(t)/D$) and phase angles (ϕ and ϕ_{VS}) for the SAS model are presented in 2.45. Unlike the 3D case where there is a clear transition from upper to lower region, the SAS simulations shown an oscillatory behaviour before the transition from one branch to another. In particular, for the case of increasing velocity an intermittent switching is shown by applying the Hilbert transform to lift-force displacement data. Indeed, in the region $6.3 < U^* < 6.6$ the total phase ϕ jump between the value 0°, corresponding to the upper branch, to 180° corresponding to the lower branch.

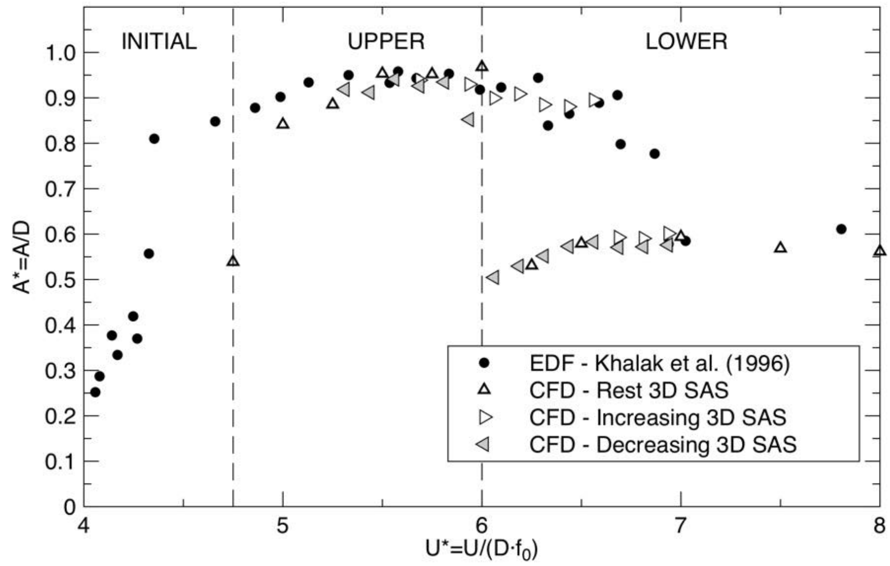

(a) Amplitude ratio A^* Vs reduced velocity U^*

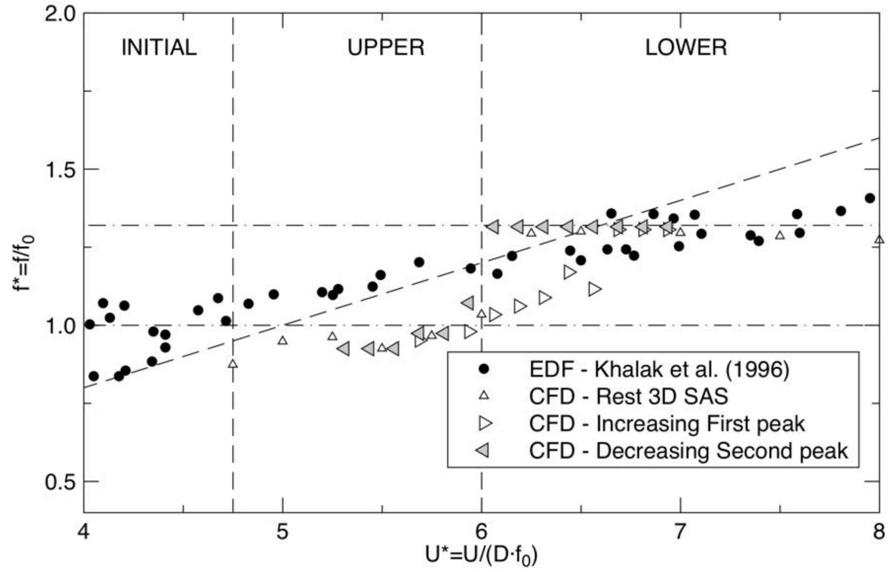

(b) Frequency ratio f^* Vs reduced velocity U^*

Figure 2.44: Comparison between experimental data by Khalak and Williamson [15] (solid circles), present SAS results from rest (empty upside triangles), increasing velocity (empty right triangles) and decreasing velocity (grey left triangles). The oblique dashed line in (b) corresponds to the Strouhal frequency.

2.7 Final remarks

In this section the results obtained by varying the initial conditions of the inflow velocity are presented. In particular, the effect of increasing the reduced velocity U^* as well as its decrease has been studied. To this extent, three different sets of computation have been carried out. These correspond to 2D URANS, 3D URANS and SAS.
As is known the two modes of translation are hysteretic, initial-upper transition, and intermittent, upper-lower transition. The hysteretic nature of the first transition is only captured with the URANS base method, while with the SAS hysteresis is not present. An hysteretic behaviour has been found in the quasi-periodical region for all the three models. Beats are observed in the time histories of the force coefficients and cylinder response in the quasi-periodic region. The frequency ratio marks the jump of the cylinder response from initial to upper branch. From the numerical simulations, it is not fully clear whether the transition between the initial and the upper branch is due to the phase jump ϕ_{VS}, between transverse oscillation and C_{VS}.
The intermittent transition mode from the upper branch to the lower branch is only captured by the SAS simulation with the increasing initial condition. However, all the simulations show an hysteretic region in the transition from upper to lower branch. In order to investigate this particular mode of transition further numerical studies are required. The onset of synchronisation marks the jump of cylinder response from upper to lower. The transition is also marked by the jump of 180° of the phase ϕ, between transverse oscillation and the lift coefficient C_L.

In the numerical studies conducted so far the $k-\omega$ SST model has been selected. This two-equation model contains some semi-empirical coefficients. In order to evaluate the influence of these semi-empirical coefficients, in the next chapter, the relative importance of these parameters on the final results will be quantified. The high number of simulations required by a sensibility analysis of nine independent semi empirical coefficients means that only 2D simulations are viable. From the comparison between the experimental results of Khalak and Willamson and the present numerical studies it can be observed that the simplified bi-dimensional approach can be accepted only in the initial and lower branch regions. Therefore for the following study the simulation will be carried out considering cases only in the lower branch.

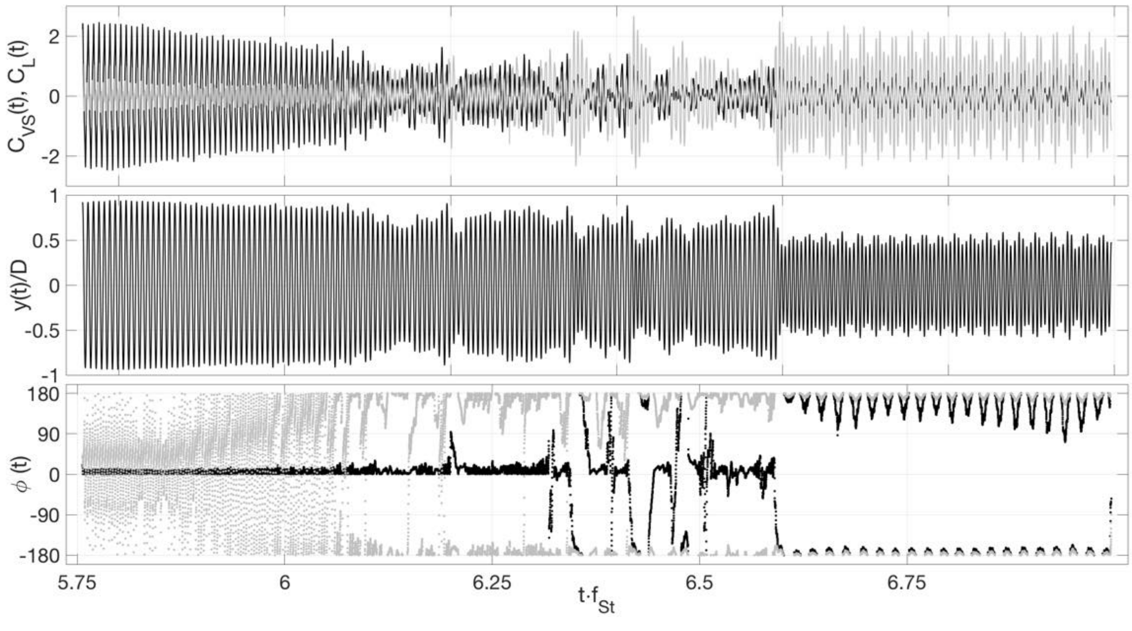

(a) SAS, Increasing velocity.

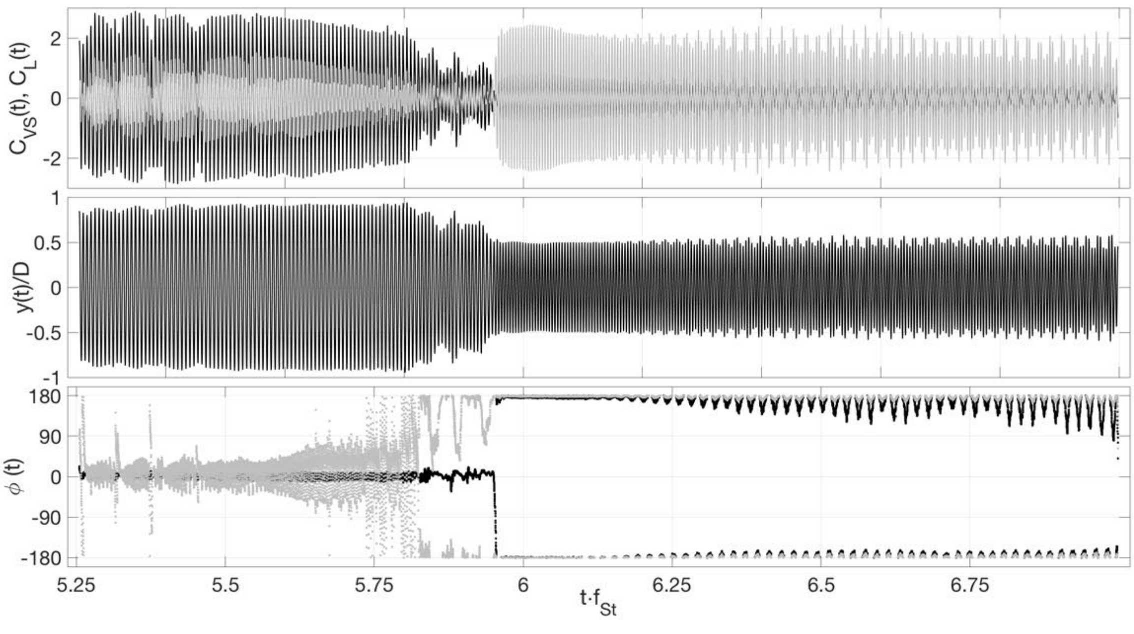

(b) SAS, Decreasing velocity.

Figure 2.45: First plot: non-dimensional total $C_L(t)$ (black line) and vortex shedding force $C_{VS}(t)$ (grey line). Middle plot: time series of the non-dimensional cylinder motion . Lower plot: phase angle ϕ between the non-dimensional total force C_L and the non-dimensional cylinder displacement $y(t)/D$ (black points) and phase angle ϕ_{VS} between the non-dimensional vortex shedding force C_{VS} and the non-dimensional cylinder displacement $y(t)/D$ (grey points).

Chapter 3

Uncertainty quantification and sensitivity analysis of the SST turbulence model applied to VIV

The purpose of this study is to present the results of an Uncertainty Quantification (UQ) for the Menter SST (Shear Stress Transport) turbulence model due to the epistemic uncertainty in closure coefficients applied to the bi-dimensional study of the VIV of an oscillating elastically mounted cylinder.
The objective of the current study is to identify a set of closure coefficients for the Menter SST models that contribute most to the uncertainty in output quantities for the selected VIV case. The knowledge of the values of these particular closure coefficients will reduce the parametric uncertainty in various output quantities of interest obtained by the URANS simulations for different problems including the VIV cases.
In the case of 2D VIV with 1-DOF, the adimensional amplitude A^* and the frequency ratio f^* are considered to be the output quantities of interest. Uncertainty quantification is conducted with DAKOTA/UQ [70] (which is the uncertainty quantification component of DAKOTA (Design Analysis Kit fot OpTimizAtion) version 6.10 [71]) using stochastic expansions based on non-intrusive polynomial chaos. The influence of the closure coefficients on output quantities is assessed using global sensitivity analysis based on variance decomposition.
The Sobol indices are used to rank the contributions of each constant. A comparison of the Sobol indices between the flow cases (obtained changing the inflow velocity) and different degree of polynomial chaos expansion, is conducted. Closure coefficients of interest are identified and compared with the previous uncertainty quantification problems in the hope of aiding modellers in improving the accuracy of the $k-\omega$ SST turbulence model.

3.0.1 The Menter Shear Stress Transport Model as implemented in OpenFOAM

The OpenFOAM (v.2.4) implemented version of the $k-\omega$ SST model is a variant of the original model presented by Menter in 1994 [49]. The OpenFOAM variant considers the improvements proposed by Menter and Esch [50] with the updated coefficients from Menter et al. [72] but with the consistent production terms from the [50] paper [1] and the addition of a new term that considers the rough walls, as proposed by Hollisten [51]. The idea behind the Menter SST model is to combine the different elements of the existing eddy viscosity model that are superior to their alternatives. In particular, the model retains the robust and accurate formulation of the Willcox $k-\omega$ model in the near wall region and takes the advantage of the $k-\varepsilon$ model in the outer part of the the boundary layer. To achieve this, first of all the $k-\varepsilon$ model is transformed into a $k-\omega$ formulation defining the ω in terms of k and ε:

$$\omega = \frac{\varepsilon}{\beta^* k}, \qquad \beta^* = C_\mu, \tag{3.1}$$

where $C_\mu = 0.09$ is the constant present in the expression for the turbulent viscosity in the $k-\varepsilon$ model.
Then the transformed $k-\varepsilon$ model is merged with the original $k-\omega$ formulation with the help of a function F_1. In detail, the original $k-\omega$ model is multiplied by F_1 and the transformed $k-\varepsilon$ model by $(1-F_1)$, and both added together. The function F_1 is designed to be one in the near wall region (activating the original $k-\omega$ model) and zero away from the surface. The resulting equation for k and ω are as follows:

$$\frac{D\rho k}{Dt} = P - \beta^* \rho k \omega + \frac{\partial}{\partial x_j}\left[(\mu + \sigma_k \mu_T)\frac{\partial k}{\partial x_j}\right], \tag{3.2}$$

$$\frac{D\rho\omega}{Dt} = \frac{\gamma\rho}{\mu_T}P - \beta\rho\omega^2 + \frac{\partial}{\partial x_j}\left[(\mu + \sigma_\omega \mu_T)\frac{\partial \omega}{\partial x_j}\right] + 2\rho\frac{(1-F_1)\sigma_{\omega_2}}{\omega}\frac{\partial k}{\partial x_j}\frac{\partial \omega}{\partial x_j}. \tag{3.3}$$

The left hand side of the previous equations is the Lagrangian derivative: $D/Dt = \partial/\partial t + u_i \partial/\partial x_i$. Note that the OpenFOAM implementation is written in terms of σ diffusion coefficient rather than the more traditional fraction of σ [51] ($\sigma = 1/\sigma_{orig}$) so that the bending can be applied to all coefficients in a consistent manner. The model constants in the Eq. (3.2) and Eq. (3.3) are evaluated from

$$\sigma_k = F_1\sigma_{k_1} + (1-F_1)\sigma k_2, \tag{3.4}$$
$$\sigma_\omega = F_1\sigma_{\omega_1} + (1-F_1)\sigma\omega_2, \tag{3.5}$$
$$\beta = F_1\beta_1 + (1-F_1)\beta_2, \tag{3.6}$$
$$\gamma = F_1\gamma_1 + (1-F_1)\gamma_2, \tag{3.7}$$

[1] As noted by the Largley Research Center [73] in the Menter et al. [72] articles there is a typo in the omega equation therefore in OpenFOAM is implemented the corrected version.

where subscripts 1 and 2 refer to constants in Wilcox's model and the transformed $k-\varepsilon$ model, respectively. The constraints of the original $k-\omega$ model (corresponding to set 1) have the following values:

$$\begin{aligned} \sigma_{k_1} = 0.85, \qquad \sigma_{\omega_1} = 0.5, \qquad \beta_1 = 0.075, \\ \beta^* = 0.09, \qquad \kappa = 0.41, \qquad \gamma_1 = \beta_1/\beta^* - \sigma_{\omega_1}\kappa^2/\sqrt{\beta^*} \approx 5/9. \end{aligned} \tag{3.8}$$

The constraints of the transformed $k-\varepsilon$ model (corresponding to set 2) have the following value:

$$\begin{aligned} \sigma_{k_2} = 1.0, \qquad \sigma_{\omega_2} = 0.856, \qquad \beta_1 = 0.0828, \\ \beta^* = 0.09, \qquad \kappa = 0.41, \qquad \gamma_2 = \beta_2/\beta^* - \sigma_{\omega_2}\kappa^2/\sqrt{\beta^*} \approx 0.44. \end{aligned} \tag{3.9}$$

In Eq. (3.2) and Eq. (3.3), P is the production of the kinetic energy of turbulence and is modelled using the Boussinesq approximation as follows:

$$P = (2\mu_T E_{ij} - \frac{2}{3}\delta_{ij}\rho k)\frac{\partial u_i}{\partial x_j}, \tag{3.10}$$

where $E_{ij} = (\partial u_i/\partial x_j + \partial u_j/\partial x_i)/2$ is the strain rate tensor. Menter suggested [68] replacing the term P with $\tilde{P}$, where $\tilde{P}$ is the limiter to prevent the build-up of turbulence stagnation region:

$$\tilde{P} = min\left(P, c_1\beta^*\rho k\omega\right). \tag{3.11}$$

Therefore, Eq. (3.11) does not change the solution but only eliminates the occurrence of spikes in the eddy-viscosity due to numerical "wiggles" in the shear-strain tensor. The constant c_1 in the Eq. (3.11) is fixed to 10 after the upgraded version of Hollister [51] The last term in the ω-equation (Eq. (3.3)) originates from the the transformed ε-equation and is called "the cross diffusion term". This term makes the model from insensitive to free-stream ω.
The blending function F_1 is given by

$$F_1 = \tanh(\Gamma_1^4), \tag{3.12}$$

where

$$\Gamma_1 = min\left(max\left(\frac{\sqrt{k}}{\beta^*\omega d}; \frac{500\nu}{\omega d^2}\right); \frac{4\rho\sigma_{\omega_2}k}{CD_{k\omega}d^2}\right). \tag{3.13}$$

The term Γ_1 goes to zero far away from solid surfaces because of the the wall-distance d dependency ($1/d$ or $1/d^2$) in all three terms in Eq. (3.13). Inside a boundary layer the three arguments in Eq. (3.13) have the following purpose: the first term is the turbulent length scale divided by the wall-distance d. This ratio is about 2.5 in the log-layer and tends towards zero in the deflect layer. The second term exceeds unity only in the sublayer. The third term is an additional safeguard argument designed to ensure correct behaviour of F_1 in cases of very low free-stream ω. $CD_{k\omega}$ is the positive portion of the cross-diffusion term

$$CD_{k\omega} = max\left(\frac{2\rho\sigma_{\omega_2}}{\omega}\frac{\partial k}{\partial x_j}\frac{\partial \omega}{\partial x_j}; 10^{-10}\right). \tag{3.14}$$

The eddy viscosity formula μ_T, with the modification of Hollisten [51], is defined by

$$\mu_T = \frac{a_1 \rho k}{max(a_1\omega; b_1|E_{ij}|F_2F_3)}, \tag{3.15}$$

where $|E_{ij}| = \sqrt{2E_{ij}E_{ij}}$ is the scalar measure of the strain-rate tensor E_{ij}.The function F_2 in Eq. (3.15) is to prevent the activation of the SST limitation in free shear flows. F_2 becomes one for boundary layer flows and zero for free shear layers. The formula of F_2 is given by

$$F_2 = \tanh(\Gamma_2^2), \tag{3.16}$$

where

$$\Gamma_2 = max\left(\frac{2\sqrt{k}}{\beta^*\omega d}; \frac{500\nu}{\omega d^2}\right). \tag{3.17}$$

The function F_3 is designed to prevent the SST limitation from being activated in the roughness layer in rough-wall flows. This function is necessary because Brashaw's assumption is not valid there. The function F_3 is given by

$$F_3 = 1 - \tanh\left[\left(\frac{150\nu}{\omega d^2}\right)^4\right] \tag{3.18}$$

In order to finally summarise all coefficients used in the Menter SST turbulence model Tab. 3.1 is presented. In Tab. 3.1 for each coefficient used, a brief explanation of their functions is also provided.

3.1 Uncertainty Quantification methodology

The followed method is to assume that there are uncertainties in the values of the model closure coefficients and to try to quantify the effect of these uncertainties on the URANS flow solution using UQ theory.

The uncertainties in computational models can be treated as aleatory or epistemic. Aleatory uncertainties represent inherent variations in a system, whereas epistemic uncertainties arise due to lack of knowledge. In this study, all turbulence model coefficients are treated as epistemic uncertain variables due to the lack of a complete physical understanding of turbulence.

This section provides the details of the polynomial chaos techniques used in this study with a description of the Legendre polynomials used in this study as the basis functions. The first part outlines the general non-intrusive polynomial chaos formulation with the point collocation approach. The second part describes the Sobol indices, global sensitivity indices, used to give a measure of sensitivity.

Coefficient	Description
$CD_{k\omega}$	Positive portion of the cross-diffusion term in ω-transport equation
P	Production of the kinetic energy of turbulence
a_1	Bradshaw's structural parameter used in the eddy viscosity definition
b_1	Constant factor in the turbulent viscosity equation
c_1	Constant factor in the production limiter
F_1, F_2, F_3	Auxiliary functions in turbulence model
δ_{ij}	Kroneker's delta
μ	Dynamic viscosity
μ_T	Turbulent viscosity
$\sigma_{k_1}, \sigma_{k_2}$	Turbulence-model coefficient in k-equation [2]
$\sigma_{\omega_1}, \sigma_{\omega_2}$	Turbulence-model coefficient in ω-equation
β_1, β_2	Turbulence-model coefficients used in the calculation of β for ω-equation
β^*/β_1,β^*/β_2	Blended ratio approximates the time decay of homogeneous isotropic turbulence experiments.
β^*	Turbulence-model coefficient that multiplies $k\omega$ in k-equation of the model
γ_1, γ_2	Coefficients involved in log calibration
Γ_1, Γ_2	Auxiliary variable in turbulence model

Table 3.1: $k-\omega$ SST coefficients descriptions.

3.1.1 Point-Collocation Non-Intrusive Polynomial Chaos

In recent studies, that is [74, 75, 76], the polynomial chaos method has been used as a means of UQ over traditional methods, such as Monte Carlo, to reduce computational expense. The point-collocation Non-Intrusive Polynomial Chaos (NIPC) creates a surrogate model via least squares approach (i.e., polynomial response surface) by using the results of the CFD simulations performed on a proper number of collocation points determined using Latin Hypercube Sampling (LHS) sampling methods for the propagation of uncertainty. Following the explanation provided by West et al. [77] with the polynomial chaos approach, a stochastic response function α^* (drag coefficient or pressure at a given point in the field as examples) can be decomposed into separable deterministic and stochastic components within a series expansion:

$$\alpha^*(\mathbf{x}, \boldsymbol{\varepsilon}) \approx \sum_{i=0}^{P_m} \alpha_i(\mathbf{x}) \Psi_i(\boldsymbol{\varepsilon}), \tag{3.19}$$

where α_i is the deterministic component and Ψ_i is the random variable basis function corresponding to the i^{th} mode. Here, α^* is assumed to be a function of a deterministic independent variable vector $\mathbf{x}$, which includes the spatial coordinates and deterministic parameters of the problem, and of the n-dimensional standard random variable vector $\boldsymbol{\varepsilon} = (\varepsilon_0, \varepsilon_1, ..., \varepsilon_n)$. In theory, the polynomial chaos expansion (PCE) given by Eq. (3.19) should include infinite number of terms, however, in practice, for practical implementation the expansion is truncated and a discrete sum is taken over a number of output modes (or total number of terms N_t) for a total-order expansion given by

$$N_t = P_m + 1 = \frac{(n+p)!}{n!p!}, \tag{3.20}$$

which is a function of the order of polynomial chaos p and the number of random dimensions n. The total number of terms N_t is the minimum number of samples required to produce a response surface. However, Hoster and al. suggested multiplying N_t for an oversampling ratio $n_p = 2.0$ in order to obtain a better approximation to the statistics at each polynomial degree considered.

The point-collocation NIPC method starts with replacing a stochastic response or a random function with its polynomial chaos expansion in Eq. (3.19). Then, a number of vectors, corresponding to the number of samples $N_s = n_p \cdot N_t$, are chosen in random space and the CFD code is evaluated at these points; this is the left-hand side of Eq. (3.19). Finally, a linear system of N_s equations is formulated and solved for the spectral modes of the random variables. This system is given by:

$$\begin{pmatrix} \alpha^*(\mathbf{x}, \varepsilon_0) \\ \alpha^*(\mathbf{x}, \varepsilon_1) \\ \vdots \\ \alpha^*(\mathbf{x}, \varepsilon_n) \end{pmatrix} = \begin{pmatrix} \Psi_0(\varepsilon_0) & \Psi_1(\varepsilon_0) & \dots & \Psi_n(\varepsilon_0) \\ \Psi_0(\varepsilon_1) & \Psi_1(\varepsilon_1) & \dots & \Psi_n(\varepsilon_1) \\ \vdots & \vdots & \ddots & \vdots \\ \Psi_0(\varepsilon_n) & \Psi_1(\varepsilon_n) & \dots & \Psi_n(\varepsilon_n) \end{pmatrix} \begin{pmatrix} \alpha_0 \\ \alpha_1 \\ \vdots \\ \alpha_n \end{pmatrix}. \tag{3.21}$$

When $n_p > 1.0$ the Eq. (3.21) is overdetermined and can be solved using a least squares approach.

The basis functions, used in the stochastic expansion given in Eq. (3.19), are polynomials that are orthogonal with respect to a weight function over the support region of the input random variable vector. The *Legendre* polynomials are optimal basis functions for uniform and exponential input uncertainty distributions. Therefore, the *Legendre* polynomials are selected as a basis function in this study. The *Legendre* polynomials $Le_n(x)$ are the solutions of the following differential equation:

$$(1 - x^2)\ddot{y} - 2x\dot{y} + n(n+1)y = 0, \qquad n \in \mathbb{N}. \tag{3.22}$$

They may be generated by the following recurrence relationship:

$$Le_0(x) = 1, \tag{3.23}$$

$$(n+1)Le_{n+1}(x) = (2n+1)xLe_n(x) - nLe_{n-1}(x). \tag{3.24}$$

They are orthogonal with respect to the uniform probability measure over $[-1; 1]$:

$$\int_{-1}^{1} Le_m(x)Le_n(x)dx = \frac{2}{2n+1}\delta_{mn}, \tag{3.25}$$

where δ_{mn} is the Kronecker delta: $\delta_{mn} = 1$ if $m = n$ and 0 otherwise. If ε is a random variable with uniform Probability Density Function (PDF) over $[-1, 1]$, the following relationship holds:

$$E[Le_m(\varepsilon)Le_n(\varepsilon)] = \frac{1}{2n+1}\delta_{mn}, \tag{3.26}$$

where $E[.]$ is the mathematical expectation. The first three Legendre. e.g. the first three Le polynomials are:

$$Le_1(x) = x, \qquad Le_2(x) = \frac{1}{2}(3x^2 - 1), \quad Le_3(x) = \frac{1}{2}(5x^3 - 3x). \tag{3.27}$$

3.1.2 Sobol Indices

Sobol indices (global nonlinear sensitivity indices) have been used to estimate the relative influence of individual closure coefficients and rank their relative contributions to the total uncertainty in the output quantities of interest.
Sobol indices can be derived via Sobol decomposition, which is a variance-based global sensitivity analysis method. This derivation utilises the PCE coefficients calculated in Eq. (3.21). Therefore, the Sobol indices can be calculated analytically with almost no additional cost. Indeed, only elementary mathematical operations are needed to compute these indices from the expansion coefficients already calculated in Eq. (3.21).
To extract the Sobol indices, as a first task, the total variance D^T can be written in terms of PCE:

$$D^T = \sum_{j=1}^{P_m} \alpha_j^2(t, \mathbf{x})\langle\Psi_j^2(\boldsymbol{\varepsilon})\rangle. \tag{3.28}$$

Then, as shown by Sudret [74] and Schaefer [75], the total variance can be decomposed as:

$$D^T = \sum_{i=1}^{i=n} D_i + \sum_{1\leqslant i<j\leqslant n}^{i=n-1} D_{i,j} + \sum_{1\leqslant i<j<k\leqslant n}^{i=n-2} D_{i,j,k} + \cdots + D_{1,2,\ldots,n}, \tag{3.29}$$

where the partial variances ($D_{i_1,\ldots,i_s}$) are given by:

$$D_{i_1,\ldots,i_s} = \sum_{\beta\in i_1,\ldots,i_s} \alpha_\beta^2\langle\Psi_\beta^2(\boldsymbol{\varepsilon})\rangle, \qquad 1 \leqslant i_1 < \cdots < i_s \leqslant n. \tag{3.30}$$

The Sobol indices ($S_{i_1,\ldots,i_s}$) are defined as,

$$S_{i_1,\ldots,i_s} = \frac{D_{i_1,\ldots,i_s}}{D^T}, \tag{3.31}$$

which satisfy the following equation:

$$\sum_{i=1}^{i=n} S_i + \sum_{1\leqslant i<j\leqslant n}^{i=n-1} S_{i,j} + \sum_{1\leqslant i<j<k\leqslant n}^{i=n-2} S_{i,j,k} + \cdots + S_{1,2,\ldots,n} = 1.0. \tag{3.32}$$

The Sobol indices provide a sensitivity measure due to individual contribution from each input uncertain variable (S_i), as well as the mixed contributions ($S_{i,j}, S_{i,j,k}, \dots$). As shown by Sudret [74], the total sensitivity indices (S_{T_i}) of an input parameter i have been defined in order to evaluate the total effect of an input parameter i. They are defined as the sum of the partial Sobol indices that include the particular parameter:

$$S_i^T = \sum_{L_i} \frac{D_{i_1,\dots,i_s}}{D^T}; \qquad Le_i = \{(i_1, \dots, i_s) : \exists k, 1 \leqslant k \leqslant s, i_k = i\}. \tag{3.33}$$

Note that Le_i corresponds to the polynomials depending only on parameter i.
For example, with $n = 3$, the total contribution to the overall variance from the first uncertain variable ($i = 1$) can be written as:

$$S_i^T = S_1 + S_{1,2} + S_{1,3} + S_{1,2,3}. \tag{3.34}$$

These formulations show that the Sobol indices can be used to provide a relative ranking of each input uncertainty to the overall variation in the output, in consideration of nonlinear correlation between input variables and output quantities of interest.

3.2 Verification of the implemented procedure

In this section the practical strategy employed in Dakota to drive the UQ analysis is provided. In order to evaluate the presented strategy, two of the application examples with analytical results, proposed by Sudret [74] have been tested.
The used approach is implemented in three separated stages as follows.

Stage 1 Using Dakota, the collocation points (samplings) for the deterministic CFD simulations are generated using LHS.

Stage 2 The overall CFD simulations are carried out for the given collocation points. The results are saved in proper text files.

Stage 3 Using Dakota, in combination with a proper ad hoc implemented interface, the polynomial chaos coefficients are determined based on the results obtained at stage 2 and the related probabilistic values as well as sensitivity indices are calculated.

Thanks to the numerical strategy described above, it is possible to perform the CFD simulation independently from Dakota which is only used at the first and third stages. Note that at stage 2 DAKOTA is not running.
In the following two example tests the calculations have been performed according to the former strategy used for the VIV, with the only exception that the results of the stage 2 are obtained using a python script.

3.2.1 Example 1: Polynomial model

Let us consider the following model:

$$Y = \frac{1}{2^n} \prod_{i=1}^{n} (3X_i^2 + 1), \tag{3.35}$$

where the input variables $X_i, i = 1, 2, \ldots, n$ are uniformly distributed over [0,1]. The Sobol sensitivity indices can be computed analytically:

$$S_{i_s,\ldots,i_s} = \frac{5^{-}5}{(6/5)^n - 1}, \qquad s = 1, \ldots, n. \tag{3.36}$$

The numerical application is carried out for n=3. In this case the model is polynomial of degree 6.
Knowing a priori that it is polynomial, it is interesting to investigate whether the proposed approach can give exact results. Thus, a PC of order $p = 6$ is chosen. The PC expansion contains N_S coefficients, given by:

$$N_t = P_m + 1 = \frac{(n+p)!}{n!p!} = \frac{(3+6)!}{3!6!} = 84. \tag{3.37}$$

Selecting an oversampling ratio $n_p = 2$ the number of collocation points $N_s = 168$ is found to be necessary.
The exact values of the sensitivity indices can be found from (3.36):

$$\begin{aligned} &S_1 = S_2 = S_3 = 25/91 = 0.2747, \\ &S_{12} = S_{23} = S_{13} = 5/91 = 0.0549, \\ &S_{123} = 1/91 = 0.0110. \end{aligned} \tag{3.38}$$

In order to obtain the blind solution, five cases are considered here: namely $p = 3, 4, 5, 6, 7$. The number of samples N_s required for every order of polynomial expansion is presented in Tab. 3.2.

In Table 3.2, the results obtained during this study are collected. It is possible to note that for the polynomial degree $p = 6$ convergence is reached. For $p = 7$ the result does not vary compared to $p = 6$. It can be noted that the less accurate solution ($p = 3$) already provides a good estimation of sensitivity indices, since the relative error (compared with the exact solution) is less than 4% for the total sensitivity indices S_i^T. These results are obtained with 40 calls to the model evaluation. Using a $4th$ order PCE ($p = 4$), this relative error decreases down to less than 0.5%, at a cost of 70 calls to the model evaluation. Finally, the relative error obtained with $p = 5$ is less than 0.1% at a cost of 112 calls to the model evaluation.

3.2.2 Example 2: Ishigami function

For the second example we consider here the so-called Ishigami function:

$$Y = \sin X_1 + a \sin^2 X_2 + b X_3^4 \sin X_1, \tag{3.39}$$

Index	Analytic value	Order of PC expansion				
		p=3	p=4	p=5	p=6	p=7
S_1	0.2747	0.2860	0.2770	0.2747	0.2747	0.2747
S_2	0.2747	0.2875	0.2751	0.2748	0.2747	0.2747
S_3	0.2747	0.2836	0.2716	0.2745	0.2747	0.2747
S_{12}	0.0549	0.04530	0.0541	0.0550	0.0549	0.0549
S_{13}	0.0549	0.04669	0.0552	0.0550	0.0549	0.0549
S_{23}	0.0549	0.04509	0.0560	0.0551	0.0549	0.0549
S_{123}	0.0110	0.0058	0.0110	0.0107	0.0110	0.0110
S_1^T	0.3955	0.3838	0.3973	0.3954	0.3955	0.3955
S_2^T	0.3955	0.3837	0.3962	0.3956	0.3955	0.3955
S_2^T	0.3955	0.3812	0.3938	0.3953	0.3955	0.3955
$(P_m + 1)$		20	35	56	84	120
N_s		40	70	112	168	240

Table 3.2: Example 1, Polynomial model influence of the degree of the PC representation.

where the input variables X_i, $i = 1, 2, 3$ are uniformly distributed over $[-\pi, \pi]$. This function, which is nonlinear and nonmonotonic, has been used in literature to benchmark sensitivity methods. The Ishigami function is particularly challenging in Sensitivity Analysis (SA). All the input variables are important, either when taken alone (e.g. X_1) or as a couple (e.g. (X_1, X_2)). This is an unusual case in real engineering problems, and thus a relatively high order of expansion is required to achieve accurate results.
The variance D^T of Y can be computed analytically:

$$\begin{aligned}
&D_1 = \frac{b\pi^4}{5} + \frac{b^2\pi^8}{50} + \frac{1}{2}, \qquad D_2 = \frac{a^2}{8}, \qquad D_3 = 0,\\
&D_{12} = D_{23} = 0, \qquad D_{13} = \frac{8b^2\pi^8}{225}, \qquad D_{123} = 0,\\
&D^T = \frac{a^2}{8} + \frac{b\pi^4}{5} + \frac{b^2\pi^8}{18} + \frac{1}{2}.
\end{aligned} \tag{3.40}$$

The application example is carried out using the numerical values of $a = 7$ and $b = 0.1$. Therefore the Sobol sensitivity indices are found:

$$\begin{aligned}
&S_1 = D_1/D^T = 0.3139, \qquad S_2 = D_2/D^T = 0.4424, \quad S_3 = D_3/D^T = 0,\\
&S_{12} = D_{12}/D^T = 0, \qquad S_{13} = D_{13}/D^T = 0.2436, \qquad S_{23} = D_{23}/D^T = 0,\\
&S_{123} = D_{123}/D^T = 0.
\end{aligned} \tag{3.41}$$

The PC expansions of increasing degree ($p = 3, 8, 9, 10$) are used. Since the random input variable is equal to 3, the PC expansions contain $(P_m + 1) = 20, 165, 220, 286$ unknown coefficients, respectively. The corresponding minimal number of regression points used, considering $n_p = 2$, are $N_s = 40, 330, 440, 572$ respectively. The results are gathered in Tab. 3.3.

Index	Analytical value	Order of PC expansion			
		$p = 3$	$p = 8$	$p = 9$	$p = 10$
S_1	0.3138	0.4184	0.3143	0.3134	0.3138
S_2	0.4424	0.0069	0.4362	0.4387	0.4427
S_3	0	0.0425	0.0001	0.0003	0.0000
S_{12}	0	0.1759	0.0006	0.0007	0.0000
S_{13}	0.2436	0.2761	0.2455	0.2441	0.2435
S_{23}	0	0.0341	0.0008	0.0007	0.0000
S_{123}	0	0.0461	0.0025	0.0015	0.0000
S_1^T	0.5574	0.9165	0.5629	0.5602	0.5573
S_2^T	0.4424	0.2629	0.4401	0.4418	0.4427
S_3^T	0.2436	0.3989	0.2489	0.2467	0.2435
$(P_m + 1)$		20	165	220	286
N_s		40	330	440	572

Table 3.3: Example 2, Ishigami function. Influence of the degree of the PC representation.

It has been observed that the respective influence of X_2 and (X_1, X_3) is miscomputed if the PC degree is too low. However, convergence is obtained as soon as $p \leqslant 8$. Note the zero value indices are computed exactly, even at a low degree of expansion.
It is valuable to remark that with $p = 10$ the numerical results almost perfectly match the analytical values.
As a conclusion, the proposed approach allows us to find the analytical solution if the degree of expansion is sufficiently large.

3.3 Complete coefficients analysis

The two-step strategy proposed by Sudret [74], is used for the UQ of the turbulence model closure coefficients. In the two-step strategy, the first step is using a low order expansion (usually $p = 2$) which allows us to find the most important variable; the second step is using a higher order expansion ($p = 4, 5$) of reduced model which leads to the computation of the main sensitivity indices. In detail, the purpose of the complete analysis is to identify the closure coefficients that contribute significantly to uncertainty in the output quantities of interest and then use these coefficients in the later reduced-dimensionality analysis.
The case of a circular cylinder, mounted on a linear spring, working in uniform cross flow velocity U, is considered. The study is carried out according to the already presented experimental set-up of Khalak and Williamson (see section 2.1.4).
In this study, VIV time series, used to identify the interested output quantities have

been obtained via 2D URANS-based CFD simulations. As highlighted in the chapter 2 the complexity of the phenomenon would probably require more sophisticated and computationally demanding 3D simulation. The study of the UQ with 3D URANS/SAS simulation are not possible. To be able to do the study in the case of two-dimensional simulations without losing the correspondence with the experimental results, only three reduced velocity ($U^* = 7, 8, 9$) of the lower branch are taken in consideration. As demonstrated in the section 2.3, in the lower branch the three-dimensional flow effects are absent. Furthermore, from the time series analysis conducted via *sdof-mf* model, it appears that in lower breach regime the cylinder motion and the vortex induced force are basically both monochromatic.
The mesh used in the current 2D simulations is the 2D NEW, for details refer to Sec. 2.2. Overall, nine coefficients of the $k-\omega$ SST model were varied in the UQ analysis. A summary of the closure coefficients to be varied and their epistemic intervals is included in Tab. 3.4. Please note that the epistemic intervals are set following [75].

Coefficient	Standard Value	Lower Bound	Upper Bound
σ_{k_1}	0.85	0.7	1.0
σ_{k_2}	1.0	0.8	1.2
σ_{w_1}	0.5	0.3	0.7
σ_{w_2}	0.856	0.7	1.0
β^*/β_1	1.20	1.19	1.31
β^*/β_2	1.0870	1.05	1.45
β^*	0.09	0.0784	0.1024
κ	0.41	0.38	0.42
a_1	0.31	0.31	0.40

Table 3.4: SST Closure Coefficients and Associated Epistemic Intervals

The values of γ_1 and γ_2, needed by OpenFOAM have been extracted using the Eq. (3.8) and Eq. (3.9). Since the simulation is carried out considering a smooth cylinder surface, the F_3 function for rough-wall (Eq. (3.18)) is switched in every simulation. The constants b_1 and c_1 are considered fixed to 1 and 10 respectively.
The boundary and the initial conditions used for velocity, pressure, turbulent kinetic energy k and turbulence specific dissipation rate ω are the same used in the previous simulation (see Tab. 2.2-2.4 for reference).
In this study, only the maximum and the minimum of the response are considered from the response surface to determine the epistemic interval for each uncertain output, even if the stochastic response surfaces, created with the NIPC approach, is able to calculate the confidence intervals along with various statistics of the output for a probabilistic (aleatory) input.
In the current study, for all the velocity U^* selected, the order of polynomial is systematically increased, from $p = 2$ to 4, in order to evaluate the effect of p on the rank of coefficients.

		Adimensional Amplitude A^*					Frequency ratio f^*				
U^*	p	Base CFD	Mean	Std	Max	Min	Base CFD	Mean	Std	Max	Min
	2		0.556	0.035	0.649	0.48		1.33	0.013	1.389	1.312
7	3	0.520	0.556	0.035	0.649	0.484	1.294	1.331	0.015	1.377	1.312
	4		0.555	0.035	0.677	0.447		1.332	0.015	1.435	1.312
	2		0.594	0.028	0.672	0.5		1.31	0.008	1.337	1.300
8	3	0.562	0.594	0.029	0.696	0.481	1.307	1.311	0.008	1.35	1.299
	4		0.591	0.03	0.704	0.477		1.312	0.011	1.427	1.299
	2		0.628	0.035	0.716	0.51		1.296	0.008	1.324	1.288
9	3	0.606	0.628	0.041	0.746	0.244	1.346	1.299	0.027	1.765	1.288
	4		0.632	0.089	3.422	0.247		1.297	0.016	1.758	1.288

Table 3.5: Adimensional amplitude A^* and frequency ratio f^* CFD results.

A value of the oversampling ratio $n_p = 2$ is used for all the UQ analyses in order to give a better approximation to the statistics at each polynomial degree considered. Therefore, the total computational cost (i.e., number of CFD evaluations required) is $N_s = 110, 440$ and 1430 for $p = 2, 3, 4$ respectively.

3.3.1 Results

The results of all uncertainty quantification analysis are presented in this section. Tab. 3.5 shows the CFD results in terms of mean value, standard deviation, minimum and maximum of A^* and f^* for the three selected reduced velocity U^*. Tab. 3.5 also reports the value obtained using the standard $k - \omega$ SST closure coefficients. From the results in Tab 3.5, it is concluded that the second- and third-order PC expansion provide almost the same output results as the forth-order polynomial, the only significant difference is in the maximum value of A^* for the reduced velocity 9.
The first order Sobol indices S_i of the closure coefficients for the $k - \omega$ SST turbulence model for A^* and f^* are presented in Fig. 3.1 and Fig. 3.2, respectively.

As a general note, the increase of the order of PC expansion leads to a different ranking of output variables. This is clearly visible in the reduced velocity $U^* = 7$ and 9 in terms of A^* (Fig. 3.1(a) and Fig. 3.1(c)) where the relative importance of the parameter κ changes as the order of PC expansion increases. It is also visible in the reduced velocity $U^* = 8$ in terms of f^* (Fig. 3.2(b)) where the $p = 2$ shows a significant contribute from σ_{ω_2} which instead becomes negligible for higher orders.
Let's consider therefore the results of the forth-order of PC expansion: the largest contributors in A^*, for all the three present velocities are κ, σ_{ω_2}, β^*/β_2 and a_1. In the case of f^*, the Fig. 3.2 shows a higher variability between the different velocities. In the case of $U^* = 7$, the largest contributor to uncertainty for f^* is a_1, but the contribute from κ,σ_{ω_2}, β^*/β_2 are still present. For $U^* = 8$ the largest contributors are a_1,σ_{ω_2}, β^*/β_2,

while the contributors from the Von Kármán constant κ is negligible. Finally, for $U^* = 9$ the largest contributor is σ_{ω_2} Note that σ_{ω_2} is significant for all of the U^* and for both the outputs A^* and f^*.

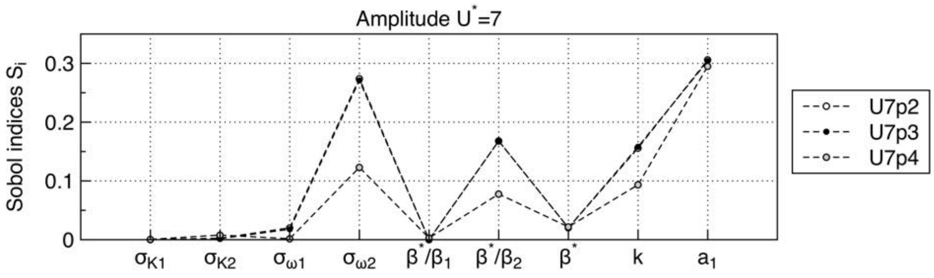

(a) $U^* = 7$

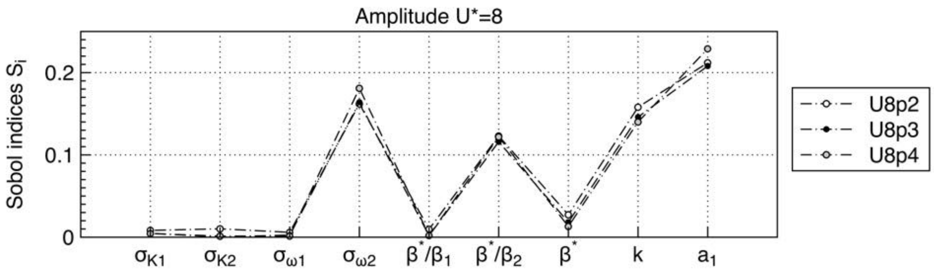

(b) $U^* = 8$

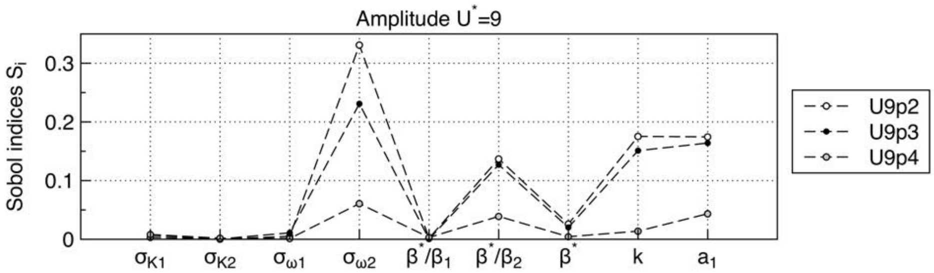

(c) $U^* = 9$

Figure 3.1: First order Sobol indices S_i of the closure coefficients for A^*.

The Sobol indices of the first order can clearly give a first indication of which are the most important input parameters, but could also give unreliable results [78].
For this reason the 'total effect' parameter index S_i^T is also analysed. As exposed in subsection 3.1.2, the total sensitivity index provides a measure of the total effect of a given parameter, including all the possible synergetic terms between that parameter and all the others.
The results of the total sensitivity indices S_i^T are seen in Fig. 3.3 and Fig. 3.3 for A^* and f^* respectively. As seen in the figures, the $p = 2$ cannot provide a reliable ranking of output parameters both in terms of adimensional amplitude and frequency ratio. The

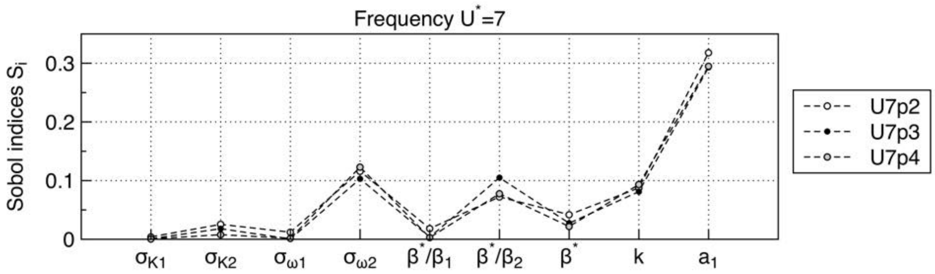

(a) $U^* = 7$

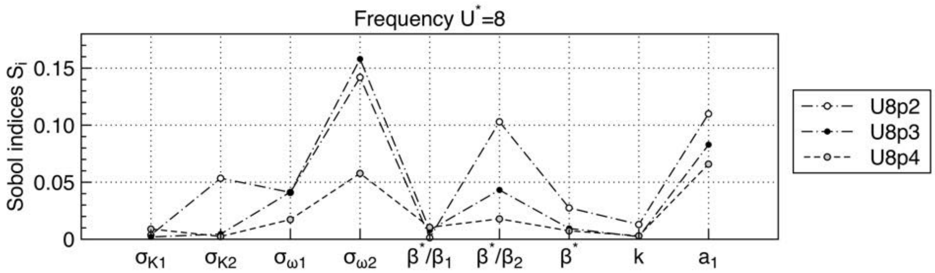

(b) $U^* = 8$

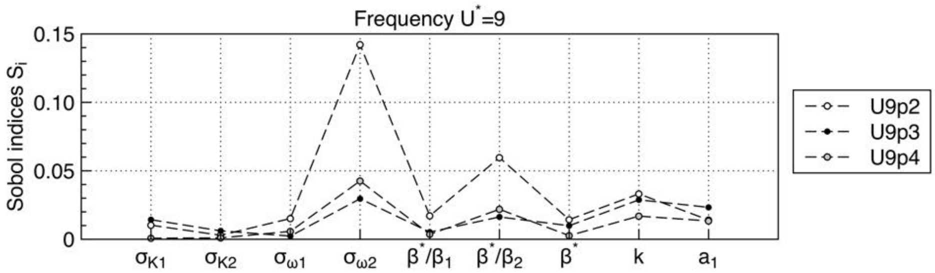

(c) $U^* = 9$

Figure 3.2: First order Sobol indices S_i of the closure coefficients for f^*.

particular case of U^* for the amplitude ratio can be seen in Fig. 3.6(c). It is observed from the Fig. 3.1(c) that the influence of σ_{k_1} is negligible. Now having considered the sensitivity estimate related to combination of the variables it can be noted that the variable σ_{k_1} has an importance that is no longer negligible.
The interference second-order Sobol indices $S_{i,j}$ are presented in Fig. 3.5 in the case of $p = 4$. Analysing in detail the interference Sobol index $S_{i,j}$, in Fig. 3.5 it can be seen that in case of A^*, there is no clear contribution to the total indices of any of the $S_{i,j}$ indices; while in the case of frequency, it can be noted that the contributions of $S_{\sigma_{\omega_2},\beta*/\beta_2}$, $S_{\sigma_{\omega_2},\kappa}$ and $S_{\beta*/\beta_2,\kappa}$ are not negligible for all three reduced velocities considered.
The high value of the Total indices $S^T_{\sigma_{k_1}}$, will therefore be linked to the contribution of the higher order terms. In order to evaluate the effective contribution of high-order interference terms and compare their contribution with the lesser-order terms, the bar

plots of Fig. 3.6 and Fig. 3.7 are used. In Fig. 3.6 and Fig. 3.7 the Sobol sensitivity indices are divided through the order. To clarify, only the Sobol indices of coefficients with significant contributions (i.e greater than 0.1) to the uncertainty are highlighted in the plot. Two things can be noticed: the first is that, as the reduced velocity U^* increases, the contribution due to higher order terms increases for both output values; the second concerns the terms of $U^* = 9$ in the case of A^*, in this case the contribution given by the terms of third- and forth-order for the parameter σ_{k_1} are significant. Using low order PC expansions, less than $p = 4$ leads us to neglect this contributor. Therefore, in the particular case of VIV in the lower-branch region, the procedure suggested by Sudret [74], where a PC expansions $p = 2$ was considered enough for the fist step procedure, it is not considered valid here.

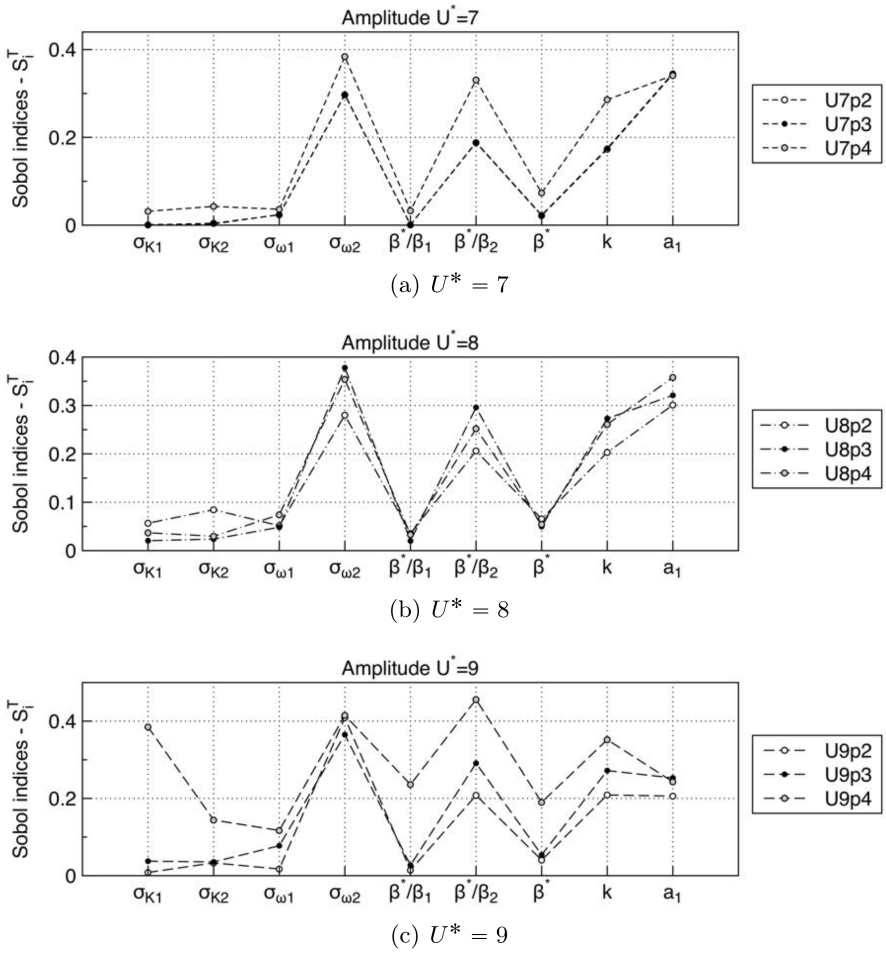

(a) $U^* = 7$

(b) $U^* = 8$

(c) $U^* = 9$

Figure 3.3: Total sensitivity indices S_i^T of the closure coefficients for A^*.

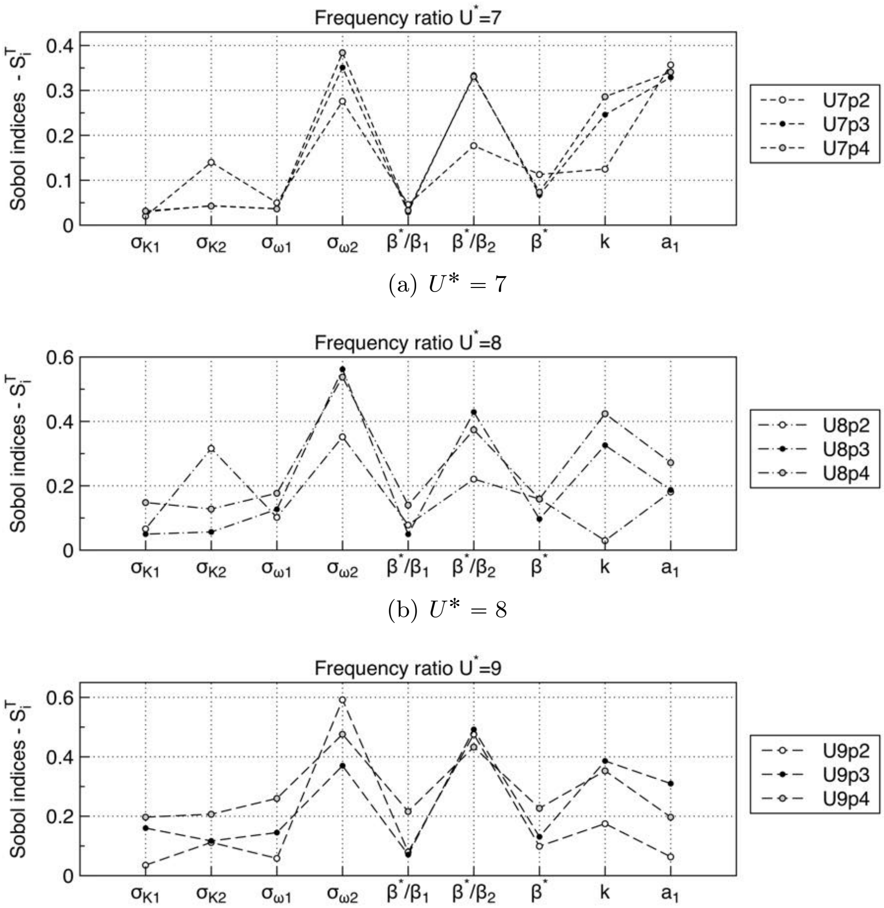

(a) $U^* = 7$

(b) $U^* = 8$

(c) $U^* = 9$

Figure 3.4: Total sensitivity indices S_i^T of the closure coefficients for f^*.

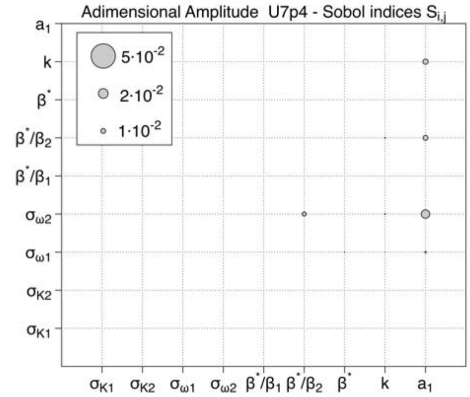

(a) $U^* = 7$ A^*

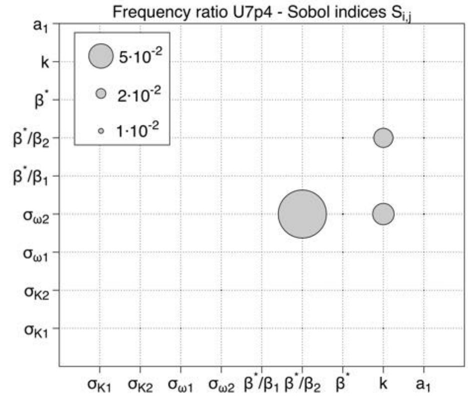

(b) $U^* = 7$ f^*

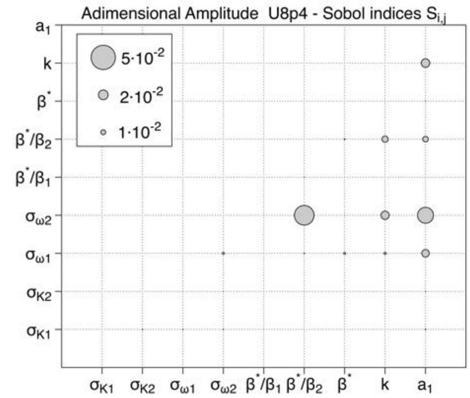

(c) $U^* = 8$ A^*

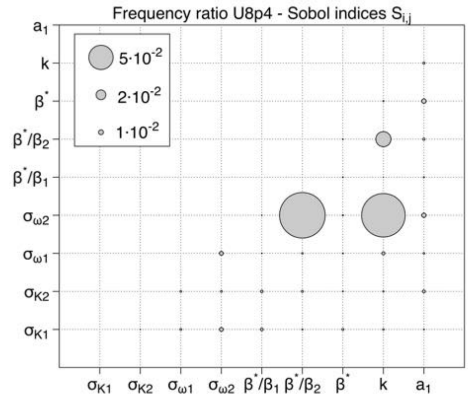

(d) $U^* = 8$ f^*

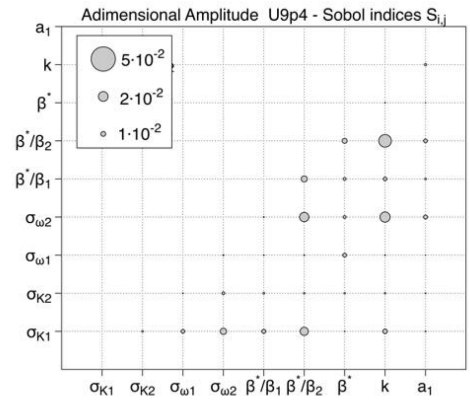

(e) $U^* = 9$ A^*

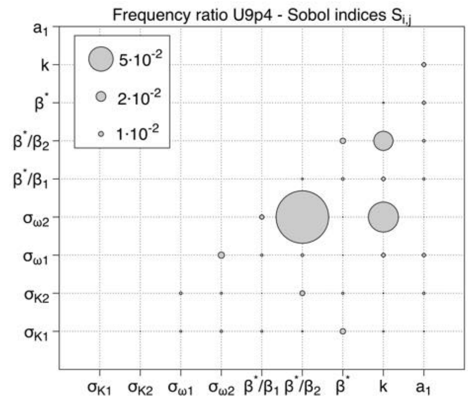

(f) $U^* = 9$ f^*

Figure 3.5: Second-order Sobol indices $S_{i,j}$ of the closure coefficients.

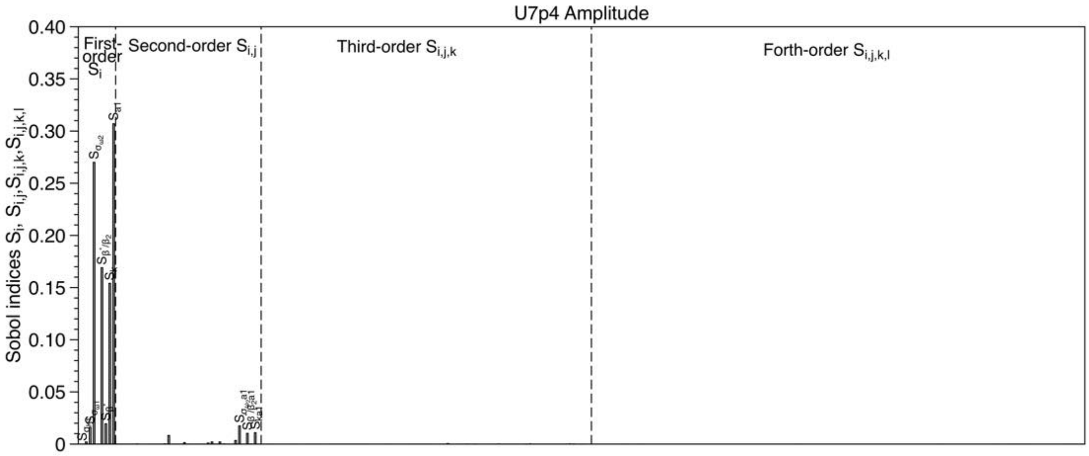

(a) $U^* = 7$

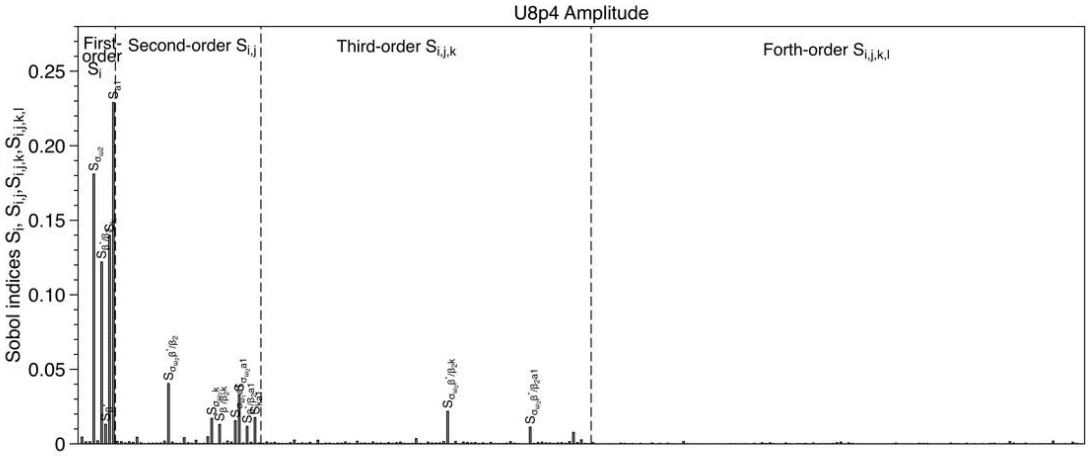

(b) $U^* = 8$

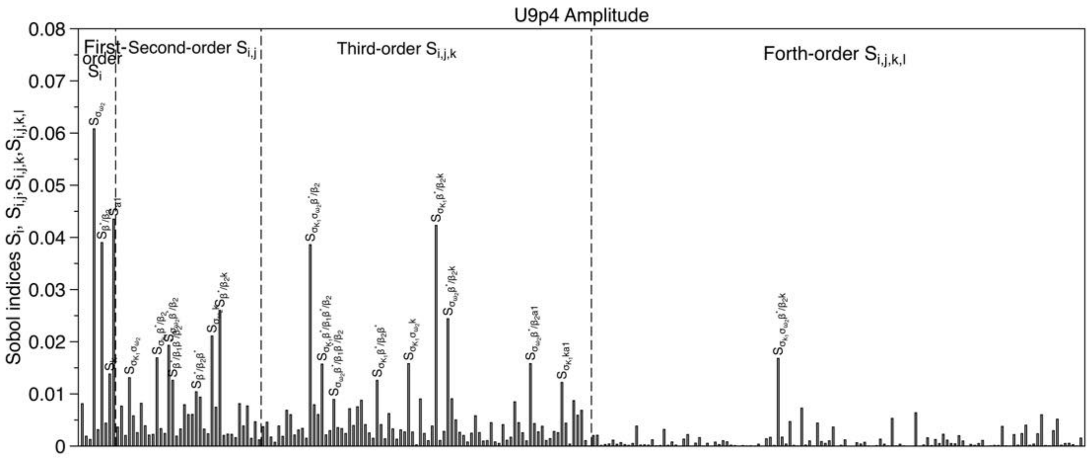

(c) $U^* = 9$

Figure 3.6: Sobol sensitivity indices divided by single terms S_i,$S_{i,j}$, $S_{i,j,k}$ and $S_{i,j,k,l}$ for A^* ($p = 4$).

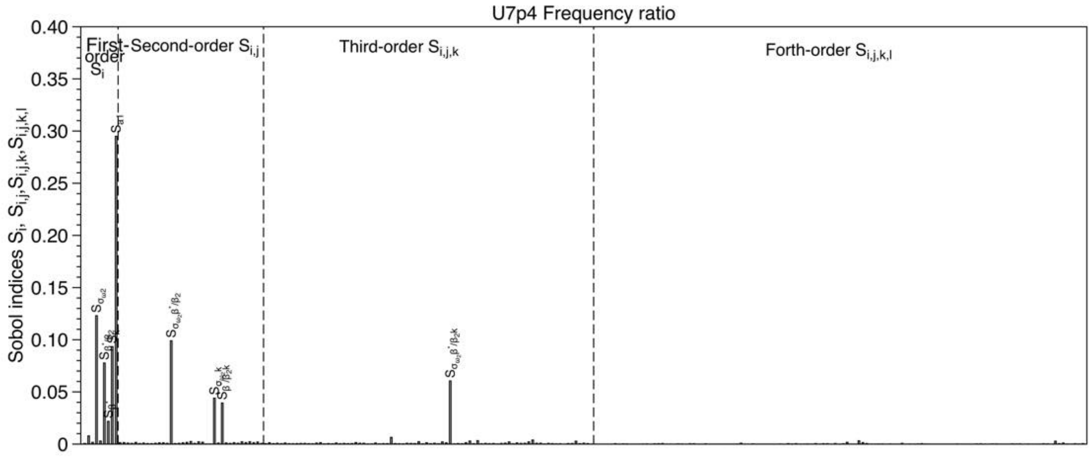

(a) $U^* = 7$

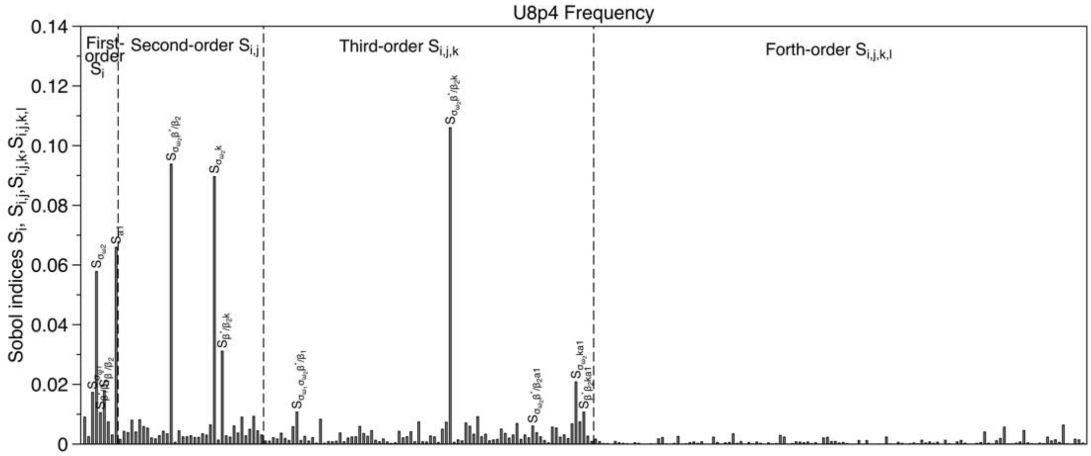

(b) $U^* = 8$

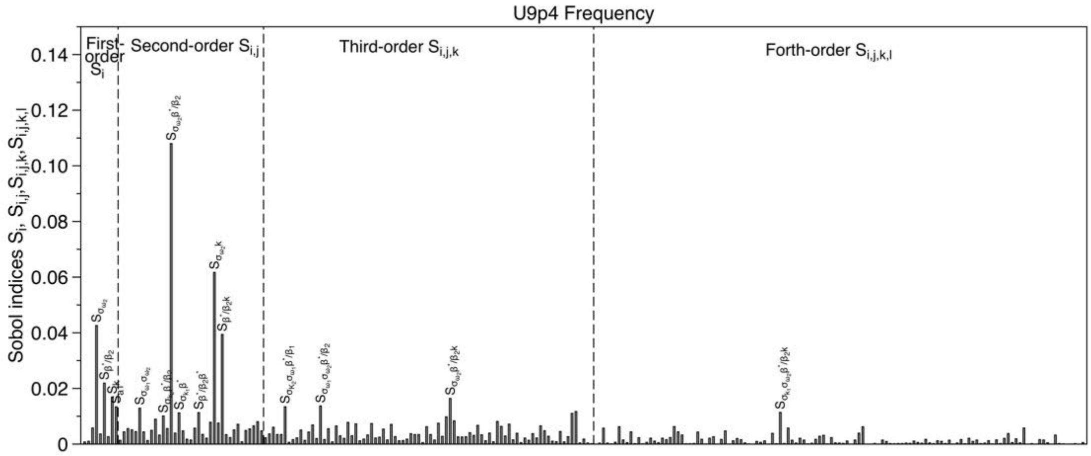

(c) $U^* = 9$

Figure 3.7: Sobol sensitivity indices divided by single terms S_i,$S_{i,j}$, $S_{i,j,k}$ and $S_{i,j,k,l}$ for f^* ($p = 4$).

3.3.2 Conclusions

Considering that, the analysis conducted by Erb et al. [76] and Schaefer et al. [75], where the $p = 2$ was selected for the fist step procedure, should be verified with higher order PC expansion in order to confirm if the convergence of total sensitivity indices has been reached.
All things considered, five closure coefficients were found to contribute significantly to the output quantity of interest for the $k{-}\omega$ SST model. These coefficients are σ_{k_1},σ_{ω_2},β^*/β_2,κ and a_1, they will be used as uncertain variables in the second set of reduced dimensionality analysis (RDA).

3.4 Reduced-dimensionality analysis

To further increase the accuracy of the uncertainty analysis, a second campaign has been carried out by using only the significant closure coefficients. The selected closure coefficients and the suggested bounds given in Tab. 3.6. Tab. 3.6 also include coefficients kept constant. Two values of $p = 4, 5$ have been used in this reduced study. The corresponding minimal number of regression points are $N_s = 252$ and 504 for $p = 4$ and $p = 5$ respectively.
As shown in the previous section 3.3, the polynomial of order 4 already provides a good estimation of the sensitivity indices. However, we must investigate whether a greater polynomial order leads to the same classification.

Coefficient	Standard Value	Lower Bound	Upper Bound
σ_{k_1}	0.85	0.7	1.0
σ_{w_2}	0.856	0.7	1.0
β^*/β_2	1.0870	1.05	1.45
κ	0.41	0.38	0.42
a_1	0.31	0.31	0.40
σ_{k_2}	1.0	-	-
σ_{w_1}	0.5	-	-
β^*/β_1	1.20	-	-
β^*	0.09	-	-

Table 3.6: SST Closure Coefficients and Associated Epistemic Intervals used in the RDA

The results of RDA in terms of mean value, standard deviation, minimum and maximum of A^* and f^* for the three selected reduced velocities U^* can be found in Tab. 3.7. The values reported in Tab. 3.7 indicate a negligible difference between the polynomial of order 4 and 5. This means that the statistics results of CFD simulation are quite insensitive to the change of the PC expansion order.
The total sensitivity indices S_i^T for each closure coefficient for each output quantity of interest are tabulated in Tab. 3.8. The largest contributors to uncertainty in each model are typed in black. The ranking of significance for every U^* is also given in the same table. Coefficients with Sobol indices of less than $3 \cdot 10^{-2}$ are not considered to be significant. Tab. 3.8 also includes a summary of the computational cost (i.e., number of CFD evaluations required) for the RDA.
In order to better appreciate the differences between the closure coefficients, the same results of Tab. 3.8, are also presented in graphical form in Fig. 3.8 and Fig. 3.9 for the output variables A^* and f^* respectively.

From the above results, it appears that the less PC expansion ($p = 4$) already provides the correct classification of the sensitivity indices. The only different classification is for the reduced velocity $U^* = 9$ in terms of the output quantity A^*. This is probably

		Adimensional Amplitude A^*					Frequency ratio f^*				
U^*	p	Base CFD	Mean	Std	Max	Min	Base CFD	Mean	Std	Max	Min
7	4	0.520	0.556	0.034	0.666	0.480	1.294	1.331	0.017	1.389	1.312
	5		0.556	0.034	0.672	0.479		1.331	0.016	1.412	1.312
8	4	0.562	0.587	0.033	0.691	0.459	1.307	1.312	0.009	1.344	1.300
	5		0.587	0.031	0.697	0.451		1.312	0.008	1.350	1.300
9	4	0.606	0.626	0.035	0.738	0.508	1.346	1.297	0.009	1.331	1.288
	5		0.627	0.035	0.743	0.507		1.297	0.009	1.324	1.288

Table 3.7: Adimensional amplitude A^* and frequency ratio f^* CFD results.

Index	Adimensional Amplitude A^*					
	$U^* = 7$		$U^* = 8$		$U^* = 9$	
	p=4	p=5	p=4	p=5	p=4	p=5
$S^T_{\sigma_{k_1}}$	0.0037(V)	0.0007(V)	0.0273(V)	0.0303(V)	0.0658(V)	0.0237(V)
$S^T_{\sigma_{\omega_2}}$	0.3221(II)	0.3159(II)	0.3922(I)	0.3924(I)	0.3927(I)	0.4522(I)
$S^T_{\beta*/\beta_2}$	0.1996(III)	0.1944(II)	0.3002(III)	0.2839(III)	0.2343(IV)	0.2634(II)
S^T_{κ}	0.1777(IV)	0.1758(IV)	0.2571 (IV)	0.2506(IV)	0.2575(III)	0.2328(IV)
$S^T_{a_1}$	0.3594(I)	0.3678(I)	0.3232(II)	0.3440(II)	0.2813(II)	0.2582(III)
	Frequency ratio f^*					
	$U^* = 7$		$U^* = 8$		$U^* = 9$	
	p=4	p=5	p=4	p=5	p=4	p=5
$S^T_{\sigma_{k_1}}$	0.0770(V)	0.0636(V)	0.0825(V)	0.1165(V)	0.0953(V)	0.0982(V)
$S^T_{\sigma_{\omega_2}}$	0.4409(I)	0.4099(I)	0.7406(I)	0.7219(I)	0.7505(I)	0.7317(I)
$S^T_{\beta*/\beta_2}$	0.4047(II)	0.4097(II)	0.5850(II)	0.5592(II)	0.5226(II)	0.5717(II)
S^T_{κ}	0.3158(IV)	0.3426(IV)	0.4274(III)	0.2839(III)	0.3871(III)	0.4983(III)
$S^T_{a_1}$	0.3493(III)	0.4027(III)	0.1451(IV)	0.2072(IV)	0.1245(IV)	0.1355(IV)
$(P_m + 1)$	126	252	126	252	126	252
N_s	252	504	252	504	252	504

Table 3.8: Sobol total sensitivity indices of closure coefficients for the RDA. I-V denotes the ranking of significance. Grey text for Sobol indices less than $3{\cdot}!0^{-2}$.

related to the small difference of the Sobol indices between the three closure coefficients β^*/β_2,κ and a_1 (see Fig. 3.8(c)).
The largest contributors to uncertainty in A^* for $U^* = 7$ are a_1 and σ_{ω_2}; for $U^* = 8$ are σ_{ω_2} and a_1; for $U^* = 9$ is σ_{ω_2}. The largest contributors to uncertainty in f^* for $U^* = 7$ are σ_{ω_2}, β^*/β_2, a_1 and κ; for $U^* = 8$ are σ_{ω_2} and β^*/β_2; for $U^* = 9$ are σ_{ω_2}, β^*/β_2 and κ. Note that σ_{ω_2} is shared by all the reduced velocities considered and for both output quantities.

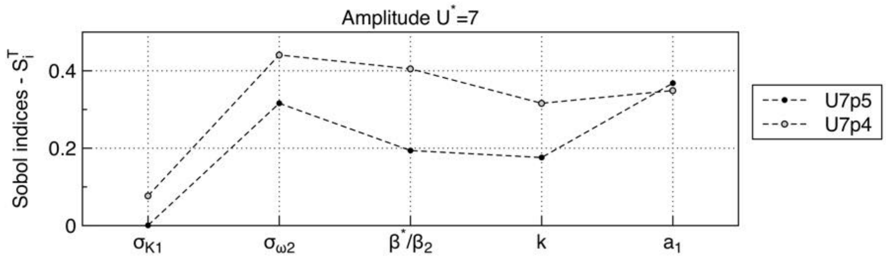

(a) $U^* = 7$

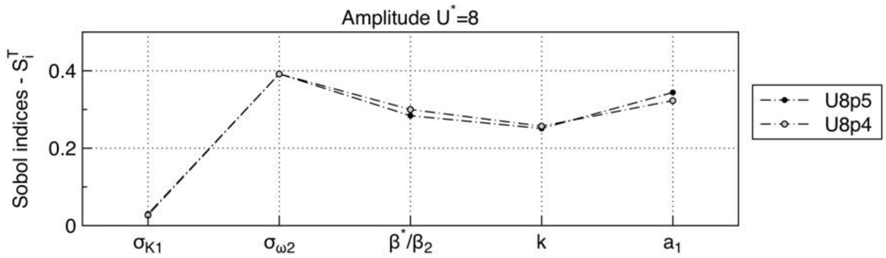

(b) $U^* = 8$

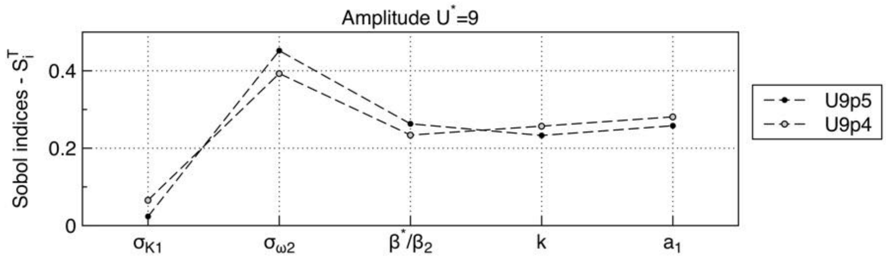

(c) $U^* = 9$

Figure 3.8: Total sensitivity indices S_i^T of the closure coefficients for A^* in RDA.

Plots of interference Sobol indices for A^* and f^* are presented in Fig. 3.10 and Fig. 3.10 respectively. To clarify, only the Sobol indices of coefficients with significant contributions (i.e greater than 0.1) to the uncertainty are highlighted in the plot.
Several similarities have been discovered while examining the uncertainty contributions from the interference Sobol indices for the thee selected reduced velocities. When we

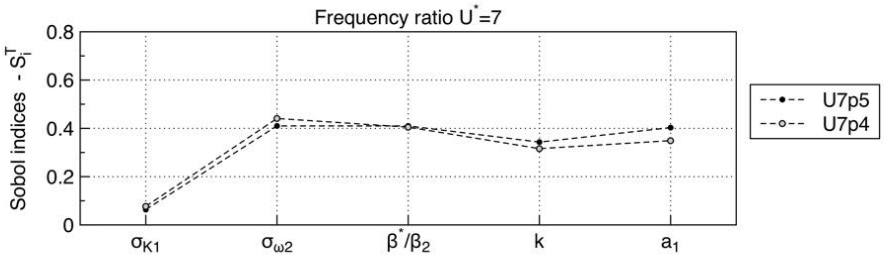

(a) $U^* = 7$

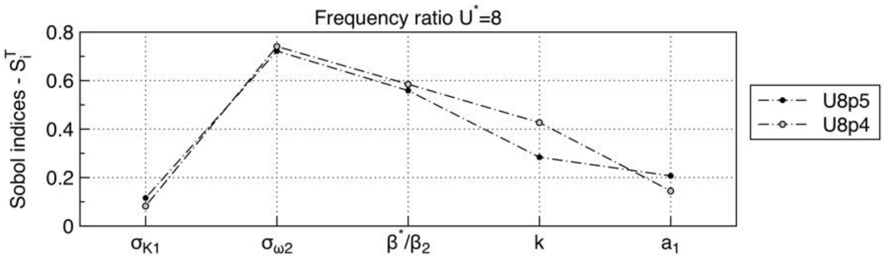

(b) $U^* = 8$

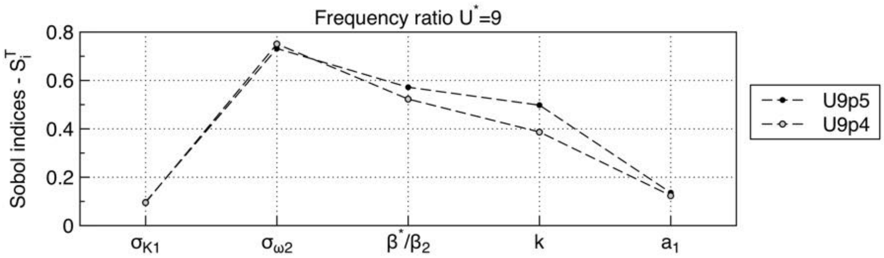

(c) $U^* = 9$

Figure 3.9: Total sensitivity indices S_i^T of the closure coefficients for f^* in RDA.

analyse the output quantity A^*, the largest contribution to the total sensitivity S_i^T indices are from the first-order Sobol indices S_i for all the U^*. The higher contribution comes from the first-order Sobol indices S_{a1} and $S_{\sigma_{\omega_2}}$ for all the velocities.
However, when we analyse the output quantity f^*, the second-order contribution $S_{i,j}$ is significant and sometimes it exceeds the first-order contribution. Third-order terms also make a significant contribution to total uncertainty for the output quantity f^*. Note that the significant uncertainty contribution from the higher-order Sobol indices for f^* are shared between the considered U^*. These are $S_{\sigma_{\omega_2}\beta*/\beta_2}$,$S_{\sigma_{\omega_2}\kappa}$,$S_{\beta*/\beta_2\kappa}$ and $S_{\sigma_{\omega_2}\beta*/\beta_2\kappa}$. We therefore want to highlight the strong link between these three variables. Although the total sensitivity indices show that, in the case of f^*, the greater contribution is given by the variable σ_{ω_2} (Fig. 3.11), the possible calibration of the SST model for the VIV case cannot neglect the contribution also of the variables β^*/β_2 and κ.

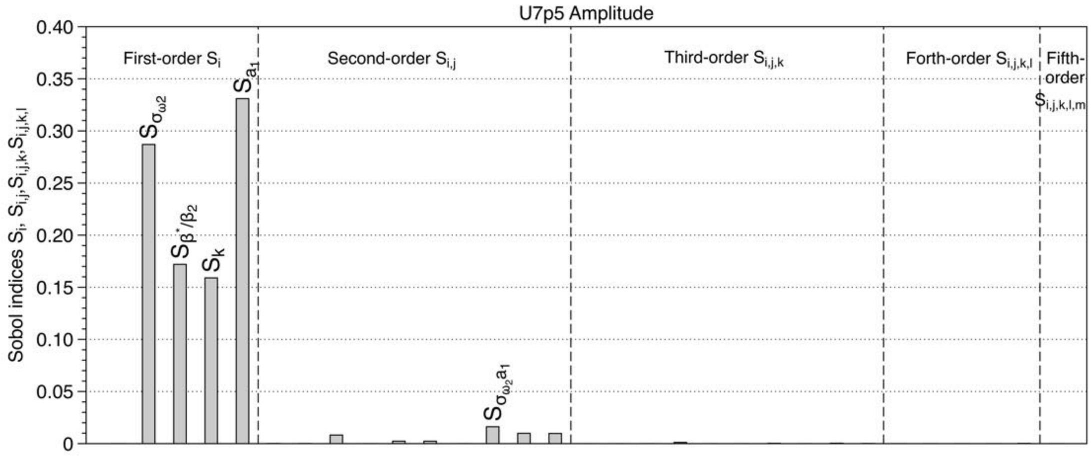

(a) $U^* = 7$

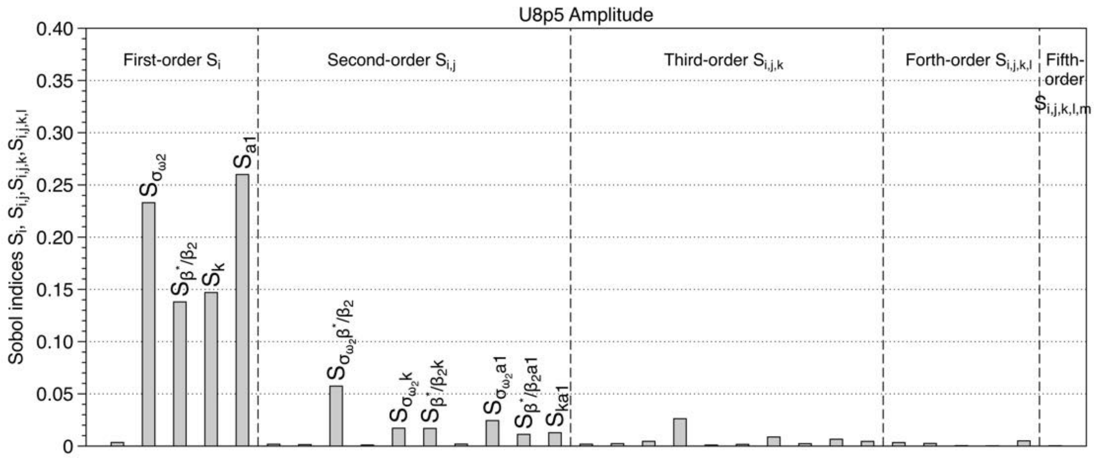

(b) $U^* = 8$

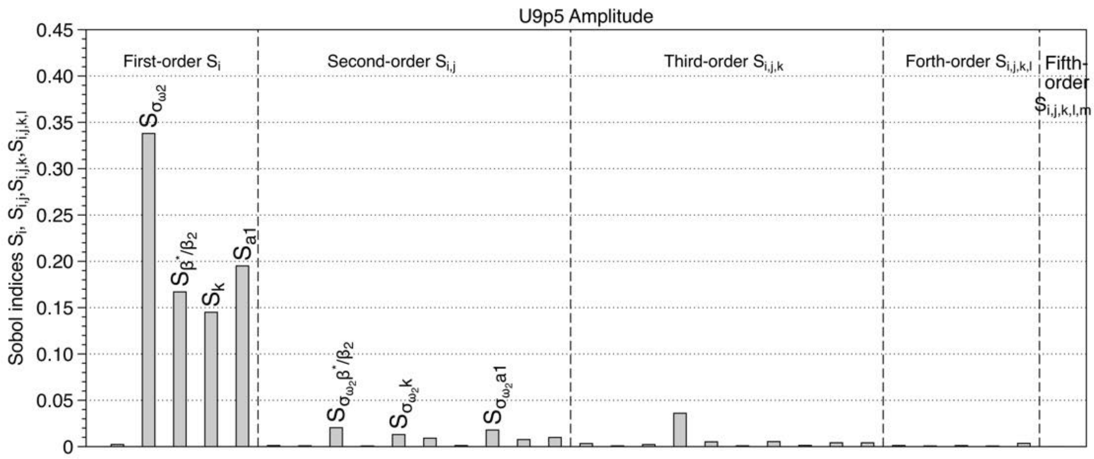

(c) $U^* = 9$

Figure 3.10: Sobol sensitivity indices divided by single terms S_i,$S_{i,j}$, $S_{i,j,k}$,$S_{i,j,k,l}$ and $S_{i,j,k,l,m}$ for A^* ($p = 5$).

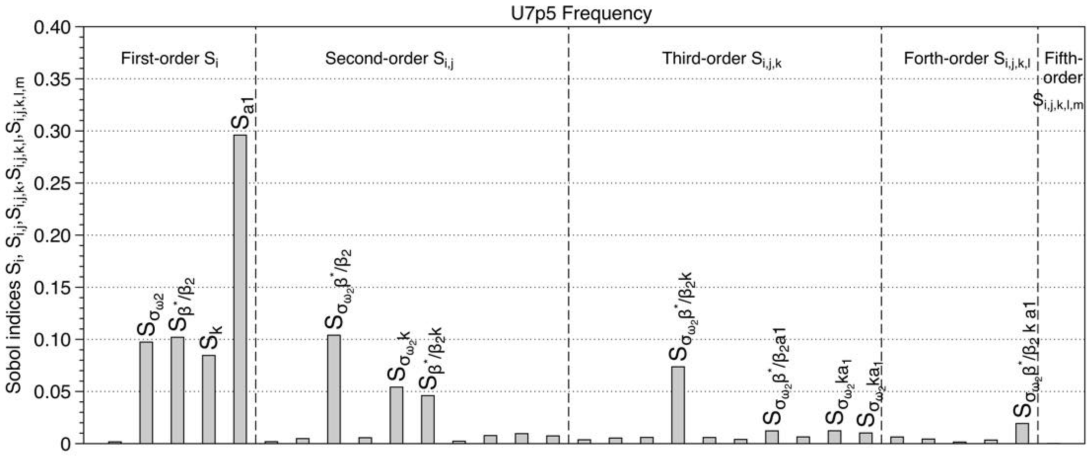

(a) $U^* = 7$

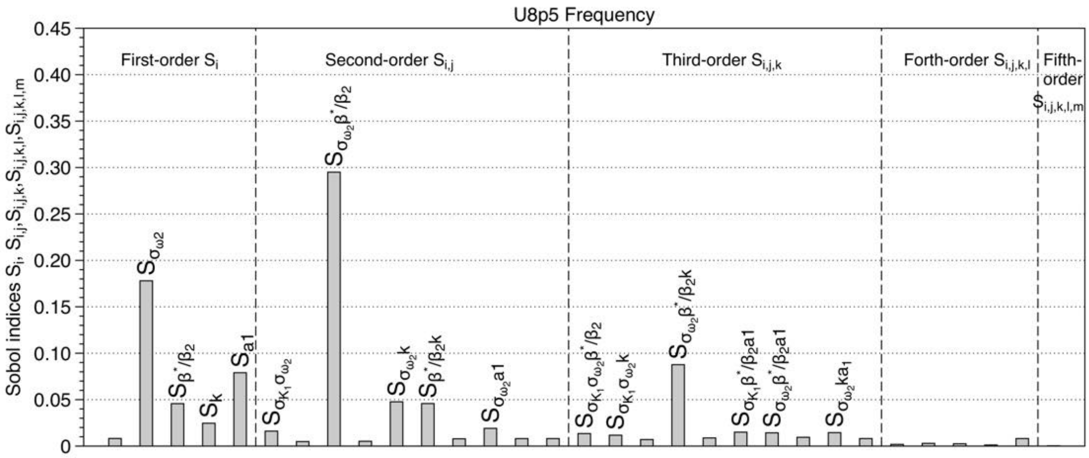

(b) $U^* = 8$

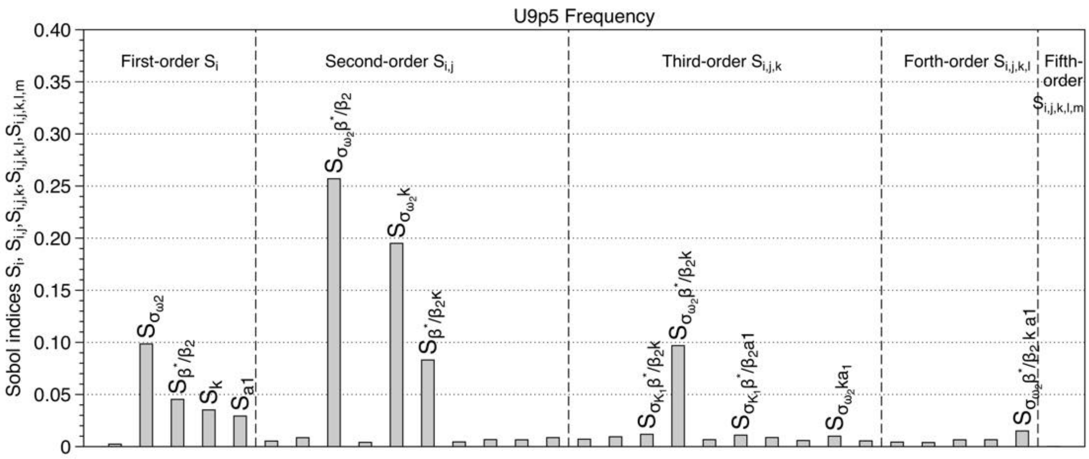

(c) $U^* = 9$

Figure 3.11: Sobol sensitivity indices divided by single terms S_i,$S_{i,j}$, $S_{i,j,k}$,$S_{i,j,k,l}$ and $S_{i,j,k,l,m}$ for f^* in RDA ($p = 5$).

3.4.1 Conclusions

Based on the reduced-dimensionality analysis results we can state that four of the coefficients found are significant in the case of 2D VIV simulation in the lower branch regime. Each of the coefficients, σ_{ω_2}, β^*/β_2,κ and a_1 play an important role for the SST model applied to VIV simulations.

3.5 Comparison with previous studies

In this section we compare the results of the current investigation with the previous studies on this topic. The first studies were conducted by Shaefer et al. [75] involving an Axialsimmetric transonic Bump (ATB), a CFD case involving shock induced flow separation and a RAE2822 transonic problem. A second study was conducted by Erb et al. [79] involving a 2D Zero pressure Gradient Flat Plate (2DZP). Recently, Erb et al. [76] conducted new studies involving an Axisymmetric Shock Wave Boundary Layer interaction (ASWBLI), the validation case including an axisymmetric cylindrical body with a training edge flare of 20 degrees at an upstream Mach number of 7.11.
This comparison aims to analyse how the SST turbulence model uncertainties, originating from the closure coefficients, under the different flows feature (attached or separated flows).
Tab. 3.9 presents a list of the significant closure coefficients in the SST model collected from the previous studies and compared with the present study.
Looking at the significant contributors in Tab. 3.9 it can be observed that there is no common coefficient between the different studies. Each of the coefficients, β^*/β_2 and a_1 play an important role in four of the five cases studied. The coefficients β^*, σ_{ω_1} and σ_{ω_1} plays a significant role for three of the cases studied. Finally, the coefficient κ is significant only for two cases studied. The SST model is therefore extremely sensitive, through its closing coefficients, to the type of numerical simulation to be solved. The only coefficients that seem to have a marginal role are σ_{ω_1} and σ_{ω_2}.

Authors	Case	Coefficients
Schefer et al. [75]	ATB	β^*,σ_{ω_1},β^*/β_1,β^*/β_2, a_1
	RAE2822	β^*,σ_{ω_1},β^*/β_2, a_1
Erb et al. [79]	2DZP	β^*,σ_{ω_2},β^*/β_1
Erb et al. [76]	ASWBLI	σ_{ω_1},σ_{ω_2},β^*/β_2,κ, a_1
Present	2D VIV	σ_{ω_2},β^*/β_2,κ, a_1

Table 3.9: Comparison between present and previous studies of significant closure coefficients in the $k-\omega$ SST model

3.6 Final remarks

The purpose of this chapter has been to present the results of an uncertainty analysis study for the $k-\omega$ SST turbulence model due to the epistemic uncertainty in closure coefficients for bi-dimensional simulation of VIV for a circular cylinder with 1-DOF. Sensitivity analysis has been performed to rank the uncertainty contribution of each coefficient to two output quantities: the adimensional amplitude and frequency ratio.The results of the current study identify a set of four coefficients that contribute most to uncertainty quantities. These are σ_{ω_2}, β^*/β_2, κ and a_1. The findings of the present studies have been compared to the previous works focusing on these topics. From the comparison it has been found that the uncertainty contribution of each coefficient changes depending on the problem under consideration. The only coefficients that do not participate significantly in the uncertainty of the SST turbulence model are σ_{ω_1} and σ_{ω_2} for all the considered studies.
The present findings will contribute to improving the knowledge of the parametric uncertainty of these closure coefficients in URANS simulations for flow problems including the vortex-induced vibration on circular cylinder.

In the next chapter, a single-degree-of-freedom multi-frequency *sdof-mf* model for the Vortex Shedding induced force will be proposed. The proposed model splits the total hydrodynamic force acting on the cylinder into conventional Morison-like inertia and drag terms related to the cylinder motion in calm water and three harmonic terms that account for the lift force induced by vortex shedding. The novelty of this model will be the no Fourier relationship of the three harmonic that will be considered.

Chapter 4

Parameter identification of a single-degree-of-freedom multi-frequency model

In this chapter a single-degree-of-freedom multi-frequency *sdof-mf* model for the Vortex Shedding induced force is proposed where a Parameter Identification (PI) method is applied in order to compute the unknown parameters of the *sdof-mf*. The proposed model splits the total hydrodynamic force acting on the cylinder in conventional Morison-like inertia and drag terms related to the cylinder motion in calm water and three harmonic terms that account for the lift force induced by vortex shedding. These harmonics are assumed to have no mutual (Fourier) relationship. Their amplitudes, frequencies and phase lags (unknown parameters) can be computed by tuning the *sdof-mf* model to available data, either experimental or numerical. In this study, the parameters are identified by a PI procedure in a wide range of the (non-dimensional) incident flow velocity available from the numerical simulations performed in the context of this study.

This chapter is organised following the time line of the conducted studies. In the following, the proposed *sdof-mf* model and the related parameter identification strategy are described. Then the results concerning the three subsequent studies made are presented. As a first study the results obtained with *sdof-mf* model applied to a VIV problem of a single elastically-mounted 2D cylinder are discussed. Secondly the studies focus on the influence of mass ratio m^* on the fluid body interaction and on cylinder. And finally, in order to overcome the problems encountered by the 2D simulations, the adoption of more sophisticated 3D URANS simulations are considered.

4.1 Mathematical Model

The governing equations of the proposed single-degree-of-freedom multi-frequency *sdof-mf* model are presented first.
Afterward, the Parameter Identification (*PI*) strategy used to compute the unknown parameters of the *sdof-mf* model is outlined.
The *PI* methodology is general, in fact it could be applied to any experimental or numerical VIV time-domain data.

4.1.1 Cylinder dynamics and sdof-mf model

According to the system sketched in Fig. 1.2, the cylinder motion (one degree of freedom, 1-DoF) in fluid at rest can be modelled as:

$$M\,\ddot{y} + H\,\dot{y} + K\,y = F_{SF}(t), \tag{4.1}$$

$F_{SF}(t)$ is the hydrodynamic force in Still Fluid (SF).
It is recognized [80, 81] that $F_{SF}(t)$ can be expressed consistently and accurately as the sum of Morison-like inertia and quadratic drag terms (Eq. (4.2)).

$$F_{SF}(t) = -M_A\,\ddot{y} - Q\,\dot{y}|\dot{y}|. \tag{4.2}$$

In the above equation $M_A = C_A\rho\frac{\pi D^2}{4}S$ is the added mass, where C_A is the added mass coefficient. Q is given by $Q = \frac{1}{2}C_D\rho DS$, where C_D is the drag coefficient.
After substitution, Eq. (4.1) becomes:

$$(M + M_A)\,\ddot{y} + H\,\dot{y} + Q\,\dot{y}|\dot{y}| + K\,y = 0. \tag{4.3}$$

Adopting the energy balance method under the assumption of a quasi-steady state harmonic response of amplitude A and frequency $2\pi f$, the equivalent linear drag Q_{eq} is easily computed as $Q_{eq} = \frac{8}{3\pi}Q2\pi fA$ so that Eq. (4.3) can be rewritten as

$$(M + M_A)\,\ddot{y} + (H + Q_{eq})\,\dot{y} + K\,y = 0. \tag{4.4}$$

The effect of this assumption is showed in Fig. 4.1. C_A and C_D can be derived from consolidated experimental data according to the Keulegan-Carpenter and Reynolds numbers of the specific system [80].

In the presence of current U, Eq. (4.1) is modified in order to include the additional force $F_{VS}(t)$ that rises from the vortex shedding (VS) process. Thus Eq. (4.1) turns into Eq. (4.5)

$$M\,\ddot{y} + H\,\dot{y} + K\,y = F_{SF}(t) + F_{VS}(t) \tag{4.5}$$

and the substitution of Eq. (4.2) in Eq. (4.5) leads to

$$(M + M_A)\,\ddot{y} + H\,\dot{y} + Q\,\dot{y}|\dot{y}| + K\,y = F_{VS}(t). \tag{4.6}$$

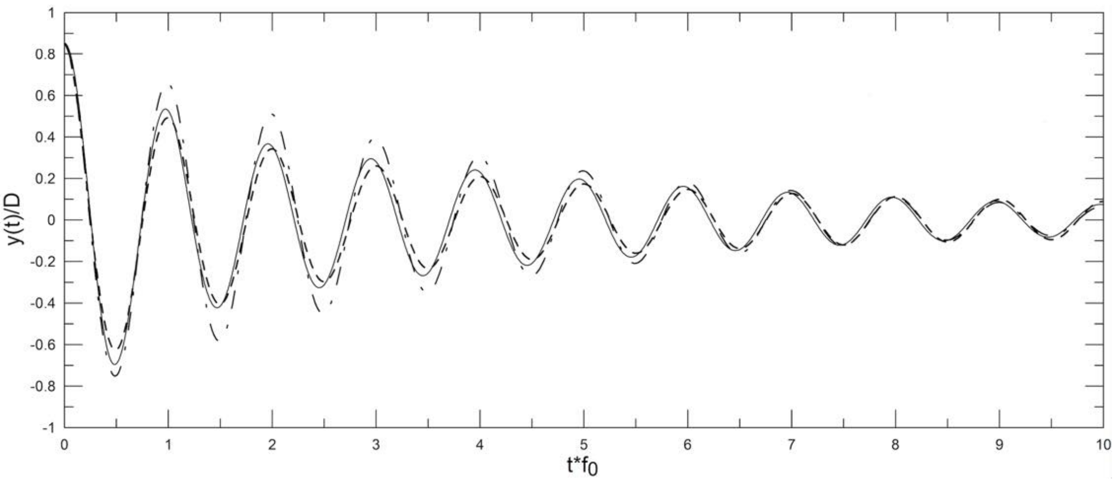

Figure 4.1: Free decay in still water. Solid line = CFD; dashed line = Eq. (4.1); dashed-dotted line = Eq. (4.3)

Assuming that the added mass and drag coefficients are known a priori or from specific tests (free decay or forced oscillations), the splitting of the total force in standard inertia/drag $F_{SF}(t)$ and vortex shedding $F_{VS}(t)$ terms, i.e $F_L(t) = F_{SF}(t) + F_{VS}(t)$, allow the RHS of Eq. (4.6) to be examined in detail.
At this stage, it is important to point out that, as a first approximation, the force and/or the response might be assumed monochromatic [15]. This is true in most of the U^* range, with some distinctions. Nevertheless (see Fig. 4.3 later on), it seems that the approximation of the vortex shedding force $F_{VS}(t)$ could be considerably improved taking into account the contribution of a larger number of harmonics. The additional requirement, for the improvement to be effective, is that these frequencies must be totally independent from each other (not Fourier dependent). In non-dimensional form, $F_{VS}(t)$ can be written conveniently as:

$$\frac{F_{VS}(t)}{F_0} = C_{VS}(t) \approx C_{VS_{mf}}(t), \tag{4.7}$$

where the non-dimensional vortex shedding lift force $C_{VS_{mf}}(t)$ is written as:

$$\begin{aligned} C_{VS_{mf}}(t) = \overline{C_{VS_1}} \sin(2\pi \cdot f_{\mathrm{St}} \cdot \theta_1 \cdot t + \phi_1) \\ +\overline{C_{VS_2}} \sin(2\pi \cdot f_{\mathrm{St}} \cdot \theta_2 \cdot t + \phi_2) \\ +\overline{C_{VS_3}} \sin(2\pi \cdot f_{\mathrm{St}} \cdot \theta_3 \cdot t + \phi_3). \end{aligned} \tag{4.8}$$

In Eq. (4.7),(4.8) the subscript mf stands for the *multi-frequency* model. $F_0 = \frac{1}{2}\rho DSU^2$ is a reference force and $f_{\mathrm{St}} = \mathrm{St} \cdot U/D$ is the Strouhal frequency, where St is the Strouhal number.

$\overline{C_{VS_i}}$, θ_i and ϕ_i $(i = 1, 3)$ are nine unknown parameters. They are assumed to be functions of U^*. In the following the RHS of Eq. (4.8) is identified in compact form as $C_{VS_{mf}}(t)$. The subscript mf stands for *multi-frequency* model.

4.1.2 Parameter Identification

For a given U^* and for a sufficiently long time series obtained from experimental measurements or CFD simulations, a subset (*stationary time window*) of the time record can be selected for the analysis. In this subset the stationary harmonic condition of the cylinder motion and related forces must be reasonably fulfilled.

For that U^* and that time-series subset:
i) Eq. (4.6) and Eq. (4.8) describe the stationary (frequency-domain) part of the fluid-body interaction due to vortex shedding;
ii) the nine unknown parameters ($\overline{C_{VS_i}}$, θ_i, ϕ_i $(i = 1, 3)$) can be assumed to be constant (time independent).

Since the vortex shedding component $F_{VS}(t)$ can be computed as $F_{VS}(t) = F_L(t) - F_{SF}(t)$, the LHS of Eq. (4.8) is known (from experiments or simulations) and a least-square fitting can be applied to the RHS of Eq. (4.8) to determine the unknown parameters (PI). Thus, for any U^* obtained with simulations or experiments, given N_s time-domain samples of the vortex shedding non-dimensional force $C_{VS}(t_j)$, the best fit model can be found setting χ^2 to its minimum, where:

$$\chi^2 = \sum_{j=1,N_s} [C_{VS}(t_j) - C_{VS_{mf}}(t_j)]^2. \tag{4.9}$$

The Levenberg-Marquardt iterative alghorithm [82, 83, 84], explained in detail in the appendix A, is here used for the purpose.

Under these premises, the computations have been performed using the URANS approach in combination with the workhorse Shear Stress Transport turbulence model. The accuracy of the expected and obtained numerical results has been assumed adequate for this first-step investigation (*sdof-mf* + *PI*).

4.2 VIV analysis of a single elastically-mounted 2D cylinder

The results obtained with the *sdof-mf* model together with the application of the Parameter Identification are discussed in paragraph 4.3.2. In particular the VIV time series, obtained by 2D URANS-based CFD simulations, are used to identify the unknown parameters of the *sdof-mf* model.
The results achieved so far within a computationally cheap 2D URANS approach are considered good enough for the main purposes of this first-step study, focused on the development and analysis of the *sdof-mf*.

4.2.1 Numerical results

Although the CFD results obtained for the case $m* = 2.4$ have already been discussed in detail in Sec.2.3, a brief summary of what has already been said is given again here.
Before presenting the results obtained with the *sdof-mf* model, the total hydrodynamic force coefficient C_L and the vortex shedding force coefficient C_{VS} are reported as reference in Fig. 4.2(a) as function af reduced velocity U^*. Since the time series of $C_L(t)$ and $C_{VS}(t)$ are generally everything but monochromatic, the amplitude is here defined as the average between the absolute values of maxima and minima.
In the same Fig. 4.2 the non-dimensional dominant frequency of the motion $f^* = f/f_0$ are shown. In Fig. 4.2(b) the oblique dashed line corresponds to the Strouhal frequency St = 0.20 or multiple of the St as shown in detail in the figure. While the horizontal dashed line, in the same Fig. 4.2(b), marks the lower branch frequency, obtained from Eq. (1.42), and when the frequency ratiof^* are equal to 1 (response frequency are equal to the natural frequency in water $f = f_0$).
Vertical dashed lines, in Fig. 4.2, marks the boundaries of branches in accordance with the literatures as presented in Sec. 1.4. In particular the start of the lower branch region has been obtained from the Eq.(1.45) while the end of lower branch (end of the synchronisation) has been obtained from Eq. (1.48). The start of the upper branch has been obtained with interpolation technique from the Fig. 1.14 considering the selected mass ratio ($m^* = 2.4$).

The total force (Fig. 4.2(a)) shows a rapid increase in its amplitude between the initial and upper branch, where it peaks. After the peak it drops sharply at the transition from upper to lower. Finally, the total force further decreases along the lower branch and desynchronisation regime. The vortex shedding force remains constant in the initial branch. It rises in the upper branch peaking at the upper-lower transition. It then drops slowly as the reduced velocity increase.
Fig. 4.2(b) shows the frequency ratio $f^* = f/f_0$ versus the reduced velocity U^*, according to Fast Fourier Transform (FFT) analysis of the cylinder displacement. Frequencies f associated to the two main peaks of the amplitude spectrum are shown. For $U^* < 4.76$ a double peak behaviour is found, the lower being the Strouhal frequency, the upper being the natural frequency in still water. For $U^* > 7.73$ the frequency ratio seems to be no

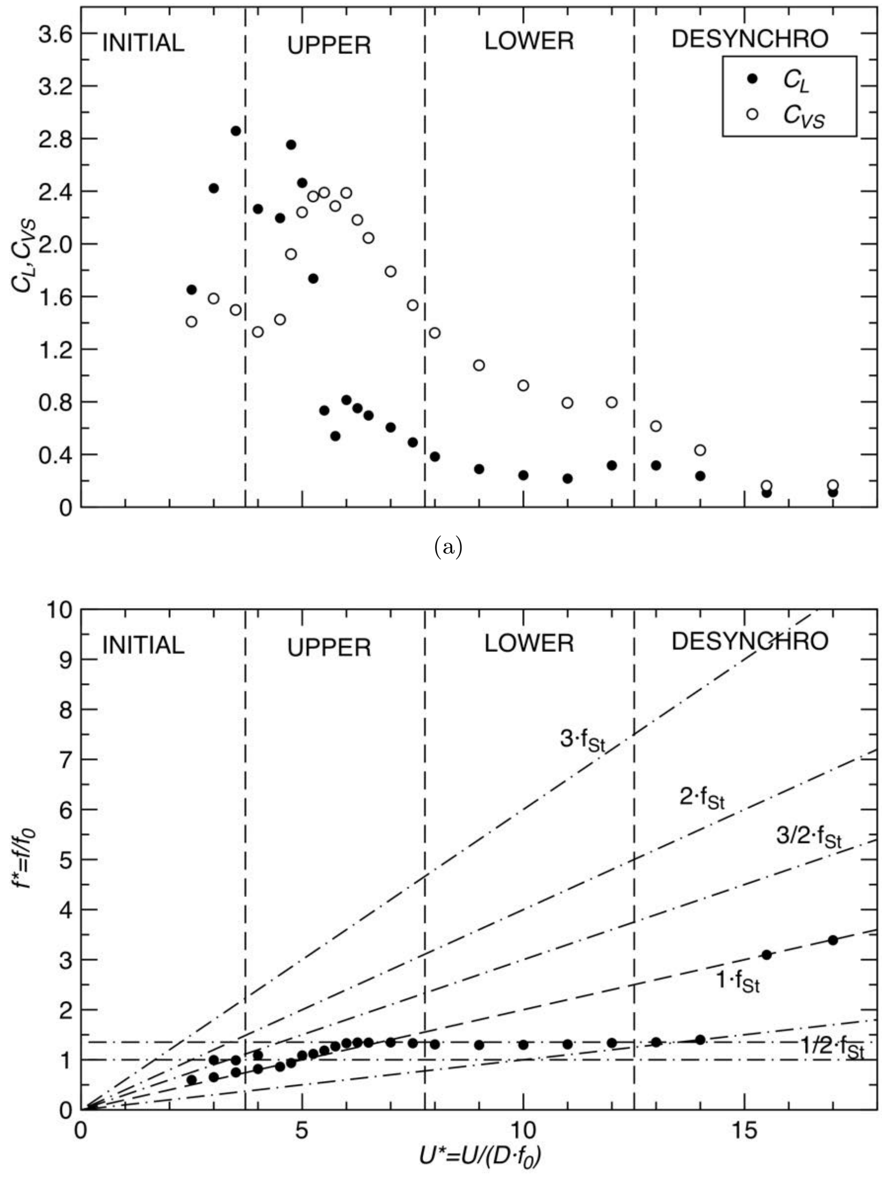

(a)

(b)

Figure 4.2: Total force coefficient C_L, vortex Shedding force coefficient C_{VS} and frequency ratio f^* variation with U^*.

longer dependent on U^* and it flattens out around $f/f_0 \approx 1.35$. This is a known behavior at lock-in [15]. Some authors [85] ascribe this increment of the natural frequency to a lower value of the added mass.

In our view, comparing the hydrodynamic forces that rise in free oscillation of the cylinder in calm water condition (not shown) and in incident flow, vortex shedding introduces a new transverse force. Depending on the value of U^*, this force can be in anti-phase with the inertia term of Eq. (4.2), thus giving an overall effect that leads to an apparent reduction (even to negative values) of the added mass.
Back to the present results, as the reduced velocity U^* enters the range $11.899 < U^* < 13.089$, f^* splits into two branches, the lower being 1.35 as for lower U^*, the upper being the Strouhal frequency. This sudden increase in oscillation frequency is accompanied by a rapid drop of the amplitude of oscillation and it is related to the end of the synchronisation range.
Summarising, even though there is large room for improvement, the current computed VIV time series can be assumed as a reference data for a first-step analysis conducted with the proposed *sdof-mf* model and PI.

4.2.2 Sdof-mf model and Parameter Identification

With reference to Eq. (4.6) and Eq. (4.8), the results discussed in the following are obtained assuming standard values of the added mass/drag coefficients and a standard value of the Strouhal number for sub-critical regime, i.e. $C_A = 1.0$, $C_D = 1.6$ and $\mathrm{St} = 0.2$ [80, 81].

In Fig. 4.3 the amplitude spectra of $F_{VS}(t)/F_0$ is shown for six representative flow regimes, namely $U^* = 3.00, 4.75, 5.50, 9.00, 10.00, 13.00$. CFD data are analysed at harmonic steady state, i.e. without transient effects induced by the warm-up of the simulation, either physical or numerical.

Fig. 4.4 compares the non-dimensional time-domain vortex shedding force obtained with CFD simulations and with the *sdof-mf* model. They refer to the same values of U^* used in Fig. 4.3. Solid thin lines represent CFD data $C_{VS}(t)$, dashed thick lines represent the *sdof-mf* model $C_{VS_{mf}}(t)$; for the sake of completeness, dashed thin lines represent the total force $C_L(t) = F_L(t)/F_0$.

From both spectral (Fig. 4.3) and time-domain (Fig. 4.4) analyses, it is evident that vortex-shedding force $F_{VS}(t)$ is not well suited for a monochromatic model for any U^*, whereas it can be approximated well by three harmonics in the whole U^* range investigated. However, the peak frequencies of these harmonics look totally independent from each other so that a standard frequency analysis does not allow us to identify the frequency values sharply.

Fig. 4.5 shows the non-dimensional cylinder displacement versus non-dimensional time, for the same values of U^* used in Fig. 4.3 and Fig. 4.4. Solid thin lines represent CFD data, dashed thick lines represent the time integral of the *sdof-mf* model, using Eq. (4.6) and (4.8).

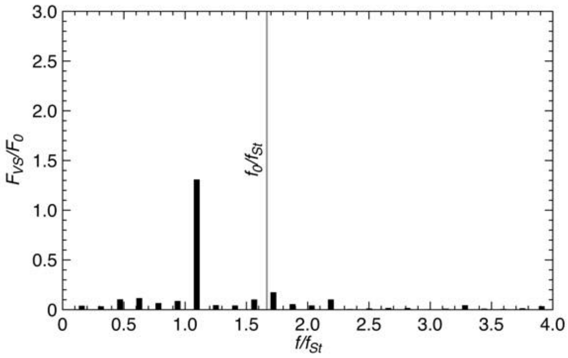

(a) Re = 2521, $U^* = 3.00$

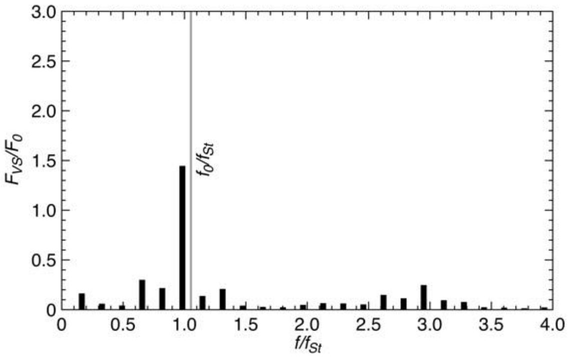

(b) Re = 3992, $U^* = 4.75$

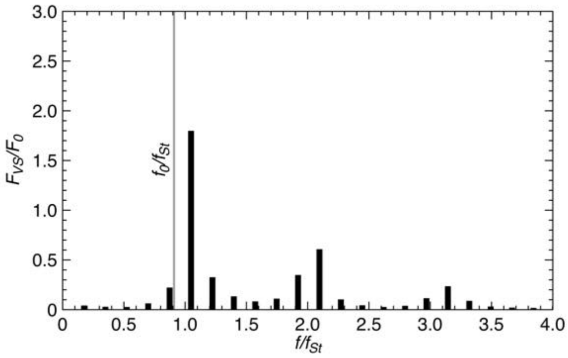

(c) Re = 4622, $U^* = 5.50$

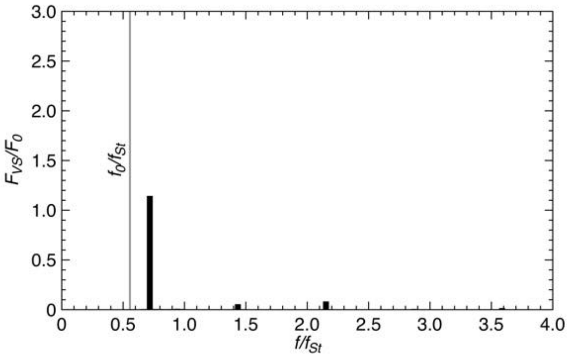

(d) Re = 7563, $U^* = 9.00$

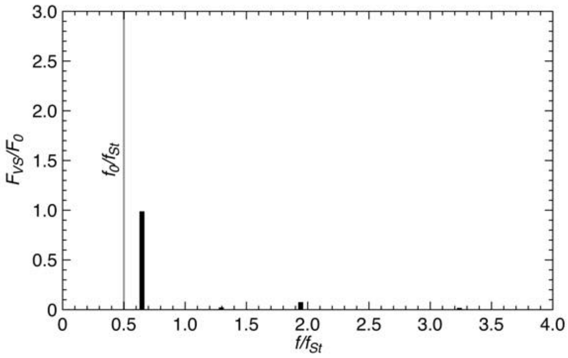

(e) Re = 8404, $U^* = 10.00$

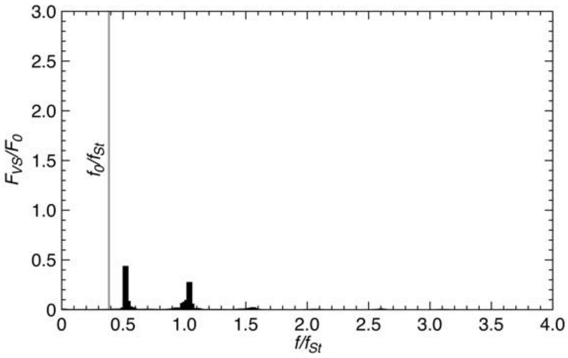

(f) Re = 10925, $U^* = 13.00$

Figure 4.3: Amplitude spectra of the non-dimensional vortex shedding force $F_{VS}(t)/F_0$ versus f/f_0. Spectral analysis is conducted on the stationary part of the signal, without transient effects. Vertical lines correspond to the non-dimensional Strouhal frequency f_{St}/f_0.

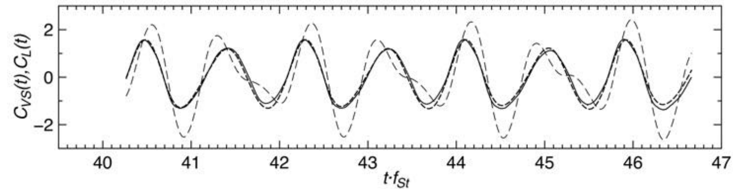

(a) Re = 2521, $U^* = 3.00$

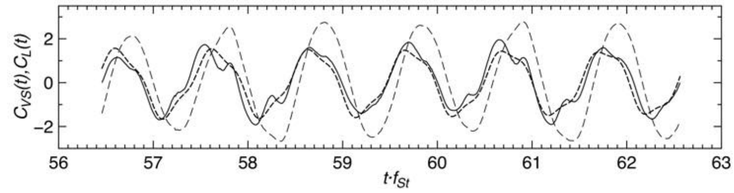

(b) Re = 3992, $U^* = 4.75$

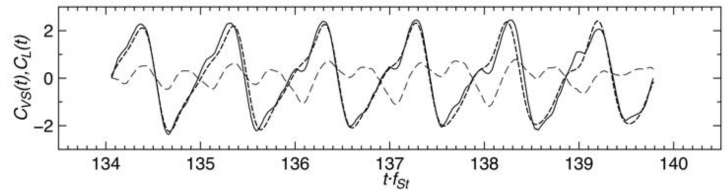

(c) Re = 4622, $U^* = 5.50$

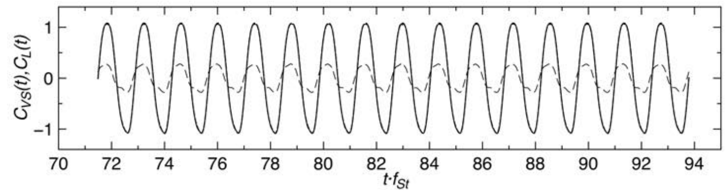

(d) Re = 7563, $U^* = 9.00$

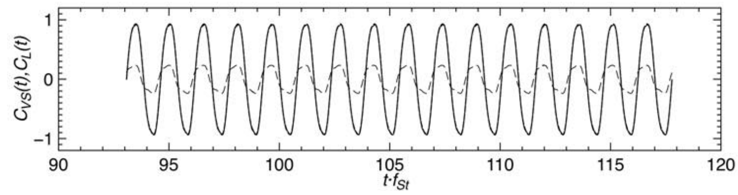

(e) Re = 8404, $U^* = 10.00$

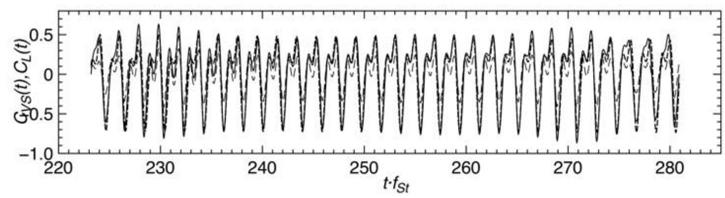

(f) Re = 10925, $U^* = 13.00$

Figure 4.4: Time series of the vortex shedding force for a given U^*. Solid thin line = CFD; dashed thick line = *sdof-mf* model in Eq. (4.6) and Eq. (4.8).

From the presented figures of the forcing terms Fig. 4.4 and of the amplitude of response Fig. 4.5, it can be observed that the proposed *sdof-mf* model captures/reproduces the vortex shedding force and consequently the cylinder motion very well, even for complex cylinder response (e.g. Fig. 4.5(a) and Fig. 4.5(f)). However, there are some noteworthy exceptions. Despite the worst fitting of the force for the case $U^* = 4.75$, showed in Fig. 4.4(b), the cylinder displacement obtained with the *sdof-mf* is rather good (Fig. 4.5(b)).

Fig. 4.6(a) and Fig. 4.6(b) show the behaviour of the non-dimensional amplitudes and frequencies of $F_{VS}(t)$, namely $\overline{C_{VS_i}}$ and $(f_i/f_0) = \theta_i \cdot f_{\mathrm{St}}/f_0$ $(i = 1, 3)$ versus U^* respectively.

From these plots, $F_{VS}(t)$ exhibits a basically monochromatic behaviour, with dominant frequency that switches back-and-forth between Strouhal and *lock-in* frequencies. The additional two frequencies may be especially pronounced, in particular in the transient zones of U^*, where the response of the cylinder changes domain of attraction (jump of amplitude A^*) and the response of the cylinder is large and complex.
In Fig. 4.6(a) and Fig. 4.6(b), the parameters obtained are collected and presented according to the characteristic frequency. Solid circles correspond to the term closest to the Strouhal frequency in the entire U^* range investigated (from now on labeled as component C1 of $F_{VS}(t)$). Empty circles (component C2) correspond to the *lock-in* frequency term or, as long as the upper branch of the response exists in the range $4.5 < U^* < 8$, it behaves as the double Strouhal frequency. Finally triangles (component C3) correspond to the triple Strouhal frequency up to $U^* \approx 8$. For higher U^* values, this frequency flattens out at the triple *lock-in* frequency. In general, amplitudes $\overline{C_{VS_i}}$ and frequencies (f_i/f_0) of the *sdof-mf* model show an extremely fair and consistent behaviour with U^*. As expected, there is a dominant frequency, either Strouhal or *lock-in* frequency, that provides the bulk of forces and motion. However, lower and higher harmonics give a fundamental contribution, mostly in the transient regimes between one domain of attraction to the next where the multi-frequency behaviour is evident.

The data presented in Fig. 4.6(c) are the phase lags of component C2 and C3 related to component C1. They are computed according to the time lag between two adjacent zero crossing up and using the Strouhal period $T_{\mathrm{St}} = 1/f_{\mathrm{St}}$ as time scale, as follows

$$\phi_{2,3} = \frac{t_{zero-up_{C2,3}} - t_{zero-up_{C1}}}{T_{\mathrm{St}}}. \tag{4.10}$$

It is worth noting that phase lags become important where the corresponding amplitudes $\overline{C_{L,C2}}$ or $\overline{C_{L,C3}}$ are non negligible, typically in the transient zones of U^*, as discussed above.
In these regions, $\phi_{2,3}$ can be well approximated by $\phi_{2,3} \approx 0.3$. Outside these regions, $\phi_{2,3}$ can be set to any value since the corresponding amplitudes are negligible.

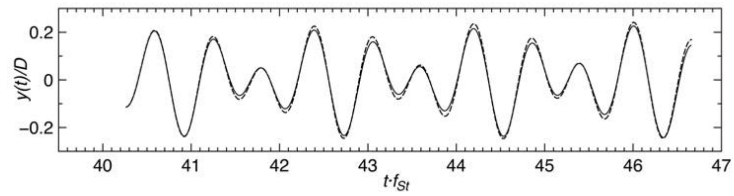

(a) Re = 2521, $U^* = 3.00$

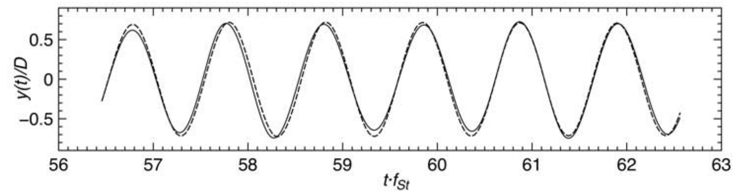

(b) Re = 3992, $U^* = 4.75$

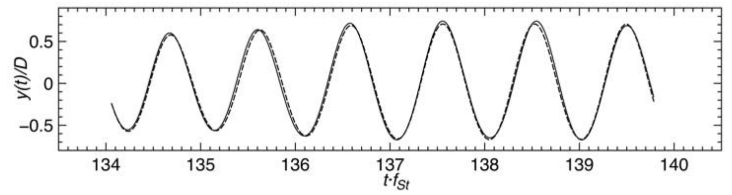

(c) Re = 4622, $U^* = 5.50$

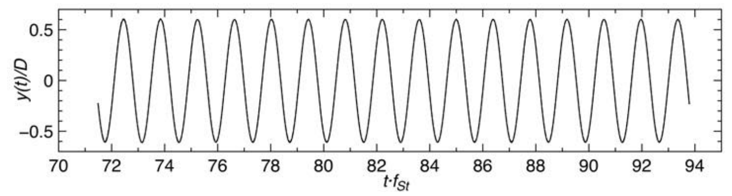

(d) Re = 7563, $U^* = 9.00$

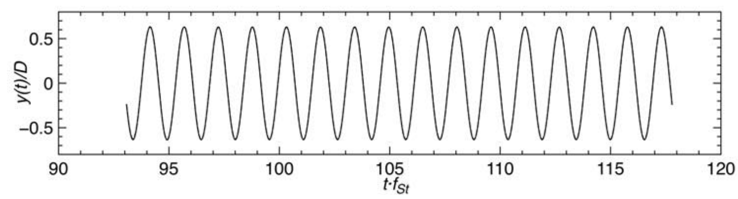

(e) Re = 8404, $U^* = 10.00$

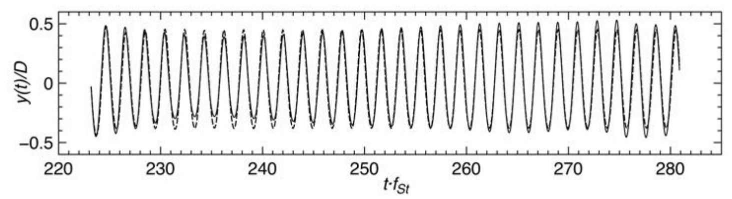

(f) Re = 10925, $U^* = 13.00$

Figure 4.5: Time series of the non-dimensional cylinder motion for a given U^*. Solid thin line = CFD; dashed thick line = *sdof-mf* model in Eq. (4.6) and Eq. (4.8).

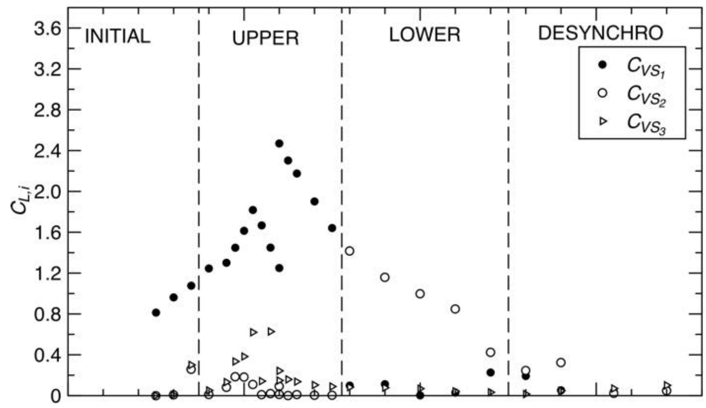

(a)

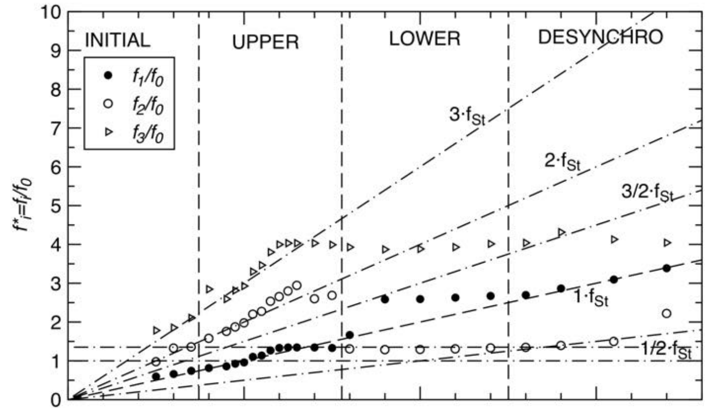

(b)

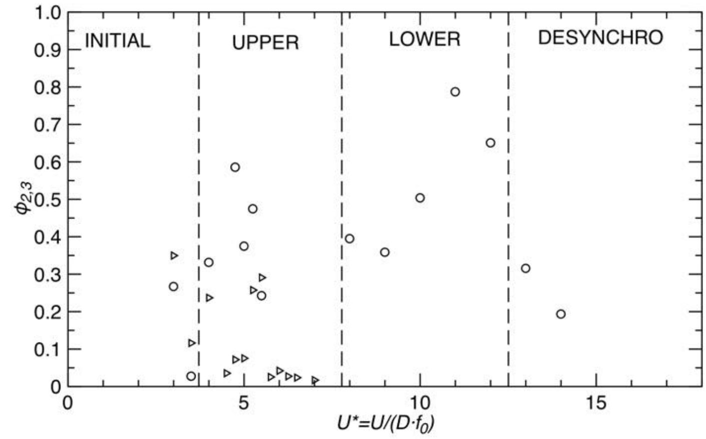

(c)

Figure 4.6: Parameters of the *sdof-mf* model versus U^*. ($\bullet$) = closest term to the Strouhal frequency in the entire U^* range investigated (C1). ($\circ$) = term related to the *lock-in* frequency or the double Strouhal frequency (C2). ($\rhd$) = term related to the triple Strouhal frequency or the triple lock-in frequency (C3).

4.2.3 Conclusions

In this section the Vortex Induced Vibrations (VIV) of an elastically-mounted 2D circular cylinder in cross flow with low mass and damping ratios, have been analysed in the frame of a single-degree-of-freedom multi-frequency (sdof-mf) model. VIV data have been obtained by 2D URANS-based CFD simulations. The Parameter Identification (PI) method, has been applied in the time domain to VIV data, in order to obtain amplitudes, frequencies and phases of the *sdof-mf* model. The unknown parameters obtained via PI show a fair and consistent variation with U^* over the entire range investigated.
From the results obtained, it is possible to state that the proposed *sdof-mf* model exhibits rather promising capabilities in the reproduction of the vortex shedding forces and cylinder motion, in terms of both amplitudes and frequencies, even in complex detached flow condition.

In order to improve the current *sdof-mf* model, the ongoing work is to apply the *sdof-mf* model to different system parameters, for instance mass and damping ratios. In particular, the study of different the mass ratio, within the range of engineering practice, will be presented in the next section.

4.3 Effect of mass ratio on the cylinder motion

In this section we want to analyse if the proposed *sdof-mf* model is allowed to examine the effect induced on hydrodynamic forces by different mechanical properties of the system. The analysis is carried out in a parametric way, focusing on the influence of mass ratio m^* on the fluid-body interaction and on the cylinder. Specifically the effect of m^* on the components of the vortex shedding lift force obtained by the force decomposition adopted in the *sdof-mf* model.

Therefore the mass ratio m^* has been changed systematically three times around a reference value whose VIV data are available [17, 15]. Mass and mechanical damping ratios are assumed small, still with values related to marine engineering applications. Following these considerations, the selected mass ratio where $m^* = 1.2, 2.4$ and 3.6. The value $m^* = 2.4$ is here taken as main reference (correspond with the previously presented experiments of [15]). For every mass ratio m^* considered, a large number of reduced velocities U^* is taken into account.
Tables 4.1 and 4.2 give further details, definitions and the full set of parameters of interest.

Cylinder diameter	D	(m)	$3.81 \cdot 10^{-2}$
Cylinder length	S	(m)	$2.50 \cdot 10^{-2}$
Cylinder volume	$\frac{\pi D^2}{4} S$	$\left(\mathrm{m}^3\right)$	$2.85 \cdot 10^{-5}$
Spring stiffness	K	$\left(\frac{\mathrm{N}}{\mathrm{m}}\right)$	1.661
Structural damping	H	$\left(\frac{\mathrm{N}}{\mathrm{m/s}}\right)$	$4.344 \cdot 10^{-3}$
Potential added mass	M_A	(kg)	$2.847 \cdot 10^{-2}$
Potential added mass coefficient	$C_A = \frac{M_A}{\rho \frac{\pi D^2}{4} S}$	$(-)$	1.0
Reynolds number range	Re	$(-)$	$\approx 0.2 \div 2.7 \cdot 10^4$

Table 4.1: Fixed parameters.

Mass ratio	$m^* = \frac{\mathbf{M}}{\pi\,\rho \mathbf{D^2 S/4}}$	$(-)$	**1.2**	**2.4**	**3.6**
Cylinder mass	M	(kg)	$3.42 \cdot 10^{-2}$	$6.83 \cdot 10^{-2}$	$10.25 \cdot 10^{-2}$
Damping Ratio	$\zeta = \frac{H}{2\sqrt{K(M+M_A)}}$	$(-)$	$6.734 \cdot 10^{-3}$	$5.416 \cdot 10^{-3}$	$4.657 \cdot 10^{-3}$
Mass-damping parameter	$m^*\,\zeta$	$(-)$	$8.08 \cdot 10^{-3}$	$13.00 \cdot 10^{-3}$	$16.76 \cdot 10^{-3}$
Modified mass-damp. parameter	$(m^* + C_A)\,\zeta$	$(-)$	$14.81 \cdot 10^{-3}$	$18.41 \cdot 10^{-3}$	$21.42 \cdot 10^{-3}$
Undamped natural frequency in air	$f_{0,a} = \frac{1}{2\pi}\sqrt{\frac{K}{M}}$	(Hz)	1.1100	0.7846	0.6408
Undamped natural frequency in water	$f_0 = \frac{1}{2\pi}\sqrt{\frac{K}{M+M_A}}$	(Hz)	0.8198	0.6592	0.5669

Table 4.2: Varying parameters.

4.3.1 Numerical results

Starting from the motion amplitude, considering Fig. 4.7, it is possible to note that at the upper branch the *maximum value* of the non-dimensional amplitude of the cylinder motion, namely A^*_{max}, is achieved for $U^* \approx 5.25$. Furthermore A^*_{max} decreases approximately from 0.98 to 0.77, as m^* increases from 1.2 to 3.6. At the lower branch $A^*_{max} \approx 0.6$. With reference to the attitude of the max value of A^* while varying $m^*\zeta$, [10] presents the results of several research works from the literature. They show the maximum value of A^* at the upper and lower branches separately Vs the modified mass-damping parameter (see also Tables 4.1 and 4.2).
In Fig. 4.8 the results of the present simulations are compared with the experimental data given by [10]. The upper limit of the lower branch of U^* decreases from $U^* \approx 12$ to $U^* \approx 9.5$ as m^* increases. In Fig. 4.7, the vertical dashed lines, marks the boundaries of branches. The start of the lower branch region has been obtained from the Eq.(1.45) while the end of lower branch (end of the synchronisation) has been obtained from Eq. (1.48). The start of the upper branch has been obtained with interpolation technique from the Fig. 1.14 for the corresponding mass ratio m^*.

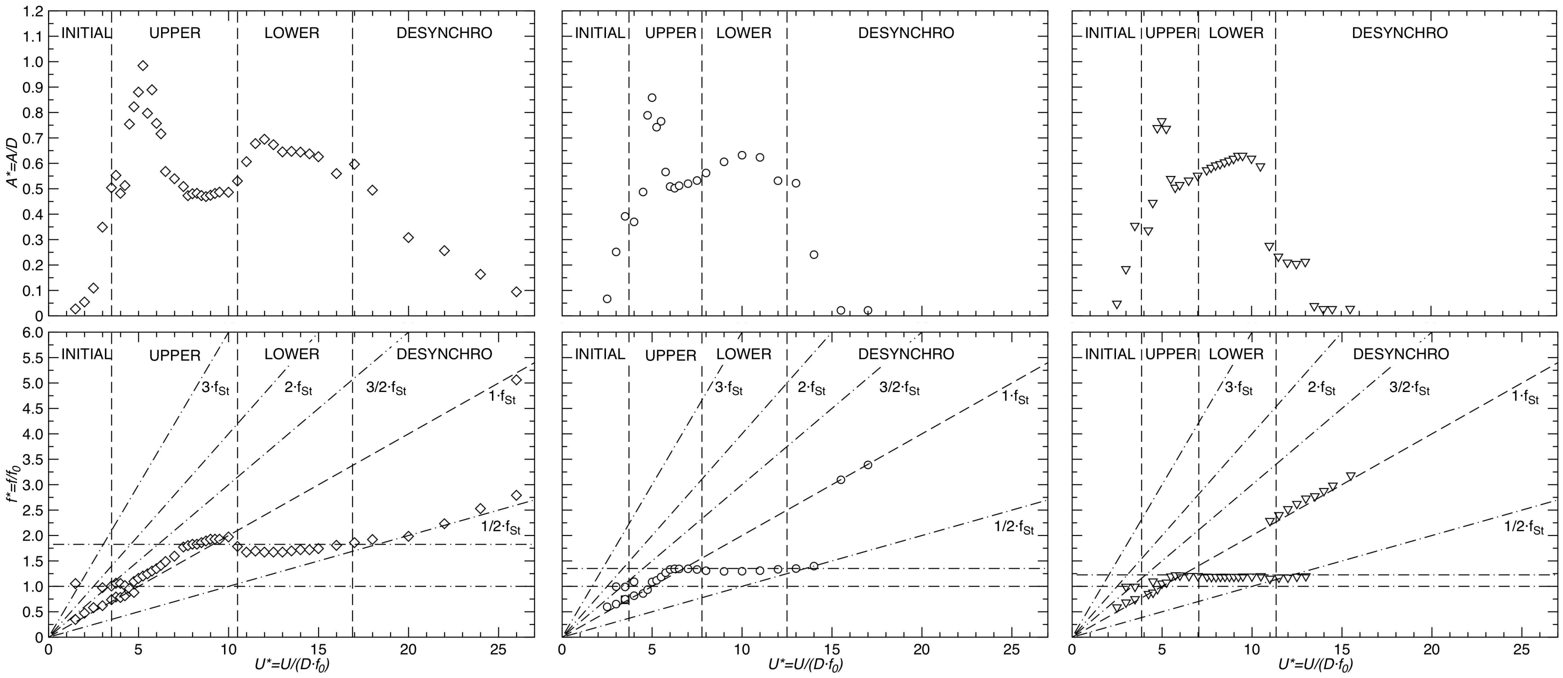

(a) $m^* = 1.2$ (b) $m^* = 2.4$ (c) $m^* = 3.6$

Figure 4.7: Amplitude ratio $A^* = A/D$ (top figures) and frequency ratio $f^* = f/f_0$ (bottom figures) Vs reduced velocity U^*. Comparison of the CFD results obtained by the variation of mass ratio: (a) $m^* = 1.2$, (b) $m^* = 2.4$ and (c) $m^* = 3.6$. The oblique dashed line in the bottom figures corresponds to the nominal Strouhal frequency f_{St} or multiple of the f_{St}.

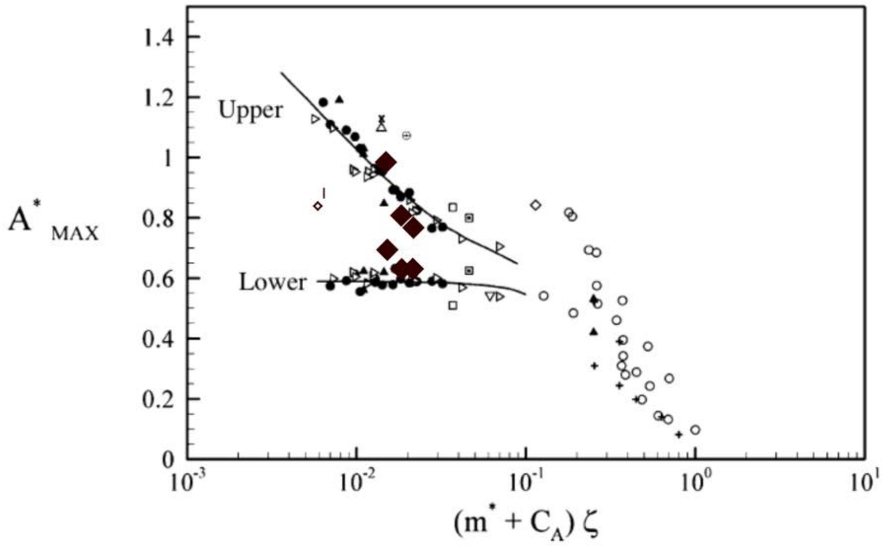

Figure 4.8: After [10]. Maximum value of A^* at the upper and lower branches separately Vs modified mass-damping parameter (see also Tables 4.1 and 4.2). (♦) = present numerical; other symbols/lines as in Fig. 6(b) in [10].

Regarding the non-dimensional dominant frequency of the cylinder motion for $m^* = 1.2$, from the bottom of Fig. 4.7(a) it is possible to note that $f^* \approx f_{\mathrm{St}}/f_0$ for $U^* < 10$, it turns to $f^* \approx 1.8$ for $10 < U^* < 17$ (right-most part of the lower branch), and then to $0.5 \cdot f_{\mathrm{St}}/f_0$ for $U^* > 17$ (sub-harmonic). It is worth mentioning that both the constant value of f^* in the lower branch and the sub-harmonic behaviour in desynchronisation regime are strongly consistent with the experimental results shown in Fig. 18 of [17]. Indeed, from $U^* > 25$ the f^* splits in two dominant frequencies, the lower being associated with $f^* \approx 0.5 \cdot f_{\mathrm{St}}/f_0$ and the upper being the Strouhal frequency $f^* \approx f_{\mathrm{St}}/f_0$.
For $m^* = 2.4$, in Fig. 4.7(b) $f^* \approx f_{\mathrm{St}}/f_0$ for $U^* < 5$, it turns to $f^* \approx 1.35$ for $6 < U^* < 14$ (lower branch), and then back to $f^* \approx f_{\mathrm{St}}/f_0$ for $U^* > 14$, as clearly shown in the experimental data from [15].
For $m^* = 3.6$, Fig. 4.7(c) shows that $f^* \approx f_{\mathrm{St}}/f_0$ for $U^* < 5$, it turns to $f^* \approx 1.2$ for $6 < U^* < 11$ (lower branch), and then back to $f^* \approx f_{\mathrm{St}}/f_0$ for $U^* > 13$. From $U^* \approx 11$ to $U^* \approx 13$ the f^* splits in two dominant frequencies the lower being associated with the synchronisation $f^* \approx 1.2$ and the upper being the Strouhal frequency $f^* \approx f_{\mathrm{St}}/f_0$.
Eventually, considering Fig. 4.7 it is worth noting that within the lower branch, the dominant frequency decreases from 1.8 to 1.2 with increasing m^*.
Finally, Fig. 4.9 shows the attitude of f^* at *lock-in* Vs m^*. The solid line is the function $f^* = \sqrt{(m^*+1)/(m^*-0.54)}$ proposed in [17]. Again, It is possible to note that in general the numerical results compare well with reference data.

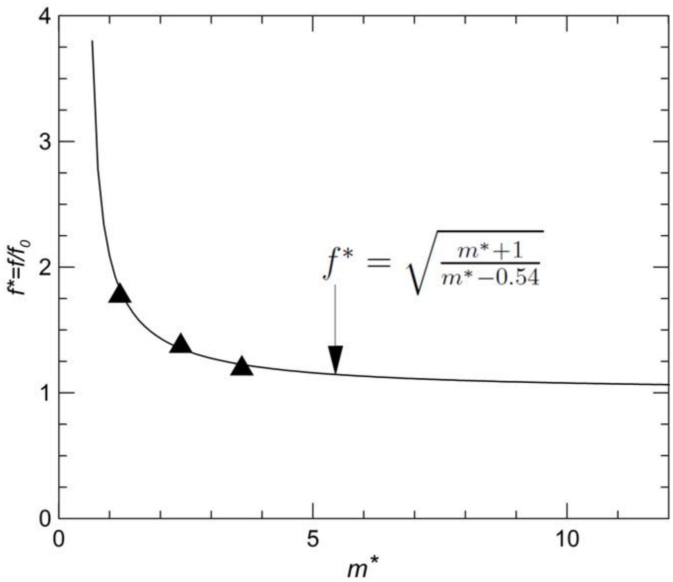

Figure 4.9: f^* at lock-in (see Fig. 4.7) Vs m^*. (▲) = present numerical; solid line = after [10].

Total and vortex shedding force

Fig. 4.15 show the root mean square (rms) of the total force C_L and vortex shedding force C_{VS} Vs U^*.
As a general comment, the total force and the vortex shedding force shows the same trend for all m^* considered. In particular, the total force C_L shows a quasi-constant value in the initial branch and in the in the early stages of initial branch, than it drops rapidly. This drop is more marked for values of lower m^*. The total force further decreases along the lower branch and desynchronisation regime more slowly as the m^* decreases.
The magnitude of the vortex shedding force C_{VS} decreases slightly with increasing m^*. What differs between the various m^* is how the maximum value is reached. Indeed, as the m^* increases the peak value is reached more quickly as U^* increases.

Phase lag

The value of the phase lag ϕ between the total force and the cylinder motion Vs U^* are presented in the bottom figures of Fig.4.15 (full symbols). The same figure (Fig.4.15) also shows the phase lag ϕ_{SF} between the cylinder response $y(t)$ and the Morison-like force $F_{SF}(t)$ (grey symbols) and the phase lag ϕ_{VS} between the cylinder response $y(t)$ and the vortex shedding lift force $F_{VS}(t)$ (full symbols).
The total force phase ϕ shows a variable value, from 0 to 50 deg in the initial branch and at the beginning of upper branch. Then a jump from ≈ 0 to 180 deg is observed for all the tree considered $m*$. From the literature [17] the jump of the total force marks the upper lower transition. This transition occurs at higher value of U^* for the case of

lower value of mass ratio ($U^* \approx 7$ for $m^* = 1.2$) and decreases for higher value of m^* ($U^* \approx 5$ for $m^* = 3.6$). The total phases of both cases remain almost identical for each m^* in the lower branch. Furthermore the phase lag ϕ_{VS} between the cylinder response $y(t)$ and the vortex shedding lift force $F_{VS}(t)$ shows a constant value of$\phi_{VS} \approx 60$ deg in the initial branch region, for all the considered mass ratios. Then in the upper branch there is a rapid increase from 0 to 165 deg as U^* increases.
A step-like (resonance) behaviour is found in the lower branch $\phi_{VS} \approx 165$ deg. At the beginning of the desynchronisation region a sharp variation is shown. As $m*$ increases the variation from 165 deg becomes more pronounced.
As far as the phase lag ϕ_{SF} between the cylinder response $y(t)$ and $F_{SF}(t)$ is concerned, considering the bottom figures of Fig. 4.15, it is possible to observe an almost in-phase behaviour over the entire range of the reduced velocity, as expected. This force is dominated by the inertia term that, for a monochromatic motion, is in anti-phase with the acceleration and thus in phase with the displacement $y(t)$; within the upper and lower branches, the force $F_{SF}(t)$ lags the displacement by approx. 30 deg.

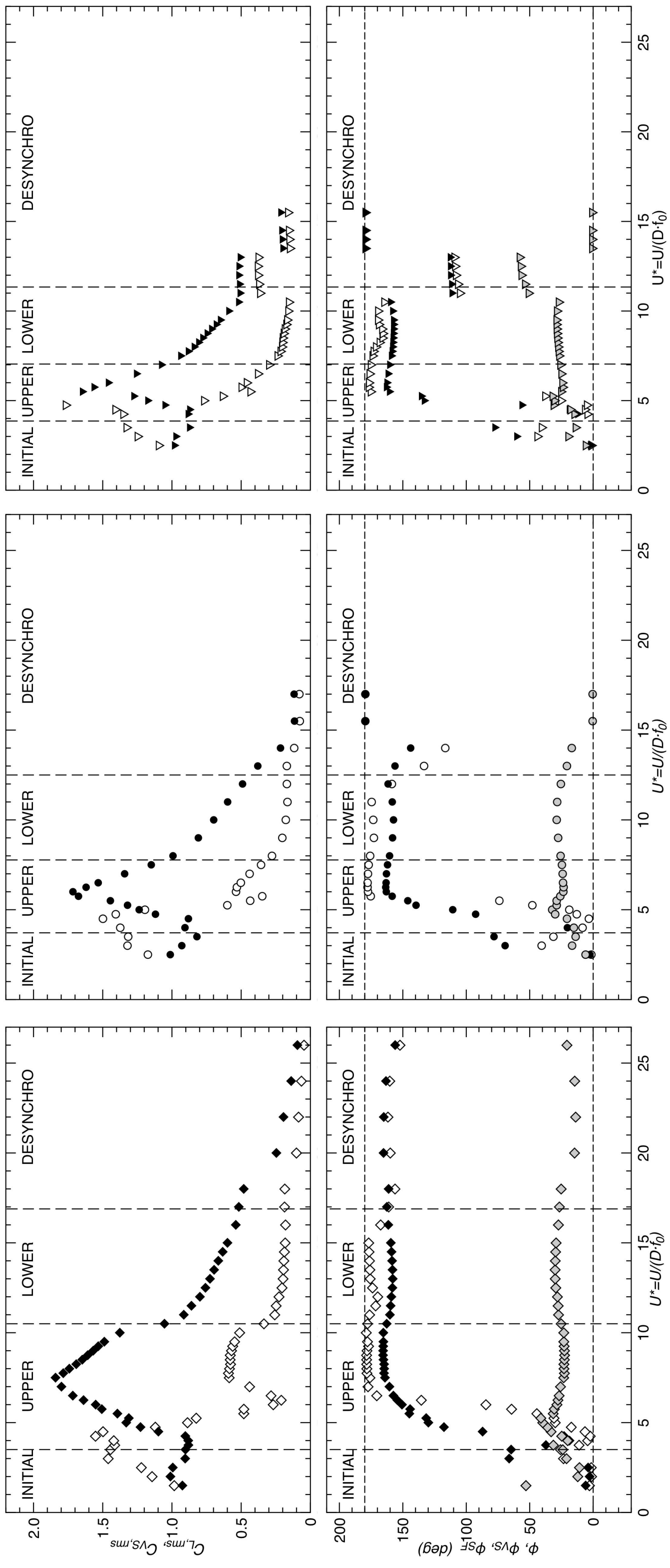

(a) $m^* = 1.2$

(b) $m^* = 2.4$

(c) $m^* = 3.6$

Figure 4.10: Upper figures root mean square (rms) of the total force C_L (empty points) and vortex shedding force C_{VS} (full points) Vs reduced velocity U^*. Bottom figures phase angle variation ϕ (empty symbols) ϕ_{VS}(full symbols) ϕ_{SF}(grey symbols) Vs reduced velocity U^*. Comparison of the CFD results obtained by the variation of mass ratio.

4.3.2 Sdof-mf model and Parameter Identification

Time-domain traces

The non dimensional time-domain traces of vortex shedding lift force $F_{VS}(t)$ and cylinder displacement $y(t)$ are shown in Fig. 4.11-4.12 and Fig. 4.13-4.14 respectively. More precisely, the time series of $C_{VS}(t)$ and $y(t)/D$ obtained via CFD simulations and the current *sdof-mf* model are compared. As for the time series of $y(t)$ from the *sdof-mf* model, Eq. (4.6) has been solved, using Eq. (4.7) and Eq. (4.8) for the RHS, adopting a time marching 4th order Runge Kutta scheme. The non-dimensional time-domain vortex shedding force obtained with CFD simulations and with the *sdof-mf* model for two new cases, $m* = 1.2$ and $m^* = 3.6$ proposed are presented respectively in Fig. 4.11 and 4.12 in terms of U^*. For the sake of completeness, in the same figures the dashed thin lines represent the total force $C_L(t)$.
The time series of the non-dimensional cylinder motion are presented in Fig. 4.13, for the case $m^* = 1.2$, and 4.14, for the case $m* = 3.6$, in terms of U^*. The proposed figures have been selected as highly representative of the U^* dependency of the harmonic content of $C_{VS}(t)$ and $y(t)/D$ in order to justify the applicability of the *sdof-mf* model. In these figures, solid lines represent CFD time-series, whereas dashed lines show *sdof-mf* time-series with best-fit parameters (PI).
Considering the harmonic content, from Fig. 4.11(a) ($m^* = 1.2$, $U^* = 3.50$) it is possible to note that a pronounced low frequency oscillation is clearly observed. In this case the dominant frequencies are f_{St} but with a particularly pronounced presence of other two additional frequencies, $f_{St}3/2$ and $f_{St}/2$. In Fig. 4.11(b) ($m^* = 1.2$, $U^* = 5.5$) the dominant frequencies are again f_{St} but, for this case, two additional frequencies are multiple of the Strouhal frequencies $2 \cdot f_{St}$ and $3 \cdot f_{St}$.
In Fig. 4.11(c) ($m^* = 1.2$, $U^* = 18.00$) the dominant frequencies are again f_{St}, $3/2 \cdot f_{St}$ and $1/2 \cdot f_{St}$ but now they are far enough from each other, this leads to a completely different time-domain behaviour of $C_{VS}(t)$.
In both cases (Fig. 4.11(a), 4.11(c)), the strongest excitation of the cylinder motion comes from a frequency which is half the conventional Strouhal frequency.
In Fig. 4.12(a) ($m^* = 3.6$, $U^* = 4.75$), here used as representative of the worst fit of the *sdof-mf* model, the harmonic content is very complex and the *sdof-mf* model, here limited to three-harmonics only, lacks additional terms that would probably make the fitting more accurate. Despite this, the use of only three harmonics (f_{St}, $1/2 \cdot f_{St}$ and $3/2 \cdot f_{St}$), makes the fitting good enough to reproduce the time-domain behaviour of $C_{VS}(t)$.
In Fig. 4.12(a) ($m^* = 3.6$, $U^* = 9..25$), the dominant frequencies are the synchronisation frequency $f^*_{lower,m^*=3.6} \approx 1.2$ and multiples of the synchronisation frequency approximately $\approx 2 \cdot f^*_{lower,m^*=3.6}$ and $\approx 3 \cdot f^*_{lower,m^*=3.6}$. Finally, in Fig. 4.12(c) ($m^* = 3.6$, $U^* = 12.00$), the dominant frequencies are back to the same main frequency of $U^* = 4.75$ (f_{St}, $1/2 \cdot f_{St}$ and $3/2 \cdot f_{St}$) though in this case the amplitude of the latter is one order of magnitude smaller than the former.
From Fig. 4.13 and 4.14, it can be observed that the *sdof-mf* model captures/reproduces

the vortex shedding force and consequently the cylinder motion very well, even when there is a worse fitting of the force ($U^* = 3.50, 5.50$ for $m^* = 1.2$ and $U^* = 9.25$ for $m^* = 3.6$).

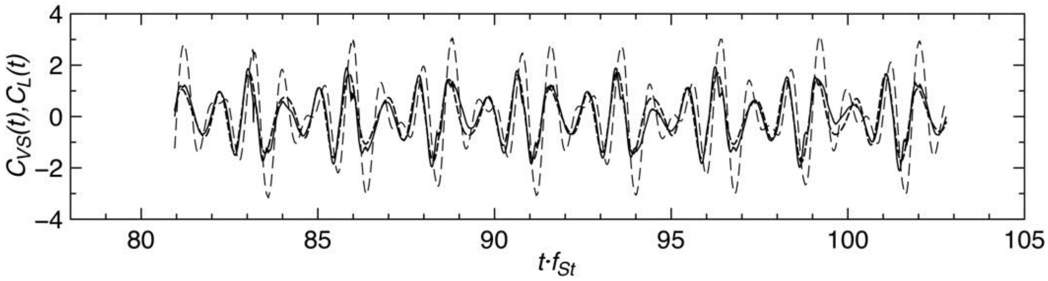

(a) Re = 3657, $U^* = 3.50$

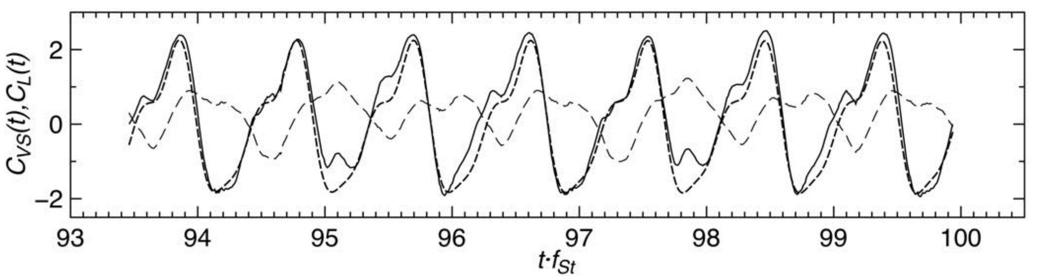

(b) Re = 5746, $U^* = 5.50$

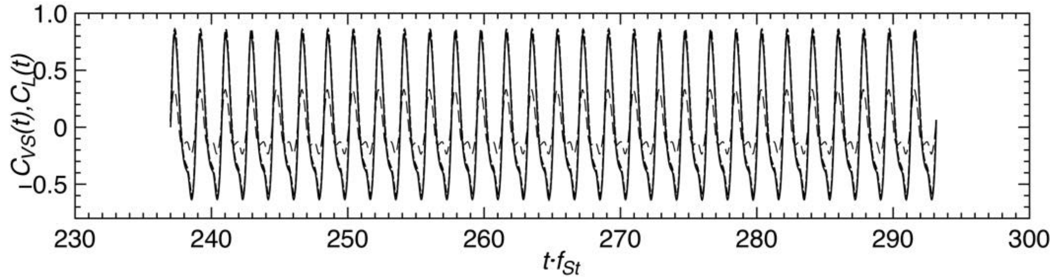

(c) Re = 18806, $U^* = 18.00$

Figure 4.11: Mass ratio $m^* = 1.2$. Comparison between time-domain non-dimensional total $C_L(t)$ and vortex shedding $C_{VS}(t)$ obtained via CFD and via *sdof-mf* model in Eq. (4.8).(- - - -) = total force (present CFD); (——) = vortex shedding force (present CFD); (**- - - -**) = *sdof-mf*.

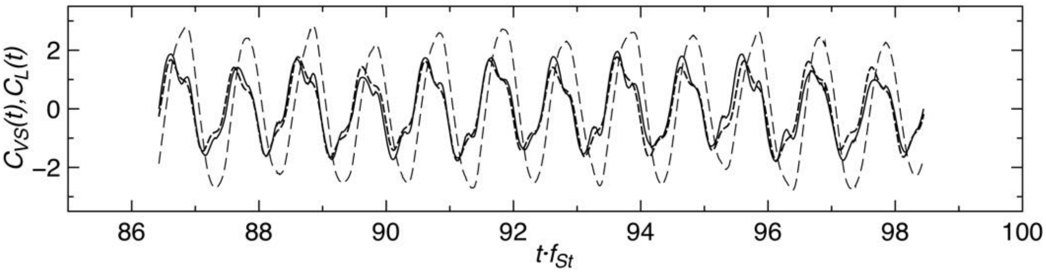

(a) Re = 3432, $U^* = 4.75$

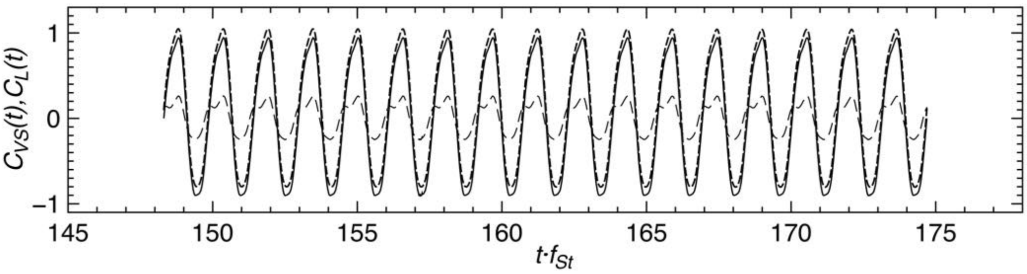

(b) Re = 6683, $U^* = 9.25$

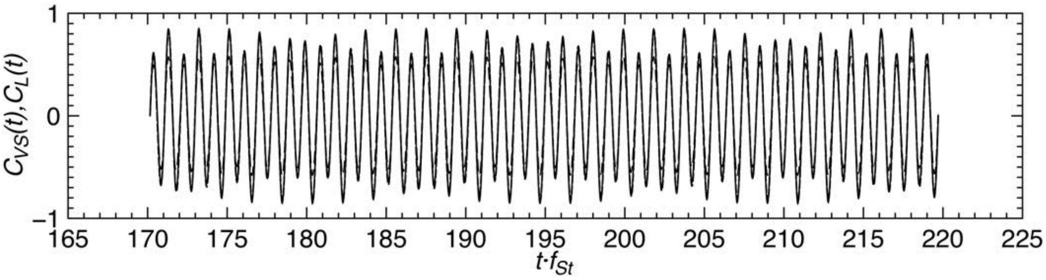

(c) Re = 8670, $U^* = 12.00$

Figure 4.12: Mass ratio $m^* = 3.6$. Comparison between time-domain non-dimensional total $C_L(t)$ and vortex shedding $C_{VS}(t)$ obtained via CFD and via *sdof-mf* model in Eq. (4.8).(- - - -) = total force (present CFD); (——) = vortex shedding force (present CFD); (**- - - -**) = *sdof-mf*.

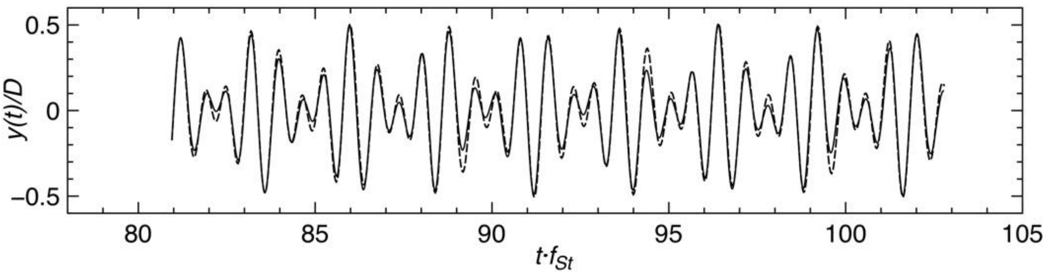

(a) Re = 3657, $U^* = 3.50$

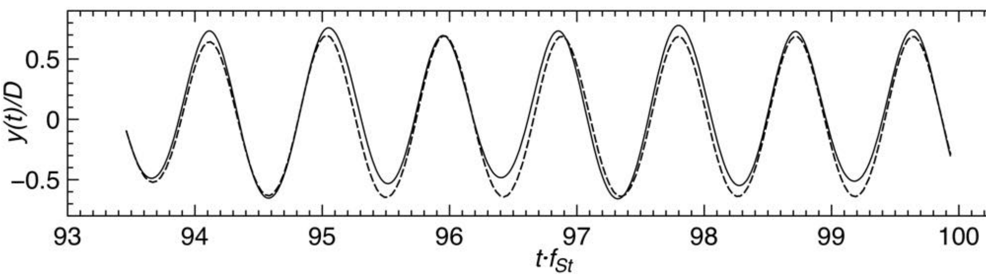

(b) Re = 5746, $U^* = 5.50$

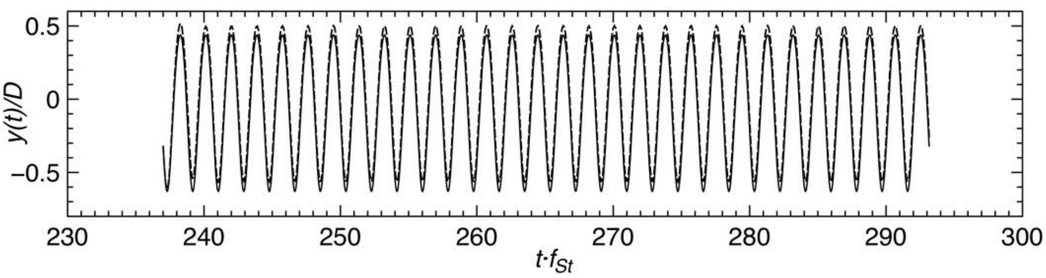

(c) Re = 18806, $U^* = 18.00$

Figure 4.13: Mass ratio $m^* = 1.2$. Comparison between time-domain non-dimensional cylinder motion $y(t)/D$ obtained via CFD and via *sdof-mf* model in Eq. (4.6). (——) = present CFD; (- - - -) = *sdof-mf*.

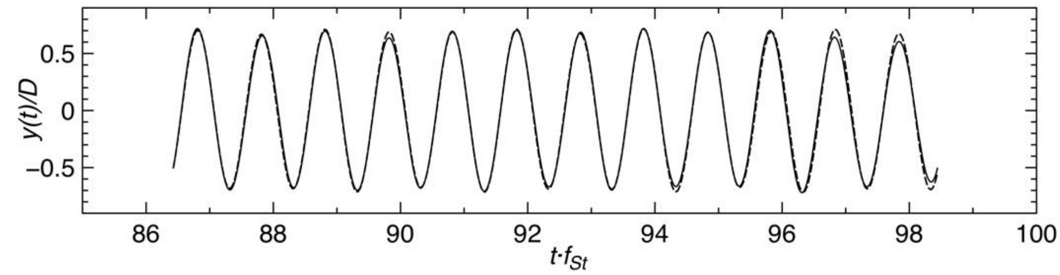

(a) Re = 3432, $U^* = 4.75$

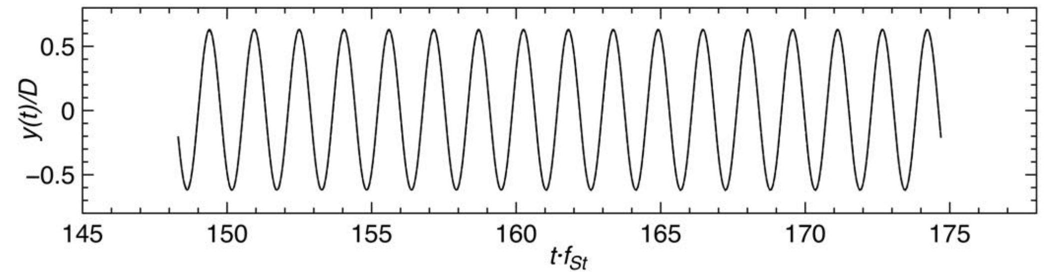

(b) Re = 6683, $U^* = 9.25$

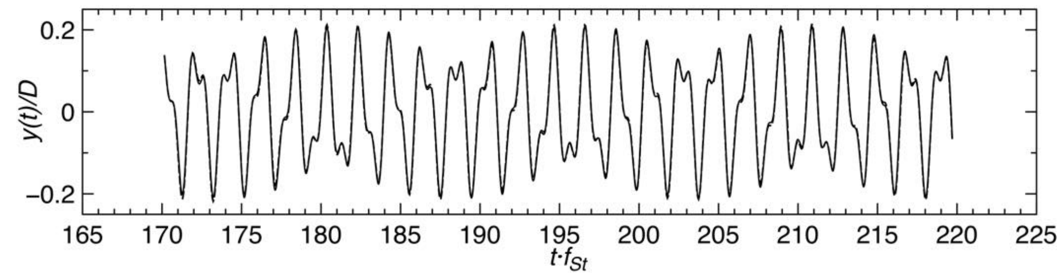

(c) Re = 8670, $U^* = 12.00$

Figure 4.14: Mass ratio $m^* = 3.6$. Comparison between time-domain non-dimensional cylinder motion $y(t)/D$ obtained via CFD and via *sdof-mf* model in Eq. (4.6).
(——) = present CFD; (- - - -) = *sdof-mf.*

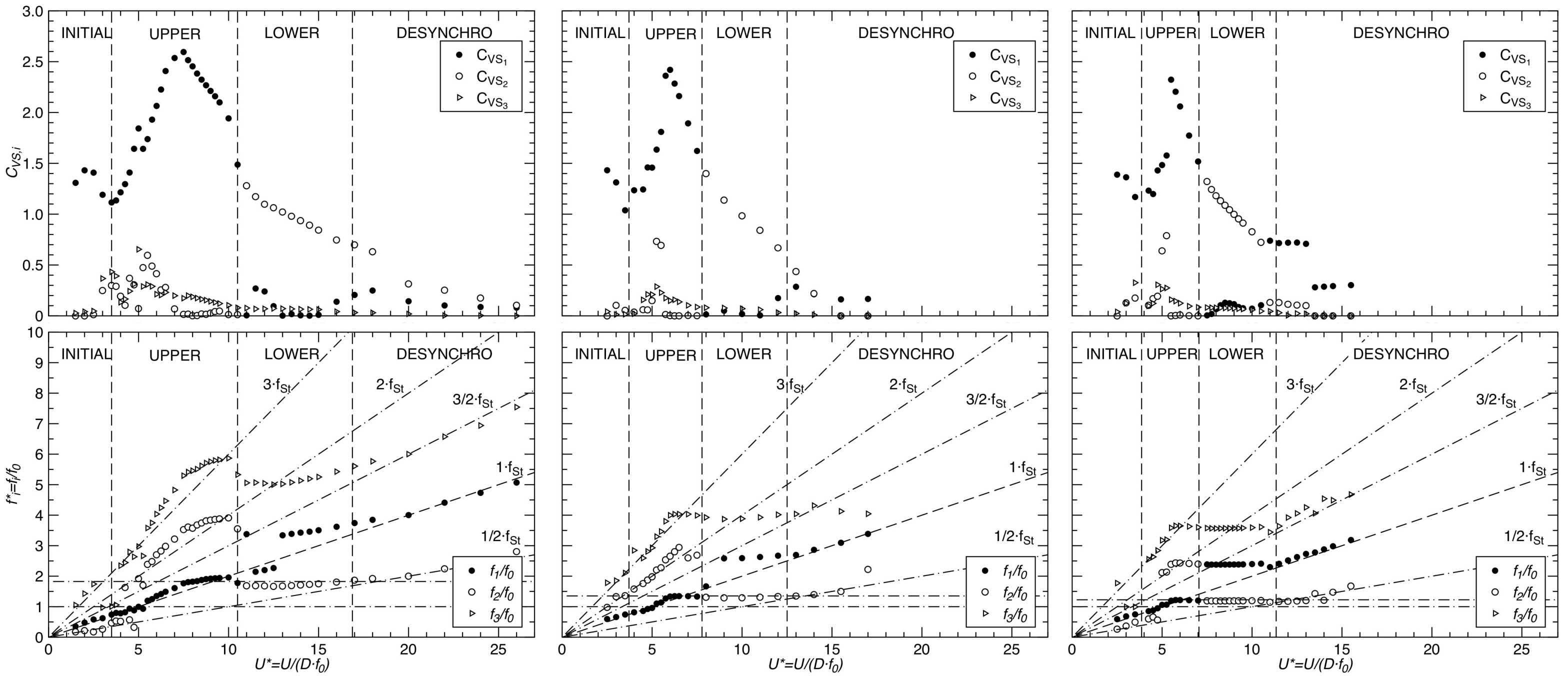

(a) $m^* = 1.2$ (b) $m^* = 2.4$ (c) $m^* = 3.6$

Figure 4.15: Upper figures: vortex shedding lift coefficients $\overline{C_{VS_i}}$. Bottom figures: frequencies $(f_i/f_0) = \theta_i \cdot f_{\mathrm{St}}/f_0$, $i = 1, 3$ of the *sdof-mf* model Vs U^*, oblique dashed lines correspond to $0.5 \cdot f_{\mathrm{St}}, 1 \cdot f_{\mathrm{St}}, 2 \cdot f_{\mathrm{St}}$ and $3 \cdot f_{\mathrm{St}}$, where f_{St} is the nominal Strouhal frequency.

Vortex shedding lift force of the sdof-mf model

As far as the vortex shedding lift force is concerned Fig. 4.15 shows that the maximum value of $\overline{C_{VS_i}}$ lies around $2.4 \div 2.6$ for the considered mass ratios. The magnitude decreases slightly with increasing m^*.
The value of U^*_{max} at which $\overline{C_{VS_i}}$ is maximum, decreases considerably as m^* increases, namely $U^*_{max} \approx 8, 6.5, 5$ for $m^* = 1.2, 2.4, 3.6$ respectively; this is also consistent with the shift, towards lower values, of the upper limit of the range of U^* corresponding to the upper branch (see Fig. 4.8). Moreover we point out that for all the investigated mass ratios, the maximum $\overline{C_{VS_i}}$ is related to the frequency closest to the Strouhal frequency, i.e. $(f_i/f_0) \approx f_{\mathrm{St}}/f_0$ (typically for $i = 1$). The maximum magnitude of the second harmonic term (i.e. $2 \cdot f_{\mathrm{St}}$) in the initial branch is found to be $\overline{C_{VS_i}} \approx 0.6$, of order of 50% of the magnitude at the dominant frequency f_{St}. The third harmonic of $F_{VS}(t)$ shows up at *lock-in*, mostly at $5 < U^* < 8$, with amplitudes of $\overline{C_{VS_i}}, i = 3$ of order of 10% (or higher) of the dominant term.

Non-dimensional frequency of the sdof-mf model

Considering the bottom figures of Fig.4.15, it is possible to note that the non-dimensional dominant frequency (f_i/f_0) of $F_{VS}(t)$ at *lock-in* converges to 1 as m^* increases, $(f_i/f_0) \approx$ 1.8, 1.4, 1.2 for $m^* = 1.2$, 2.4, 3.6 respectively; this is also consistent with the dominant frequency of the cylinder motion (see Fig. 4.9).
Next the influence of the the mass ratio on the value of the dominant term of $F_{VS}(t)$ is discussed.
From 4.15(a) related to $m^* = 1.2$ it is possible to observe that the dominant term of $F_{VS}(t)$ is found for $U^* < 10.5$ at $(f_i/f_0) \approx f_{\mathrm{St}}/f_0$; for $10.5 < U^* < 17$ (lower branch) at $(f_i/f_0) \approx 1.8$; for $U^* > 17$ it shows a distinct frequency at exactly half the nominal Strouhal frequency (sub-harmonic) $(f_i/f_0) \approx 0.5 \cdot f_{\mathrm{St}}/f_0$, consistently with the dominant frequency of the cylinder motion at large U^* values (see Fig. 4.7(a) and the experimental results presented in Fig. 8 of [17]).
In the case of $m^* = 2.4$, Fig. 4.15(b) shows that the dominant term of $F_{VS}(t)$ for $U^* < 6$ is found at $(f_i/f_0) \approx f_{\mathrm{St}}/f_0$; for $6 < U^* < 14$ at $(f_i/f_0) \approx 1.4$, even though the multiple of the synchronisation frequency $f{*}_{lower} \approx 1.35$ is clearly present. A particular case is the reduced velocity $U^* = 8$,where the transition from the upper to the lower branch occurs; for this case the dominant frequency is the Strouhal frequency. Finally, for $U^* > 14$ the nominal Strouhal frequency takes the control of the forcing term again.
For $m^* = 3.6$, Fig. 4.15(c) shows that the dominant term of $F_{VS}(t)$ for $U^* < 5.5$ is found at $(f_i/f_0) \approx f_{\mathrm{St}}/f_0$; for $5.5 < U^* < 11$, at $(f_i/f_0) \approx 1.2$; for $U^* > 11$ the nominal Strouhal frequency takes the control of the forcing term again.

4.3.3 Conclusions

The systematic application of the *sdof-mf* model to the study of Vortex-Induced Vibrations (VIV) of an elastically-mounted 2D circular cylinder in cross-flow, provides a rather deep insight in the characterisation of the vortex induced lift force. In particular, the study has been carried out varying systematically the mass ratio m^* of the system, within a range of interest for practical engineering applications in water.
For this study, the VIV data used in the coupled *sdof-mf* / PI approach are obtained by 2D URANS simulations, keeping the same CFD framework already used in a previous work.
From the overall results, it emerges that the *sdof-mf* model reproduces the time-domain cylinder motion and vortex shedding lift force quite accurately. The parameters of the *sdof-mf* model show a fair and consistent variation over the entire range of U^* and for all m^*.
The main outcome of the analysis of this force is found in the presence of ultra- and sub-harmonic terms. For specific pairs (U^*,m^*), these ultra and sub-harmonic terms are observed to take the control of the VIV process, both at lock-in and in desynchronisation regions.

In the following section the same analysis of the present section will be conducted for the three-dimensional cases in order to discover if the use of the *sdof-mf* may highlight further differences between the 2D and the 3D CFD cases, compared to what has already been found in the study conducted in Sec: 2.3.

4.4 Sdof-mf comparison between 2D and 3D URANS simulations

The 3D URANS results are presented here and analysed with the *sdof-mf* model in order to confirm the capabilities of the model to give a further interpretation of the difference between the 2D and 3D CFD approaches. The analysis is carried out with the three mass ratios previously selected for the 2D computations ($m^* = 1.2, 2.4$ and 3.6). Tab. 4.3 and 4.4 give the details of the full set of parameters of the 3D URANS simulations.

Cylinder diameter	D	(m)	$3.81 \cdot 10^{-2}$
Cylinder length	S	(m)	0.38
Cylinder volume	$\frac{\pi D^2}{4} S$	(m^3)	$4.33 \cdot 10^{-4}$
Undamped natural frequency in air	$f_{0,a} = \frac{1}{2\pi}\sqrt{\frac{K}{M}}$	(Hz)	0.7846
Damping Ratio	$\zeta = \frac{H}{2\sqrt{K(M+M_A)}}$	$(-)$	$4.353 \cdot 10^{-2}$
Potential added mass	M_A	(kg)	$4.328 \cdot 10^{-1}$
Potential added mass coefficient	$C_A = \frac{M_A}{\rho \frac{\pi D^2}{4} S}$	$(-)$	1.0
Reynolds number range	Re	$(-)$	$\approx 0.2 \div 2.7 \cdot 10^4$

Table 4.3: Fixed parameters.

Mass ratio	$m^* = \frac{\mathbf{M}}{\pi\,\rho \mathbf{D^2 S/4}}$	$(-)$	**1.2**	**2.4**	**3.6**
Cylinder mass	M	(kg)	0.519	1.038	1.558
Spring stiffness	K	$\left(\frac{\mathrm{N}}{\mathrm{m}}\right)$	12.623	25.246	37.869
Structural damping	H	$\left(\frac{\mathrm{N}}{\mathrm{m/s}}\right)$	$7.512 \cdot 10^{-2}$	$6.603 \cdot 10^{-2}$	$6.271 \cdot 10^{-2}$
Mass-damping parameter	$m^*\,\zeta$	$(-)$	0.695	1.582	2.498
Modified mass-damp. parameter	$(m^* + C_A)\,\zeta$	$(-)$	$9.576 \cdot 10^{-2}$	$1.480 \cdot 10^{-1}$	$2.002 \cdot 10^{-1}$
Undamped natural frequency in water	$f_0 = \frac{1}{2\pi}\sqrt{\frac{K}{M+M_A}}$	(Hz)	0.5794	0.6592	0.6941

Table 4.4: Varying parameters.

In the present study, firstly, a description of the the numerical results will be presented in terms of adimensional amplitude ratio and frequency ratio. Following that the results in terms of force coefficient and phase will be discussed. Then the results will be analysed via *sdof-mf* model after performing the PI on the 3D time traces. This will be followed by the conclusions.

4.4.1 Numerical results

The results from current 3D VIV simulations are compared with the corresponding 2D results for the selected mass ratios $m^* = 1.2, 2.4$ and 3.6.

Non-dimensional amplitude and frequency ratio

In Fig. 4.16 the 3D URANS results are shown in terms of non-dimensional amplitude $A^* = A/D$ and its non-dimensional frequency $f^* = f/f_0$ with respect to the reduced velocity U^*.
For all the selected mass ratios, 3D simulations show good agreement with corresponding 2D results in terms of response amplitude and frequency ratio. The greatest discrepancies between the two CFD approaches are found in the upper branch and in the transition zone between lower branch and desynchronisation. In general, the 3D simulation shows a wide range of large cylinder motions (close to the peak value) in the upper branch. In particular for $m^* = 1.2$ the maximum value of non-dimensional amplitude A^*_{max} is in

accordance with the 2D results. Indeed for the mass ratios $m^* = 2.4$ and $m^* = 3.6$ the 2D simulations are unable reach the peak value A^*_{max} obtained with 3D simulations.
In the transition zone between lower branch and desynchronisation the non-dimensional amplitude found by the 3D simulations are smaller than the corresponding 2D cases for $m^* = 1.2$ and 2.4, while for $m^* = 3.6$ they are greater. As regards the frequency ratio, the 3D simulations in the upper branch show slightly lower frequencies in respect to the 2D results, otherwise a good agreement with experimental data is found. At this point it must be remembered that the frequency results of Fig. 4.16 have been obtained using spectral peak analysis. In Fig. 4.16 the time series of the non-dimensional time domain vortex shedding force C_{VS}, the non-dimensional total force C_L, non-dimensional cylinder displacement $y(t)/D$ and instantaneous phase $\phi(t)$ and frequency ratios $f^*(t)$ (obtained using the Hilbert transform) for the 2D and the 3D CFD simulations are presented. As shown in Fig. 4.16 and already highlighted in Sec. 2.3, the oscillation frequency for the 2D case during the upper branch is not steady. This means that the value of the frequency ratio (obtained using spectral peak analysis) is an average value, that is never steadily achieved by the simulations. From Fig. 4.16 it can be noted that the oscillation decreases as the mass ratio increases. The decrease in the oscillation, as the mass ratio increases, is certainly linked to the decrease in the synchronisation frequency value f^*_{lower} as the mass ratio increases.
Differently from the 2D cases, for the 3D cases the frequency ratio of simulations obtained using the Hilbert transform is equal to the spectral peak frequency through the entire window.

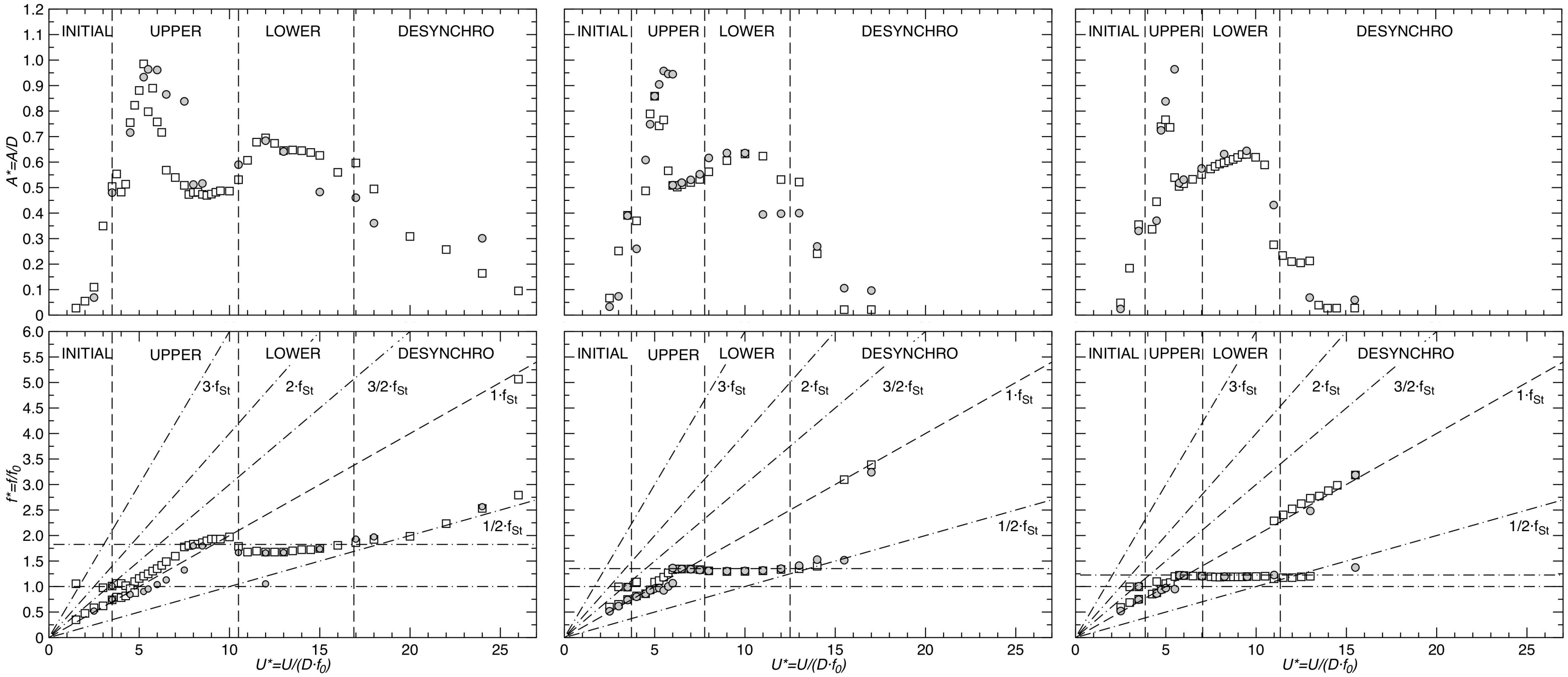

(a) $m^* = 1.2$

(b) $m^* = 2.4$

(c) $m^* = 3.6$

Figure 4.16: Amplitude ratio $A^* = A/D$ (top figures) and frequency ratio $f^* = f/f_0$ (bottom figures) Vs reduced velocity U^*. Comparison of the CFD results obtained by the variation of mass ratio: (a) $m^* = 1.2$, (b) $m^* = 2.4$ and (c) $m^* = 3.6$. The oblique dashed line in the bottom figures corresponds to the nominal Strouhal frequency f_{St} or multiple of the f_{St}.

2D 3D

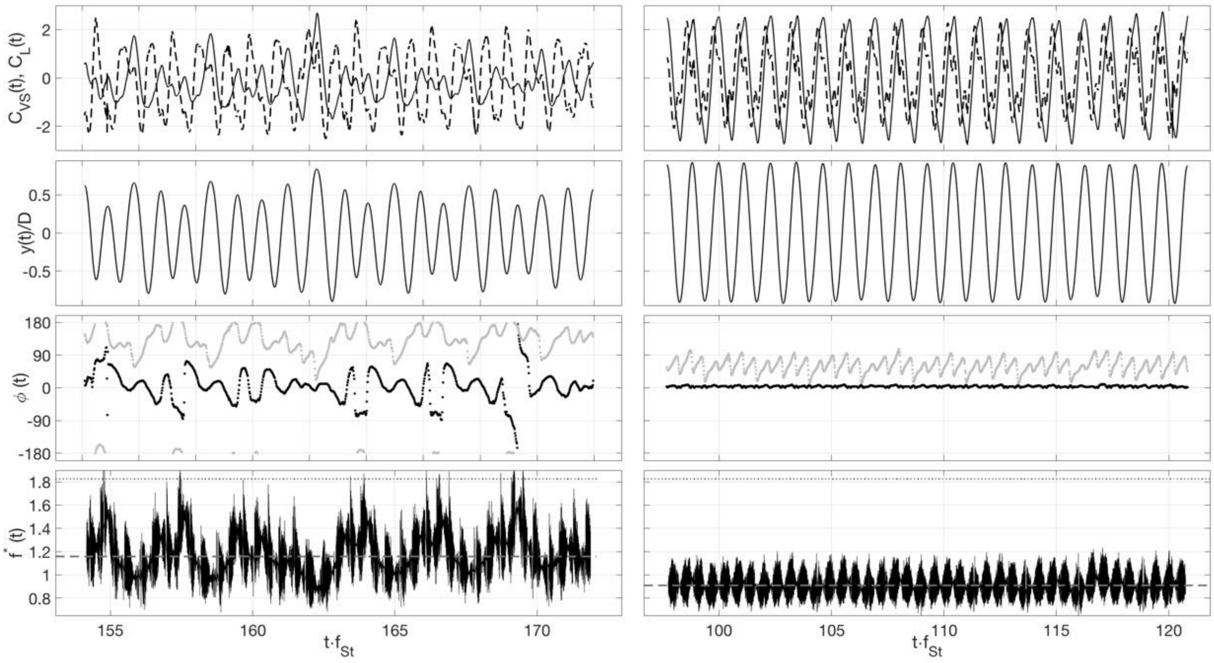

(a) $m^* = 1.2$, $U^* = 5.25$

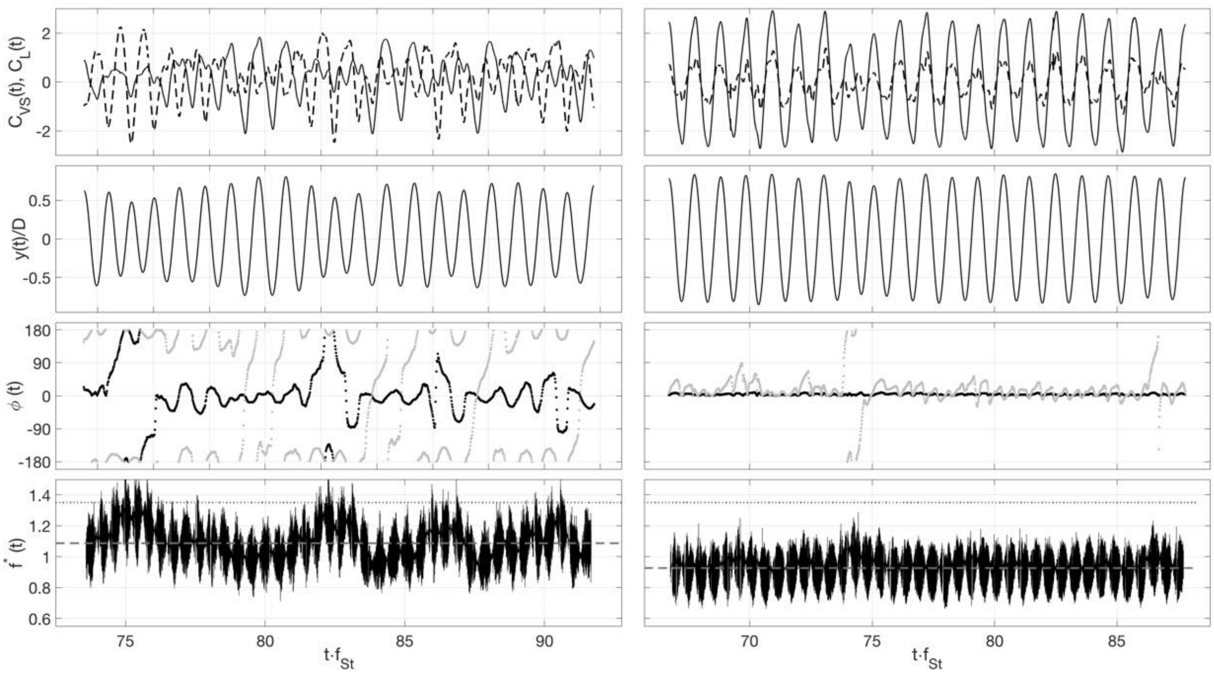

(b) $m^* = 2.4$, U^*=5.00

Figure 4.17: First plot: total $C_L(t)$ (solid line) and vortex shedding force coefficient $C_{VS}(t)$ (dashed line). Second plot: non-dimensional cylinder displacement $y(t)$. Third plot: phase angle ϕ between C_L and $y(t)$ (black points) and phase angle ϕ_{VS} between C_{VS} and $y(t)$ (grey points). Fourth plot: frequency ratio $f^*(t)$ (using Hilbert transform), dashed line shows the main oscillation frequency (from analysis of spectral peaks) and dotted line shows the synchronisation frequency at lower branch.

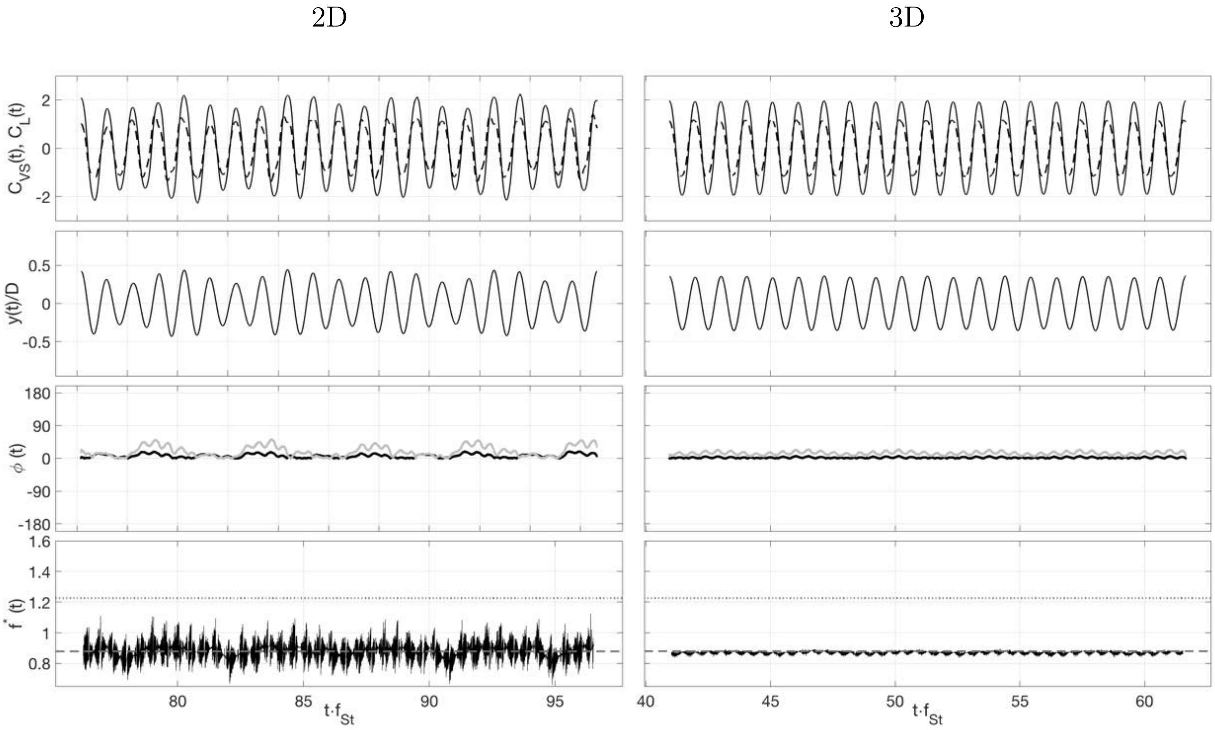

(c) $m^* = 3.6$, $U^* = 4.50$

Figure 4.16: (*Cont.*) First plot: total $C_L(t)$ (solid line) and vortex shedding force coefficient $C_{VS}(t)$ (dashed line). Second plot: non-dimensional cylinder displacement $y(t)$. Third plot: phase angle ϕ between C_L and $y(t)$ (black points) and phase angle ϕ_{VS} between C_{VS} and $y(t)$ (grey points). Fourth plot: frequency ratio $f^*(t)$ (using Hilbert transform), dashed line shows the main oscillation frequency (from analysis of spectral peaks) and dotted line shows the synchronisation frequency at lower branch.

Force coefficient and phase

The root mean square (rms) of the total force C_L amplitude and phase ϕ between the total force and the displacement are presented in Fig. 4.19 with respect to reduced velocity U^* for the selected mass ratio m^*.
The main discrepancy between the 2D and 3D cases where in the upper branch and at the beginning of the desnchronisation regime. In general, the total force obtained from the 3D cases shows higher value in the upper branch. Otherwise it is almost identical for both cases 2D and 3D in the lower branch for all m^*. Finally, the 3D case shows slightly lower values once the desynchronisation range starts for $m^* = 1.2$ and $m^* = 3.6$.
The total force phase ϕ comparison shows that the 3D case exhibits a sharp jump of the total force phase jump between upper and lower branch, from 0 to 180 deg, while for the 2D results the phase rises gradually before reaching 180 deg.

The root mean square (rms) of the vortex shedding force C_{VS} amplitude and phase ϕ_{VS} between the vortex shedding force and the displacement are presented in Fig. 4.18 with respect to reduced velocity U^* for the selected mass ratio m^*.
Differences between 2D and 3D are most visible in the initial and upper branches. The 2D simulations show higher vortex shedding force, in the initial stage of upper branch, in particular the 2D cases show a rapid increase in its amplitude where the 3D case shows a more steady value. In general, the 3D case shows higher vortex shedding force in the upper branch with respect to the 2D case, allowing for larger amplitudes. No significant differences are present both in the lower branch and desynchronisation regime as 2D and 3D results overlap.
Also for the the vortex shedding force ϕ_{VS} phase the main differences between the two cases are found in the early stages of initial branch and in the upper branch. In this branch both cases, 2D and 3D, show an increasing phase angle from 0 to 180 deg but the 2D cases are in general higher than the corresponding 3D cases.

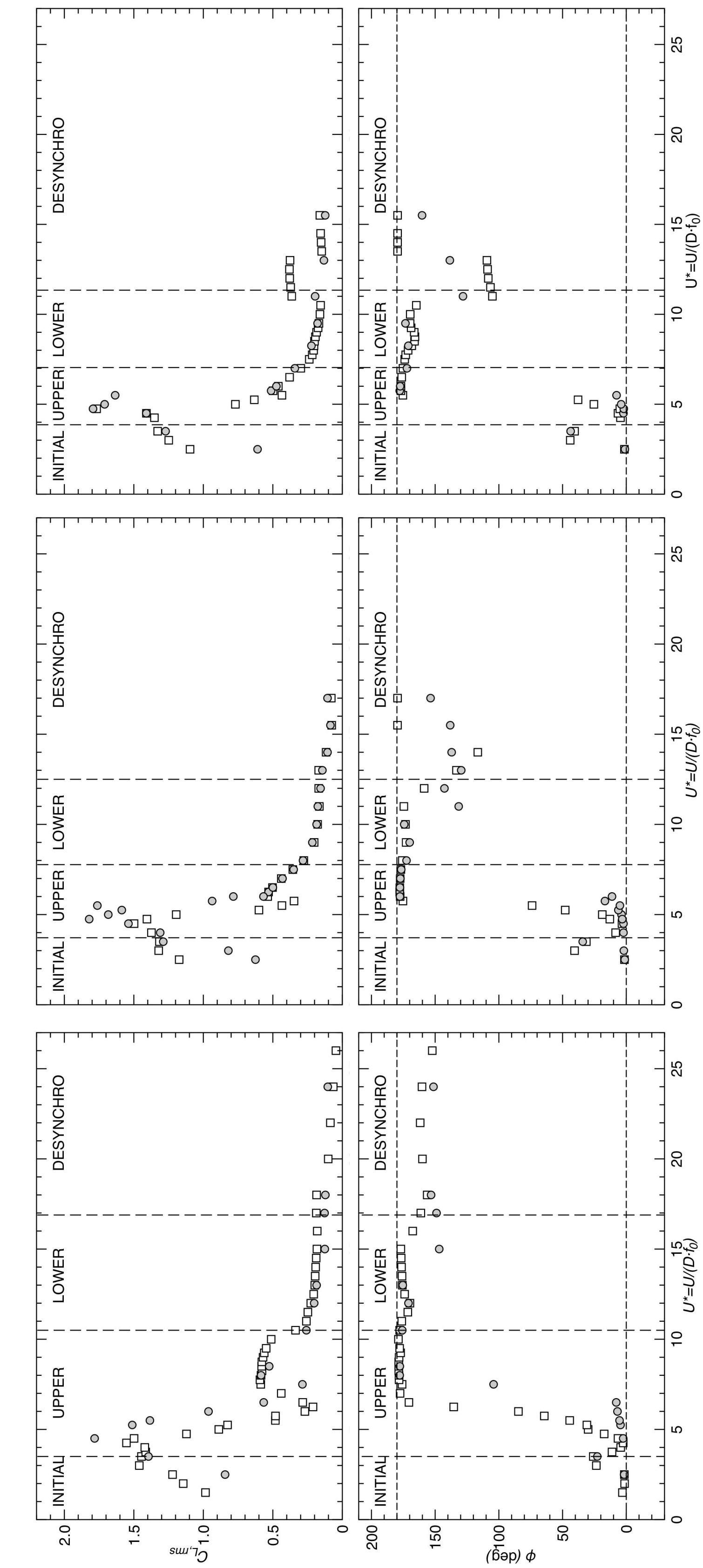

(d) $m^* = 1.2$ (e) $m^* = 2.4$ (f) $m^* = 3.6$

Figure 4.17: Comparison of the CFD results obtained by the variation of mass ratio. Upper figures root mean square (rms) of the total force C_L Vs reduced velocity U^*. Bottom figures phase angle variation ϕ Vs reduced velocity U^*. For all figures empty square 2D URANS and grey points 3D URANS.

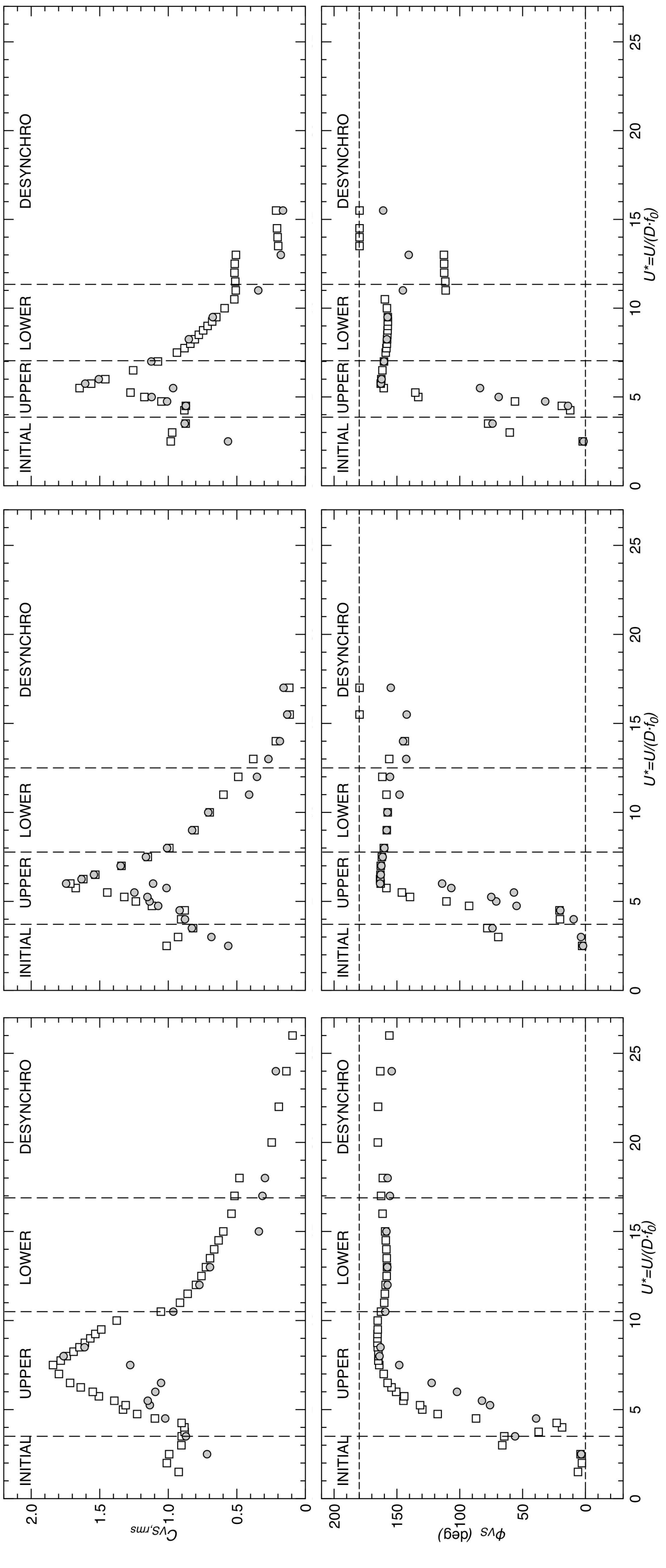

(a) $m^* = 1.2$

(b) $m^* = 2.4$

(c) $m^* = 3.6$

Figure 4.18: Comparison of the CFD results obtained by the variation of mass ratio. Upper figures root mean square (rms) of the vortex shedding force C_{VS} Vs reduced velocity U^*. Bottom figures phase angle variation ϕ_{VS} Vs reduced velocity U^*. For all figures empty square 2D URANS and grey points 3D URANS.

4.4.2 Sdof-mf model results

The results obtained performing CFD simulations were analysed using the already presented *sdof-mf* model. The following plots were obtained assuming standard values of the added mass/drag coefficients and a standard value of the Strouhal number for subcritical regime, i.e. $C_A = 1.0$, $C_D = 1.6$ and St $= 0.2$[81, 80].
The application of the *sdof-mf* model enables us to highlight the differences in the harmonic content of the forcing term using both 2D and 3D simulations to identify the model coefficients.
The vortex shedding lift force is presented according to the characteristic frequency in Fig. 4.19(c) with emplty symbols for the 2D cases and grey symbols for the 3D cases.
Squares correspond to the term closest to the Strouhal frequency in the entire U^* range investigated. Circles correspond to the double Strouhal frequency in the initial and upper branch, then the synchronisation frequency f^*_{lower} at lock-in and finally $1/2 \cdot f_{\mathrm{St}}$ in the desynchronisation region. Triangles correspond to the triple Strouhal frequency in the initial and upper branch, the triple lock-in frequency in the synchronisation region and $3/2 \cdot f_{\mathrm{St}}$ in the desynchronisation region.
Both the 2D and the 3D cases, show the same harmonic content even in areas where different values of non-dimensional amplitude and frequency ratio are found.
From the results of the *sdof-mf* parameter identification shown in Fig. 4.19, it is clear that the 3D case shows much lower amplitudes of the first component of the forcing term in the upper branch. Nonetheless, as seen in Fig. 4.16, the motion response of the 3D case shows higher amplitudes in the upper branch compared to the 2D case. This can be explained by the major contribution given by the third harmonic in this range of reduced velocity. From this it is evident that vortex-shedding force $C_{VS}(t)$ is not well suited for a monochromatic model for any U^*, whereas it can be approximated well by three harmonics in the whole U^*. This once again shows the capabilities of the *sdof-mf* model in the reproduction of the cylinder response even for complex vortex shedding forces. Due to their representativeness, Fig. 4.20 and Fig. 4.21 show respectively the fitting of the force and the cylinder displacement obtained with the *sdof-mf* for the cases $m^* = 1.2$ $U^* = 5.50$ and $m^* = 3.6$ $U^* = 3.50$.

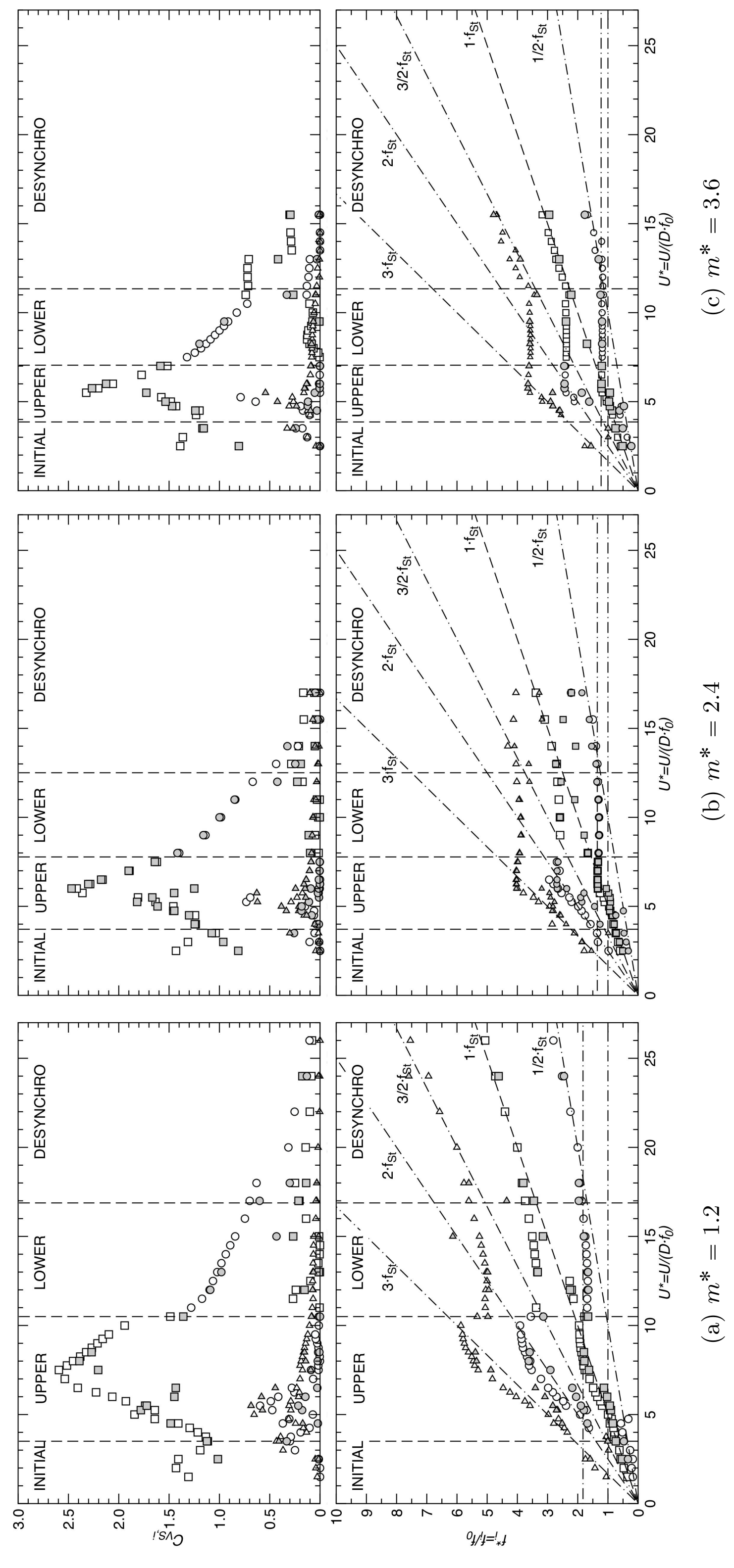

(a) $m^* = 1.2$

(b) $m^* = 2.4$

(c) $m^* = 3.6$

Figure 4.19: Upper figures: vortex shedding lift coefficients $\overline{C_{VS_i}}$. Bottom figures: frequencies $(f_i/f_0) = \theta_i \cdot f_{St}/f_0$, $i = 1, 3$ of the *sdof-mf* model Vs U^*, oblique dashed lines correspond to $0.5 \cdot f_{St}, 1 \cdot f_{St}, 2 \cdot f_{St}$ and $3 \cdot f_{St}$, where f_{St} is the nominal Strouhal frequency. For all figures empty symbols 2D URANS and grey symbols 3D URANS.

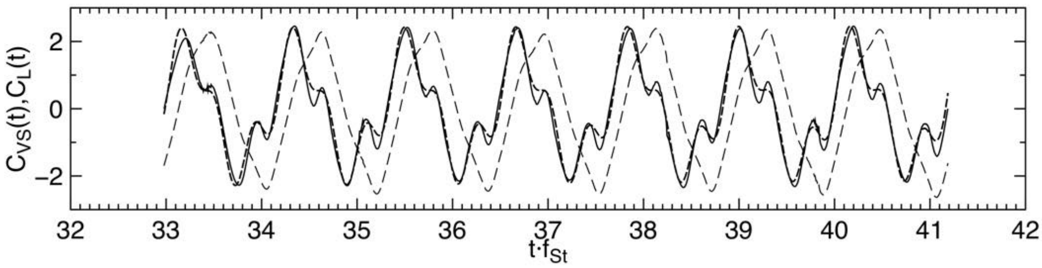

(a) $m^* = 1.2$, $U^* = 5.50$

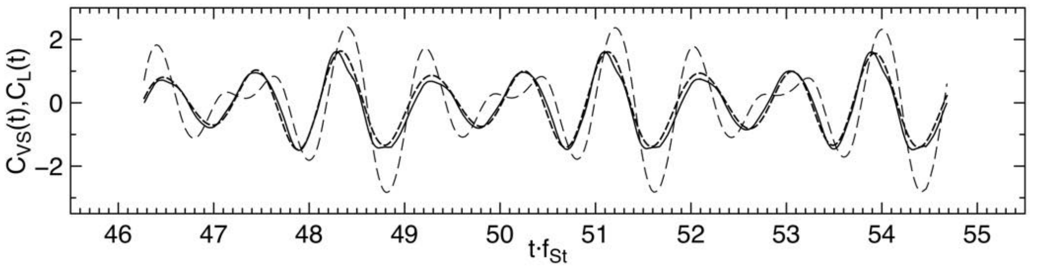

(b) $m^* = 3.6$, $U^* = 3.50$

Figure 4.20: Comparison between time-domain non-dimensional total $C_L(t)$ and vortex shedding $C_{VS}(t)$ obtained via CFD and via *sdof-mf* model in Eq. (4.8).(- - - -) = total force (present CFD); (——) = vortex shedding force (present CFD); (**- - - -**) = *sdof-mf*.

4.4.3 Conclusions

Summarising, the analysis has been conducted with the proposed *sdof-mf* model and PI on the 3D URANS. The simulations are carried out changing systematically the values of the mass ratio for a wide range of reduced velocity. The results from the application of the *sdof-mf* highlight the large influence of the ultra/sub harmonic content of the cylinder motion on maximum amplitude at lock-in.

From the comparison of the 3D results with the corresponding 2D results, it has been found that the bi-dimensional simulations do not show important discrepancies among each other. Nevertheless the non-dimensional amplitude of the cylinder motion and/or the frequency ratio differ for some reduced velocity, the harmonic content found by the application of *sdof-mf* model is the same for both 2D and 3D cases. From these results it can be argued that, in order to discover the influences of other main VIV parameters (such as damping ratio or Reynolds number), the VIV time series from a simplified 2D approach can be used for a first-step analysis with the *sfof-mf* model.

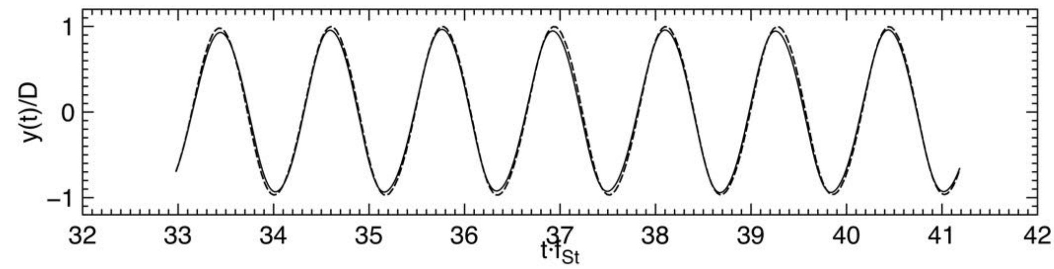

(a) $m^* = 1.2$ $U^* = 5.50$

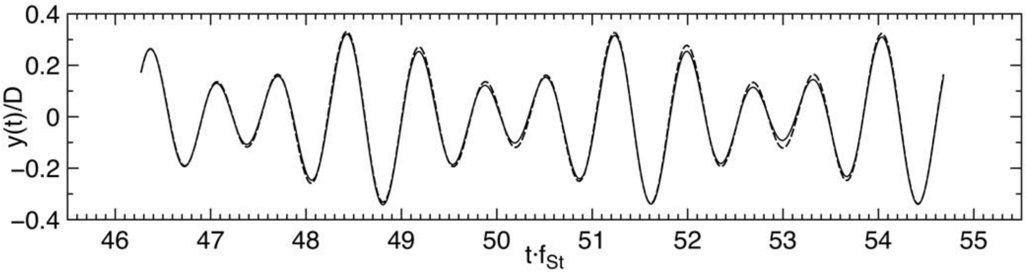

(b) $m^* = 3.6$, $U^* = 3.50$

Figure 4.21: Comparison between time-domain non-dimensional cylinder motion $y(t)/D$ obtained via CFD and via *sdof-mf* model in Eq. (4.6).
(——) = present CFD; (- - - -) = *sdof-mf*.

4.5 Final remarks

In the presented chapter we have focused on the presentation and evaluation of the applicability of proposed *sdof-mf* model with PI. From the overall results, it emerges that the *sdof-mf* model reproduces the time-domain cylinder motion and vortex shedding lift force quite accurately. The parameters of the *sdof-mf* model show a fair and consistent variation over the entire range of U^* and for all m^*.
The systematic application of the *sdof-mf* model on the 2D URANS time trace, provides a rather deep insight into the characterisation of the vortex induced lift force. In particular, it emerges that ultra- or sub-harmonic behaviour is systematically found, with the magnitude of these additional harmonic terms that depend on the mass ratio m^*. In some cases, they become the dominant part of the vortex shedding lift force. In particular at low m^*, the typical sharp drop of A^* between the lower branch and the desynchronisation regime disappears, and a dominant sub-harmonic term in both motion and vortex shedding lift force is observed; for increasing U^*, this sub-harmonic frequency keeps the control of the system, it grows almost linearly and correspondingly A^* decreases slowly. The further application of the *sdof-mf* model on the 3D URANS results for the same range of values (m^*-U^*) highlight how the considerations made starting from the study conducted with *sdof-mf* model on temporal traces obtained from the 2D approach are valid. The only discrepancy were found in the upper branch region where the magnitude of the additional harmonic terms become more pronounced in the 3D cases. Therefore, in order to discover the influence of the other main VIV parameters (such as damping ratio or Reynolds number) the use of 2D CFD simulation cloud be valid.

Chapter 5

Summary and Conclusions

This Thesis focuses on the numerical study of the Vortex-Induced Vibrations phenomenon of an elastically mounted rigid circular cylinder with one-degree-of-freedom (1-DOF). The numerical simulations presented follow the time-line of the undertaken studies. The new knowledge acquired during the studies done has been used to extend the research itself. The results achieved during the development of this thesis are briefly summarized here.

In the first part, an in-depth numerical study of 1-DOF VIV in cross-flow direction is extensively investigated. The numerical studies have been carried out using different numerical model techniques. The verification process has been made considering the numerical experiments of Khalak and Williamson. The numerical results found can be briefly summarised considering each used model one at a time. The bi-dimensional URANS simulations have been able to capture the experimental amplitude response only in the initial and in the lower branch, while the frequency response has been reasonably well captured for all the ranges of flow regimes considered.
The three-dimensional URANS simulations predict correctly the maximum amplitude in the upper branch region, where the bi-dimensional simulation fails, but some over-predictions of the values of amplitude remain in the desynchronisation zone. Some discrepancies with the experimental data regarding the frequency response have been found in the upper branch region. As reported in the experiments in the upper branch region, the oscillation frequency follows the Strouhal frequency, while in 3D simulation cases it is equal to the natural frequency in water.
The more advanced SAS method improves the overall results in terms of amplitude of cylinder response. In particular it happens in the desynchronisation zone where the major deviations with the experimental results have been highlighted. Regarding the response in terms of frequency the same results as the 3D URANS simulation have been found.
The application of different initial conditions has shown that both URANS and SAS models are able to capture the hysteretic or/and the intermittent nature of the transition between one branch and the next. Despite the variation of initial conditions, the deviations in terms of oscillation frequency with the experimental data remain along the upper branch region.

At this point it is necessary to note that Khalak and Williamson conducted the experiments with a vertical-piercing cylinder in a free-surface water channel; in order to minimize the 3D effects at the bottom of the cylinder they installed a fixed flat horizontal plate at $0.04D$ from the bottom of the cylinder. This could have led to some variations in the results compared to the same experiments without the fixed flat horizontal plate at the bottom of the cylinder. These assumptions should however be validated using more advanced numerical techniques (i.e. LES) before a definitive answer can be given to the deviation found in the upper branch region.
From the analysis of the wake flow in span-wise direction it has been found that the three-dimensionality of the flow is stronger in the the transition zones. In the initial and lower branch regions three-dimensional flow effects are lower. The visualization of the wake velocity field confirms that the vortex shedding modes agree with the Willamson-Rosko map plotted on the "true" reduced velocity.
The analysis of the phase between the cylinder response and the fluid forces confirms that the transition between the upper and lower branch is associated with the phase jump ϕ_L between the transverse oscillation and the total force. On the other hand, it is not clear if the phase jump ϕ_{VS} between the transverse oscillation and the vortex shedding force could be the cause of the transition between the initial branch and the upper branch as it is not shown in our 3D simulations results. The only correspondence with the ϕ_{VS} phase jump concerns the relationship with oscillation frequency. Indeed it has been experimentally verified that as soon as the oscillation frequency exceeds the value of the natural frequency, phase jump ϕ_{VS} occurs.

In the second part, an Uncertainty Quantification (UQ) study for the Menter SST (Shear Stress Transport) turbulence models due to the epistemic uncertainty in closure coefficient has been conducted. A methodology based on a Polynomial Chaos Expansion (PCE) decomposition has been developed to be applied to the VIV case of a bi-dimensional oscillating cylinder mounted elastically with a single degree of freedom. The Sobol indices (non-linear global sensitivity indices based on the variance decomposition) are used to give a classification to the relative contribution of each closing coefficient to the total uncertainty of the output variables. As output variables the non-dimensional amplitude and the non-dimensional frequency are taken. The quantification results identify a set of four coefficients that contribute most to uncertainty quantities. This information will reduce the amount of uncertainty in the output significantly for vortex-induced vibration on a circular cylinder.

In the third part, a novel single-degree-of-freedom multi-frequency model (*sdof-mf*) for the prediction of VIV of an elastically mounted circular cylinder in cross flow has been developed. The model treats the total hydrodynamic force as the sum of conventional Morrison-like inertia and drag terms related to the cylinder motion in still fluid plus additional harmonics that account for the lift force induced by vortex shedding. Amplitudes, frequencies and phase lags of these harmonics are identified using a Parametric Identification (PI) procedure applied to time domain data of vortex induced force,

obtained by numerical simulations. From the overall results, it emerges that the *sdof-mf* model exhibits promising and consistent capabilities in the reproduction of the vortex shedding forces and cylinder motion, in terms of both amplitudes and frequencies.
The systematic application of the *sdof-mf* model for a wide range of U^* and for all m^* provides a rather deep insight into the characterisation of the vortex induced lift force. In particular, it emerges that ultra- or sub-harmonic behaviour is systematically found, with a magnitude of these additional harmonic terms that depend on the mass ratio m^*. In some cases, they become the dominant part of the vortex shedding lift force. Especially at low m^*, the typical sharp drop of A^* between the lower branch and the desynchronisation regime disappears and a dominant sub-harmonic term in both motion and vortex shedding lift force is observed; for increasing U^*, this sub-harmonic frequency keeps the control of the system, it grows almost linearly and correspondingly A^* decreases slowly.

5.1 Proposals for Future Work

The simpler problem of only 1-DOF with a single rigid circular cylinder has been specially selected in order to validate the CFD procedures and acquire a better assessment of the mesh requirements, turbulence models and computational resource for more complex VIV problems such as flexible cylinders or two or more circular cylinders in tandem arrangement. However, before moving on to the study of these more complex problems, a series of studies on the 1-DOF single cylinder must be undertaken. The first concerns the use of more advanced numerical techniques. In particular, the DES and LES techniques have been the subject of the last doctoral period. A series of studies based on fixed cylinder in uniform flow have already been undertaken in order to find the best numerical and grid assessment that these advanced techniques need.
A second parallel study concerns the application of the uncertainty analysis strategy to the three-dimensional VIV case of an oscillating cylinder. The idea is to use only the four coefficients that contribute most to uncertainty quantities for the bi-dimensional case in order to reduce the number of evaluations needed to quantify the uncertainty in the three-dimensional cases.
Another proposal is to consider the study of the cross flow motion of two elastically mounted cylinders in tandem arrangement. The first step investigation, via 2D URANS based simulations, has already been presented during the NAV2018 conference [86]. In the case of two elastically mounted cylinders in tandem arrangement, the downstream cylinders is affected not only by the VIV phenomenon but also by the wake flow of the upstream cylinder. This phenomenon is called Wake Induced Vibration (WIV). The results of this first step investigation are in good agreement with experimental data. But considering the strong complexity of the phenomena involving VIV and WIV, a close insight with more sophisticated 3D simulations is required in order to properly capture the coupling between wake and cylinder motion.
Finally, the application *sdof-mf* model to the case of two elastically mounted cylinders in tandem arrangement is planned.

Appendices

Appendix A

Levenberg-Marquardt Method

The Levenberg-Marquardt algorithm was developed in the early 1960's to solve non-linear least squares problems. Least squares problems arise in the context of fitting a parametrised function to a set of measured data points by minimizing the sum of the squares of errors between the data points and the function. When the fit function depends nonlinearly on the set of M unknown parameters a_k $(k = 1, 2, \ldots, M)$ the least squares problem is nonlinear.
Nonlinear least squares methods iteratively reduce the sum of the squares of the errors between the function and the measured data points through a sequence of updates to parameter values. Marquardt [83] put forth an elegant method, related to an earlier suggestion of Levenberg [82], for varying smoothly between the extremes of the inverse-Hessian method and the steepest descent method. The later method is used far from the minimum, switching continuously to the former as the minimum is approached. This Levemberg-Marquardt method works very well in practice and has become the standard of nonlinear least-squares routines.

Chi-Squared error criterion

Suppose that we are fitting a function $y(x; a)$ of an independent variable x and a vector of M parameters $\mathbf{a}$ to a set of N data points (x_i, y_i), it is customary and convenient to minimise the sum of the weighted squares of the errors (or weighted residuals) between the measured data y_i and the curve-fit function $y(x, \mathbf{a})$. This scalar-valued goodness-of-fit measure is called the *chi-squared error criterion* because the sum of squares of normally-distributed variables is distributed as the chi-squared distribution.

$$\chi^2(\mathbf{a}) = \sum_{i=1}^{N} \left[\frac{y(x_i) - y(x_i; \mathbf{a})}{\sigma_i} \right] \tag{A.1}$$

where σ_i is the measurement error (standard deviation) for measurement $y(x_i)$.
If the function $y(x, \mathbf{a})$ is nonlinear in the model parameters $\mathbf{a}$, then the minimisation

of χ^2 with respect to the parameters must be carried out iteratively. The goal of each iteration is to find a perturbation $\delta\mathbf{a}$ to the parameters $\mathbf{a}$ that reduces χ^2.

Nonlineal model

Take some particular point P as the origin of the coordinate system with coordinates $\mathbf{x}$. Then any function f can be approximated by its Taylor series

$$\begin{aligned} f(\mathbf{x}) &= f(P) + \sum_i \frac{\partial f}{\partial x_i} x_i + \frac{1}{2} \sum \sum_{i,j} \frac{\sum^2 f}{\partial x_i \partial x_j} + \dots \\ &\approx c - \mathbf{b} \cdot x + \frac{1}{2} \mathbf{x} \cdot \mathbf{A} \cdot \mathbf{x} \end{aligned} \tag{A.2}$$

where

$$c \equiv f(P) \qquad \mathbf{b} \equiv -\nabla f|_P \qquad [A]_{ij} \equiv \frac{\partial^2 f}{\partial x_i \partial x_j}\Big|_P . \tag{A.3}$$

The matrix $\mathbf{A}$ whose components are second partial derivative matrix of the function is called *Hessian matrix* of the function at P.
We now consider the χ^2 merit function, previously defined (A.1), and determine best-fit parameters by its minimisation. Sufficiently close to the minimum, we expect the χ^2 function to be well approximated by a quadratic form (A.2), which we can write as

$$\chi^2(\mathbf{a}) \approx \gamma - \mathbf{d} \cdot \mathbf{a} + \frac{1}{2} \mathbf{a} \cdot \mathbf{D} \cdot \mathbf{a}. \tag{A.4}$$

where d is an M-vector and D is an $M \times M$ matrix. If the approximation is a good one, we know how to jump from the current trial parameters $\mathbf{a}_{cur}$ to the minimising ones $\mathbf{a}_{min}$ in a single leap, namely

$$\mathbf{a}_{min} = \mathbf{a}_{cur} + \mathbf{D}^{-1} \left[-\nabla \chi^2(\mathbf{a}_{cur}) \right] \tag{A.5}$$

On the other hand, (A.4) might be a poor local approximation to the shape of the function that are tying to minimise at $\mathbf{a}_{cur}$. In that case, just about all we can do is to take a step down the gradient, as in the steepest descendent method. In other words,

$$\mathbf{a}_{next} = \mathbf{a}_{cur} - const. \times \nabla \chi^2(\mathbf{a}_{cur}) \tag{A.6}$$

where the constant is small enough not to exhaust the downhill direction.
To use (A.5) and (A.7), we must be able to compute the gradient of the χ^2 function at any set of parameters $\mathbf{a}$. To use (A.5) we also need the matrix $\mathbf{D}$, which is the second derivative matrix (Hessian matrix) of the χ^2 merit function, at any $\mathbf{a}$.
At this point we have no way of directly evaluating the Hessian matrix. We are only given the ability to evaluate the function to be minimized and (in some cases) its gradient. Therefore, we have to resort to iterative methods not just because our function is non linear, but also in order to build up information about the Hessian matrix. Through the use of iterative techniques the Hessian matrix is known to us. Thus we are free to use (A.5) whenever we care to do so. The only reason for using (A.7) will be failure of (A.5) to improve the fit, signaling failure of (A.4) as good local approximation.

Calculation of the Gradient and Hessian

The gradient of χ^2 with respect to the parameters $\mathbf{a}$, which will be zero at the χ^2 minimum, has components

$$\frac{\partial \chi^2}{\partial a_k} = -2 \sum_{i=1}^{N} \frac{[y_i - y(x_i;\mathbf{a})]}{\sigma_i^2} \frac{\partial y(x_i;\mathbf{a})}{\partial a_k} \qquad k = 1, 2, \ldots, M. \tag{A.7}$$

Taking an additional partial derivative gives

$$\frac{\partial^2 \chi^2}{\partial a_k \partial a_l} = 2 \sum_{i=1}^{N} \frac{1}{\sigma_i^2} \left[\frac{\partial y(x_i;\mathbf{a})}{\partial a_k} \frac{\partial y(x_i;\mathbf{a})}{\partial a_l} - [y_i - y(x_i;\mathbf{a})] \frac{\partial^2 y(x_i;\mathbf{a})}{\partial a_l \partial a_k} \right]. \tag{A.8}$$

It is conventional to remove the factors of 2 by defining

$$\beta_k \equiv -\frac{1}{2} \frac{\partial \chi^2}{\partial a_k} \qquad \alpha \equiv \frac{1}{2} \frac{\partial^2 \chi^2}{\partial a_k \partial a_l} \tag{A.9}$$

making $[\alpha] = 1/2\,D$ in equation (A.5), in terms of which that equation can be rewritten as the set of linear equations

$$\sum_{l=1}^{M} \alpha_{kl} \delta a_l = \beta_k \tag{A.10}$$

This set is solved for the increments δa_l that, added to the current approximation, give the next approximation.
The steepest descent formula (A.7) by contrast simply step off from the current trial value in the direction of the negative gradient of χ^2. Thus

$$\delta a_l = const. \times \beta_l. \tag{A.11}$$

Note that the components α_{kl} of Hessian matrix (A.8) depend both on first derivatives and second derivatives of the basis functions with respect to their parameters. The inclusion of the second-derivative term can in fact be destabilising if the model fits badly or is contaminated by outlier points that are unlikely to offset by compensating points of opposite sign. Therefore, in this treatment we will ignore the second derivative. We will always use as the definition of α_{kl} the formula

$$\alpha_{kl} = \sum_{i=1}^{N} \frac{1}{\sigma_i^2} \left[\frac{\partial y(x_i;\mathbf{a})}{\partial a_k} \frac{\partial y(x_i;\mathbf{a})}{\partial a_l} \right] \tag{A.12}$$

This expression has no effect at all on what final set of parameters $\mathbf{a}$ is reached, but only affects the iterative route that is taken in getting there. The condition at the χ^2 minimum, that $\beta_k = 0$ for all k, is independent from how $[\alpha]$ is defined.

Marquardt algorithm

The algorithm is based on two elementary, but important, insights. The first insight is that the components of the Hessian matrix, even if they are not usable in any precise fashion, give some information about the order-of-magnitude scale of the problem.
The quantity χ^2 is nondimensional, i.e. it is a pure number; this is evident from definition (A.1). On the other hand, β_k has the dimensions of $1/a_k$, which may well be dimensional. In fact, each component of β_k can have different dimensions.
The constant of proportionality between β_k and δa_k must therefore have the dimension of a_k^2. Scan the components of $[\alpha]$ and you see that there is only one obvious quantity with these dimensions, and that is $1/\alpha_{kk}$, the reciprocal of the diagonal element. So that must set the scale of constant by some (nondimensional) fudge factor λ, with the possibility of setting $\lambda >> 1$ to cut down the step. In other words, replace equation (A.11) by:

$$\delta a_l = \frac{1}{\lambda \alpha_{ll}} \beta_l \qquad \lambda \alpha_{ll} \delta a_l = \beta_l. \tag{A.13}$$

It is necessary that a_{ll} be positive, but this is guaranteed by definition (A.12).
The second insight is that equations (A.13) and (A.10) can be combined if we define a new matrix α' by the following prescription

$$\begin{aligned} \alpha'_{jj} &\equiv \alpha_{jj}(1+\lambda), \\ \alpha'_{jk} &\equiv \alpha_{jk} \qquad (j \neq k) \end{aligned} \tag{A.14}$$

and then replace both (A.13) and (A.10) by

$$\sum_{l=1}^{M} \alpha'_{kl} \delta a_l = \beta_k. \tag{A.15}$$

When λ is very large, the matrix α' is forced into being diagonally dominant so equation (A.15) goes over to be identical to (A.13). On the other hand, as λ approaches zero, equation (A.15) goes over (A.10).
Given an initial guess for the set of fitted parameters $\mathbf{a}$, the recommended Marquardt recipe is as follows:

1. Compute $\chi^2(\mathbf{a})$.
2. Pick a modest value for λ, say $\lambda = 0.001$.
3. Solve the linear equation (A.15) for $\delta\mathbf{a}$ and evaluate $\chi^2(\mathbf{a} + \delta\mathbf{a})$.
4. If $\chi^2(\mathbf{a}+\delta\mathbf{a}) \geqslant \chi^2(\mathbf{a})$, increase λ by a factor of 10 (or any other substantial factor) and go back to (3).
5. If $\chi^2(\mathbf{a} + \delta\mathbf{a}) < \chi^2(\mathbf{a})$, decrease λ by a factor of 10, update the trial solution $\mathbf{a} \leftarrow \mathbf{a} + \delta\mathbf{a}$, and go back to (3).

A condition for stopping is also necessary. One might stop iterating on the first or second occasion that χ^2 decreases by a negligible amount, say either less than 0.1 absolutely of (in case roundoff prevents that being reached) some fractional amount like 10^{-3}. Do not stop after a step where χ^2 increases: that only shows that λ has not yet adjusted itself optimally.
Once the acceptable minimum has been found, $\lambda = 0$ is set and the matrix is computed as

$$[C] \equiv [\alpha]^{-1} \tag{A.16}$$

which is the estimated covariance matrix of the standard errors in the fitted parameters **a**.

List of Publications

Riccardo Pigazzini, Giorgio Contento, **Simone Martini**, Thomas Puzzer, Mitja Morgut e Andrea Mola. «VIV analysis of a single elastically-mounted 2D cylinder: Parameter Identification of a single-degree-of-freedom multi-frequency model». In: Journal of Fluid and 78 (2018), pp. 299–313. doi: 10.1016/j.jfluidstructs.2018.01.005.

Thomas Puzzer, Riccardo Vasco Pigazzini, Giorgio Contento, Mitja Morgut e **Simone Martini**. «An open-source fully-automated pre-processing procedure for planing hull CFD simulations». In: 23th Symposium on Theory and Practice of Shipbuilding SORTA 2018. Vol. 1. Branko Blagojevic, 2018, pp. 1–8.

Riccardo Vasco Pigazzini, Giorgio Contento, **Simone Martini**, Mitja Morgut e Thomas Puzzer. «An investigation on VIV of a single 2D elastically-mounted cylinder with different mass ratios». In: Journal of marine science and technology (2018), pp. 1–14. doi: 10.1007/s00773-018-0607-6

Riccardo Pigazzini, Thomas Puzzer, **Simone Martini**, Mitja Morgut, Giorgio Contento, Inno Gatin, Vuko Vukcevic, Hrvoje Jasak, Ermina Begovich, Sebastiano Caldarella, Marco De Santis e Amedeo Migali. «Experimental and Numerical Prediction of the Hydrodynamic Performances of a 65 ft Planing Hull in Calm Water». In:NAV2018 - Technology and Science for the Ships of the Future. Vol. 1. Amsterdam, Berlin, Washington DC: IOS Press, 2018. isbn: 9781614998709. doi: 10.3233/978-1-61499-870-9-480.

Mitja Morgut, Dragica Jošt, Aljaž Škerlavaj, Enrico Nobile, Giorgio Contento, Riccardo Pigazzini, Thomas Puzzer e **Simone Martini**. «Numerical Predictions of a Model Scale Propeller in Uniform and Oblique Flow». In: NAV2018 - Technology and Science for the Ships of the Future. Vol. 1. IOS Press, (2018), pp. 426–433.doi: 10.3233/978-1-61499-870-9-426.

Simone Martini, Riccardo Pigazzini, Thomas Puzzer, Mitja Morgut e Giorgio Contento. «Numerical Investigation of 2D Vortex Induced and Wake Induced Vibrations of Two Circular Cylinders in Tandem Arrangement». In: NAV2018 - Technology and Science for the Ships of the Future. Vol. 1. IOS Press, (2018), pp. 348–355. doi0.3233/978-1-61499-870-9-348.

Marco De Santis, Amedeo Migali, Riccardo Pigazzini, Thomas Puzzer, **Simone Martini**, Mitja Morgut, Giorgio Contento, Riccardo Buiatti, Fabio De Luca, Flavio Balsamo e Fabio Brunetti. «Case Study: Sea Trials on a 65 ft Planing Hull in Waves». In: Full Scale Ship Performance. The Royal Institution of Naval Architects, (2018). isbn: 978-1-

909024-81-6

Mitja Morgut, Dragica Jošt, Aljaž Škerlavaj, Enrico Nobile, Giorgio Contento, Riccardo Pigazzini, Thomas Puzzer e **Simone Martini**. «Numerical simulations of a cavitating propeller in uniform and oblique flow». In: International Shipbuilding Progress 66 (2019), pp. 77–90. doi: 10.3233/ISP-180257

Simone Martini, Riccardo Pigazzini, Mitja Morgut. «Numerical VIV analysis of a single elastically-mounted cylinder: comparison between 2D and 3D URANS simulations». (*Submitted to Journal of Fluids and Structures on 09/07/2020*)

References

[1] Michael M Bernitsas et al. "VIVACE (Vortex Induced Vibration Aquatic Clean Energy): A new concept in generation of clean and renewable energy from fluid flow". In: *Journal of Offshore Mechanics and Arctic Engineering* 130.4 (2008), p. 041101.

[2] T. Sarpkaya. *A critical review of instrinsic nature of vortex induced vibration*. Tech. rep. Naval Postgraduate School, Montery, California, 2003.

[3] Anatol Roshko. *Experiments on the flow past a circular cylinder at very high Reynolds*. Tech. rep. Guggenheim Aeronautical Laboratory, California Institute of Technology, 1960.

[4] John H. Lienhard. "Synopsis of lift, drag, and vortex frequency data for rigid circular cylinders". In: *Washington state University* Bulletin 300 (1966), p. 30.

[5] A. Khalak and C.H.K. Williamson. "Motions, forces and mode transitions in vortex-induced vibrations at low mass-damping". In: *Journal of Fluids and Structures* 13 (1999), pp. 813–851.

[6] P.W. Bearman. "Vortex shedding from oscillating bluff bodies". In: *Annual review of fluid mechanics* 16.1 (1984), pp. 195–222.

[7] T. Sarpkaya. "Fluid forces on oscillating cylinders". In: *Journal of Waterway, Port, Coastal and Ocean Engineering* 107 (1978), pp. 275–291.

[8] R.D. Gabbai and H. Benaroya. "An overview of modeling and experiments of vortex-induced vibration of circular cylinders". In: *Journal of Sound and Vibration* 282 (2005), pp. 575 –616.

[9] C.H.K. Williamson and R. Govardhan. "Vortex-Induced Vibration". In: *Annual review of fluid mechanics* 36.423-55 (2004).

[10] C.H.K. Williamson and R.N. Govardhan. "A brief review of recent results in vortex-induced vibrations". In: *Journal of Wind Engineering and Industrial Aerodynamics* 96 (2008), pp. 713–735.

[11] R.D. Blevins. *Flow-induced vibrations*. Van Nostrad Reinold, New York, 1990.

[12] B. M. Summer and J. Fredsøe. *Hydrodynamics around cylindrical structures*. Word scientific, Singapore, 1997.

[13] C.C. Feng. "The measurement of vortex-induced effects in flow past a stationary and oscillating circular and D-section cylinders". Master's Thesis. University of British Columbia, 1968.

[14] D. Brika and Laneville A. "Vortex-induced vibrations of a long flexible circular cylinder." In: *Journal of Fluids Mechanics* 250 (1993), pp. 481–508.

[15] A Khalak and CHK Williamson. "Dynamics of a hydroelastic cylinder with very low mass and damping". In: *Journal of Fluids and Structures* 10.5 (1996), pp. 455–472.

[16] A. Khalak and C. H. K. Williamson. "Fluid forces and dynamics of a hydroelastic structure with very low mass and damping". In: *Journal of Fluid and Structures* 11 (1997), pp. 973–982.

[17] R. Govardhan and C. H. K. Williamson. "Modes of vortex formation and frequency response of a freely vibrating cylinder". In: *Journal of Fluid Mechanics* 420 (2000), pp. 85–130.

[18] H. Lamb. *Hydrodynamics*. Cambridge university press, 1932.

[19] O. M. Griffin and S. E. Ramberg. "Some recent studies of vortex shedding with application to marine tubulars and risers." In: *Transactions ASME Journal of Energy Resource Technology* 104 (1982), pp. 2–13.

[20] R. A. Skop and S. Balasubramanian. "A new twist on an old model for vortex-excited vi- brations". In: *Journal of Fluid and Structures* 11 (1997), pp. 395–412.

[21] M.S. Triantafyllou and M.A. Grosenbaugh. "Prediction of vortex-induced vibrations in sheared flows". In: *Flow-Induced Vibration Bearman* (1995).

[22] C.H.K. Williamson and A. Roshko. "Vortex formation in the wake of an oscillating cylinder". In: *Journal of fluids and structures* 2.4 (1988), pp. 355–381.

[23] J. Lighthill. "Wave loading on offshore structures". In: *Journal of Fluid Mechanics* 173 (1986), pp. 667–681.

[24] E.l Guilmineau and P. Queutey. "Numerical simulation of vortex-induced vibration of a circular cylinder with low mass-damping in a turbulent flow". In: *Journal of fluids and structures* 19.4 (2004), pp. 449–466.

[25] Z.Y. Pan, W.C. Cui, and Q.M. Miao. "Numerical simulation of vortex-induced vibration of a circular cylinder at low mass-damping using RANS code". In: *Journal of Fluids and Structures* 23.1 (2007), pp. 23–37.

[26] J.B.V. Wanderley et al. "Vortex-induced vibration of an elastically mounted circular cylinder using an upwind TVD two-dimensional numerical scheme". In: *Ocean Engineering* 35.14 (2008), pp. 1533–1544.

[27] Wei Wu, Michael M. Bernitsas, and Kevin Maki. "RANS simulation versus experiments of flow induced motion of circular cylinder with passive turbulence control at 35,000< RE < 130,000". In: *Journal of Offshore Mechanics and Arctic Engineering* 136.4 (2014), p. 041802.

[28] O. K. Kinaci. "2-D URANS Simulations of Vortex Induced Vibrations of Circular Cylinder at Trsl3 Flow Regime". In: *ournal of Applied Fluid Mechanics* 9.5 (2016), pp. 2537–2544.

[29] H. M. Blackburn, R. N. Govardhan, and C. H. K. Williamson. “A complementary numerical and physical investigation of vortex-induced vibration A complementary numerical and physical investigation of vortex-induced vibration”. In: *Journal of Fluids and Structures* 15 (2000), pp. 481–488.

[30] G.E. Karniadakis D. Lucor J. Foo. “Vortex mode selection of a rigid cylinder subject to VIV at low mass-damping”. In: *Journal of Fluids and Structures* 20 (2005), pp. 483–503.

[31] J.S. Leontini, M.C. Thompson, and K. Hourigan. “The beginning of branching behaviour of vortex-induced vibration during two-dimensional flow”. In: *Journal of Fluids and Structures* 22 (2006), pp. 857–864.

[32] Ming Zhao et al. “Three-dimensional numerical simulation of vortex-induced vibration of an estically mounted rigid circular cylinder in steady current”. In: *Journal of Fluids and Structures* (2014).

[33] S. Dong and G. E. Karniadakis. “DNS of flow past a stationary and oscillating cylinder at Re=10000”. In: *Journal of Fluids and Structures* 20 (2005), pp. 519–531.

[34] F. Saltara, A. D’Agostini Neto, and J. I. H. Lopez. “3D CFD Simulation of Vortex-induced Vibration of Cylinder”. In: *International Journal of Offshore and Polar Engineering* 21.2 (2011), pp. 1–6.

[35] Proceedings of the Royal Society Series, ed. *The lift and drag forces on a circular cylinder in a flowing fluid.* Vol. A 277. 32–50. 1963.

[36] R.T. Hartlen and I.G. Currie. “Lift-oscillator model of vortexinduced vibration”. In: *Journal of the Engineering Mechanics* 5 (1970), pp. 577–591.

[37] Leslie Ng et al. *An Examination of Wake Oscillator Models for Vortex-Induced Vibrations.* Tech. rep. 11,298. Naval Undersea Warfare Center Division Newport, Rhode Island NUWC-NPT Technical Report, 2001.

[38] R.A. Skop and O.M. Griffin. “A model for the vortex-excited resonant response of bluff cylinders”. In: *Journal of Sound and Vibration* 2.27 (1973), pp. 225–233.

[39] W.D. Iwan and R.D. Blevins. “A model for vortex-induced oscillation of structures”. In: *Journal of Applied Mechanics* 3.41 (1974), pp. 581–586.

[40] R. Landl. “A mathematical model for vortex-excited vibrations of bluff bodies”. In: *Journal of Sound and Vibration* 2.42 (1975), pp. 219–234.

[41] M.L. Facchinetti, E. de Langrea, and F. Biolleyb. “Coupling of structure and wake oscillators in vortex-induced vibrations”. In: *Journal of Fluids and Structures* 19 (2004), pp. 123–140.

[42] E. Simiu and R.H. Scanlan. *Wind Effects on Structures.* Wiley, New York, 1986.

[43] R.I. Basu and B.J. Vickery. “Across-wind vibrations of structures of circular cross-section-part 2: development of a mathematical model for full-scale application”. In: *Journal of Wind Engineering and Industrial Aerodynamics* 1.12 (1983), pp. 75–97.

[44] I. Goswami, R.H. Scanlan, and N.P. Jones. "Vortex-induced vibration of circular cylinders—part 1: experimental data". In: *Journal of Engineering Mechanics* 11.119 (1993), pp. 2270–2287.

[45] I. Goswami, R.H. Scanlan, and N.P. Jones. "Vortex-induced vibration of circular cylinders—part 2: new model". In: *Journal of Engineering Mechanics* 11.119 (1993), pp. 2288–2302.

[46] S.S. Chen, S. Zhu, and Y. Cai. "An unsteady flow theory for vortex-induced vibration". In: *Journal of Sound and Vibration* 1.184 (1995), pp. 73–92.

[47] G.H. Koopman O.M. Griffin. "The vortex-excited lift and reaction forces on resonantly vibrating cylinders". In: *Journal of Sound and Vibration* 54.3 (1977), pp. 435–448.

[48] O. M. Griffin. "Vortex-excited cross-flow vibrations of a single cylindrical tube". In: *ournal of Pressure Vessel Technology* 102 (1980), pp. 158–166.

[49] F.R. Menter. "Two-equation eddy-viscosity turbulence models for engineering applications". In: *AIAA Journal* 32.8 (1994).

[50] F. Menter and T. Esch. "Elements of Industrial Heat Transfer Predictions". In: *16th Brasilian Congress of Mechanical Engineering*. 2001.

[51] A. Hellsten. "Some Improvements in Menter's k - w SST Turbulence Model". In: *29th AIAA Fluid Dynamics Conference*. Vol. AIAA-98-2554. 1997.

[52] U.O. Unal and O. Goren. "Vortex shedding from a circular cylinder at high Reynolds number". In: *Proc. 11th International Congress of the International Maritime Assnociation of the Mediterranean (IMAM 2005), Lisbon, Maritime Transportation and Exploitation of Ocean and Coastal Resources* 2 (2005), pp. 301–307.

[53] Andrew Li Jian Pang, Martin Skote, and Siow Yong Lim. "Modelling high Re flow around a 2D cylindrical bluff body using the k-ω (SST) turbulence model". In: *Progress in Computational Fluid Dynamics* 16.1 (2016).

[54] T.L. Morse, R.N. Govardhan, and C.H.K. Williamson. "The effect of end conditions on the vortex-induced vibrations of cylinders". In: *Journal of Fluids and Structures* 24 (2008), pp. 1227 –1239.

[55] S. Martini. "Analysis of 2D VIV of a single circular cylinder by an open-source CFD solver". MA thesis. Dept. of Engineering and Architecture, University of Trieste, 2016.

[56] R. Löhner and C. Yang. "Improved ALE mesh velocities for moving bodies". In: *Journal for Numerical Methods in Biomedical Engineering* (1996).

[57] D.A. Lysenko, I.S. Ertesvag, and K.E. Rian. "Large-Eddy Simulation of the Flow Over a CircularCylinder at Reynolds Number 2×10^4". In: *Flow turbulence and Combustion* 92.3 (2014), pp. 673–698.

[58] Tobias Holzmann. *Mathem atics, Numerics, Derivations and OpenFOAM®*. Ed. by Tobias Holzmann. 4th ed. Holzmann CFD, Dec. 2016.

[59] D.C. Wilcox. *Turbulence Modeling for CFD*. DCW Industries, Inc., 1994.

[60] R. Pigazzini et al. "VIV analysis of a single elastically-mounted 2D cylinder: Parameter Identification of a single-degree-of-freedom multi-frequency model". In: *Journal of Fluids and Structures* 78 (2018), pp. 299–313.

[61] Valerio D'Alessandro, Sergio Montelpare, and Renato Ricci. "Detached-Eddy Simulations of the flow over a cylinder at Re=3900 using OpenFOAM". In: *Computers and Fluids* 136 (2016), pp. 152–169.

[62] P. J. Roache. "Perspective: A Method for Uniform Reporting of Grid Refinement Studies". In: *Journal of Fluids Engineering* 116 (1994).

[63] L.F. Richardson and J.A. Gaunt. "The deferred approach to the limit. Part I. Sigle lattice. Part II Interpenetrating lattices." In: *Philosophical Transactions of the Royal Society of London. Series A, Containing Papers of a Mathematical or Physical Character* 226 (1927), pp. 299–361.

[64] I.B. Celik et al. "Procedure for Estimation and Reporting of Uncertainty Due to Discretization in CFD Applications". In: *Journal of Fluids Engineering* (2008).

[65] H.W. Coleman et al. "The problem with oscillatory behaviour in Grid Convergence Studies". In: *Transactions ASME* 123 (2001).

[66] M. Shur et al. "Three Dimensionality in Reynolds-Averaged Navier–Stokes Solutions Around Two-Dimensional Geometries". In: *AIAA JOURNAL* 43.6 (2005).

[67] Jinhee Jeong and Flazle Hussain. "On the identification of a vortex". In: *Journal of Fluid Mechanics* 285 (1995), pp. 69–94.

[68] F. R. Menter, M. Kuntz, and R. Bender. "A Scale-Adaptive Simulation Model for turbulent flow prediction". In: *AIAA 2003-0767 41st Aerospace Science Meeting and Exhibit, Reno,Nevada*. 2003.

[69] Y. Ergov and F. Menter. "Development and Application of SST-SAS Model in the DESIDER Project". In: *Advances in Hybrid RANS-LES Modelling*. Vol. 97. 2008, pp. 261–270.

[70] S.F. Wojtkiewicz et al. "Uncertainty Quantification In Large Computational Engineering Models". In: *Proceedings of the 42nd AIAA/ASME/ASCE/AHS/ASC-Structures, Structural Dynamics, and Materials Conference, AIAA Paper No.2001-1455*. 2001.

[71] M. Eldred et al. *DAKOTA, A Multilevel Parallel Object-Oriented Framework for Design Optimization,Parameter Estimation ,Uncertainty Quantication, and Sensitivity Analysis*. Version 4.0 Reference Manual. 2006.

[72] F.R. Menter, M. Kuntz, and R. Langtry. "Ten years of industrial experience with the SST turbulence model". In: *Proceedings of the fourth international symposium on turbulence, heat and mass transfer*. Vol. 4. 2003, pp. 625–632.

[73] NASA Langley Research Center. *The Wilcox k-omega Turbulence Model*. URL: `https://turbmodels.larc.nasa.gov/wilcox.html`.

[74] Bruno Sudret. “Global sensitivity analysis using polynomial chaos expansions”. In: *Reliability Engineering and System Safety* 93 (2008), pp. 964–979.

[75] John Schaefer et al. “Uncertainty Quanti cation of Turbulence Model Closure Coecients for Transonic Wall-Bounded Flows”. In: *22nd AIAA Computational Fluid Dynamics Conference* (2015).

[76] Aaron Erb and Serhat Hosder. “Uncertainty Analysis of Turbulence Model Closure Coecients for Shock Wave-Boundary Layer Interaction Simulations”. In: *AIAA Aerospace Sciences Meeting* (2018).

[77] T. K.West and S. Hosder. “Uncertainty Quanti cation of Hypersonic Reentry Flows with Sparse Sampling and Stochastic Expansions”. In: *Journal of Spacecraft and Rockets* 52.1 (2015), pp. 120–133.

[78] Toshimitsu Homma and Andrea Saiteli. “Importance measures in global sensitivity analysis of nonlinear models”. In: *Reliability Engineering and System Safety* 52 (1996), pp. 1–17.

[79] A. Erb and S. Hosder. “Uncertainty Analysis of Turbulence Model Closure Coecients for Wall-Bounded Attached and Separated Flows”. In: *19th AIAA Non-Deterministic Approaches Conference AIAA Paper 2017-2018.* 2017.

[80] T. Sarpkaya and M. Isaacson. *Mechanics of wave forces on offshore structures.* New York - Van Nostrand Reinhold, 1981.

[81] J.R. Morison et al. “The force exerted by surface waves on piles”. In: *Petroleum Transactions* 189 (1950), pp. 149 –154. DOI: `http://dx.doi.org/10.2118/950149-G`.

[82] K. Levenberg. “A Method for the Solution of Certain Non-linear Problems in Least Squares”. In: *Quarterly of Applied Mathematics* 2.2 (1944), pp. 164–168.

[83] D.W. Marquardt. “An Algorithm for the Least-Squares Estimation of Nonlinear Parameters”. In: *Journal of the Society for Industrial and Applied Mathematics* 11.2 (1963), pp. 431–441.

[84] W. H. Press et al. *Numerical Recepes, The art of Scientific Computing.* Cambridge University press, 1986.

[85] K. Vikestad, J.K. Vandiver, and C.M. Larsen. “Added mass and oscillation frequency for a circular cylinder subjected to vortex-induced vibrations and external disturbance”. In: *Journal of Fluids and Structures* 14 (2000), pp. 1071 –1088. DOI: `10.1006/jfls.2000.0308`.

[86] S. Martini et al. “Numerical Investigation of 2D Vortex Induced and Wake Induced Vibrations of Two Circular Cylinders in Tandem Arrangement”. In: *NAV2018 - Technology and Science for the Ships of the Future. IOS Press* 1 (2018), pp. 348–355.